



HAL
open science

Study of the anode in direct borohydride fuel cells

Pierre-Yves Olu

► **To cite this version:**

Pierre-Yves Olu. Study of the anode in direct borohydride fuel cells. Other. Université Grenoble Alpes; Université de Liège, 2015. English. NNT : 2015GREAI101 . tel-01285520

HAL Id: tel-01285520

<https://theses.hal.science/tel-01285520>

Submitted on 9 Mar 2016

HAL is a multi-disciplinary open access archive for the deposit and dissemination of scientific research documents, whether they are published or not. The documents may come from teaching and research institutions in France or abroad, or from public or private research centers.

L'archive ouverte pluridisciplinaire **HAL**, est destinée au dépôt et à la diffusion de documents scientifiques de niveau recherche, publiés ou non, émanant des établissements d'enseignement et de recherche français ou étrangers, des laboratoires publics ou privés.

Université
de Liège



UNIVERSITÉ
GRENOBLE
ALPES

THÈSE

Pour obtenir le grade de

DOCTEUR DE L'UNIVERSITÉ GRENOBLE ALPES

**préparée dans le cadre d'une cotutelle entre
l'Université Grenoble Alpes et
l'Université de Liège**

Spécialité : **Matériaux, Mécanique, Génie Civil, Electrochimie**

Arrêté ministériel : le 6 janvier 2005 - 7 août 2006

Présentée par

Pierre-Yves OLU

Thèse dirigée par **Marian CHATENET**

et codirigée par **Nathalie JOB**

préparée au sein du **Laboratoire d'Électrochimie et de Physicochimie
des Matériaux et Interfaces (Grenoble)**

et du **Department of Chemical Engineering (Liège)**

dans l'**École Doctorale I-MEP2 (Grenoble)**

et le **Collège Doctoral en Chimie Appliquée (Liège)**

Étude de l'anode pour la pile à combustible directe aux borohydrures

Thèse soutenue publiquement le **29 Octobre 2015**,
devant le jury composé de :

Monsieur, Jean-Pierre PETIT

Professeur, Université Grenoble Alpes, Président

Monsieur, Christophe COUTANCEAU

Professeur, Université de Poitiers, Rapporteur

Monsieur, Umit DEMIRCI

Professeur, Université de Montpellier, Rapporteur

Monsieur, Renaut MOSDALE

Docteur, PaxiTech, Examineur

Monsieur, Marian CHATENET

Professeur, Université Grenoble Alpes, Directeur de thèse

Madame, Nathalie JOB

Professeur, Université de Liège, Co-Directrice de thèse



Acknowledgements

First I want to thank my two advisors Nathalie Job (Liège) and Marian Chatenet (Grenoble) for being, each one in his/her own way, the two best advisors I could hope for. They were always there when needed, supportive and full of motivation as well as great scientific ideas. I enjoyed a lot these 3 years thanks to them !

I am very grateful to the members of the jury for reviewing this manuscript, and for the nice discussion during the defense. As for the reviewing, I am also grateful to the anonymous referees who discussed about the articles we submitted during this thesis, and by doing so, helped improving the overall quality of this work.

I also greatly acknowledge IDS FunMat for the financial support of this Ph.D thesis (Project 2012-10LF).

Below is a (perhaps non-exhaustive, even though I tried my best) list of thanks for the people whose help and support contributed to the work performed during this thesis:

In Strasbourg: Elena Savinova for welcoming me in her team. Marlène Rouhet for teaching me all the experimental. Sébastien Bozdech for the help with the synthesis and polishing of the VACNF electrodes. Finally, a special thanks to Antoine Bonnefont for all the good time (good at least for me) we spent working on the modeling, I learned a lot during this time.

In Grenoble: Bruno Gilles for the AFM and STM. Frédéric Maillard, Luis Castanheira and Marc Zimmermann for the FTIR experiments. Bruno Alarcon for all the experimental advices to improve my cleanness. Gwenn Cognard for her electrodes, her great singing and for finding the F11 key to go in presentation mode 2 minutes before the drama. Caio Ribeiro Barros for the experiments on the Pt/GC electrodes. Anielli Pasqualetti for the Pd/C and DEMS experiments, Pascal Pleurdeau for teaching me the RRDE setup and the camera, Eric Sibert for the STM, Nicolas Sergent for the RAMAN, Vincent Martin for the DEMS, Karine Guilly and Muriel Merenda for the TP, Thierry Encinas and Stéphane Coindeau for the XRD, Joëlle Calabro for the SEM, Belen Molina Concha for the \LaTeX and the discussions, Jean-Paul Diard and Claude Montella for their teachings and advices, Claire Girardi, Claire Benoit, Yasmine Bouhadjar, Augustine Alessio and Martine Lovato for their patience in all the administrative procedures.

In Liège: Jean Mansuy for the SEA experiments. Fabien Deschamps and Giuseppe Caldarella for the help in the DBFC configuration. Jérémy Geens for all the technical help. Cedric Gommès for his nanoparticles counting program, the space in his office and the nice discussions. Julien Mahy for recycling my Pt colloid solution, as well as for his kindness. Carlos Alberto Paez for the grinding and sharing his ideas and recent results, Sigrid Douven for always taking the time to help in the lab everytime I was in need for something (thanks also for all the free coffees). Vincent Claude for his warm welcome and for lending me his great peristaltic pump. Anthony Zubiaur for the ATG, the XRD and the jokes. Marie-Laure Piedboeuf and Alexandre Leonard for showing me the synthesis of the carbon xerogel as well as the BET and the mercury porosimetry. Martine Deneffe for the TEM. Marlène Goffin for all the help in the administrative papers I struggled with.

In Alicante: Juan Feliu for welcoming me in his team. Valentin Briega Martos for taking so much good care of me with the single-crystals experiments. Carlos Buso Rogero for the fun FTIR tentative.

In every place I was, I had the chance to be surrounded by wonderful and passionate people who made these 3 years so enjoyable for me (even some people I didn't work directly with, not mentioned above). Some of them became good friends and made my life even better... they won't need to see their names written on this paper to recognize themselves.

At last, thanks to everyone who hosted a freeloader like me during the thesis and stopped me from sleeping under some bridges: Antoine, Marc, Lyk et Mazam, Fabien, Luigi et Zazou.

Contents

General introduction	1
Direct borohydride fuel cells (DBFC)	3
Life cycle of sodium borohydride	4
Commercial aspects of the DBFC	8
Structure of the thesis	13
I The anode catalyst in DBFC	17
1 Investigation of Pt and Pd as potential anode catalysts	19
1.1 Half-cell characterization at 25°C	22
1.2 Fuel cell characterization at 25°C	24
1.3 Influence of the operating temperature on the fuel cell characterization	26
1.4 Influence of the anode morphology on the fuel cell characterization	30
1.5 Stability of Pt/C and Pd/C anodic active layers during fuel cell operation	33
1.6 Conclusions	35
2 Literature review of anode catalysts in DBFC	37
2.1 Single direct borohydride fuel cell (DBFC) configuration	39
2.1.1 Influence of the anode catalyst on the performance of DBFC	39
2.1.2 Experimental variables external to the choice of the anodic catalyst in DBFC configuration	42
2.2 Electrocatalytic activity towards the borohydride oxidation reaction (BOR)	53
2.2.1 Rotating disk electrode (RDE) configuration	53
2.2.2 Chronopotentiometry (CP) and chronoamperometry (CA)	61
2.3 Hydrogen generation and escape during the BOR	62
2.4 Stability of the anode catalyst upon DBFC operation	73
2.5 Summary	74
II Study of the borohydride oxidation reaction (BOR) mechanism on Pt	77
3 Bulk platinum	81
3.1 Polycrystalline Pt	83
3.2 Single crystal Pt	88
3.3 Conclusions	92

4 Pt nanoparticles supported on flat glassy carbon (Pt/GC)	95
4.1 Characterization of the Pt/GC electrode	97
4.2 Poisoning of the Pt surface during the borohydride oxidation reaction (BOR) . . .	99
4.3 Conclusions	106
5 Pt nanoparticles supported on vertically-aligned carbon nanofilaments	107
5.1 Characterization of the Pt/VACNF electrodes	109
5.2 Electrochemistry of the borohydride oxidation reaction (BOR)	114
5.3 Conclusions	121
6 Modelling of the BOR on Pt	123
6.1 Construction and variables of the model	125
6.2 Simulation of the model	132
6.3 Model development prospects	135
6.3.1 Borohydride hydrolysis during the BOR	135
6.3.2 BOR on other metal catalysts	139
6.4 Conclusions	141
General conclusions	143
Appendices	151
A Experimental	151
A.1 Characterizations in electrochemical cell	151
A.1.1 Electrochemical cell setup	151
A.1.2 Preparation and synthesis of the model electrodes	152
A.2 Characterizations in fuel cell configuration	154
A.3 Physical characterizations	156
B Stripping of the BOR 'surface poisons'	157
C Pt/VACNF: supplementary figures	161
D BOR Modelling	165
D.1 Supplementary figures	165
D.2 Approximation for the mass-transfer	167
Bibliography	169

General introduction

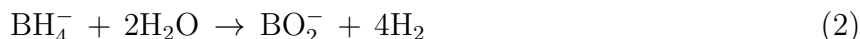
Direct borohydride fuel cells (DBFC)

The direct borohydride fuel cell (DBFC) is an alkaline fuel cell system fed with an aqueous solution of (usually sodium) borohydride. Ideally, the anodic reaction of the DBFC is the borohydride oxidation reaction (BOR), *i.e.* the direct and complete 8-electron oxidation of the BH_4^- anion, as proposed in Eq.1 [1, 2].



The standard potential of the BOR (Eq.1) was calculated to be $E^0 = -1.24 \text{ V vs. SHE}$ at $\text{pH} = 14$ [1, 3].

In practice, this ideal BOR competes with the homogeneous and heterogeneous hydrolysis reactions of BH_4^- [1, 2, 4, 5, 6], that occur within the solution or at the catalyst surface, respectively. The complete hydrolysis of a BH_4^- anion is illustrated by the reaction proposed below (Eq.2).



The hydrolysis reactions of BH_4^- are detrimental to the operation of a DBFC (as further discussed in the section 2.3 of this manuscript). However, this hydrolysis is also the basic principle of another way for converting energy using sodium borohydride. Indeed, sodium borohydride can react on appropriate catalysts and produce hydrogen from the heterogeneous hydrolysis reactions (Eq.2). Homogeneous hydrolysis reactions of the sodium borohydride in the liquid phase can also occur (even in the absence of any catalytic surfaces) in acidic conditions for instance. The homogeneous hydrolysis reactions of sodium borohydride is further detailed in the next section of this introduction. This gaseous hydrogen can then be valorized, among other possibilities, as a fuel for standard proton exchange membrane fuel cells (PEMFC) [7, 8, 9, 10]. Although interesting, this field of study will not be treated in the work presented here, which only focusses on DBFC (*i.e.* the direct utilization of sodium borohydride as an anodic fuel for a direct liquid fuel cell).

Indig *et al.* [11] first suggested in the 1960s that the sodium borohydride could be a suitable fuel for a direct liquid fuel cell. It is interesting to note that, during the measurement of the polarization discharge curve of a sodium borohydride alkaline solution on a Ni anode in half-cell configuration, it was already observed that the hydrolysis reactions (Eq.2) hindered the performances of the system: *'One of the major problems encountered in the discharges was the formation of large amounts of hydrogen gas. Although the sodium borohydride solutions were quite stable on storage, in contact with the porous nickel electrodes, the solutions gassed slowly. The gassing rate increased with the electrochemical oxidation, and at a rate of 775 mA/cm² much hydrogen was evolved. This indicated that hydrogen was formed as a product of the electrochemical oxidation.'* [11].

When oxygen is used as the oxidant, the oxygen reduction reaction (ORR) occurs at the cathode of the DBFC (Eq.3). The standard potential of the ORR (Eq.3) is equal to 0.40 V vs. SHE at $\text{pH} = 14$.



In this case, the theoretical DBFC voltage is 1.64 V and the overall DBFC reaction is (Eq.4):



The first characterization of a single DBFC configuration using oxygen as the oxidant was reported by Amendola *et al.* in 1999 [12]. The single cell was composed of an anode made of finely divided 97% Au/3% Pt particles deposited on carbon cloth held in an alkaline sodium borohydride reservoir, separated from an air-breathing cathode compartment using an anion-exchange membrane; a power density of 60 mW.cm⁻² was obtained at 70°C.

Note that other types of oxidants can be used, such as hydrogen peroxide [13, 14] (in so-called direct borohydride hydrogen peroxide fuel cells, and often denoted DBPFC, DBHFC or DBHPFC). In these systems, the use of an acidic catholyte enables to raise the theoretical cell voltage up to 3.02 V when the anolyte pH is set at 14 and the catholyte pH at 0 [15]. However, the pH gradient between the two sides of the membrane-electrodes assembly (MEA) raises other practical issues of junction potential, reactant crossover and electrolyte intermixing that will not be discussed further here. Therefore, this work focuses only on DBFC using oxygen or air oxidants, thereafter simply denoted DBFC.

The sketches presented in Fig.1 summarize the working principle of the DBFC. Both cation-exchange membranes (CEM) and anion-exchange membranes (AEM) have been used in order to construct DBFCs. A review of the different DBFC configurations used through the literature to characterize the system is presented and discussed in the chapter 2 of this manuscript. The AEM is theoretically the most logical choice of membrane for the DBFC. Indeed, since OH⁻ anions are the main charge carrier inside the AEM, the chemical balance is achieved for the AEM-DBFC (Fig.1b). On the contrary, Na⁺ cations are the main charge carrier inside the CEM, causing accumulation and depletion of NaOH at the cathode (Eq.3) and the anode (Eq.1) of the CEM-DBFC, respectively (Fig.1a). The decrease of the anolyte pH upon CEM-DBFC operation leads to instability of the borohydride anion due to the enhancement of the hydrolysis rate (see the following section of this introduction), while the accumulation of NaOH at the cathode of the CEM-DBFC causes obvious practical issues such as the physical blocking of the cathode compartment. However, to the author's knowledge, no AEM with sufficient activity in the conditions required for DBFC operation (*i.e.* at pH equal to or higher than 14) is currently commercially available, contrary to the already widespread Nafion[®] CEM. Moreover, the BH₄⁻ crossover rate is obviously faster using a AEM compared to a CEM, hindering the overall performances of the AEM-DBFC. This issue may be dealt with using cathode catalysts which are active for the ORR while inactive for the BOR (this discussion is further developed in the part II of this manuscript). Note that in the case of a fuel-tolerant cathode catalyst (*i.e.* a catalyst inactive towards the BOR in the cathode conditions upon DBFC operation), it is also possible to consider a DBFC constructed with a 'simple' porous separator, which electrically insulates the DBFC electrodes from each other. The ionic conduction in the latter proposition of DBFC configuration is ensured by the liquid electrolyte.

Life cycle of sodium borohydride

Sodium borohydride was discovered by Schlesinger and Brown in the early 1940s. However, the work of this group was classified during wartime, so that the first publication in a scientific journal about this discovery occurred later, in 1953 [17]. The fascinating story of the discovery of sodium borohydride and its interesting properties have been humorously retold later by

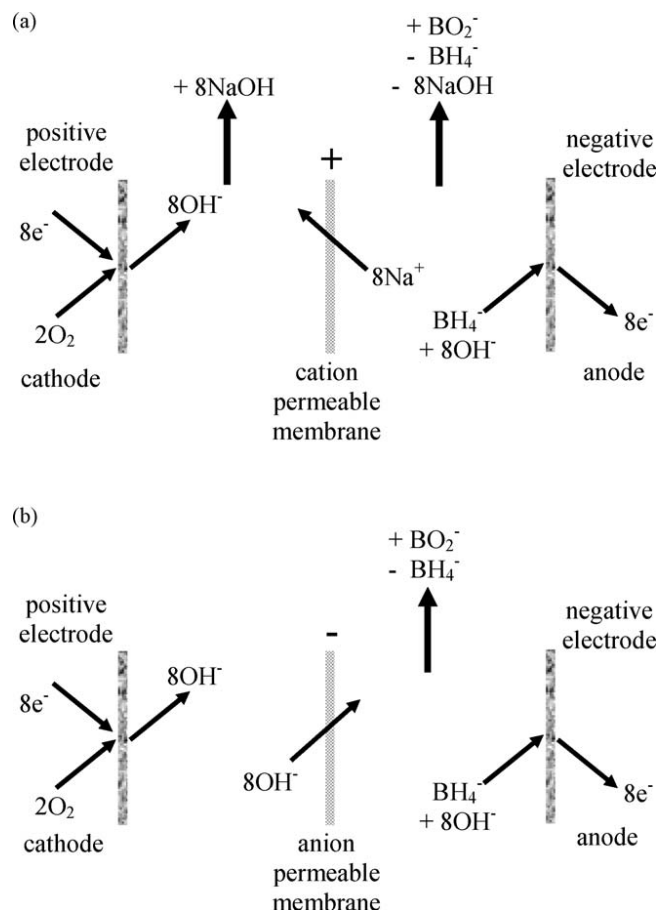
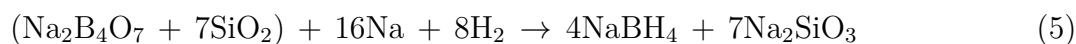


Figure 1: Working principle schemes of direct borohydride fuel cells with: (a) a cation permeable membrane and (b) an anion permeable membrane, drawn to emphasize the chemical balance. Reproduced from Ref.[16] with permission from Elsevier.

Brown [18]. This group also proposed a process for the synthesis of sodium borohydride at atmospheric pressure and *ca.* 250°C [19]. The Brown-Schlesinger process is currently widespread in the industry in order to produce sodium borohydride [20, 21]. A schematic summary of the Brown-Schlesinger process is presented in Fig.2.

Another industrial way for producing sodium borohydride is the Bayer process, used by Bayer AG corporation [22, 23]. The Bayer process consists of a one-pot reaction at relatively high temperature (400-500°C) and under H₂ pressure of borosilicate glass (fused from borax and quartz sand) with metallic sodium and hydrogen, as shown in Eq.5. The sodium borohydride/silicate mixture obtained is then extracted with liquid ammonia under pressure. A schematic summary of the Bayer process is presented in Fig.3. Note that many other processes exist [21], but are not widespread in the industry yet [20].



Borates are defined in the Oxford dictionaries as 'salts in which the anion contains both boron and oxygen, as in borax'. A photograph of borax crystals is presented in Fig.4. Turkey is the world first producer of borate, and is also considered to own the world largest borate reserve, although the detailed figures of the borate world reserve repartition do not exactly

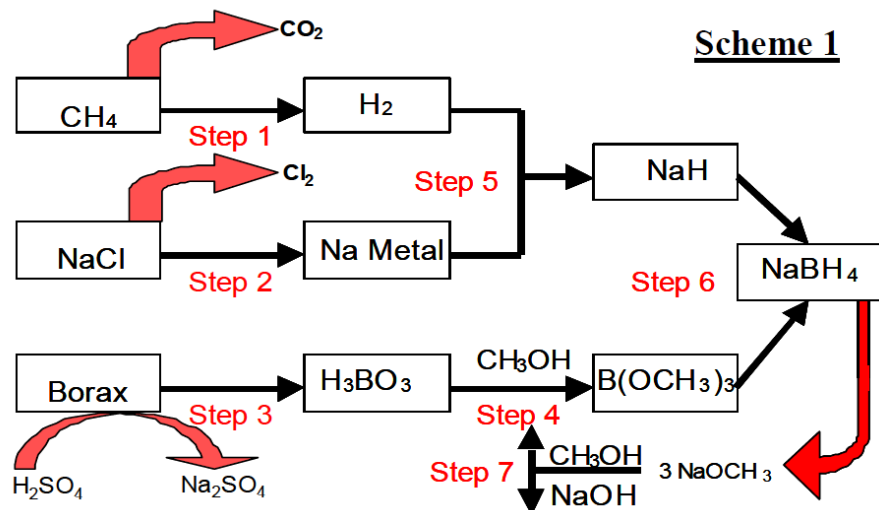


Figure 2: Schematic of the Brown-Schlesinger process for the synthesis of sodium borohydride. Step 1: Steam reforming of methane to produce hydrogen. Step 2: Electrolysis of sodium chloride to produce sodium metal. Step 3: Refining of borax to produce boric acid. Step 4: Conversion of boric acid to trimethylborate with methanol. Step 5: Reaction of sodium metal and hydrogen to produce sodium hydride. Step 6: Combination of sodium hydride and trimethylborate to produce sodium borohydride. Step 7: Recycling of sodium methoxide by-product to methanol. Reproduced from Ref.[20].

concur, depending on which country the said studies originated from. The borate reserve of Turkey was reported to be *ca.* 70% and 29% of the world reserve of borate in Refs. [24, 25] and [26], respectively, whereas the borate reserve of the United States (considered as the second world largest borate reserve) was reported to be *ca.* 7% and 19% of the world reserve of borate in Refs. [24] and [26], respectively. The borate world reserve was estimated to be *ca.* 1176 and 210 millions metric tons B₂O₃ equivalent in Refs.[24] and [26], respectively. The world production was estimated to be *ca.* 2 millions metric tons B₂O₃ equivalent per year for the last decade [24, 25, 26]. The main utilization of borate is currently related to the glass fiber market.

Sodium borohydride is highly soluble in water; *ca.* 35 g of NaBH₄ per 100 g of water at 25°C [27]. However, BH₄⁻ is unstable in water due to the homogeneous hydrolysis reactions (Eq.2). It was first reported that BH₄⁻ hydrolysis rate increases with the increase of the acidity of the solution [28, 29]. Although it is necessary to be able to increase the BH₄⁻ hydrolysis rate when the ultimate goal is to generate gaseous hydrogen from borohydride, it is rather the contrary in the case of the DBFC where the highest chemical stability of the borohydride in the anolyte is required. In that frame, increasing the pH of the borohydride-containing solution hinders the hydrolysis reactions [1, 30]. Brown *et al.* [31] observed the KBH₄ degradation rate to be linearly dependent on the pH of the solution (measured for solution pH between 12 and 14). The stability of a borohydride-containing solution at given pH and temperature values can be estimated using the equation established by Mochalov *et al.* [32] presented below (Eq.6).

$$\log[t_{1/2}] = pH - 0.034T - 1.92 \quad (6)$$

Where $t_{1/2}$ is the half-life of BH₄⁻ in minutes, and T is the temperature in Kelvin. According to Eq.6, the half-life of BH₄⁻ at 25°C is 6.1 min, 10.2 h, 42.6 days and 426.2 days at a pH of 9, 11, 13 and 14, respectively. According to Eq.6, high temperature is not favorable either for

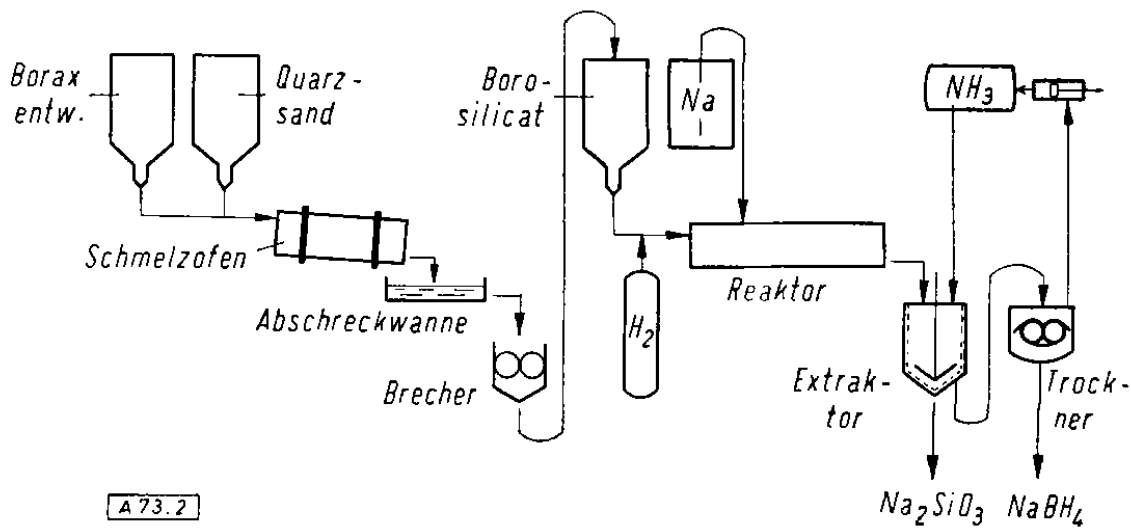


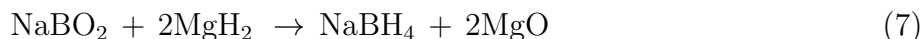
Abb. 2. Fließschema der Natriumborohydrid-Herstellung

Figure 3: Schematic of the Bayer process for the synthesis of sodium borohydride. Tentative translation of the german words: 'Schmelzofen' ↔ 'Melting furnace', 'Abschreckwanne' ↔ 'Quenching tub', 'Brecher' ↔ 'Crusher', 'Trockner' ↔ 'Dryer'. Reproduced from Ref. [22] with permission from Wiley-VCH.

the stability of the borohydride. Minkina *et al.* [33] observed a very slow NaBH_4 degradation (less than 1% loss in NaBH_4) after 50 h at 22°C for the system 27 wt.% NaBH_4 -10 wt.% NaOH . However, higher temperature and lower concentration in NaOH led more severe losses in stability: ca. 70% loss in NaBH_4 after 350 days at 50°C for the system 29 wt.% NaBH_4 -5 wt.% NaOH [33]. Note that, in this work, Minkina *et al.* [33] did not actually measure the hydrogen escape from the system for 350 days, but instead constructed the curve of sodium borohydride degradation from the measurement of the hydrolysis rate of several intermediate NaBH_4 - NaBO_2 - NaOH compositions. Nevertheless, one can deduce that relatively large concentration in NaOH as well as a low temperature are required for long-time storage of borohydride-containing solutions.

The final product of the BOR is believed to be the metaborate anion BO_2^- (Eq.1). In order to propose a sustainable DBFC, an efficient way for recycling BO_2^- back to BH_4^- is required. To the author's knowledge, no satisfactory method mature enough for efficient recycling has emerged yet. Among other developments, Kojima *et al.* [34] investigated the reaction of NaBO_2 to NaBH_4 using Mg_2Si alloy as reducing agent. A recycling yield of 98% at 550°C under 7 MPa pressure of H_2 was achieved [34]. Fig.5 shows the recycling yield of NaBO_2 to NaBH_4 at various H_2 pressure [34]. Note that the relatively high H_2 pressure required to achieve satisfactory recycling yields is not very practical for industrial upscaling.

A promising result was presented by Li *et al.* [35], where MgH_2 was used as a reducing agent to react with NaBO_2 in a planetary ball mill at room temperature and pressure. The predicted recycling reaction is detailed below (Eq.7). As shown in Fig.6, almost 100% recycling yield was obtained for a MgH_2 over-stoichiometry of 1.25.



Methane and coke were also considered as reducing agents for this recycling reaction [34]. However, the large positive free-energy of these reactions for temperature values below 1000°C



Figure 4: Photograph of borax crystals. Reproduced from Wikipedia: 'Borax' english page. Public domain.

makes them thermodynamically unfavorable and thus, not sustainable at an industrial scale [20]. Another way for recycling BO_2^- is to use electrochemical technique; considering the $\text{BH}_4^-/\text{BO}_2^-$ half-reaction (Eq.1) to be reversible, it is theoretically possible to perform the electrolysis of BH_4^- from BO_2^- [36]. Several patents and articles claimed recycling yield around 20% in aqueous electrolyte. However, Gyenge *et al.* [37] did not observe any production of BH_4^- using various methods of electrolysis presented in the past. The choice of the method for measuring the amount of borohydride produced during the electrolysis was suspected to be responsible for the erroneous results [37]. The electrolysis of BH_4^- in aqueous electrolyte does not seem very suitable, as the standard potential of Eq.1 is out of the water electrochemical stability domain for most of the possible electrocatalysts (in other terms, H_2 generation is most likely to occur rather than the BO_2^- reduction into BH_4^- at the cathode of the electrolyzer). In that frame, further development concerning the electrolysis of BH_4^- is still possible in non-aqueous electrolytes such as molten salts or ionic liquids [20, 21, 38]. This will not be studied in the present thesis.

Commercial aspects of the DBFC

The thermodynamic calculations performed on the overall (and ideal) DBFC reaction (Eq.4) lead to a theoretical cell voltage of 1.64 V [1, 3], which is higher than the theoretical cell voltages of the proton exchange membrane fuel cell (PEMFC: 1.23 V) and of the direct methanol fuel cell (DMFC: 1.21 V). Considering an ideal 8-electron borohydride oxidation reaction (BOR, Eq.1), the theoretical specific energy of the DBFC considering the NaBH_4 compound only (*i.e.* ignoring the contribution of NaOH as part of the fuel) is given by [12]:

$$\frac{(8 e^- \text{ per NaBH}_4)(1.64 \text{ V})(96485 \text{ A}\cdot\text{s}^{-1}\cdot\text{mol}^{-1})}{(37.83 \times 10^{-3} \text{ kg}_{\text{NaBH}_4}\cdot\text{mol}_{\text{NaBH}_4}^{-1})(3600 \text{ s}\cdot\text{h}^{-1})(1000)} = 9.30 \text{ kW}\cdot\text{h}\cdot\text{kg}_{\text{NaBH}_4}^{-1}$$

This value of DBFC theoretical specific energy is higher than the DMFC theoretical specific energy ($6.07 \text{ kW}\cdot\text{h}\cdot\text{kg}_{\text{MeOH}}^{-1}$) but lower than the PEMFC theoretical specific energy ($32.71 \text{ kW}\cdot\text{h}\cdot\text{kg}_{\text{H}_2}^{-1}$) [39].

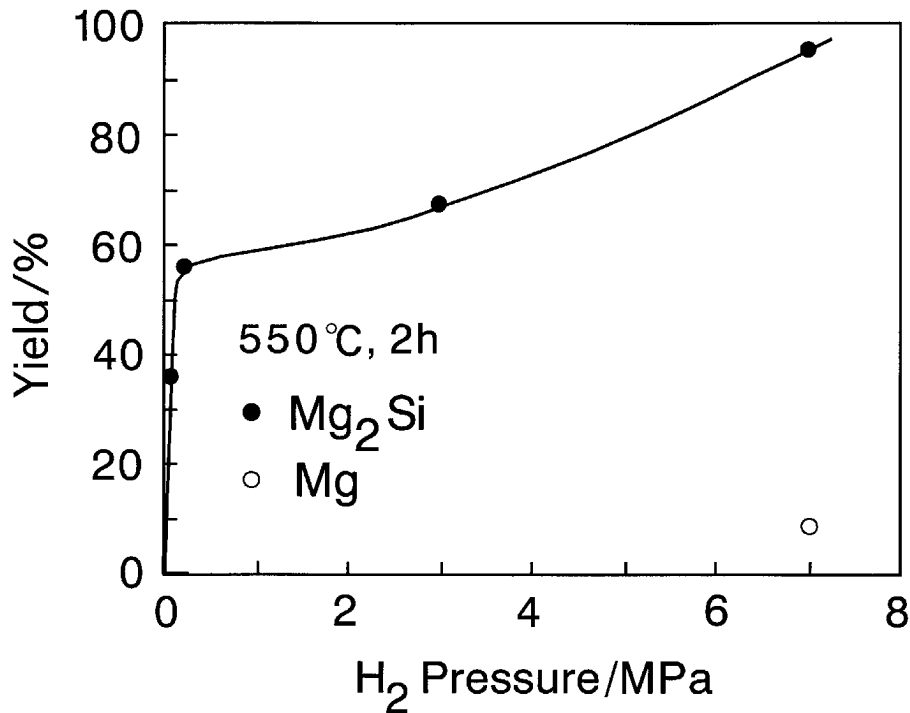


Figure 5: Influence of pressure on NaBH₄ recycling yield from NaBO₂ (reducing agents Mg₂Si or Mg, 550°C, 2 h). Reproduced from Ref.[34] with permission from Elsevier.

The main advantage of the DBFC, from the thermodynamics point of view, is its high theoretical energy density. Indeed, compared to pure hydrogen which can be either compressed or liquefied in the case of the PEMFC, sodium borohydride can be dissolved in an aqueous alkaline solution and therefore easily leads to higher theoretical energy density for the DBFC. Let us consider a practical DBFC fed with an anolyte composed of 10 wt.% NaBH₄ and 20 wt.% NaOH. Given the density of this solution (1.19 g.cm⁻³ at room temperature [40]), the partial specific volume of the anolyte is 8.40 L.kg_{NaBH₄}⁻¹ and thus the theoretical energy density of the DBFC (considering the theoretical specific energy calculated above) is in this case 1.11 kW.h.L_{anolyte}⁻¹. The same reasoning can be applied for a DMFC fed with an anolyte composed of 2 M MeOH in water (density of 0.99 g.cm⁻³): the partial specific volume of the anolyte is 15.61 L.kg_{MeOH}⁻¹ and the theoretical energy density of the DMFC is then 0.39 kW.h.L_{anolyte}⁻¹. For the PEMFC, let us consider a tank of H₂ compressed at 200 atm and at a temperature of 298 K. A first approximation using the ideal gas law leads to a specific volume of 60.50 L.kg_{H₂}⁻¹, and to a theoretical energy density of 0.54 kW.h.L_{anolyte}⁻¹ for the PEMFC.

The major current impediment to the DBFC, commercially speaking, is the high cost of sodium borohydride. Considering the current purchase cost (20 US\$.kg_{NaBH₄}⁻¹) and the theoretical specific energy calculated above, the NaBH₄ contribution to the cost of theoretical energy for the DBFC is 2.15 US\$.kW.h)⁻¹. For comparison, the contributions of H₂ and methanol to the cost of theoretical energy are 0.15 and 0.66 US\$.kW.h)⁻¹ for the PEMFC and the DMFC, respectively (assuming purchase costs for H₂ and methanol of 5 US\$.kg_{H₂}⁻¹ and 4 US\$.kg_{MeOH}⁻¹, respectively). In 2005, Li *et al.* [41] estimated the fuel contribution to the cost of electricity to be 100 times higher for NaBH₄ in the DBFC compared to H₂ in the PEMFC (the purchase cost of sodium borohydride at this time was taken as 55 US\$.kg_{NaBH₄}⁻¹). In the same paper, Li *et al.* [41] estimated a target of 0.55 US\$.kg_{NaBH₄}⁻¹ for the DBFC to be competitive for the automotive market. In the author's opinion, the portable market should rather be targeted for the DBFC (see below).

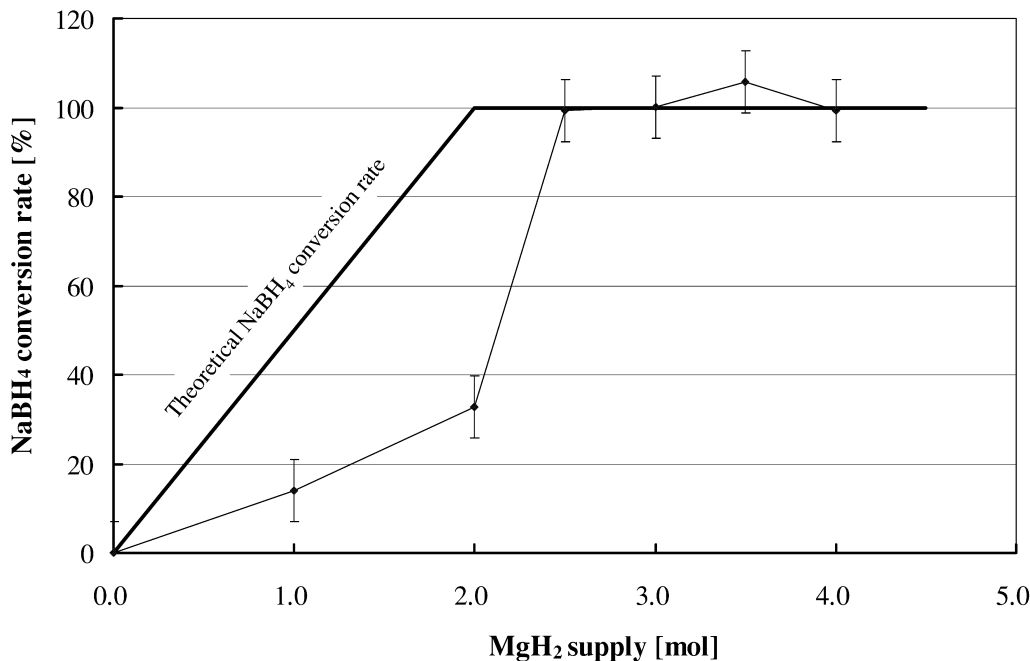


Figure 6: NaBH₄ formation from NaBO₂ by ball milling (atmospheric temperature and pressure), using MgH₂ as reducing agent. Reproduced from Ref.[35] with permission from Elsevier.

Wee *et al.* [42] performed a comparative 20 W fuel cell study on DBFC and DMFC. As the energy density of the DBFC is higher than that of the DMFC (see above), and as higher values of maximum power density for the DBFC compared to the DMFC were obtained in the literature in practical conditions, the DBFC was found to lead to a smaller cell size compared to the DMFC for identical power output. Moreover, and contrary to the DMFC, it is possible to consider a DBFC that uses non-noble anode and cathode catalysts without detrimental losses of performance. Indeed, at the anode of the DBFC, the BOR can be efficiently catalyzed by non-noble electrocatalysts (Ni- or Co- based, for instance), while at the cathode of the DBFC, the oxygen reduction reaction (ORR) occurs in alkaline conditions, which enables the use of non-noble electrocatalysts for the ORR (such as MnO₂ or perovskite-based electrocatalysts). For further information, please refer to the chapter 2 of this manuscript, where a review of the different types of catalysts for the DBFC is made. In the case of the DMFC, the general low activity for the methanol oxidation reaction leads to the use of relatively high loadings of Pt-based anode catalysts [43]. As the ORR occurs in acidic conditions at the cathode of the DMFC, the use of noble catalyst such as Pt is also necessary in order to achieve sufficient performances. Considering a state-of-the-art DMFC with a peak power density of 100 mW.cm⁻² using a Pt catalyst loading of 3 mg_{Pt}.cm⁻², the Pt need per power output can be estimated as 30 g_{Pt}.kW⁻¹, which is a serious drawback considering a current Pt price (35 US\$.g_{Pt}⁻¹) and the limited availability of the Pt ore. Therefore, Wee *et al.* [42] estimated the production cost of a DBFC to be lower than that of the DMFC (1.5 US\$.W⁻¹ and 5 US\$.W⁻¹ for the DBFC and the DMFC, respectively).

Although the DBFC was estimated to be cheaper to produce compared to the DMFC, Wee *et al.* [42] also estimated that the relatively high cost of NaBH₄ compared to methanol (see above) makes the DBFC uneconomical for long operation duration. As shown is Fig.7, a 20 W DBFC system without any hydrolysis reaction occurring at the anode is economically competitive compared to a 20 W DMFC system as long as the fuel cells operation time does not exceed 280 h [42]. Considering the high cost of NaBH₄, the fuel efficiency of the DBFC should be maximized.

This means that the non-valorized H_2 escaped from the anode upon DBFC operation due to BH_4^- hydrolysis reactions (Eq.2), as well as the BH_4^- crossover from the anode to the cathode, should be minimized in order to enhance the economical competitiveness of the DBFC. Indeed, as shown in Fig.7, the cost of electricity raises when considering a $6e^-$ -DBFC (*i.e.* a configuration where only $6e^-$ are valorized per BH_4^- anion, due the escape of one H_2 per BH_4^- *via* hydrolysis) compared to a $8e^-$ -DBFC (*i.e.* a configuration where the full $8e^-$ are valorized per BH_4^- anion).

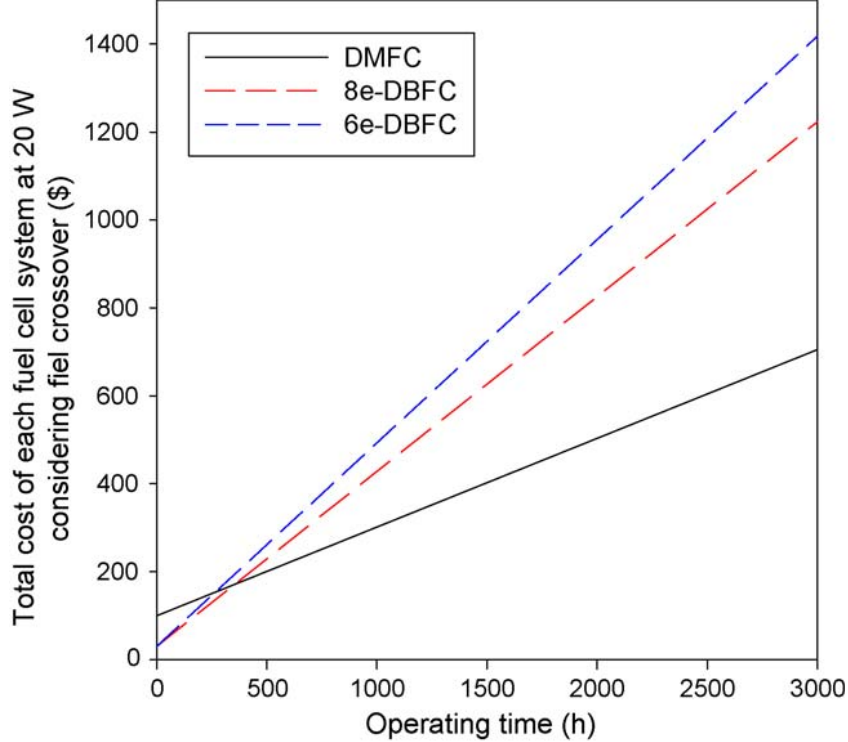


Figure 7: Total cost of DMFC, $8e^-$ -DBFC and $6e^-$ -DBFC operated at power output of 20 W during 3000 h considering crossover; prices of fuels assumed to be $10.4 \text{ US}\$. \text{kg}_{\text{MeOH}}^{-1}$ and $55 \text{ US}\$. \text{kg}_{\text{NaBH}_4}^{-1}$. Reproduced from Ref.[42] with permission from Elsevier.

Considering the cost of the DBFC, there is still room for improvement. Lowering the manufacturing cost of the DBFC requires to develop non-noble anode and cathode electrocatalysts active for the BOR (with minimum H_2 escape) and the ORR, respectively. In addition, the development of performant but cheap anion-exchange membranes (AEM) is necessary. As already mentioned, it is also possible to consider a DBFC system with a mixed-reactant electrolyte, using simply a cheap porous electrical insulator between the two electrodes. However, in the case of DBFC using an AEM or a mixed-reactant electrolyte, one should be aware that the fuel efficiency is likely to be relatively low (due to fast BH_4^- crossover rate). Thus, as the cost of NaBH_4 is a limiting step in the commercial competitiveness of the DBFC, the operation cost of these systems may be uneconomical. Considering the cost of NaBH_4 production, the most costly step in the Brown-Schlesinger and Bayer processes is the production of metallic sodium by the electrolysis of sodium chloride (step 2 in Fig.2). In order to reduce the cost of NaBH_4 , this step could be improved and also integrated into the production of sodium borohydride, which would save the high cost associated to the transportation of reactive raw sodium to the production site [20]. The development of NaBO_2 recycling methods would also contribute to lower the cost of NaBH_4 , and improve the sustainability of the DBFC. To the author's opinion, the production cost of NaBH_4 could be strongly reduced, if the demand for the compound increases (*i.e.* if the whole DBFC system becomes sufficiently mature to be attractive).

Besides the above considerations on cost, another drawback of the DMFC compared to the DBFC is that methanol (an organic molecule) oxidation reaction inevitably leads to the formation of adsorbed CO that poisons the Pt active surface, and ultimately of gaseous CO₂. This raises issues in the management of gas formation in a direct liquid fuel cell system [43]. However, the DBFC is likely to suffer from the same main drawback as the alkaline fuel cells (AFC), *i.e.* the formation of solid carbonate at the cathode side of the DBFC, coming from the reaction of the CO₂ (contained in the air) with the alkaline electrolyte [44]. Moreover, the BOR could lead to the formation of solid boron oxides such as NaBO₂ (Eq.1) which might block the anode or the cathode (considering the crossover of borohydride) of a DBFC [45]. The formation of a solid material blocking the air channels of the cathode bipolar plate is shown in Fig.8 after long-term operation of the DBFC; this solid was analyzed to be a mix of sodium borate and sodium carbonate [46].



Figure 8: Photograph of the air cathode current collector after long-term operation of a DBFC. Reproduced from Ref.[46] with permission from Elsevier.

In the light of the commercial aspects of the DBFC system discussed above, this technology could suit the market segment of low power portable applications, and be a substitute to the batteries of mobile phones, computer notebooks, etc. [41]. Indeed in this market, the high cost of NaBH₄ is not an unacceptable issue: for instance, a commercial 1.4 W.h AAA Cell primary battery costs 1.25 US\$, leading to a cost of electricity of 890 US\$. (kW.h)⁻¹. Furthermore, the great energy density of the DBFC is very attractive for this application. In that frame, the research company MERIT Ltd. (Materials and Energy Research Institute Tokyo) in conjunction with Kogakuin University (Japan) developed some DBFC prototypes for low power portable applications, as illustrated by the prototype micro DBFC of 10 W shown in Fig.9. The only once commercially available DBFC known to the author was the 'Medis 24-7 Power Pack' developed by Medis Technology Ltd. This system was supposed to enable 5 to 6 full charges of an iPhone (see Fig.10) with a power of 4 W and a capacity of 4.5 A.h, and cost 40 US\$ (the replacement pack of anolyte solution cost 20 US\$). The product had a guaranteed storage time of 18 months before activation. The activation of the device occurred by squeezing the external device shell in order to connect the anolyte tank to the rest of the DBFC. Once activated, the life-time of the device was claimed to be 3 months [47]. However, Medis Technology Ltd. collapsed in 2009

[48], so that no further developments of this system have been reported since. It is unknown to the author how this system reacted to carbonation from atmospheric CO₂ and to the possible precipitation/accumulation of borates.

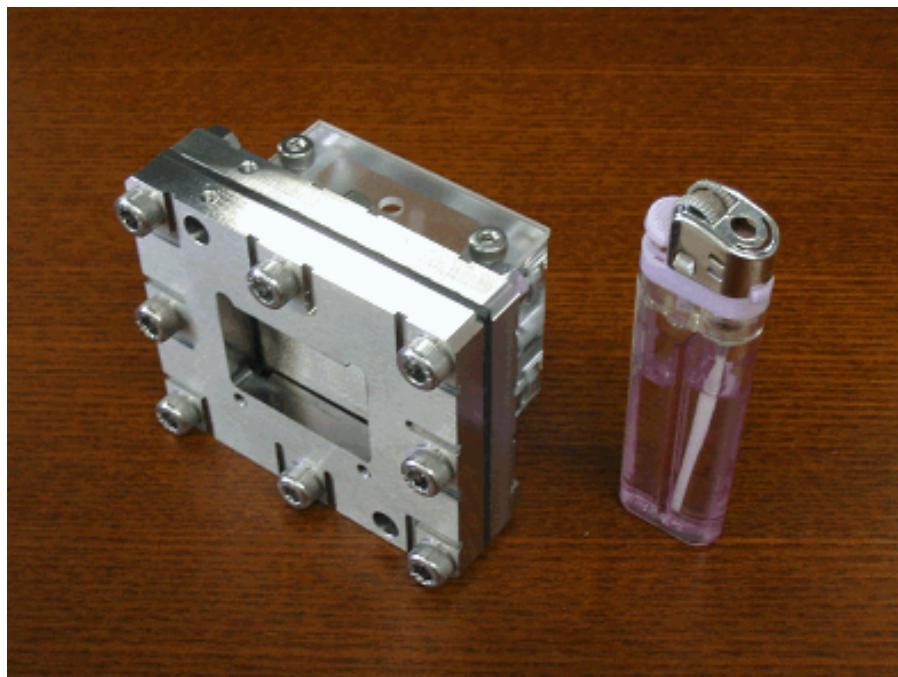


Figure 9: Prototype of flat-type DBFC [10W], without auxiliary devices (for experimental purposes only). Reproduced from the website of MERIT Ltd. [49].

Structure of the thesis

This study focuses on the anode of direct borohydride fuel cells (DBFC). The ideal anode for the DBFC meets the following specifications:

- Fast kinetics of the borohydride oxidation reaction (BOR) on the anode electrocatalyst. An active anode electrocatalyst towards the BOR enables low polarization potentials, leading to high overall electrical performances (*e.g.* high value of maximum power density) for the DBFC;
- Low H₂ escape upon DBFC operation, leading to high values of fuel efficiency. The choice of the electrocatalyst material as well as the global design of the anode can influence this parameter;
- High stability of the anode upon DBFC long-term operation;
- Low cost of anode materials and anode manufacturing.

Through the literature of the DBFC systems, two different strategies are traditionally employed in order to study and/or develop the anode of the DBFC. The first one is the systemic approach, which studies the anode inside the global and very complex DBFC system. A typical example for this approach would be to characterize several DBFC using different types of anodes (different electrocatalysts materials, support material, binder, etc.) under similar experimental



Figure 10: 'Medis 24-7 Power Pack' DBFC charging a smartphone. Reproduced from the website of CNET [47]. Martin LaMonica/CNET News.

conditions, and to observe the influence of the considered variables on the overall performances of the global DBFC system (polarization curve, H_2 escape rate, etc.). A study realized using the systemic approach is very close to the real conditions of the system. However, the huge number of experimental variables (which can be strongly correlated) leads to a poor understanding of the details ruling the behavior of the system towards the variable studied. The second strategy is the analytic approach, which isolates one element of the considered system (in our case, the anode of the DBFC taken apart from the global system) and reduces this element in order to be able to control all the variables ruling its behavior. In terms of experiment, this analytic strategy is typically performed using a half-cell configuration in a three-electrode setup, where some elements of the anode are placed in a controlled environment, thereby enabling the study of few experimental variables. This approach leads to further understanding of fundamental interactions. However, the lower the number of experimental variables, the further from the reality of a practical DBFC system.

In the author's opinion, the systemic and analytic approaches are not opposed, but rather complementary. A strategy purely based on the global systemic approach would certainly lead to a slow development of the DBFC technology, considering the huge number of interconnected experimental variables. One needs to understand, to the most detailed level accessible, the phenomena occurring during the DBFC operation in order to optimize the system in an intelligent way. On the other hand, understanding the phenomena occurring at every separate element of the system is not sufficient: the findings on one element have to be confronted to the reality of the global system, which may behave in a way totally unexpected by the study of separate elements. In the following, let us consider a not-so-imaginary case study illustrating this complementarity between the systemic and analytic approaches, in relation to the study of the anode in the DBFC. The first study of the BOR mechanism in three-electrode electrochemical cell conditions leads to the selection and optimization of an electrocatalyst that is highly active for the BOR. A DBFC using the selected electrocatalyst is characterized in real conditions; the value of maximum power density being high, as expected. However, harsh H_2 escape from the anode is observed upon DBFC operation, hindering the fuel efficiency of the DBFC. This finding finally leads to new directions of study, such as the investigation of the influence/contribution

of the hydrolysis reaction in the BOR mechanism (further understanding of the hydrolysis mechanisms shall enable to propose new electrocatalysts which will solve this issue), or the optimization of the anode catalyst support in order to manage the gaseous hydrogen. The thesis presented here attempts to follow this philosophy of study.

The first part of this thesis studies the anode electrocatalyst in the DBFC. The chapter 1 of this first part characterizes two different DBFC configurations using either Pt/C or Pd/C as anode catalyst. The fuel cells are also fed with another type of boron-based fuel; ammonia borane. The characterizations of the liquid fuel cells are performed at various operating temperature, and the corresponding performances are compared. The influence of the anode macroporosity towards the performances of the DBFC is reported. The stability of the Pt and Pd nanoparticles is also evaluated using TEM imaging. In this chapter, experiments are also performed in a three-electrode electrochemical cell using either bulk polycrystalline Pt or Pd (in rotating disk electrode configuration) in alkaline sodium borohydride or alkaline ammonia borane electrolytes. Based on the results in three-electrode electrochemical cell configuration, the overall performances of the fuel cells are predicted. The chapter 2 of the first part presents a literature review of anode catalysts for the DBFC. Along with the experimental conditions used in the literature to characterize the DBFC and the corresponding performances, this chapter presents and discusses experimental variables external to the anode in the DBFC characterizations. It also reviews and discusses different methods and the corresponding results obtained in the literature to evaluate the electrocatalytic activity of several materials towards the BOR, as well as the H₂ escape rate upon conditions close the DBFC operation.

The second part of this thesis investigates the BOR mechanism on platinum surfaces. Different types of Pt-based model electrodes are used in order to achieve further understanding of the BOR mechanism. Each type of model electrode enables to control a precise variable related to the Pt electrocatalyst, and thus to study different aspects of the BOR. In chapter 3, the use of platinum in the form of bulk polycrystalline and single-crystal flat electrodes enables to study the structure-sensitivity of the BOR. More complex model electrodes are prepared and studied in chapter 4: Pt nanoparticles supported on flat glassy carbon (GC) substrate. In this chapter, the poisoning of the Pt active surface by BOR intermediates/products is investigated. To increase the complexity level of the model electrodes, Pt nanoparticles supported on vertically-aligned carbon nanofiber (VACNF) electrodes are prepared and characterized in chapter 5. The deposition of various amounts of Pt nanoparticles on the VACNF substrate enables to study the influence of the density of Pt active sites towards the BOR. Also, the release of some intermediates formed during the BOR is measured using a gold-ring rotating ring-disk electrode setup. Finally, the chapter 6 gathers the findings mentioned above as well as other experimental and computational results from the literature; a tentative mechanism for the BOR on Pt is proposed. The simulated curves of this mechanism are compared with the experimental ones. Further development of this model, in order to account for the experimental observations of the first part of this thesis, is proposed and briefly discussed.

The work presented in this thesis has been published (or is currently in the process of submission) in several paper articles co-authored by Pierre-Yves Olu, where all the experiments were performed or supervised by Pierre-Yves Olu.

Chapter 1 is based on: P.-Y. Olu, F. Deschamps, G. Caldarella, M. Chatenet and N. Job, 'Investigation of platinum and palladium as potential anodic catalysts for direct borohydride and ammonia borane fuel cells', *J. Power Sources* 297 (2015) 492–503.

Chapter 2 is based on: P.-Y. Olu, N. Job and M. Chatenet, 'The anode catalyst material in direct borohydride fuel cells: a review', currently (September 2015) in the process of submission.

Chapter 3 is partly based on: P.-Y. Olu, B. Gilles, N. Job and M. Chatenet, 'Influence of the surface morphology of smooth platinum electrodes for the sodium borohydride oxidation reaction', *Electrochem. Commun.* 43 (2014) 47–50.

Chapter 4 is based on: P.-Y. Olu, C. R. Barros, N. Job and M. Chatenet, 'Electrooxidation of NaBH_4 in alkaline medium on well-defined Pt nanoparticles deposited onto flat glassy carbon substrate: evaluation of the effects of Pt nanoparticle size, inter-particle distance, and loading', *Electrocatalysis* 5 (2014) 288–300.

Chapter 5 and Chapter 6 are partly based on: P.-Y. Olu, A. Bonnefont, M. Rouhet, S. Bozdech, N. Job, M. Chatenet and E. Savinova, 'Insights into the potential dependence of the borohydride electrooxidation reaction mechanism on platinum nanoparticles supported on ordered carbon nanomaterials', *Electrochim. Acta* (2015) *In Press*.

Part I

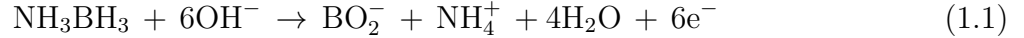
The anode catalyst in DBFC

Chapter 1

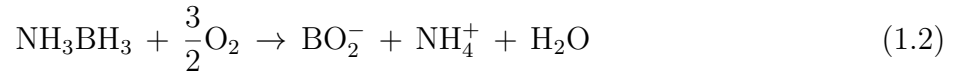
Investigation of Pt and Pd as potential anode catalysts

The direct borohydride fuel cell (DBFC) is the main topic of this thesis. The DBFC system has already been extensively described in the general introduction of this thesis. However and specifically in this chapter, another type of direct liquid fuel cell (DLFC), the direct ammonia borane fuel cell (DABFC), is also studied. The DABFC has a relatively recent history, and few studies have been carried out on the complete system. Yoa *et al.* [50] used Ag/C anodic catalyst in DABFC configuration, while Zhang *et al.* [51] used Pt/C. To the author's knowledge, no study comparing different anodic materials for the same DABFC characterization system has been performed to date.

The anodic reaction of the DABFC is ideally the direct and complete ammonia borane oxidation reaction (ABOR). It is a 6-electron reaction, as proposed below (Eq.3) [51].



The standard potential for the ABOR (Eq.3) was calculated to be $E^0 = -1.21 \text{ V vs. SHE}$ at $\text{pH} = 14$ [51]. When oxygen is used as the oxidant, the theoretical DABFC voltage is 1.61 V and the overall DABFC reaction is (Eq.4):



It has also been proposed that NH_3BH_3 spontaneously generates BH_3OH^- in alkaline electrolyte, the latter then reacting in a 6-electron oxidation reaction [52]. It is acknowledged that the ammonia moiety (NH_3) is not oxidized in the ABOR: NH_3 oxidation actually happens at too high potential values to be relevant at a DABFC anode on standard catalysts [53, 54]. Note that, like the BOR, the ABOR also competes with the heterogeneous hydrolysis reactions of NH_3BH_3 , which generates gaseous hydrogen and thus reduces the fuel efficiency of the DABFC.

In this chapter, Pt/C and Pd/C are studied as potential anodic catalysts for the DBFC and the DABFC. The electrocatalytic activities of these carbon-supported metal catalysts towards the BOR and the ABOR at 25°C are compared using the half-cell configuration. The predictive power of the half-cell experiments is evaluated and discussed by comparison with the performances obtained in the fuel cell configuration, using Pt/C and Pd/C as anodic catalysts and at an operating temperature of 25°C. DBFC and DABFC are also characterized at higher operating temperatures (60°C and 80°C), the subsequent evolution of the fuel cell performances being reported and discussed. The uncertainty around the measurement of the performances in the fuel cell configuration is highlighted by studying the great sensitivity of the experiments with regards to the morphology of the anodic active layer. Furthermore, the issue of the stability of the Pt/C and Pd/C anodic layers during DBFC and DABFC characterizations is evaluated, based on TEM observation of the catalysts before and after electrochemical experiments.

Note that the purpose of this work is to study different types of anodes for application in the DBFC and the DABFC systems, using different types of catalysts (Pt/C or Pd/C) or different morphologies. The achievement of the best possible fuel cell performances was not the primary aim, the main goal was the use of similar (and thus comparable) fuel cell configurations, with few different experimental variables which could be investigated. It is also important to note that the aim of the present chapter is not to discuss the whole mechanisms of borohydride and ammonia borane oxidation reactions on Pt and Pd, but rather to compare the electrocatalytic behaviors of these two model catalysts towards the borohydride and ammonia borane oxidation reactions, in order to explain further the different performances obtained in fuel cell configuration. Investigation and discussion of the BOR mechanism on Pt are developed in the second part of this thesis.

1.1 Half-cell characterization at 25°C

The electrocatalytic behavior of platinum and palladium catalysts towards the sodium borohydride (NaBH_4) and ammonia borane (NH_3BH_3) electrooxidation reactions were found to differ greatly. Cyclic voltammograms of smooth Pt and Pd characterized in rotating disk electrode (RDE) configuration (for a controlled mass-transfer) were performed in a three-electrode electrochemical cell. For further information concerning the experimental details, please refer to the corresponding Appendix A.1.1 of this thesis. Fig.1.1 shows the cyclic voltammograms plotted at room temperature (ca. 25°C), for a scan rate of $25 \text{ mV}\cdot\text{s}^{-1}$ and a revolution rate of 1000 rpm of smooth platinum and palladium RDE in 1 M NaOH + either 10 mM NaBH_4 or 10 mM NH_3BH_3 . The cyclic voltammograms of Fig.1.1A show a better overall electrocatalytic activity of the platinum electrode for the ammonia borane oxidation reaction compared to the sodium borohydride oxidation reaction at room temperature. Indeed, the open circuit potential (OCP) for the Pt electrode is slightly more negative when in contact with an electrolyte containing ammonia borane (-52 mV *vs.* RHE) than sodium borohydride (-24 mV *vs.* RHE), and the oxidation current is slightly larger for ammonia borane compared to sodium borohydride at low potential values (below 0.2 V *vs.* RHE). Unlike platinum, the palladium electrode displays very different electrocatalytic behaviors for sodium borohydride and ammonia borane electrooxidation, respectively. As presented in Fig.1.1B, the palladium electrode in contact with sodium borohydride displays an OCP value comparable with the platinum electrode (-26 mV *vs.* RHE) but yields sluggish oxidation reaction kinetics. On the contrary, the palladium electrode in contact with ammonia borane displays surprisingly low OCP (-274 mV *vs.* RHE) and relatively fast oxidation reaction kinetics.

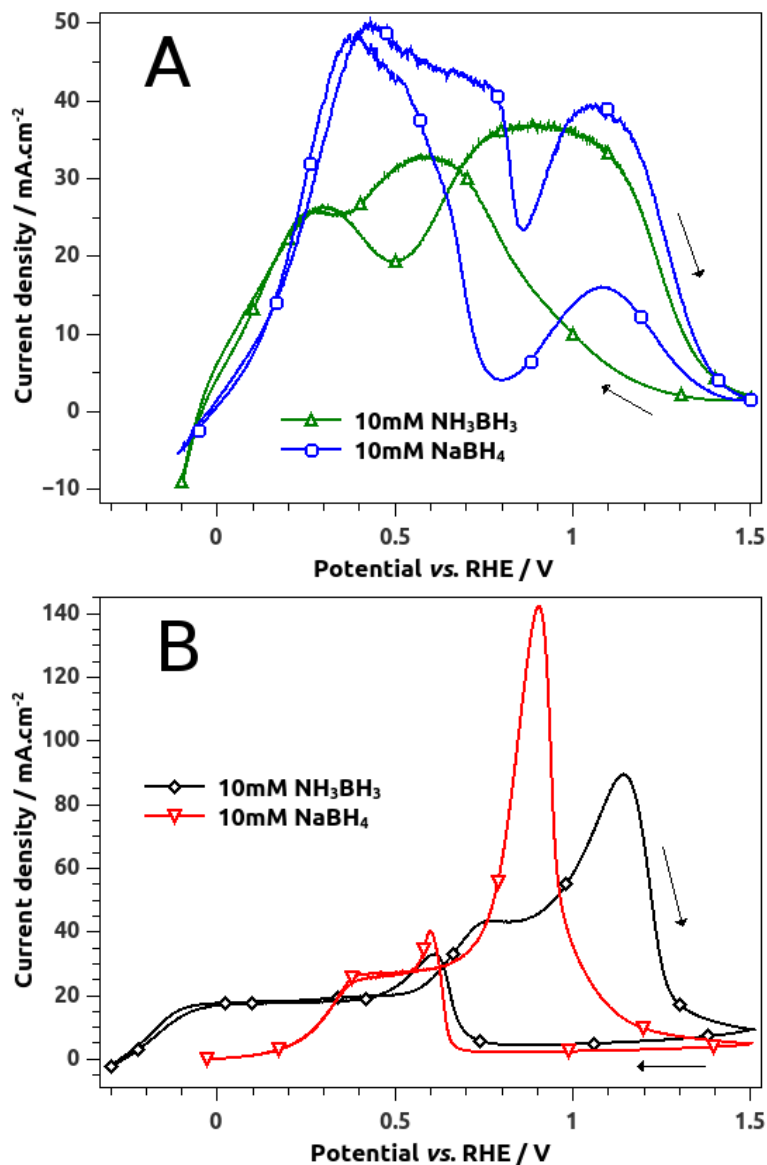


Figure 1.1: Platinum (A) and palladium (B) RDE voltammograms in either 10 mM NaBH₄ or 10 mM NH₃BH₃ in 1 M NaOH. Scan rate of 25 mV.s⁻¹ and revolution rate of 1000 rpm.

The BOR and ABOR are relatively fast on Pt and Pd (with the exception of the BOR on Pd); the calculation of oxidation kinetics parameters is not straightforward, as the reactions are already in mixed control of kinetics and mass-transfer at low overpotential. Indeed, the Tafel plot of the voltammograms of Fig.1.1 would not exhibit sufficiently wide linear domains in order to measure pertinent Tafel slopes, with the exception of the BOR on Pd. Therefore, in order to investigate Pt and Pd as anodic catalysts for the DBFC or the DABFC, the benchmarks proposed for the half-cell experiments are values of the potential obtained at open circuit, and for current densities of $j = 1 \text{ mA.cm}^{-2}$, 10 mA.cm^{-2} , 20 mA.cm^{-2} and 30 mA.cm^{-2} . These values were deduced from the curves presented in Fig.1.1, which gathers data obtained using 10 mM of NaBH₄ or NH₃BH₃ in 1 M NaOH, at a revolution rate of 1000 rpm and a scan rate of 25 mV.s⁻¹. This benchmark is reported in Table 1.1 along with the performances of the fuel cells at 25°C. At low current density values (*i.e.* at $j = 1 \text{ mA.cm}^{-2}$ and 10 mA.cm^{-2}), the Pd RDE with ammonia borane electrolyte is the most interesting configuration as it displays (by far) the lowest potential values at these current densities. For a current density of $j = 20 \text{ mA.cm}^{-2}$, the most interesting configuration is the Pt RDE with ammonia borane. This is because 20

mA.cm^{-2} is higher than the value of the first oxidation current plateau of Pd with ammonia borane. Even if the low-potential ABOR on Pd occurs on the lowest potential range with fast kinetics, the number of electrons involved in this oxidation step is relatively low and makes it interesting for low current values only.

1.2 Fuel cell characterization at 25°C

Fuel cell characterizations were carried out to study the influence of the catalyst materials (Pt/C or Pd/C) and of the anodic fuel (sodium borohydride or ammonia borane) on the fuel cell performances, all other experimental variables (e.g. fuels flow rates and concentrations, Nafion® 212 membrane, commercial air cathode) being kept identical. The experimental details of the fuel cells can be found in the Appendix A.2 of this thesis. It was checked that the two anodic active layers were comparable, such as the Pt/C and the Pd/C nanoparticle size (nanoparticle mean diameter of 2.2 nm and 2.5 nm for Pt/C and Pd/C catalysts, respectively, calculated by measuring at least 300 nanoparticles from the TEM imaging) or the metal loading (ca. 0.5 mg of Pt or Pd per cm^2 of carbon cloth, confirmed by ICP-AES analysis).

The half-cell characterizations presented above in this chapter enabled to study the anodic part of the fuel cell isolated from the other fuel cell variables. Therefore, in order to draw a pertinent comparison between the half-cell and the fuel cell characterizations, one should make sure that the fuel cell is not mostly limited by the cathodic reaction and the ohmic drop, otherwise the study of anodic catalyst material and/or anodic fuel would be pointless. The cathodic reaction is not the main limiting step in the overall fuel cell performances of our study, thanks to the high Pt loading at the cathode ($2 \text{ mg}_{\text{Pt}}.\text{cm}^{-2}$) as well as high pure oxygen cathodic flow ($300 \text{ mL}.\text{min}^{-1}$).

Fig.1.2 shows voltammograms obtained at a scan rate of $25 \text{ mV}.\text{s}^{-1}$ for fuel cells operated at 25°C, using Pt/C or Pd/C anodic catalysts fed with $7.5 \text{ mL}.\text{min}^{-1}$ of 5 M NaOH + either 1 M NaBH_4 or 1 M NH_3BH_3 . The fuel cell using Pd/C and ammonia borane as anodic catalyst and anodic fuel, respectively, displays the highest open cell voltage (OCV) with a value of 1.05 V, while the fuel cell using the same ammonia borane as anodic fuel but Pt/C as anodic catalyst displays the highest performances in terms of maximum power density ($181 \text{ mW}.\text{cm}^{-2}$). The main features of these fuel cell characterizations (OCV and maximum power density) are reported in Table 1.1 along with the benchmarks obtained from half-cell measurements at room temperature.

The main features of the half-cell characterizations reported in Table 1.1. are in agreement with the performances of the fuel cells. Indeed, as the Pd RDE displays the lowest OCP when in contact with ammonia borane, the Pd/C anodic catalyst fed with ammonia borane (Pd/C- NH_3BH_3) shows the highest OCV in fuel cell configuration (ca. 100 mV higher than the other fuel cells) and so the best performances at low current densities (below ca. $200 \text{ mA}.\text{cm}^{-2}$). At higher current densities, this configuration is outperformed by the Pt/C anode fed with ammonia borane, which shows the highest peak in power density among all other fuel cells. The Pd catalyst with sodium borohydride displays the worst performances in both half-cell and in fuel cell configurations. However in this case, the correlation between the half-cell OCP and the fuel cell OCV is not straightforward. This can be explained by the sluggish oxidation kinetics of BH_4^- on the Pd RDE, which induces uncertainties on the OCP measurement. Indeed, the double layer capacitive current will, for example, lead to a non-negligible positive shift of the OCP value (when this potential value is taken as the intersection of the positive-going curve of

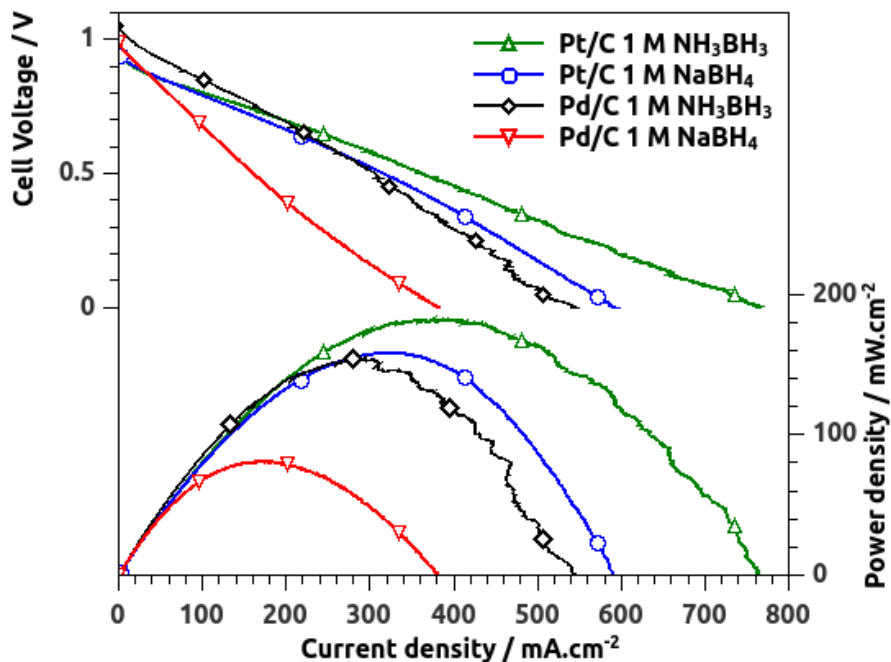


Figure 1.2: Voltammograms at 25°C in fuel cell configuration using homemade Pt/C or Pd/C on carbon cloth as anodes (0.5 mg of Pt or Pd per cm²) fed by 7.5 mL.min⁻¹ of 5 M NaOH + either 1 M NaBH₄ or 1 M NH₃BH₃, commercial Pt/C on Toray paper as cathode (2 mg of Pt per cm²) fed by 300 mL.min⁻¹ of pure oxygen (atmospheric pressure) and Nafion[®] 212 as a cationic membrane. Scan rate of 25 mV.s⁻¹.

the voltammogram with the $j = 0$ x-axis).

Another possible explanation for the drop in performances at higher currents for Pd/C-NH₃BH₃ (besides the relatively low number of electrons involved in the low-potential ABOR on Pd observed in Fig.1.1B) is the gas generated from the heterogeneous hydrolysis of NaBH₄ and NH₃BH₃ on Pt and Pd. Indeed, during the fuel cell operation, it was visually observed that NH₃BH₃ generated more gas (possibly H₂, NH₃ or N₂) than NaBH₄ (H₂) both with Pt/C and Pd/C. This gas generation also likely accounts for the noisier fuel cell voltammograms using NH₃BH₃ in Fig.1.2 and could explain the better performances of Pt/C-NaBH₄ compared to Pd/C-NH₃BH₃, which could not be expected from the half-cell results. Indeed, the latter were performed under hydrodynamic regime (in RDE) for smooth electrodes, thereby favoring the fast removal of the gas bubbles that could render to the catalyst surface inaccessible. This is obviously less likely for active sites spread within a volumic porous layer in the fuel cell configuration, in which gas evolution leads to a deterioration of the performances of the fuel cell [55, 56, 57]. The molar ratio between sodium borohydride or ammonia borane and sodium hydroxyde also differs between the half-cell configuration (1:100, respectively) and the fuel cell configuration (1:5, respectively). This difference tends to minimize the hydrolysis issue encountered in half-cell configuration, compared to the fuel cell configuration.

From the voltammograms in fuel cell configuration of Fig.1.2, ammonia borane is more efficient than sodium borohydride as an anodic fuel at 25°C. It leads the highest OCV value and maximum power density when Pd/C and Pt/C are used as anodic catalysts, respectively. This conclusion agrees with the half-cell results, and highlights the relatively good predictive power of the half-cell characterization for comparing the anodic catalyst material as well as the anodic

Table 1.1: Performances of the fuel cells operating at 25°C. Benchmarks of the half-cell characterizations.

Half-cell configuration				
Working electrode	Pt	Pt	Pd	Pd
Electrolyte	NaBH ₄	NH ₃ BH ₃	NaBH ₄	NH ₃ BH ₃
OCP <i>vs.</i> RHE (V)	-0.024	-0.052	-0.027	-0.274
Potential <i>vs.</i> RHE at 1 mA.cm ⁻² (V)	-0.009	-0.046	0.084	-0.261
Potential <i>vs.</i> RHE at 10 mA.cm ⁻² (V)	0.122	0.045	0.280	-0.170
Potential <i>vs.</i> RHE at 20 mA.cm ⁻² (V)	0.212	0.167	0.342	0.460
Potential <i>vs.</i> RHE at 30 mA.cm ⁻² (V)	0.273	0.669	0.654	0.641
Fuel cell configuration				
Anodic catalyst	Pt/C	Pt/C	Pd/C	Pd/C
Anodic fuel	NaBH ₄	NH ₃ BH ₃	NaBH ₄	NH ₃ BH ₃
OCV (V)	0.941	0.947	0.991	1.050
Maximum power density (mW.cm ⁻²)	158	181	81	154

fuel for an alkaline fuel cell application (being kept in mind the bias coming from the generation of H₂ mentioned above). The link between the half-cell and the fuel cell can in some cases not be straightforward, as the many variables influencing the fuel cell experiments may change the conclusions of the half-cell results. For example, the fuel cross-over occurring in the fuel cell may lead to low OCV values unexpected by the OCP measurements in half-cell configuration. The hydrogen produced during the hydrolysis reactions also likely influences the OCV in the fuel cell experiments; especially in the case of Pd in contact with ammonia borane in which the presence of H₂ can drag the anode open circuit potential to values closer to the H₂/H₂O equilibrium potential, and thus lead to lower OCV values than expected from the half-cell results. Moreover, the cross-over issue in fuel cell configuration has certainly a stronger impact for the DABFC, as NH₄⁺ possibly generated during the anodic reaction can easily cross the Nafion[®] membrane and reduce the cathodic potential. In spite of these uncertainties, characterization in half-cell configuration appears to be the most pertinent comparison means of anodic catalyst materials and/or anodic fuel performances for alkaline fuel cell application.

1.3 Influence of the operating temperature on the fuel cell characterization

Fuel cell characterizations were performed at various operating temperatures; the voltammograms (at a scan rate of 25 mV.s⁻¹) are shown in Fig.1.3 for Pt/C and Pd/C anodic catalysts. The performances of the fuel cells (OCV and maximum power density) are reported in Table 1.2. The highest peak in power density, shown in Fig.1.3A, is reached for the fuel cell using Pt/C as anodic catalyst and sodium borohydride as anodic fuel, at 60°C (Pt/C-NaBH₄-60°C) with a value of 420 mW.cm⁻² for a current density of 890 mA.cm⁻².

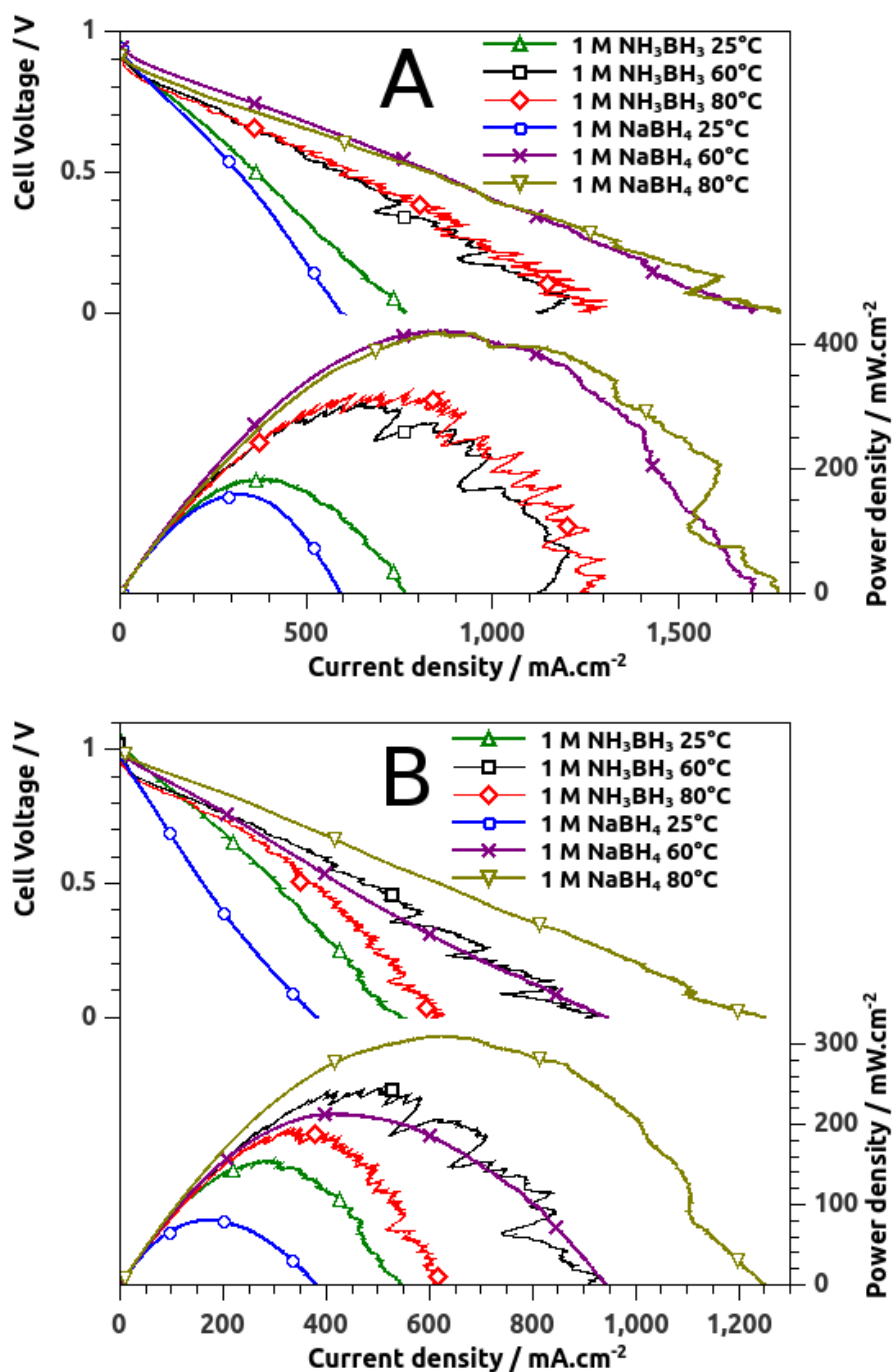


Figure 1.3: Voltammograms in fuel cell configuration operating at various temperature, using homemade Pt/C (A) and Pd/C (B) on carbon cloth as anodic catalysts (0.5 mg of Pt or Pd per cm^2) fed by $7.5 \text{ mL}\cdot\text{min}^{-1}$ of 5 M NaOH + either 1 M NaBH_4 or $1 \text{ M NH}_3\text{BH}_3$, commercial Pt/C on Toray paper as cathodic catalyst (2 mg of Pt per cm^2) fed by $300 \text{ mL}\cdot\text{min}^{-1}$ of pure oxygen (atmospheric pressure) and Nafion[®] 212 as a cationic membrane. Scan rate of $25 \text{ mV}\cdot\text{s}^{-1}$.

Please note that our fuel cell characterizations were performed using voltammetry ($25 \text{ mV}\cdot\text{s}^{-1}$), while most of DBFC characterizations in the literature are performed by plotting a polarization curve; however, the rate at which it was obtained, *i.e.* the time spent at each potential/current prior acquisition of the data point, is rarely specified. A voltammetry likely leads to higher values of power density than a characterization using the polarization technique, owing to the capacitive contribution and the decreased poisoning effects that were reported to hinder the BOR catalysis [58, 59, 60]. The author points out that the voltammetry technique

Table 1.2: Performances of the fuel cells operating at various temperature. The fuel cell operating conditions are denoted as follows: 'anodic catalyst-anodic fuel-operating temperature'. All other operating conditions are identical.

Fuel cell operating conditions	OCV (V)	Maximum power density ($\text{mW}\cdot\text{cm}^{-2}$) at [Current density ($\text{mA}\cdot\text{cm}^{-2}$)]
Pt/C-NH ₃ BH ₃ -25°C	0.947	181 [400]
Pt/C-NH ₃ BH ₃ -60°C	0.941	300 [690]
Pt/C-NH ₃ BH ₃ -80°C	0.929	305 [770]
Pt/C-NaBH ₄ -25°C	0.941	158 [325]
Pt/C-NaBH ₄ -60°C	0.942	420 [890]
Pt/C-NaBH ₄ -80°C	0.935	415 [870]
Pd/C-NH ₃ BH ₃ -25°C	1.050	154 [300]
Pd/C-NH ₃ BH ₃ -60°C	1.019	240 [520]
Pd/C-NH ₃ BH ₃ -80°C	0.975	190 [340]
Pd/C-NaBH ₄ -25°C	0.991	81 [180]
Pd/C-NaBH ₄ -60°C	0.985	212 [420]
Pd/C-NaBH ₄ -80°C	0.985	310 [640]

was chosen here in order to measure reliable and reproducible cell potential *vs.* current density curves for characterizing the fuel cell and to study the influence of the anodic catalyst material and fuel. Indeed, plotting a polarization curve takes a long time (during which hydrogen can evolve and accumulate) and requires a large amount of fuel, so that it can prove difficult to obtain reproducible polarization curves with the same fuel cell assembly [61]. On the contrary, the voltammograms presented in this work were stable upon voltage cycling (except for the noise in the voltammograms due to gaseous hydrogen generation). As stated before, the primary aim of this work is not the achievement of the best possible performances in fully optimized systems, but rather the study of different types of anodes using similar fuel cells configuration and characterization method. Cyclic voltammetry is a suitable characterization method for this purpose. One of the disadvantages of the voltammetry technique though, is that it does not allow measuring the gas generation within the fuel cell during operation, unless an on-line gas flow meter is installed [46, 62].

The improvement of the performances when increasing the operating temperature are much less visible when ammonia borane is used as an anodic fuel compared to sodium borohydride. Indeed, while ammonia borane is more efficient than sodium borohydride at 25°C (highest OCV and highest maximum power density using Pd/C and Pt/C as anodic catalysts, respectively), the ammonia borane fuel cells are outperformed by the fuel cell using Pt/C fed with sodium borohydride operating at 60°C and 80°C in terms of power density. The advantage of ammonia borane, which displays the highest OCV at 25°C when Pd/C is used as the anodic catalyst, also disappears when the operating temperature increases. Indeed, the OCV sharply decreases with the increase of the operating temperature for the fuel cell using Pd/C as anodic catalyst and ammonia borane as anodic fuel (1.050 V, 1.019 V and 0.975 V for respectively 25°C, 60°C and 80°C), while the OCV remains relatively constant with the increase of the operating temperature in the case of sodium borohydride. It is likely that the increase of the hydrolysis rate of NH₃BH₃ on Pd/C and Pt/C versus the temperature is responsible for this phenomenon. Indeed, a harsh gas generation inside the fuel cell was observed at 60°C and 80°C when ammonia borane was used as the anodic fuel, which accounts for the noisiness of the fuel cell voltammograms in these cases (Fig.1.3). The cross-over of NH₄⁺ is also enhanced by the increase of the operating

temperature and likely contributes to the loss of performance in fuel cell configuration at higher temperature when NH_3BH_3 is used as the anodic fuel, compared to NaBH_4 .

Increasing the operating temperature usually increases the fuel cell performances, by enhancing the reactions and mass-transfer kinetics, and by decreasing the ohmic losses. However in our case, although the results show that raising the operating temperature from 25°C to 60°C indeed increases all the fuel cell performances, the trend is not true anymore from 60°C to 80°C , in which case the fuel cell performances remain equal or even decrease (Fig.1.3). This behavior is likely explained by the increase of the sodium borohydride and ammonia borane hydrolysis rate, that opposes the usual beneficial effects of an increased operating temperature on the performances of the fuel cells. As a result, the optimum temperature is found around 60°C in this setup. An exception to this general observation is for the fuel cell using Pd/C as an anodic catalyst and sodium borohydride as anodic fuel, for which the performances still increase at 80°C . This behavior can be explained by the very sluggish BH_4^- oxidation reaction kinetics on Pd, as observed at 25°C in the half-cell characterizations (Fig.1.1B, Table 1.1); the enhancement of the oxidation reaction kinetics upon temperature increase still compensates for the combined increase of the hydrolysis rate. In all cases, the voltammograms of Fig.1.3 do not present any well-defined limiting current densities, which rules out any consequent mass-transfer limitation in the fuel cell setup in the present operating conditions.

Potentiostatic electrochemical impedance spectroscopy (PEIS) measurements were performed around the OCV in fuel cell configuration at various operating temperatures using sodium borohydride as anodic fuel; the Nyquist plots are presented in Fig.1.4A. The value of the polarization resistance (real part of impedance at the lowest frequency of the sinusoidal potential input signal in the Nyquist plot of Fig.1.4A) is related to the reaction kinetics and mass-transfer limitations in the fuel cells. The fuel cell operating at 25°C and using Pd/C as anode catalyst (Pd/C- NaBH_4 - 25°C) displays the highest polarization resistance. This is in agreement with the sluggish BH_4^- oxidation reaction kinetics on Pd observed in the half-cell characterizations (Fig.1.1B). Raising the operating temperature from 25°C to 60°C decreases all the polarization resistances values, as the reactions and mass-transfer kinetics improve. However, the polarization resistance of Pt/C- NaBH_4 - 80°C is higher than for Pt/C- NaBH_4 - 60°C (Fig.1.4A). As mentioned previously in this section, this result is attributed to the influence of the BH_4^- hydrolysis reaction on Pt, enhanced by increased operating temperature. In agreement with the fuel cell voltammograms of Fig.1.3A, the optimal operating temperature for the fuel cell using sodium borohydride and Pt/C as respectively anodic fuel and catalyst is around 60°C . The experimental Nyquist plots of Fig.1.4A were examined using Kramers-Kronig (K-K) transform (performed using the EC-Lab[®] software). The only parts of the Nyquist plots that did not satisfy the K-K transform were the 'tails' formed by the points obtained for the lowest frequencies of the potential input signal in the Nyquist plots of Pt/C and Pd/C at 25°C (Fig.1.4A), suggesting a time-dependent behavior. One possible explanation for this dependence in time would be the blocking of the catalysts (even at OCV) when in contact with sodium borohydride [59].

The ohmic resistance of the cell corresponds to the real part of the impedance for the points measured with the highest frequency of the sinusoidal potential input signal in the Nyquist plot (Fig.1.4B). As expected, the ohmic resistance values of the fuel cell assemblies decrease for increasing operating temperature. This decrease of the ohmic resistance contributes to the general improvement in fuel cell performances, along with the enhanced reaction kinetics, when increasing the operating temperature. It is also worth noting that the 'Pt/C' and 'Pd/C' fuel cell assemblies' do not show exactly the same values of ohmic resistance at the same operating temperature (Fig.1.4B). This difference in ohmic resistance can be explained by differences in

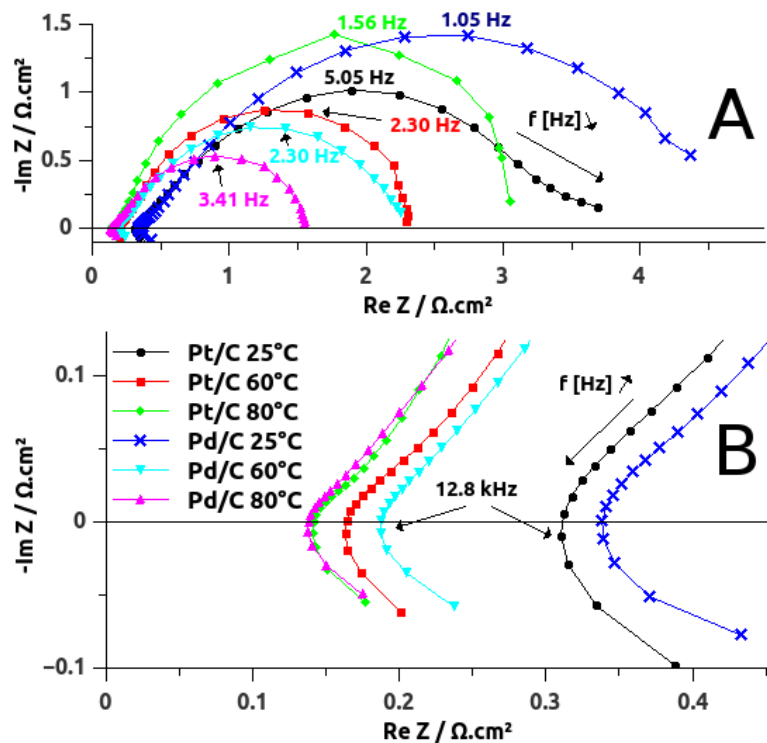


Figure 1.4: A: Nyquist plot of potentiostatic electrochemical impedance spectroscopy performed on DBFC operating at various temperature, using homemade Pd/C or Pt/C on carbon cloth as anodic catalysts ($0.5 \text{ mg of Pt or Pd per cm}^2$) fed by $7.5 \text{ mL}\cdot\text{min}^{-1}$ of $5 \text{ M NaOH} + 1 \text{ M NaBH}_4$, commercial Pt/C on Toray paper as cathodic catalyst ($2 \text{ mg of Pt per cm}^2$) fed by $300 \text{ mL}\cdot\text{min}^{-1}$ of pure oxygen and Nafion[®] 212 as a cationic membrane. Potential oscillations around the OCV with a peak to peak amplitude of 20 mV , frequency from 62 kHz to 0.1 Hz . 6 points per frequency decade. B: Zoom of graph A in the high frequency region.

the set-up of these two assemblies, which can lead to slight variation of the contact resistance. However, this difference in ohmic resistance between the two fuel cell assemblies at the same operating temperature has a negligible influence on the fuel cell voltammograms of Fig.1.3. For example, in the case of Pt/C- NaBH_4 - 25°C and Pd/C- NaBH_4 - 25°C , the difference in ohmic resistance is *ca.* $0.03 \text{ } \Omega\cdot\text{cm}^2$ (Fig.1.4B). This induces a difference in ohmic drop of *ca.* 11 mV at a current density of $380 \text{ mA}\cdot\text{cm}^{-2}$ (current density for which the cell voltage of Pd/C- NaBH_4 - 25°C reaches 0 V in the fuel cell characterization of Fig.1.2), while the difference in cell voltage at $380 \text{ mA}\cdot\text{cm}^{-2}$ between Pt/C- NaBH_4 - 25°C and Pd/C- NaBH_4 - 25°C is *ca.* 390 mV in Fig.1.2. Thus, the fuel cell voltammograms of Fig.1.2 and Fig.1.3 were not corrected for the ohmic drop.

1.4 Influence of the anode morphology on the fuel cell characterization

In the previous fuel cell characterizations presented in this study using Pt/C and sodium borohydride as, respectively, anodic catalyst and fuel, the Pt/C + Nafion[®] ink was pasted on the carbon cloth (as further described in the dedicated Appendix A.2 of this thesis). In order to study the influence of the anodic active layer morphology on the fuel cell behavior, another configuration was used where the anodic Pt/C layer is coated by spray on one side of the Nafion[®]

212 membrane (commercial Pt/C layer sprayed on N212, purchased from PaxiTech). As the other variables between these two fuel cell assemblies are identical or comparable (comparable anodic Pt loading of *ca.* $0.5 \text{ mg}_{\text{Pt}}.\text{cm}^{-2}$ with finely distributed Pt nanoparticles of *ca.* 2-3 nm mean diameter, same N212 cationic membrane and same cathode using commercial $2 \text{ mg}_{\text{Pt}}.\text{cm}^{-2}$ Pt/C on Toray paper), the main difference is the structure of the anodic Pt/C active layer, either pasted on the carbon cloth or sprayed on the Nafion[®] membrane. The configurations of the two assemblies are as follows: (i) anodic graphite bipolar plate - Pt/C anodic active layer pasted on carbon cloth - N212 - commercial Pt/C cathodic active layer on Toray paper - cathodic graphite bipolar plate for the assembly denoted as 'Pt/C pasted on carbon cloth' and (ii) anodic graphite bipolar plate - carbon cloth - N212 coated on the anodic side by sprayed Pt/C anodic active layer - commercial Pt/C cathodic active layer on Toray paper - cathodic graphite bipolar plate for the assembly denoted as 'Pt/C sprayed on N212'.

Fig.1.5 shows voltammograms obtained at a scan rate of $25 \text{ mV}.\text{s}^{-1}$ for the 'Pt/C pasted on carbon cloth' and the 'Pt/C sprayed on N212' fuel cell assemblies at 25°C ; in each case, the anodic compartment was fed with $7.5 \text{ mL}.\text{min}^{-1}$ of $5 \text{ M NaOH} + 1 \text{ M NaBH}_4$ and the cathodic compartment with $300 \text{ mL}.\text{min}^{-1}$ of humidified pure oxygen. The maximum power density of the 'Pt/C sprayed on N212' is at least three times lower than that of the 'Pt/C pasted on carbon cloth' assembly ($46.5 \text{ mW}.\text{cm}^{-2}$ at $86 \text{ mA}.\text{cm}^{-2}$ for the 'Pt/C sprayed on N212' assembly *vs.* $158 \text{ mW}.\text{cm}^{-2}$ at $325 \text{ mA}.\text{cm}^{-2}$ for the 'Pt/C pasted on carbon cloth' assembly). In addition, the shape of the voltammogram for the 'Pt/C sprayed on N212' fuel cell assembly clearly shows signs of increased mass-transfer limitations compared to that of the 'Pt/C pasted on carbon cloth' assembly. This difference in performance likely comes from the ability of the Nafion[®] membrane to be wetted by the anolyte in the anodic compartment. Indeed, SEM images of the anodic active layer presented in Fig.1.6 display a cracked morphology when Pt/C is pasted on the 3D carbon cloth matrix, while the Pt/C active layer sprayed on the flat Nafion[®] membrane shows a smooth surface. As the Nafion[®] is supposed to carry Na^+ and water from the anode to the cathode, a good contact between the Nafion[®] membrane and the anolyte is required in order to reach high performances in fuel cell configuration. While the 'Pt/C pasted on carbon cloth' anodic active layer is made of macroscopic cracks where the anolyte can easily circulate, the smooth 'Pt/C sprayed on N212' anodic active layer hinders the anolyte circulation, as this circulation is made through the fine porosity of the active layer. Furthermore, the gaseous H_2 generated by the sodium borohydride hydrolysis reaction is likely to intensify the issue of Nafion[®] wetting by the anolyte. This blocking of the membrane interface by gaseous H_2 in the anode was reported to be one of the main factors hindering the performances of the DBFC in other studies. Indeed, Park *et al.* [55] observed a decrease of the performances of the fuel cell when thicker anode active layers were used. Liu *et al.* [56] observed better performances in their fuel cell characterizations when more porous anodes were used. In a recent study, Li *et al.* [63] used Pt nanoparticles supported on different porous carbon materials as anodic catalyst. They pointed out the influence of gaseous H_2 bubbles on the performances of the DBFC. These H_2 bubbles either (i) reduced the coulombic efficiency of BH_4^- oxidation when they were removed through the anolyte circulation, or (ii) deteriorated the ionic transfer within the anodic compartment (thus increasing the anode polarization) when they were trapped inside the pores of the carbon. These observations, as well as the results presented in this work, point out that a good wetting of the anode compartment (the anode active layer and the membrane interface) is an important requirement for an efficient operation of the DBFC. Therefore, the structure of the anode has to be considered when characterizing the DBFC. The main resistance limiting the performance of the DBFC or the DABFC does not seem to be the electrical resistance of the assembly, *i.e.* the intrinsic Na^+ conductivity of the Nafion[®] membrane (PEIS experiments showed low values of ohmic resistances at high frequencies, Fig.1.4B), but rather a resistance to mass-transfer of the

reactants to the catalytic sites and/or of the Na^+ to the interface of the Nafion[®] membrane. Of course, this might not be the case if anion-exchange membranes (AEM) are used.

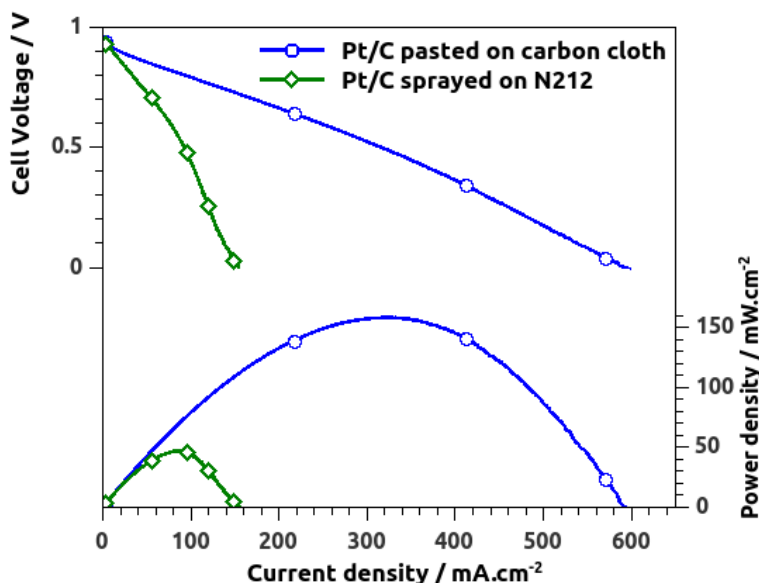


Figure 1.5: Voltammograms at 25°C in fuel cell configuration, using either homemade Pt/C pasted on carbon cloth (noted as 'Pt/C pasted on carbon cloth') or commercial Pt/C sprayed on the anodic side of the Nafion[®] membrane (noted as 'Pt/C sprayed on N212') as anodic catalysts (0.5 mg of Pt per cm²) fed by 7.5 mL.min⁻¹ of 5 M NaOH + 1 M NaBH₄, commercial Pt/C on Toray paper as cathodic catalyst (2 mg of Pt per cm²) fed by 300 mL.min⁻¹ of pure oxygen (atmospheric pressure) and Nafion[®] 212 as a cationic membrane. Scan rate of 25 mV.s⁻¹. Note the mass-transfer limitation in the case of 'Pt/C sprayed N212'

The results presented in Fig.1.5 show that a simple modification of the active layer morphology may lead to a three-fold difference in the maximum power density of the fuel cell. This result also raises an important concern for the development of the DBFC (and DABFC) technology: the comparison of fuel cell characterizations in the literature made using different catalyst materials but also different electrode structures and fuel cell setup does not enable a straightforward conclusion on which material is the most promising for the DBFC application. Taking aside all other variables making the catalyst material appreciation even more difficult (such as different fuel concentration or flow rate, different catalyst loading, operating temperature, etc.), the results presented in this work suggest that a lower power density in the fuel cell characterization does not necessary come from the choice of the catalyst material, but could simply originate from the design of the fuel cell, and notably of its anodic active layer. Being unable to reliably compare anodic catalyst materials through the DBFC literature is a serious impediment for the development of the DBFC technology. As it is not realistic to ask for common fuel cell characterization conditions among all future studies on the subject, another option would be the uniformization of the half-cell characterization conditions. Common benchmarking coming from comparable half-cell experiments would enable a pertinent comparison of catalyst materials for the BH₄⁻ oxidation reaction. This discussion is further developed in the following chapter 2 of this thesis.

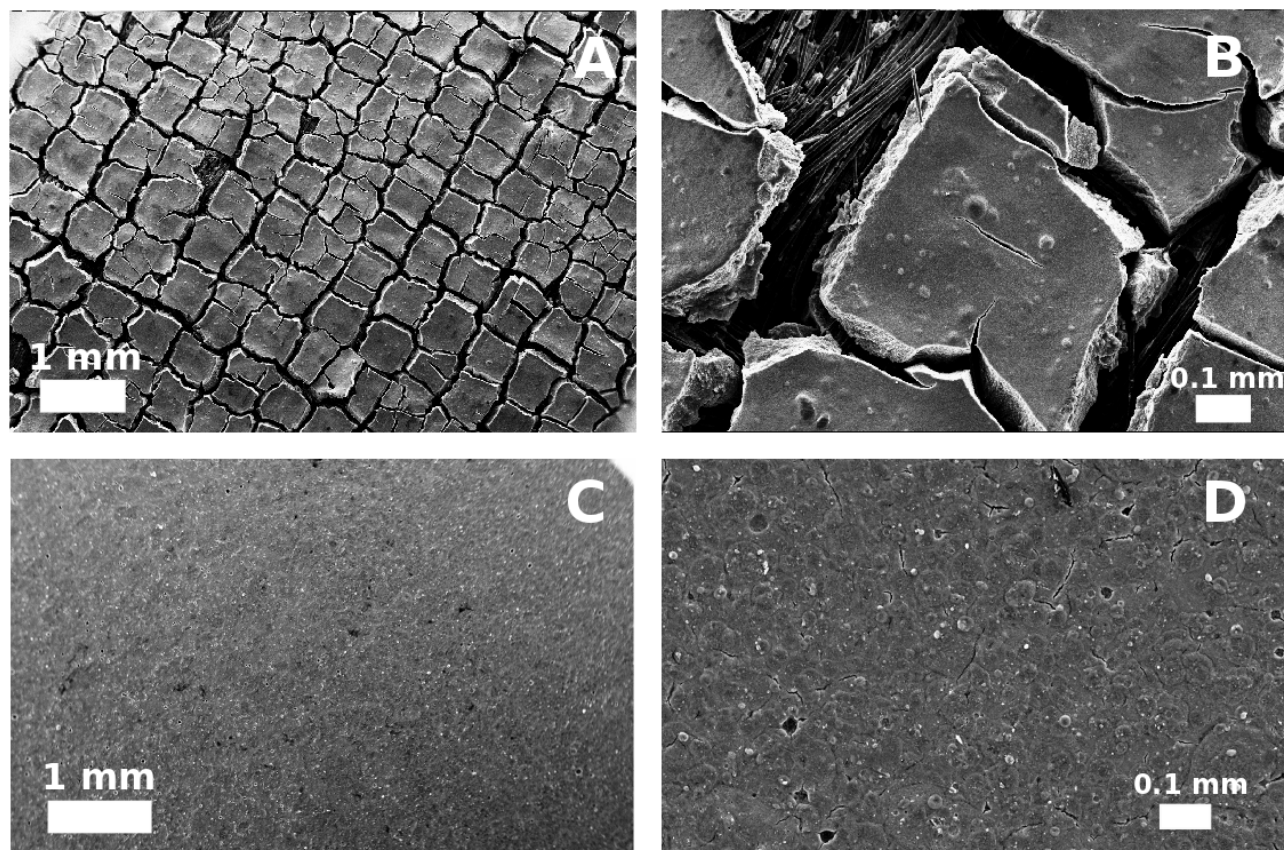


Figure 1.6: SEM images of the homemade anodic Pt/C active layer pasted on carbon cloth (A and B) and of the commercial anodic Pt/C active layer sprayed on the Nafion[®] surface (C and D).

1.5 Stability of Pt/C and Pd/C anodic active layers during fuel cell operation

Fig.1.7 shows TEM images of Pt/C and Pd/C catalysts before and after the fuel cell experiments. Prior to the experiments, both the Pt/C and the Pd/C nanoparticles are finely distributed with a mean diameter of 2.2 nm and 2.5 nm, respectively. Almost no metal agglomeration is observed. After the fuel cell characterizations (which consisted of a total of *ca.* 100 potential cycles between the OCV and 0 V using sodium borohydride and ammonia borane as anodic fuel and at operating temperatures of 25°C, 60°C and 80°C), both Pt/C and Pd/C catalysts are deteriorated. Agglomerated particles are observed for both Pt/C and Pd/C after the fuel cell experiments, indicating a sintering of the isolated nanoparticles during the operation. More striking, the remaining number of Pt nanoparticles seems to have decreased upon the fuel cell operation, which results in the observation of materials with abnormally low nanoparticle density over the carbon substrate.

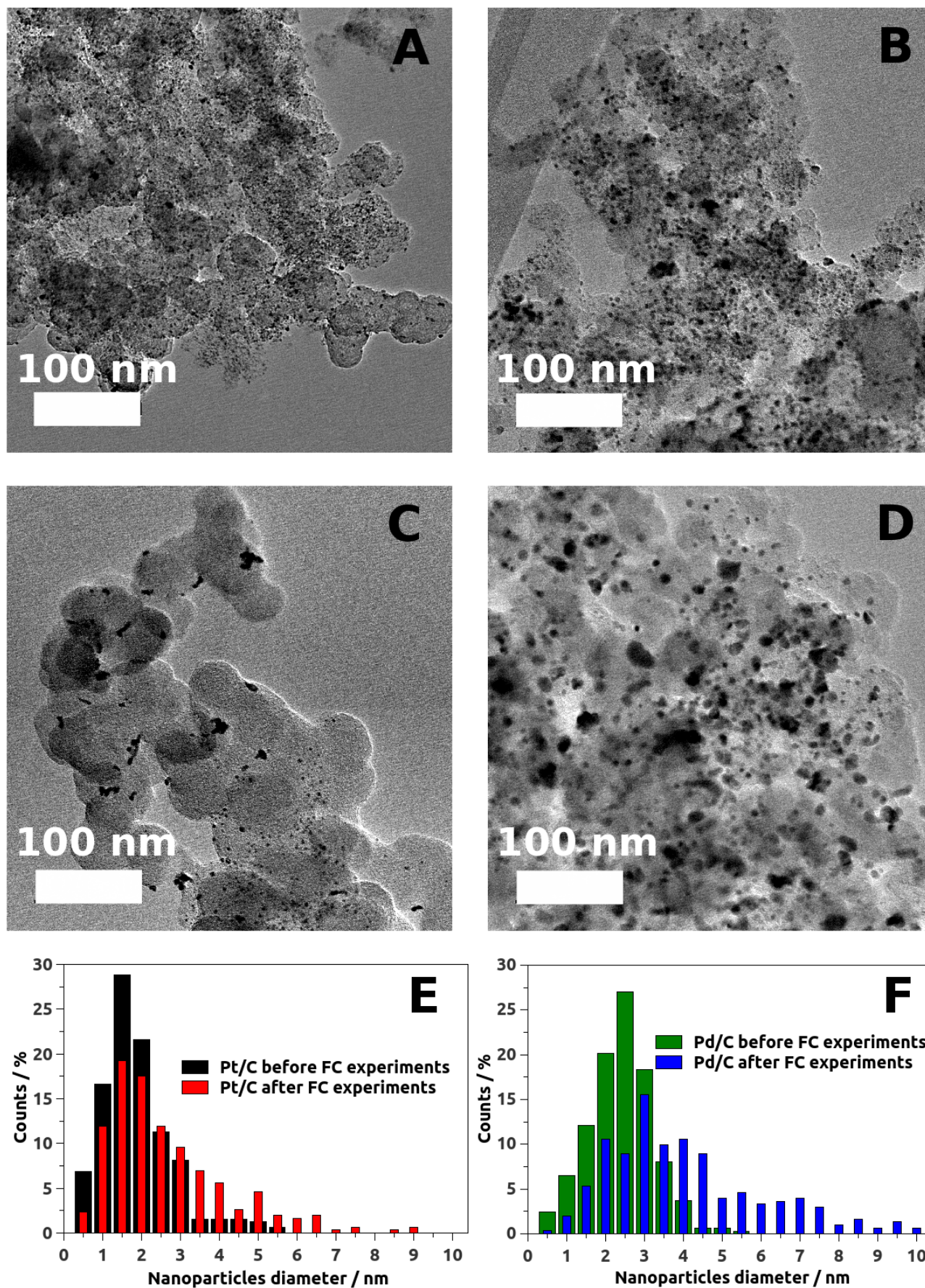


Figure 1.7: TEM images of the anodic catalysts before the fuel cell characterizations: Pt/C (A), Pd/C (B) and after the fuel cell characterizations: Pt/C (C), Pd/C (D). Nanoparticle diameter histograms of Pt/C (E) and Pd/C (F) before and after the fuel cell characterizations.

The diameter of isolated spherical nanoparticles was measured on at least 300 nanoparticles for each case and reported on the histograms of Fig.1.7. The increase of the nanoparticle mean diameter after the fuel cell experiments (from 2.2 nm to 2.9 nm for Pt/C and from 2.5 nm to 4.3 nm for Pd/C) likely indicates an Ostwald ripening, consisting of a deterioration of the smallest catalyst nanoparticles which redeposit on larger ones, thereby shifting the histogram to larger sizes. The dissolution/detachment of the smallest nanoparticles would have the same effect, and it is for now difficult to isolate the effect at stake here. Please note that the nanoparticle diameter histograms were obtained by measuring isolated spherical nanoparticles only and does not enable to quantify the agglomeration occurring to the catalysts.

It is not the aim of this chapter to further discuss the degradation mechanism of the catalysts occurring during the fuel cell operation, as these experiments are not designed for this study. Indeed, for example, platinum was detected by X-EDS in the Pd/C anodic layer after the fuel cell characterizations, indicating a dissolution-redeposition of the cathodic platinum onto the anode (no Pt was detected by X-EDS in the Pd/C anodic layer prior to the fuel cell characterizations). In order to evaluate the part of the catalyst degradation on the deterioration of performances, analysis of carbon-supported catalyst should be performed after long-term operation in DBFC and/or DABFC configurations (taking into account the possible bias induced by the dissolution/redeposition of the cathode catalyst mentioned above). However, to the author's knowledge, no measurement of the catalyst stability has ever been shown in the DBFC literature, which values the present (preliminary) results. Along with the study of the kinetics of the anodic fuels oxidation reactions, as well as the behavior towards gaseous hydrogen generation, the stability of the catalyst used in the anodic environment is a development goal to be considered. Zadick *et al.* [64] recently performed accelerated stress tests in half-cell configuration. The electrode tested was made by the deposition on a glassy carbon rod of an ink composed of Pt/C (platinum nanoparticles supported on Vulcan XC-72 carbon black) and Nafion[®] binder. The tests were carried out in alkaline (NaOH) and acidic (H₂SO₄ or HClO₄) electrolytes. In this work [64], it was shown that the loss in electrochemical active surface area of the Pt/C catalyst was three times higher in alkaline media compared to acidic media after the accelerated stress tests. Future studies of our group will focus on the degradation of various catalysts in conditions closer to the DBFC and the DABFC operation, *i.e.* with the presence of either sodium borohydride or ammonia borane in the alkaline electrolyte.

1.6 Conclusions

Pt/C and Pd/C were studied as potential anodic catalysts for the direct borohydride fuel cell (DBFC) and the direct ammonia borane fuel cell (DABFC). By using comparable variables for the anodic active layer (morphology, metal loading of *ca.* 0.5 mg of Pt or Pd per cm² and catalysts nanoparticles mean diameter of *ca.* 2-3 nm) and identical variables for the fuel cell experiments, it was shown that ammonia borane is an interesting anodic fuel at 25°C, displaying the highest OCV (1.05 V) and the highest peak power density (181 mW.cm⁻²) when respectively Pd/C and Pt/C are used as anodic catalyst. These results agree with the evaluation of the electrocatalytic activities made in half-cell configuration using Pt and Pd electrodes in sodium borohydride and ammonia borane alkaline electrolytes at 25°C.

Changing the morphology of the anodic active layer to denser layers (without any observable pores of μm size) leads to a relatively big drop in the performances of the fuel cells at 25°C, suggesting that macro-pores in the anodic active layer are necessary to enable the circulation of

the anolyte from the bipolar plate to the Nafion[®] membrane. Considering how much the results in fuel cell configuration can vary depending on the variables chosen, the half-cell configuration is likely one useful tool in order to compare all potential anodic materials for the DBFC and the DABFC.

Characterizations of the fuel cells were also conducted by raising the operating temperature up to 60°C and 80°C. Sodium borohydride is then the most interesting fuel, displaying a maximum power density value of 420 mW.cm⁻² at 60°C when Pt/C is used as the anodic catalyst. Raising the operating temperature to 80°C did not lead to global improvement of the fuel cell performances: the issue of sodium borohydride and ammonia borane heterogeneous hydrolysis reactions, indirectly observed during DBFC and DABFC operation *via* the strong gas escape, is likely at the origin of such decreased performances. A better understanding of the BOR and ABOR mechanisms is needed in order to develop anodic catalysts that will both lower the rate of the hydrolysis reactions and promote sufficient BOR or/and ABOR kinetics values.

Another development goal that should be studied in parallel is the stability of the anodic active layer in DABFC or DBFC operating conditions. Using TEM imaging, Pd/C and Pt/C were compared before and after the DBFC and DABFC characterizations presented in this study. Fast ripening, loss of nanoparticle density, coarsening and agglomeration of the Pt and Pd nanoparticles catalyst were observed. These results showed the need to further understand the degradation mechanisms of the anode catalysts upon DBFC and DABFC operation.

Chapter 2

Literature review of anode catalysts in DBFC

Several review articles about the DBFC system have already been published and cover their general principles of operation, recent developments, practical issues, costs, etc. [10, 16, 21, 39, 42, 57, 65, 66, 67, 68, 69, 70]. In the present chapter, through a selected review of the DBFC literature, we try to draw a relevant picture of the suitable catalysts for the DBFC anode. In addition, being admitted that the separator as well as the cathode are also fundamental elements of the DBFC, one shall not forget to improve these elements in order to achieve commercial maturity for the DBFC system. Briefly, it is likely that the most suitable membrane in a DBFC should conduct OH^- with the least possible permeability for BH_4^- . This key step in the development of the DBFC technology will hopefully be solved by advances in the field of membrane chemistry. Considering the cathode, the use of non-noble (and in occasion BOR-inactive) cathode catalysts is also likely to enable the DBFC technology to be commercially attractive. This being said, the separator (membrane) and the cathode of the DBFC will not be discussed further in this chapter, and the reader is kindly invited to refer to the already published reviews mentioned above for further discussion on these topics. These two elements, *i.e.* the separator and the cathode, will only be treated as 'external experimental variables of the DBFC configuration' in the section 2.1. In this chapter, we will consider only relevant works which enable to investigate the contribution of the anode for the DBFC application.

2.1 Single direct borohydride fuel cell (DBFC) configuration

2.1.1 Influence of the anode catalyst on the performance of DBFC

Table 2.1 describes single DBFC setup characterized in the literature, along with the relevant values in power density obtained during these experiments. As previously stated in the general introduction of this thesis, the first characterization of a single DBFC configuration was reported by Amendola *et al.* [12]. The single cell was composed of an anode made of finely divided 97% Au/3% Pt particles deposited on carbon cloth, an alkaline sodium borohydride reservoir, an anion-exchange membrane and an air-breathing cathode compartment; a power density of 60 mW.cm^{-2} was obtained at 70°C .

Considering the scope of this chapter, *i.e.* the investigation of potential anode catalyst materials for the DBFC, some interesting insight were obtained looking at the results of the pure performances of DBFC (*i.e.* the polarization curve only) reported in Table 2.1. Benhmenyar *et al.* [71] reported an increase in maximum power density for anode catalysts composed of $\text{Pd}_x\text{Cu}_y/\text{C}$ alloys compared to Pd/C , while keeping a constant anodic metal loading (meaning a lower Pd loading for the Pd_xCu_y catalysts): the best performances were obtained using the $\text{Pd}_{50}\text{Cu}_{50}/\text{C}$ anode catalyst.

Jamard *et al.* [62] have characterized DBFC using anode catalysts composed of Pt/C + Pt black ($1.3 \text{ mg}_{\text{Pt}}.\text{cm}^{-2}$) or $\text{Ni}_1\text{Pt}_1/\text{C}$ ($0.6 \text{ mg}_{\text{Pt}}.\text{cm}^{-2}$, mass ratio Ni:Pt = *ca.* 10:33). The maximum power density is lower in the case of $\text{Ni}_1\text{Pt}_1/\text{C}$ (115 mW.cm^{-2}) than in the case of Pt/C + Pt black (200 mW.cm^{-2}). However, $\text{Ni}_1\text{Pt}_1/\text{C}$ still leads to relatively good performances, when ratioed to the mass of Pt, as the Pt loading was reduced by a factor of 2.1. The comparison between these two DBFC setup is however less straightforward as both the Pt loading and the total anode metal loading differ between the two experiments. Furthermore, the $\text{Ni}_1\text{Pt}_1/\text{C}$ anode catalyst enhanced the anodic fuel efficiency by lowering the H_2 escape rate (see the dedicated

section 2.3 of this chapter).

Geng *et al.* [72] observed better overall performances, *i.e.* higher open cell voltage (OCV) and power density, using Ni/C anode catalysts compared to Pt/C. However, Ni/C was not stable, as demonstrated by the decay of the oxidation current during potential cycling in sodium borohydride alkaline electrolyte. Bimetallic NiPt/C catalysts with various atomic ratios were synthesized and used as anodic catalysts in DBFC configuration. The OCV values of the bimetallic NiPt/C catalysts fell between those of Ni/C and Pt/C, and shifted negative for increased Pt content. Furthermore, NiPt/C catalysts yield higher power density values than both Pt/C and Ni/C (keeping the anode metal loading constant) and showed better stability than Ni/C. The best performance was achieved by the DBFC using Ni₄₁Pt₁/C anode catalyst (mass ratio, Ni:Pt = 37:3), which was composed of a relatively low amount of Pt, by comparison to Jamard *et al.* [62].

Geng *et al.* [73] also synthesized and investigated Pt-modified Au nanoparticles on carbon support (Pt₂Au₁₈/C). Used as an anode catalyst, Pt₂Au₁₈/C led to a maximum power density value twice higher than simple Au/C in DBFC configuration at constant anode metal loading. However, there was no comparison of this synthesized catalyst material with Pt/C in the same configuration.

Cheng *et al.* [74] compared carbon-supported Au, Pt, Ag, Pd, and Ni (prepared by an impregnation method) as potential DBFC anode catalysts. The OCV values of the DBFC operated with the various anode catalysts followed the order Ag/C > Ni/C > Pt/C > Au/C > Pd/C from the highest to the lowest OCV, while the maximum power density values of the DBFC followed the order Pd/C > Au/C > Pt/C > Ag/C > Ni/C from the highest to the lowest maximum power density value. This comparison does not match the results of Geng *et al.* [72] described above, for which Ni/C led to better DBFC performances than Pt/C. However, Cheng *et al.* [74] also observed the fast decay of the Ni/C catalyst activity upon DBFC operation. Thus, the difference between the two studies could be explained by differences in the experimental procedure for plotting the polarization curves of the DBFC, knowing that a long-duration experimental procedure is likely detrimental to the absolute performances of the DBFC using an unstable Ni/C anode. In the same study [74], Ag/C was also found to be a relatively unstable anode catalyst as well as Pd/C, the anodic activity of which showed the fastest decay among all the investigated materials. The deactivation of the Pd/C catalyst was suspected to originate either from a dissolution/detachment of the Pd nanoparticles, or from the Pd/C catalyst 'leaching' during DBFC operation. This was deduced from the observation of the outlet anode tubing, which became black upon DBFC operation. This dissolution, observed by Cheng *et al.* [74], may be due to the morphology of the anode catalysts; however, little information about the characterization of the catalyst were given so that further discussion about these results may be speculative. In another study, Cheng *et al.* [75] confirmed that the Au/C catalyst leads to better DBFC performances than Ag/C. They also observed slightly better performances when these metal catalysts were supported on a more 'open' titanium mesh instead of a carbon support. However, different support material for the metal deposition may lead to different morphologies of the metal particles, and thus to different behaviors in DBFC.

Gyenge and coworkers [76, 77] compared carbon-supported Pt, PtAu, PtNi, PtIr, Au and AuPd under the form of colloids prepared according to the Bönneiman method, the atomic ratio of the alloys being fixed at 1:1. The values of power density of the DBFC at 0.5 V followed the order PtNi/C = PtIr/C > PtAu/C > Pt/C > AuPd/C > Au/C from the highest to the lowest power density value. The observation of lower power density values for the Au/C anode

catalyst compared to Pt/C does not match the findings of Cheng *et al.* [74] presented above. Note that the anode catalysts synthesized by Gyenge and coworkers [76, 77] were characterized in similar DBFC conditions, with the exception of the anolyte flow rate, which was faster for the characterization of the Au-based alloys (see Table 2.1), although the anolyte flow rate did not seem to lead to significant changes in the performances. Recently, Gyenge and coworkers [78, 79, 80] developed a Swiss-roll mixed-reactant direct borohydride fuel cell (SR-MR DBFC). This type of DBFC is membrane-free and uses a cathode catalyst that is relatively inactive towards the BOR, such as MnO_2 [81, 82, 83, 84] or Ag/C, even if the latter was proven to be less suitable than MnO_2 [81, 84]. Among all the results published by this group so far, Pt/C gave the highest performances when used as anode catalyst of the SR-MR DBFC [80], outperforming the PtRu/C catalyst [78]. However, relatively good performances were also observed for the SR-MR DBFC using the anode composed of Os electrodeposited on carbon cloth [79]: in the referenced work, similar performances were achieved using an Os-based anode compared to a Pt-based anode. Gyenge and coworkers also investigated Os as potential anode catalyst in more classical DBFC configuration, either electrodeposited Os on carbon paper [85] or carbon-supported Os nanoparticles prepared according to the Bönnehan method [86].

Composite anodes based on Ni powder with the addition of small amounts of other metals were also investigated as potential materials for the DBFC. Li *et al.* [87] used a constant mass of Ni powder, possibly mixed with a constant and small mass of M/C ($M = \text{Pd}, \text{Au}, \text{Ag}$) deposited on Ni foam as anodes in DBFC configuration. The maximum power density values depending on the catalyst added to the Ni powder followed the order $\text{Pd/C} > \text{Ag/C} > \text{Au/C} > \text{Ni powder}$, from the highest to the lowest maximum power density value. Ma *et al.* [88] found, in similar experimental conditions, that the addition of small amounts of Pt/C instead of Pd/C to the Ni powder led to better DBFC performances. However, in more recent studies made by this group, Pd/C was always used along with Ni powder as composite anode in DBFC configuration [89, 90, 91]. These results suggest that the most suitable catalysts for this type of composite Ni anode are those with the highest activity for the hydrogen oxidation reaction (HOR). This is related to the management of the H_2 generated inside the anode during DBFC operation (see the dedicated section 2.3 of this chapter).

Using polymer fiber membrane (KOH-doped polyvinyl alcohol) as separator in DBFC configuration, Huang *et al.* [92] observed higher values in maximum power density with Pt-Ru/C as the anode catalyst compared to Pt/C. During the investigation of Pt/C and Pd/C as potential anode catalysts for direct liquid fuel cells fueled by sodium borohydride or ammonia borane, Olu *et al.* [93] (see also the chapter 1 of this thesis) reported higher values of maximum power density in DBFC configuration using Pt/C compared to Pd/C, at every DBFC operation temperature studied.

Liu and coworkers [94] investigated Co-based anode catalysts. They first reported better performances in DBFC configuration using CoO powder compared to a hydrogen storage alloy material as anode catalyst. On a similar DBFC configuration, the performances were improved by the same team using CoB powder as anode catalyst [95]. Anodes based on CoO powder were characterized by this team using several different DBFC configurations: high performances were obtained using Nafion[®] membrane and a RuO_2 powder-based cathode [96], as well as another DBFC configuration using polymer fiber membrane and perovskite-type oxides-based cathode (LaNiO_3) [97]. As other materials besides CoO powder were not characterized as potential anode catalysts within the same DBFC configuration conditions in [97] and [96], it is not possible for the moment to conclude on the value of CoO as a potential DBFC anode catalyst, although these first results are promising.

Cobalt-based catalyst were also synthesized by Qin *et al.* [98, 99, 100, 101] and characterized in several publications as anode and cathode materials in DBFC configuration. The catalysts were composed of $\text{Co}(\text{OH})_2$ supported on several types of polypyrrole-modified carbons (PPY-C), the carbon being either acetylene black (AB) [99], Super P (SP) [100] or BP 2000 (BP) [100]. The choice of the polypyrrole-modified carbon support was found to influence the performances of the DBFC. Indeed, the $\text{Co}(\text{OH})_2$ -PPY-BP catalyst showed better DBFC performances than $\text{Co}(\text{OH})_2$ -PPY-SP [100]. Although these catalysts were used both as anode and cathode catalysts, polarization curves of the anode and the cathode upon DBFC operation demonstrated a decrease in both anodic and cathodic polarization, so that the improvement in DBFC performances using $\text{Co}(\text{OH})_2$ -PPY-BP was attributed to the decrease of the charge transfer resistance with polypyrrole-modified BP 2000 carbon (PPY-BP). Shortly after this publication, another DBFC configuration was characterized by Qin *et al.* [101] using $\text{Co}(\text{OH})_2$ -PPY-C as the cathode catalyst (with various heat-treatment of the catalyst) and Zr-Ni alloy-based composite anode. However, the DBFC operation conditions were not similar between [100] and [101] (various anolyte flow rates, operating temperature and oxidant humidity), and it is therefore not possible to determine from the pure comparison of the results which material is the most suitable anode catalyst for the DBFC.

Pure hydrogen storage alloys were also used as anode catalyst in the DBFC. The advantage of these materials is their ability to absorb and valorize gaseous hydrogen possibly generated upon DBFC operation, and thus increase the performances or at least the fuel efficiency of the DBFC (see the dedicated section 2.3 of this chapter). From the Table 2.1, DBFC using hydrogen storage alloys as anodic catalyst seem to reach relatively good performances [102, 103, 104, 105, 106, 107]. However so far, no study compared different hydrogen storage alloys within similar DBFC configuration and operating conditions. In addition, no comparison exists between a hydrogen storage alloy material and a common noble metal-based catalyst (for example Pt/C) in similar DBFC configuration conditions. Thus, it is difficult to evaluate the suitability of these materials for application as anode catalyst in the DBFC. Note that Choudhury *et al.* [13] investigated several types of hydrogen storage alloys as anode catalysts for the direct borohydride hydrogen peroxide fuel cell. They characterized AB_5 -type (A = a rare earth metal such as La, Ce, Nd, Pr, Y or mischmetal, B = a non-hydride forming element such as Ni) or AB_2 -type (A = Ti, Zr or Hf, B = a transition metal) hydrogen storage alloys, AB_5 -type alloys leading to higher values of power density than AB_2 -type alloys for this type of fuel cell [13]. This result was explained by the better ability of AB_5 -type alloys to store hydrogen compared to AB_2 -type alloys.

2.1.2 Experimental variables external to the choice of the anodic catalyst in DBFC configuration

The comparison of prospective anode catalysts based on pure values of maximum power density in DBFC configuration (Table 2.1), as done in the discussion above, is pertinent in the one condition that only the anode material is changed while the other variables of the DBFC setup and the characterization procedure are kept identical. Indeed, the DBFC unit cell is a complex system, the numerous variables of which are likely to influence the apparent performances. Below is discussed a non-exhaustive list of variables external to the choice of the anode material, as well as their influence on the performances in DBFC configuration.

Anode composition and structure/geometry

The composition, structure and geometry of the anode, besides the bare choice of the anode catalyst, also influences the performances of the DBFC. Park *et al.* [55] observed a decrease of the performance of the DBFC when thicker anodes were used. An increase of the PTFE content in the anode also led to a decrease of the performances of the DBFC [55]. The choice of the anode binder also influences the behavior of the DBFC. Indeed, Li and coworkers [87, 108] observed better performances in DBFC configuration using Nafion[®] instead of PTFE as the anode binder. Kim *et al.* [109] also used various content of Nafion[®] binder in the anode active layer and observed, as well as Li and coworkers [87, 108], that the performances of the DBFC first increased with higher Nafion[®] content, up to an optimum content value above which the performances started to deteriorate. A larger macro-porosity of the anode was observed to be beneficial to the performances of the DBFC [56, 63, 93, 110]. All these variables related to the composition and structure/geometry of the anode (besides the choice of the catalyst) are likely linked to the DBFC performances *via* the management of gaseous hydrogen generated upon DBFC operation. This issue will be further discussed in the dedicated section 2.3 of this chapter.

Another variable that is likely to enhance the values of power density is the geometric surface area of the anode. Indeed, Li *et al.* [95] observed that decreasing the anode geometric surface area (all other variables of the DBFC configuration being kept identical) leads to an increase of the absolute value of maximum power density (from 75 mW.cm⁻² to 220 mW.cm⁻² when the anode area is reduced from 1 cm² to 0.25 cm², respectively [95]). Liu *et al.* [56] also observed that the maximum power density decreased from 190 mW.cm⁻² to 50 mW.cm⁻² when the anode geometric surface area increased from 6 cm² to 68 cm², in similar DBFC setup conditions. In the works of Yang *et al.* [96, 97], where relatively high values of maximum power density were obtained compared to most of the DBFC literature, the values of geometric surface areas of the DBFC configuration were not specified. However, it has been known from a mail inquiry to the corresponding author (Ref. [111]) that the geometric surface area of the DBFC was equal to 1 cm² in [97] and [96], which is coherent with the relatively slow oxidant flow rate of 5 standard cubic centimeters per minute (sccm) used in these works. This small area, compared to most of the DBFC characterizations presented in Table 2.1, where most of the DBFC active areas were larger than 5 cm², is also likely to (at least partially) explain these high performances.

Anolyte properties

The power density values of the DBFC usually increase with faster anolyte flow rates, as the mass-transfer of reacting species through the anode active layer is enhanced. However, the increase of the anolyte flow rate may lead to either a relatively limited [77, 106, 112, 113] or significant [55, 92, 114, 115] influence on the DBFC performances, depending on the experimental system. Note that Kim *et al.* [106] observed that increasing the anolyte flow rate has a negative effect in their DBFC configuration; this contradictory result was attributed to a cooling effect of the anolyte (enhanced by the increase of the flow rate) on the temperature of the MEA. The increase of the concentration in borohydride species in the anolyte is generally beneficial to the performances of the DBFC, as mass-transfer limitations of borohydride anions decrease as BOR kinetics improve in this case [40, 73, 112, 113]. However, in the DBFC system of Boyacı San *et al.* [114], the increase of NaBH₄ concentration was beneficial to the performances of the DBFC at low operating temperature only (close to 50°C), whereas it was detrimental at higher operating temperatures (close to 80°C). Kim *et al.* [109] observed first an increase of the value of maximum power density with the increase of NaBH₄ concentration up to 0.5 M, but the

maximum power density then decreased for higher NaBH_4 concentrations. The possible negative effects of higher borohydride concentration come from the enhancement of the cross-over of borohydride species through the separator (illustrated by a decrease of the OCV [112]) or a faster gaseous hydrogen escape rate due to the improved hydrolysis reactions [114]. Jamard *et al.* [46] also observed a decrease of the performances in DBFC with the increase of the NaBH_4 concentration for relatively high NaBH_4 concentrations values (from 2 M to 5 M NaBH_4 in 1 M NaOH). The concentration of the hydroxide anion in the anolyte was reported to hold little influence on the performances of the DBFC [40, 109, 112, 113, 115]. A high concentration in OH^- can indeed improve the performances of the DBFC as it increases the conductivity of the anolyte and reduces the hydrolysis rate; however it can also be detrimental for the DBFC as the solution viscosity increases [40]. The choice of counter-ions in the composition of the anolyte was also found to influence the performances of the DBFC. Huang *et al.* [92] observed better performances using KOH/KBH_4 rather than $\text{NaOH}/\text{NaBH}_4$. This variable is likely to depend on the design of the system. Indeed, Na^+ has the highest cationic mobility (with the exception of protons) inside a Nafion[®] type membrane, whereas K^+ has a higher cationic mobility in aqueous solution [116]. Thus, depending on the separator (anion- *vs.* cation-exchange membranes or porous separator) used in the DBFC configuration, the behavior of the DBFC is likely to be sensitive to the type of cation in the anolyte.

Cathode compartment

The cathode compartment is also defined by several variables that influence the behavior of the DBFC. The value of maximum power density of the DBFC usually increases when the oxygen content [80, 88, 112, 115], oxygen partial pressure [112], relative humidity [88, 106, 115] and flow rate [88, 106, 114] of the cathode gas increase. Higher oxygen content and partial pressure enhance the kinetics of the oxygen reduction reaction (ORR). A high relative humidity of the cathode gas is beneficial to the DBFC as water (i) is a reactant in the ORR, (ii) participates to the good ionic conducting properties of most of the ion-exchange membranes and (iii) can favor the removal of sodium hydroxide possibly formed at the cathode side. The relative humidity as well as the flow rate of the cathode gas have to be optimized in order to sufficiently hydrate the membrane without flooding the cathodic compartment.

The type of catalyst used at the cathode influences the performances of the DBFC depending on the kinetics of the catalyst for the ORR [74, 96, 97, 101]. Various types of catalysts were used as cathode material in DBFC, as shown in Table 2.1. However, it is beyond the scope of this chapter to discuss the suitability of every material as a potential cathode catalyst.

Nevertheless, one should be aware that, depending on the DBFC setup design, the cell voltage of the DBFC at a given current density may be driven by: (i) the anode polarization [112, 113], (ii) the cathode polarization [40, 46, 99, 100, 107, 117], or (iii) both the anode and cathode polarization [98]. In order to study the influence of the type of anode catalyst on the DBFC performances, one should ensure the smallest possible influence of the cathode polarization on the DBFC cell voltage by using cathodic catalysts with relatively high loading (as well as an active catalyst for the ORR, such as Pt) and pure humidified oxygen cathode gas at relatively fast flow rates. Note that these precautions were taken in the work presented in the chapter 1 of this thesis. The addition of a reference electrode in the anolyte fuel tank enables the monitoring of the anode polarization potential upon DBFC operation. However, this reference electrode does not monitor directly the cathode polarization potential, but rather the cathode polarization potential minus the voltage loss (ohmic drop) due to the ohmic resistance between the anode and the cathode, which is usually ruled by the membrane ionic resistance.

Ponce de Leon *et al.* [16] monitored both the anode and cathode polarization potentials upon direct borohydride hydrogen peroxide fuel cell (DBPFC) operation. This task is much more straightforward in the DBPFC system, as the cathode feed is liquid and enables positioning a second reference electrode directly into the catholyte tank. They observed that the DBPFC cell voltage was not equal to the difference between the cathode and anode polarization potentials and that the influence of the ohmic drop on the DBPFC cell voltage increases with the increase of the current density (as one would naturally expect): at the highest value of current density, the DBPFC voltage drop was almost equally due to the sum of anode and cathode polarization losses compared to the ohmic drop [16]. Although this study was made in a slightly different system than the DBFC, it is worth noting that monitoring a stable anode polarization potential upon DBFC operation using a reference electrode placed in the anolyte does not necessarily demonstrate that the cathode polarization is entirely responsible for the decrease of the DBFC cell voltage. However, it is a relatively reliable method for the determination of the anode polarization potential upon DBFC operation.

Separator

The choice of the separator, which ensures the electrical insulation between the anode and the cathode in the DBFC setup, obviously influences the performances of the system. Depending on the type of separator, *i.e.* (i) a simple electrical insulator (enabling the passage of the anolyte to the cathode and the catholyte to the anode), (ii) a cation-exchange membrane (the charge carriers being Na^+ or K^+) or (iii) an anion-exchange membrane (the charge carriers being OH^- and BH_4^-), the DBFC is likely to behave singularly. As such, the DBFC would respond differently to most of the variables inherent to the DBFC system, depending on the type of separator/membrane used in the experiment. The majority of the DBFC characterizations presented in Table 2.1 used Nafion[®]-type cation-exchange membranes. However, several studies dealt with the synthesis of other types of membrane that, in some occasions, led to an improvement of the DBFC performances compared to the use of Nafion[®] membranes. Among others, the alkali-doped poly (4,4'- diphenylether-1,3,4-oxadiazole) (POD-DPE) solid electrolyte membrane [118], polybenzimidazole (PBI) porous membrane [119], radiation grafted ion-exchange membranes [120], chitosan-based (CS) polymer electrolyte membranes [89, 90, 91] and alkali-doped polyvinyl alcohol (PVA) solid electrolyte membranes [92, 97], showed better performances than Nafion[®]-type membranes in similar DBFC configuration. In that frame, note that Choudhury *et al.* [89] achieved a maximum power density value of 810 mW.cm^{-2} at 70°C using an eco-friendly Na_2HPO_4 -based ionically cross-linked chitosan (CS) hydrogel membrane electrolyte and chitosan chemical hydrogel (CCH) anode binder. To the author's knowledge, this is the highest absolute value of power density obtained in the literature for a DBFC (Table 2.1).

The reduction of the membrane thickness leads to a decrease of the membrane ionic resistivity but also to an increase in BH_4^- permeability [56, 117, 119]. Despite faster rates of reactant cross-over (characterized by the decrease of the OCV values), the use of a thinner membrane usually leads to better performances of the DBFC [56, 96, 97, 117, 119]. Impedance spectroscopy is a powerful tool in order to evaluate (among other things) the part of the ohmic resistance in the polarization curve of the DBFC [93]. This ohmic resistance is likely to change depending on the conditions chosen for the DBFC configuration (such as the current collectors, the operating temperature, the anolyte composition, the type of membrane, etc.). The value of this ohmic resistance may even differ among identical DBFC configurations because of the non-reproducibility of the system assembly. Unfortunately, this value of the DBFC ohmic resistance is usually not specified along with the DBFC characterization curves in the literature,

so that the comparison of different DBFC setup is hindered. In particular, it is very often not possible to present ohmic drop-corrected fuel cell performances, as it is usually the case in the literature dealing with the proton exchange membrane fuel cells (PEMFC) [121].

Operating temperature

The operating temperature has contradictory influences on the performances of the DBFC. Increasing the operating temperature enhances (i) the mass-transfer of the reacting species, (ii) the kinetics of the anodic and cathodic electrochemical reactions and (iii) the ionic conductivities of the anolyte and the membrane. These effects are beneficial to the DBFC performances and lead to an increase of the values of maximum power density of the DBFC when the operating temperature is raised [76, 77, 88, 89, 90, 91, 93, 96, 106, 107, 112, 113, 114, 122] (see also the chapter 1 of this thesis). However, higher operating temperatures also enhance the cross-over rates (leading to a decrease of the OCV [93, 112]) and the kinetics of the hydrolysis reactions generating gaseous hydrogen [93, 114]. Olu *et al.* [93] observed almost no improvement of the performances in DBFC configuration between operating temperatures of 60°C and 80°C when Pt/C was used as the anode catalyst (see the Fig.1.3 of the chapter 1), and this was attributed to the enhancement of the heterogeneous hydrolysis of the fuel and the related hydrogen production and escape, as visually observed. Boyacı San *et al.* [114] also witnessed a decrease of the power density of the DBFC when the operating temperature was raised from 50°C to 80°C for high sodium borohydride concentrations (around 1.5 M in NaBH₄). This decrease of the DBFC power density was linked to the increase of the monitored hydrogen escape along with the operating temperature [114].

Characterization method

Among all the operating variables that influence the DBFC characterization, the procedure for plotting the characterization curve of the DBFC often remains unspecified. Among others, Jamard *et al.* [46, 62] used the amperometry technique with a current scan rate of 2 mA.s⁻¹ while Olu *et al.* [93] (chapter 1) used the cyclic voltammetry technique with a voltage scan rate of 25 mV.s⁻¹ until a stable voltammogram plot was achieved. Most of the other DBFC characterizations presented in Table 2.1 were made using polarization techniques, for which the curve of the cell voltage versus the current density consists of a certain number of polarization points. The waiting time for recording every polarization point is rarely mentioned in the literature, hindering the comparison between different DBFC studies. It is likely that faster characterization procedures of the DBFC leads to better apparent performances. One of the risks of the polarization technique is that the measurement made at a given value of the current density may be influenced by the history of the DBFC, *i.e.* by the previous measurements performed at other values of current density. Indeed, these previous measurements could temporarily change the hydration of the membrane, temperature of the MEA, etc. Therefore, the reproducibility of random polarization points could be checked after plotting the whole polarization curve of the DBFC. For example, Liu *et al.* [61] plotted two different DBFC polarization curves; one before and one after a 1 h constant current operation of the DBFC at 50 mA.cm⁻². They observed that the second polarization curve, plotted after the constant current operation, displayed better performances than the first one. This result was attributed to the reduction of the cross-over after the constant current operation [61]. It is worth noting that one of the disadvantages of dynamic characterization techniques such as voltammetry is the difficulty to monitor the gaseous hydrogen escape upon the DBFC operation, whereas it is much more

straightforward to measure the amount of gas escaping at a given polarization point during a given time. A solution for this issue consists in integrating a flow meter on-line to the system to record the gas escape flow rate along with the determination of the characterization curve [46, 62].

Considering the numerous and dependent variables inherent to the operation of a DBFC, it is not possible to investigate further the anode catalysts only from the pure DBFC performances presented in Table 2.1. The only reliable base for discussion, as was attempted above, is made of studies using different anode materials characterized using similar DBFC configuration; obviously, the more detailed the experimental conditions, the more reliable the comparison. It is not realistic to ask for an identical DBFC characterization setup between all laboratories. Therefore, one recommendation for a study presenting a novel anode catalyst would be to also perform the characterizations of a DBFC using a Pt/C-based anode (with a Pt loading of 0.5 mg.cm^{-2}), all other operating conditions being identical to the characterization of the DBFC based on the novel anode catalyst. This reference characterization curve of a DBFC using a Pt/C-based anode would also enable the community (i) to compare the novel anode material with the standard platinum catalyst and (ii) to compare this reference characterization curve to others from the literature, which would help to evaluate the performances of the DBFC setup presented, and thus help to determine the contribution of the anode catalyst to these performances.

Table 2.1: Review of DBFC configurations. Symbols: T is the operating temperature, S is the geometric active surface area, P is the power density (not necessarily the maximum value, depending on the information available) obtained at the current density j

Ref.	Anode composition	Cathode composition	Separator ^a	Anodic fuel	Cathodic fuel	T (°C)	S (cm ²)	P (mW.cm ⁻²) [j (mA.cm ⁻²)]
[12]	97% Au 3% Pt electrodeposited on carbon cloth	Air cathode	AEM	5 wt.% NaBH ₄ in 20 wt.% NaOH reservoir	Ambient air	70	3.6	63 [158]
[114]	PtRu/C + Nafion [®] on carbon cloth (0.89 mg _{metal} .cm ⁻²)	Pt/C (1 mg _{Pt} .cm ⁻²)	N117	0.5 M NaBH ₄ in 6 M NaOH 5 mL.min ⁻¹	Humidified O ₂ 100 mL.min ⁻¹	80	25	112 [240]
[122]	Pt ₃ - Au ₂ /C on carbon cloth (0.5 mg _{metal} .cm ⁻²)	Pt/C (0.5 mg _{Pt} .cm ⁻²)	N115	1 M NaBH ₄ in 6 M NaOH 3 mL.min ⁻¹	Humidified O ₂ 200 mL.min ⁻¹	65	25	161 [298]
[72]	Ni/C + Nafion [®] on carbon paper (1 mg _{metal} .cm ⁻²)	Pt/C (1 mg _{Pt} .cm ⁻²)	N212	5 wt.% NaBH ₄ in 10 wt.% NaOH 1 mL.min ⁻¹	Dry O ₂ 0.2 MPa 100 mL.min ⁻¹	60	5	151 [360] ^b
[73]	Ni ₄₁ - Pt ₁ /C + Nafion [®] on carbon paper (1 mg _{metal} .cm ⁻²)	Pt/C (0.5 mg _{Pt} .cm ⁻²)	N212	1 M NaBH ₄ in 3 M NaOH 0.5 mL.min ⁻¹	Dry O ₂ 0.2 MPa 100 mL.min ⁻¹	40	5	65 [180]
[118]	Au/C + Nafion [®] on carbon paper (1 mg _{metal} .cm ⁻²)	Pt/C (0.5 mg _{Pt} .cm ⁻²)	POD-DPE	1 M NaBH ₄ in 3 M NaOH 0.5 mL.min ⁻¹	Dry O ₂ 0.1 MPa	40	5	112 [240]
[119]	Pt ₂ - Au ₁₈ /C + Nafion [®] on carbon paper (1 mg _{metal} .cm ⁻²)	Pt/C (0.5 mg _{Pt} .cm ⁻²)	N115	1 M NaBH ₄ in 3 M NaOH 0.5 mL.min ⁻¹	Dry O ₂ 0.1 MPa	40	5	123 [260]
[62]	Pt/C on carbon paper (1 mg _{metal} .cm ⁻²)	Pt/C (0.5 mg _{Pt} .cm ⁻²)	PBI-60	1 M NaBH ₄ in 3 M NaOH 0.5 mL.min ⁻¹	Dry O ₂ 0.1 MPa	40	5	262 [550]
[62]	Pt/C + Pt black + PTFE on carbon cloth (1.3 mg _{metal} .cm ⁻²)	Pt/C (0.5 mg _{Pt} .cm ⁻²)	N115	1 M NaBH ₄ in 3 M NaOH 0.5 mL.min ⁻¹	Dry O ₂ 0.1 MPa	40	5	140 [250]
[46]	Pt ₁ - Ni ₁ /C + PTFE on carbon cloth (0.8 mg _{metal} .cm ⁻²)	Air cathode (non Pt based)	AEM	2 M NaBH ₄ in 1 M NaOH (flow rate unknown)	Ambient air	RT	9	200 [400]
[88]	Pt/C + Pt black + PTFE on carbon cloth (0.6 mg _{Pt} .cm ⁻²)	Air cathode (non Pt based)	AEM	2 M NaBH ₄ in 1 M NaOH 10 mL.min ⁻¹	Ambient air	RT	9	115 [300]
[88]	Ni (0.96 mg _{Ni} .cm ⁻²) + Pt/C (0.04 mg _{Pt} .cm ⁻²) + Nafion [®]	Pt/C (1 mg _{Pt} .cm ⁻²)	N212	5 wt.% NaBH ₄ in 10 wt.% NaOH 5 mL.min ⁻¹	Humidified O ₂ 150 mL.min ⁻¹	60	5	194 [400]
[90]	Ni (0.96 mg _{Ni} .cm ⁻²) + Pd/C (0.04 mg _{Pd} .cm ⁻²) + Nafion [®]	Pt/C (1 mg _{Pt} .cm ⁻²)	N212	5 wt.% NaBH ₄ in 10 wt.% NaOH 5 mL.min ⁻¹	Humidified O ₂ 150 mL.min ⁻¹	60	5	270 [600]
[90]	Ni (4.8 mg _{Ni} .cm ⁻²) + Pd/C (0.2 mg _{Pd} .cm ⁻²) + Nafion [®] (on carbon paper)	Pt/C (1 mg _{Pt} .cm ⁻²)	N212	5 wt.% NaBH ₄ in 10 wt.% NaOH 5 mL.min ⁻¹	Humidified O ₂ 150 mL.min ⁻¹	60	5	237 [600]
[90]	Ni (3.68 mg _{Ni} .cm ⁻²) + Pd/C (0.13 mg _{Pt} .cm ⁻²) + Nafion [®]	Pt/C (1 mg _{Pt} .cm ⁻²)	CS	5 wt.% NaBH ₄ in 10 wt.% NaOH 5 mL.min ⁻¹	Humidified O ₂ 150 mL.min ⁻¹	60	5	261 [600]
[90]	Ni (3.68 mg _{Ni} .cm ⁻²) + Pd/C (0.13 mg _{Pt} .cm ⁻²) + Nafion [®] (on Ni foam)	Pt/C (1 mg _{Pt} .cm ⁻²)	CS	5 wt.% NaBH ₄ in 10 wt.% NaOH 5 mL.min ⁻¹	Humidified O ₂ 150 mL.min ⁻¹	60	5	261 [600]
[91]	Ni (3.68 mg _{Ni} .cm ⁻²) + Pd/C (0.13 mg _{Pt} .cm ⁻²) + Nafion [®]	Pt/C (1 mg _{Pt} .cm ⁻²)	N212	5 wt.% NaBH ₄ in 10 wt.% NaOH 5 mL.min ⁻¹	Humidified O ₂ 150 mL.min ⁻¹	60	5	382 [810]
[91]	Ni (3.68 mg _{Ni} .cm ⁻²) + Pd/C (0.13 mg _{Pt} .cm ⁻²) + CCH ^c (on Ni foam)	Pt/C (1 mg _{Pt} .cm ⁻²)	CS	5 wt.% NaBH ₄ in 10 wt.% NaOH 5 mL.min ⁻¹	Humidified O ₂ 150 mL.min ⁻¹	60	5	402 [800]
[89]	Ni (3.68 mg _{Ni} .cm ⁻²) + Pd/C (0.13 mg _{Pt} .cm ⁻²) + CCH ^c (on Ni foam)	Pt/C	CS	5 wt.% NaBH ₄ in 10 wt.% NaOH 5 mL.min ⁻¹	O ₂ 150 mL.min ⁻¹	70	5	450 [900]
[89]	Ni (3.68 mg _{Ni} .cm ⁻²) + Pd/C (0.13 mg _{Pt} .cm ⁻²) + CCH ^c (on Ni foam)	Pt/C	CS	5 wt.% NaBH ₄ in 10 wt.% NaOH 5 mL.min ⁻¹	O ₂ 150 mL.min ⁻¹	70	5	448 [900]
[89]	Ni (3.68 mg _{Ni} .cm ⁻²) + Pd/C (0.13 mg _{Pt} .cm ⁻²) + CCH ^c (on Ni foam)	Pt/C	CS	5 wt.% NaBH ₄ in 10 wt.% NaOH 5 mL.min ⁻¹	O ₂ 150 mL.min ⁻¹	70	5	685 [1400]
[89]	Ni (3.68 mg _{Ni} .cm ⁻²) + Pd/C (0.13 mg _{Pt} .cm ⁻²) + CCH ^c (on Ni foam)	Pt/C	CS	5 wt.% NaBH ₄ in 10 wt.% NaOH 5 mL.min ⁻¹	O ₂ 150 mL.min ⁻¹	70	5	810 [1,680]

Table 1 continued

Ref.	Anode composition	Cathode composition	Separator ^a	Anodic fuel	Cathodic fuel	T (°C)	S (cm ²)	P (mW.cm ⁻²) [j (mA.cm ⁻²)]
[102]	MmNi _{3.55} Co _{0.75} Mn _{0.4} Al _{0.3} + C + CoO on Ni foam (150 mg _{alloy} .cm ⁻²)	FePc + Carbon	none	0.8 M KBH ₄ in 6 M KOH (flow rate unknown)	Ambient air	RT	n.a.	92 [175]
[103]	MmNi _{3.55} Co _{0.75} Mn _{0.4} Al _{0.3} + C + CoO on Ni foam (150 mg _{alloy} .cm ⁻²)	CoPc + Carbon (7.5 mg _{CoPc} .cm ⁻²)	none	0.8 M KBH ₄ in 6 M KOH (flow rate unknown)	Ambient air	RT	4	90 [175]
[104]	MmNi _{3.55} Co _{0.75} Mn _{0.4} Al _{0.3} + C + CoO on Ni foam (150 mg _{alloy} .cm ⁻²)	LaNiO ₃ + Carbon (7.5 mg _{LaNiO₃} .cm ⁻²)	none	0.8 M KBH ₄ in 6 M KOH (flow rate unknown)	Ambient air	65	1	127 [280]
[94]	CoO powder + PTFE on Ni foam (70 mg _{CoO} .cm ⁻²)	LaCoO ₃ + Carbon (7.5 mg _{LaCoO₃} .cm ⁻²)	none	0.8 M KBH ₄ in 6 M KOH (flow rate unknown)	Ambient air	30	1	78 [140]
[95]	MmNi _{3.55} Co _{0.75} Mn _{0.4} Al _{0.3} + PTFE on Ni foam	LaCoO ₃ + Carbon (7.5 mg _{LaCoO₃} .cm ⁻²)	none	0.8 M KBH ₄ in 6 M KOH (flow rate unknown)	Ambient air	30	1	62 [100]
[97]	CoB powder + PTFE on Ni foam (70 mg _{CoB} .cm ⁻²)	LaCoO ₃ + Carbon (7.5 mg _{LaCoO₃} .cm ⁻²)	PFM	0.8 M KBH ₄ in 6 M KOH (flow rate unknown)	O ₂	65	n.a. ^e	663 [1,200]
[96]	CoO powder + PTFE on Ni foam (70 mg _{CoO} .cm ⁻²)	LaNiO ₃ + CNT (7.5 mg _{LaNiO₃} .cm ⁻²)	NRE211	20 mL.min ⁻¹	5 SmL.min ⁻¹	60	n.a. ^e	425 [900]
[106]	Zr based AB alloy on Ni micro fibre	RuO ₂ + CNT (7.5 mg _{RuO₂} .cm ⁻²)	N115	10 wt.% NaBH ₄ in 20 wt.% NaOH 25.3 mL.min ⁻¹	Humidified air 10 L.min ⁻¹	75	100	220 [420]
[105]	Ni powder + MmNi _{3.35} Co _{0.75} Mn _{0.4} Al _{0.3} O ₂ + PTFE on Ni mesh (200 mg _{alloy} .cm ⁻²)	MnO ₂ + Carbon (2 mg _{MnO₂} .cm ⁻²)	none	0.037 M KBH ₄ in 6 M KOH reservoir	Ambient air	25	n.a.	70 [180]
[123]	Platinized functionalized MWCNT + paraffin oil (0.09 mg _{Pt} .cm ⁻²)	Air cathode	n.a.	10 wt.% NaBH ₄ in 4 M NaOH reservoir	Ambient air	RT	125	44 [98]
[71]	Pd/C + Nafion [®] on carbon cloth (0.5 mg _{metal} .cm ⁻²)	Pt/C (0.5 mg _{Pt} .cm ⁻²)	N115	1 M NaBH ₄ in 6 M NaOH 3 mL.min ⁻¹	Humidified O ₂ 200 mL.min ⁻¹	60	25	28 [52]
	Pd ₇₅ Cu ₂₅ /C + Nafion [®] on carbon cloth (0.5 mg _{metal} .cm ⁻²)							37 [57]
	Pd ₅₀ Cu ₅₀ /C + Nafion [®] on carbon cloth (0.5 mg _{metal} .cm ⁻²)							98 [223]
	Pd ₂₅ Cu ₇₅ /C + Nafion [®] on carbon cloth (0.5 mg _{metal} .cm ⁻²)							65 [123]
[55]	Pt/C + Nafion [®] on carbon paper (0.4 mg _{Pt} .cm ⁻²)	Pt/C (0.4 mg _{Pt} .cm ⁻²)	N115	10 wt.% NaBH ₄ in 20 wt.% NaOH 10 mL.min ⁻¹	Humidified O ₂ 200 mL.min ⁻¹	70	25	152 [n.a.]

Table 1 continued

Ref.	Anode composition	Cathode composition	Separator ^a	Anodic fuel	Cathodic fuel	T (°C)	S (cm ²)	P (mW.cm ⁻²) [j (mA.cm ⁻²)]
[76]	Pt/C + Nafion [®] on carbon cloth (5 mg _{metal} .cm ⁻²) Pt ₁ Au ₁ /C + Nafion [®] on carbon cloth (5 mg _{metal} .cm ⁻²) Pt ₁ Ni ₁ /C + Nafion [®] on carbon cloth (5 mg _{metal} .cm ⁻²) Pt ₁ Ir ₁ /C + Nafion [®] on carbon cloth (5 mg _{metal} .cm ⁻²) Au/C + Nafion [®] on carbon cloth (5 mg _{metal} .cm ⁻²) Au ₁ Pd ₁ /C + Nafion [®] on carbon cloth (5 mg _{metal} .cm ⁻²) Pt ₁ Au ₁ /C + Nafion [®] on carbon cloth (5 mg _{metal} .cm ⁻²) Os/C + Nafion [®] on the membrane (1 mg _{Os} .cm ⁻²)	Pt based (4 mg _{Pt} .cm ⁻²) Pt based (4 mg _{Pt} .cm ⁻²) Pt black (4 mg _{Pt} .cm ⁻²) Pt black (4 mg _{Pt} .cm ⁻²) Pt black (4 mg _{Pt} .cm ⁻²)	N117	2 M NaBH ₄ in 2 M NaOH 50 mL.min ⁻¹	O ₂ 2.7 atm (abs) 200 SmL.min ⁻¹	60	5	42 [84] 47 [94] 54 [108] 54 [108] 15 [30] 31 [62] 47 [94] 69 [n.a.]
[77]	Au/C + Nafion [®] on carbon cloth (5 mg _{metal} .cm ⁻²) Au ₁ Pd ₁ /C + Nafion [®] on carbon cloth (5 mg _{metal} .cm ⁻²) Pt ₁ Au ₁ /C + Nafion [®] on carbon cloth (5 mg _{metal} .cm ⁻²) Os/C + Nafion [®] on the membrane (1 mg _{Os} .cm ⁻²)	Pt based (4 mg _{Pt} .cm ⁻²) Pt black (4 mg _{Pt} .cm ⁻²) Pt black (4 mg _{Pt} .cm ⁻²) Pt black (4 mg _{Pt} .cm ⁻²)	N117	2 M NaBH ₄ in 2 M NaOH 85 mL.min ⁻¹	O ₂ 2.7 atm (abs) 200 SmL.min ⁻¹	60	5	15 [30] 31 [62] 47 [94] 69 [n.a.]
[86]	Os/C + Nafion [®] on the membrane (1 mg _{Os} .cm ⁻²)	Pt black (4 mg _{Pt} .cm ⁻²)	N117	0.5 M NaBH ₄ in 2 M NaOH 10 mL.min ⁻¹	O ₂ 4.4 atm (abs) 1.25 SL.min ⁻¹	60	5	130 [275] 80 [150] 35 [60]
[110]	Pt ₁ Ru ₁ /Graphite Felt + Nafion [®] (1 mg _{metal} .cm ⁻²) Pt ₁ Ru ₁ /Carbon XC-72 + Nafion [®] (1 mg _{metal} .cm ⁻²) Pt ₁ Ru ₁ black + Nafion [®] (1 mg _{metal} .cm ⁻²) Os electrodeposited on carbon paper (1.7 mg _{Os} .cm ⁻²)	Pt black (4 mg _{Pt} .cm ⁻²) Ag/C MnO ₂ /C MnO ₂ /C (0.5 mg.cm ⁻²) MnO ₂ /C (15 mg _{MnO2} .cm ⁻²) MnO ₂ /C (15 mg _{MnO2} .cm ⁻²)	N117	0.5 M NaBH ₄ in 2 M NaOH 10 mL.min ⁻¹	O ₂ 4.4 atm (abs) 1.25 SL.min ⁻¹	60	5	109 [280]
[85]	Os electrodeposited on carbon paper (1.7 mg _{Os} .cm ⁻²)	Pt black (4 mg _{Pt} .cm ⁻²)	N117	0.5 M NaBH ₄ in 2 M NaOH 10 mL.min ⁻¹	O ₂ 4.4 atm (abs) 1.25 SL.min ⁻¹	60	5	100 [250] 64 [150] 28 [80]
[78]	Pt/C + Nafion [®] on carbon cloth (0.8 mg _{Pt} .cm ⁻²) Pt/C + Nafion [®] on carbon cloth (0.8 mg _{Pt} .cm ⁻²) Pt ₁ Ru ₁ /C + Nafion [®] on carbon cloth (0.8 mg _{metal} .cm ⁻²)	Ag/C MnO ₂ /C MnO ₂ /C (0.5 mg.cm ⁻²) MnO ₂ /C (15 mg _{MnO2} .cm ⁻²) MnO ₂ /C (15 mg _{MnO2} .cm ⁻²)	PPFM	1 M NaBH ₄ in 2 M NaOH 8 mL.min ⁻¹	O ₂ 105 kPa (abs) 10 SL.min ⁻¹	50	20	100 [250] 64 [150] 28 [80]
[79]	Os electrodeposited on carbon cloth (0.32 mg _{Os} .cm ⁻²)	MnO ₂ /C (0.5 mg.cm ⁻²) MnO ₂ /C (15 mg _{MnO2} .cm ⁻²) MnO ₂ /C (15 mg _{MnO2} .cm ⁻²)	PPFM	1 M NaBH ₄ in 2 M NaOH 12 mL.min ⁻¹	O ₂ 105 kPa (abs) 10 SL.min ⁻¹	50	20	188 [420]
[80]	Pt/C + Nafion [®] on carbon cloth (0.8 mg _{Pt} .cm ⁻²)	MnO ₂ /C (0.5 mg.cm ⁻²) MnO ₂ /C (15 mg _{MnO2} .cm ⁻²) MnO ₂ /C (15 mg _{MnO2} .cm ⁻²)	PD	1 M NaBH ₄ in 2 M NaOH 12 mL.min ⁻¹	O ₂ 105 kPa (abs) 10 SL.min ⁻¹	50	20	223 [520]
This work [93]	Pt/C + Nafion [®] on carbon cloth (0.5 mg _{Pt} .cm ⁻²)	Pt/C (2 mg _{Pt} .cm ⁻²)	N212	1 M NaBH ₄ in 5 M NaOH 7.5 mL.min ⁻¹	Humidified O ₂ 300 mL.min ⁻¹	85	25	420 [890] ^f 212 [420] ^f
[115]	Pd/C + Nafion [®] on carbon cloth (0.5 mg _{Pd} .cm ⁻²) Pd/C + PTFE on Ni foam (0.3 mg _{Pd} .cm ⁻²)	Pt/C (0.3 mg _{Pt} .cm ⁻²)	N117	1.5 M NaBH ₄ in 20 wt.% NaOH 2 mL.min ⁻¹	Humidified O ₂ 150 mL.min ⁻¹	60	25	28 [56]
[92]	Pt-Ru/C (5 mg.cm ⁻²) ^d Pt/C (5 mg.cm ⁻²) ^d	Pt/C (5 mg.cm ⁻²) ^d	PVA	1 M KBH ₄ in 4 M KOH 130 mL.min ⁻¹	Humidified O ₂ 100 mL.min ⁻¹	30	5	184 [290] 117 [200]

Table 1 continued

Ref.	Anode composition	Cathode composition	Separator ^a	Anodic fuel	Cathodic fuel	T (°C)	S (cm ²)	P (mW.cm ⁻²) [j (mA.cm ⁻²)]
[41]	Zr _{0.9} Ti _{0.1} Mn _{0.6} V _{0.2} Co _{0.1} Ni _{1.1} + Pd/C	Pt/C	NRE211	10 wt.% NaBH ₄ in 20 wt.% NaOH 150 mL.min ⁻¹	Humidified air 5 L.min ⁻¹	60	67	290 [600]
[107]	Zr _{0.9} Ti _{0.1} Mn _{0.6} V _{0.2} Co _{0.1} Ni _{1.1} + PTFE on Ni foam (200 mg _{alloy} .cm ⁻²)	Pt/C (2 mg _{Pt} .cm ⁻²)	N117	10 wt.% NaBH ₄ in 20 wt.% NaOH 200 mL.min ⁻¹	Humidified O ₂ 200 mL.min ⁻¹	85	6	190 [300]
[61]	Ni powder + PTFE on Ni foam	Ag/C (1.6 mg _{Ag} .cm ⁻²)	N112	5 wt.% NaBH ₄ in 6 M NaOH reservoir	Ambient air	RT	6	33 [70]
[98]	Ni powder + Pt/C + Zr-Ni AB alloy on Ni foam (10 mg.cm ⁻²) ^d	Co-PPY-C (1.2 mg _{Co} .cm ⁻²)	N117	5 wt.% NaBH ₄ in 10 wt.% NaOH 10 mL.min ⁻¹	Dry O ₂ 150 mL.min ⁻¹	RT	5	65 [140]
[99]	Co(OH ₂)-PPY-C + Nafion [®] on Ni foam (10 mg.cm ⁻²) ^d	Co(OH ₂)-PPY-C (10 mg.cm ⁻²)	N117	5 wt.% NaBH ₄ in 10 wt.% NaOH 10 mL.min ⁻¹	Dry O ₂ 150 mL.min ⁻¹	RT	5	83 [140]
[100]	Co(OH ₂)-PPY-BP + Nafion [®] on Ni foam (5 mg.cm ⁻²) ^d	Co(OH ₂)-PPY-BP (5 mg.cm ⁻²)	N112	5 wt.% NaBH ₄ in 10 wt.% NaOH 10 mL.min ⁻¹	Dry O ₂ 150 mL.min ⁻¹	RT	5	160 [350]
[101]	Ni powder + Pt/C + Zr-Ni AB alloy on Ni foam (10 mg.cm ⁻²) ^d	Co(OH ₂)-PPY-C (5 mg.cm ⁻²)	N112	5 wt.% NaBH ₄ in 10 wt.% NaOH 50 mL.min ⁻¹	Humidified O ₂ 150 mL.min ⁻¹	60	5	390 [800]
[117]	Ni powder on Ni foam (167 mg _{Ni} .cm ⁻²)	Pt/C (1 mg _{Pt} .cm ⁻²)	NRE211	5 wt.% NaBH ₄ in 6 N NaOH reservoir	Ambient air	RT	6	40 [80]
[108]	Ni powder (13.0 mg _{Ni} .cm ⁻²) + Pd/C (0.5 mg _{Pd} .cm ⁻²) + Nafion [®] Pd/C (1.7 mg _{Pd} .cm ⁻²) + Nafion [®]	Pt/C (1 mg _{Pt} .cm ⁻²)	N112	5 wt.% NaBH ₄ in 20 wt.% NaOH reservoir	Ambient air	25	6	80 [170] 37 [70] 32 [70]
[87]	Ni powder (12.7 mg _{Ni} .cm ⁻²) + Pd/C (0.51 mg _{Pd} .cm ⁻²) + PTFE (on Ni foam) Ni powder (14.4 mg _{Ni} .cm ⁻²) + + Pd/C (0.6 mg _{Pd} .cm ⁻²) + PTFE on Ni foam ... + Pd/C (0.6 mg _{Pd} .cm ⁻²) + Nafion [®] on Ni foam ... + Ni powder (0.6 mg _{Ni} .cm ⁻²) + Nafion [®] on Ni foam ... + Au/C (0.6 mg _{Au} .cm ⁻²) + Nafion [®] on Ni foam ... + Ag/C (0.6 mg _{Ag} .cm ⁻²) + Nafion [®] on Ni foam Pt/MPC + Nafion [®] on Ni foam (0.25 mg _{Pt} .cm ⁻²) Pt/XC-72 + Nafion [®] on Ni foam (0.25 mg _{Pt} .cm ⁻²) Pt/CA + Nafion [®] on Ni foam (0.25 mg _{Pt} .cm ⁻²)	Pt/C (1 mg _{Pt} .cm ⁻²)	N112	10 wt.% NaBH ₄ in 20 wt.% NaOH 150 mL.min ⁻¹	Humidified air 5 L.min ⁻¹	60	100	180 [340] 240 [430] 180 [430] 190 [430] 205 [430] 66 [160] 56 [120] 20 [40] 19 [39]
[63]		Pt/C (0.25 mg _{Pt} .cm ⁻²)	N117	0.75 M NaBH ₄ in 1.5 M NaOH 20 mL.min ⁻¹	Dry O ₂ 150 mL.min ⁻¹	RT	6	66 [160] 56 [120] 20 [40] 19 [39]
[124]	Pt based commercial anode	MnO ₂ (3 mg _{MnO₂} .cm ⁻²)	none	1 M NaBH ₄ in 3 M KOH stirred, 1 mL.min ⁻¹	Ambient air	RT	10	20 [30]
[125]	Pt black + Nafion [®] (1 mg _{Pt} .cm ⁻²)	MnO ₂ (3 mg _{MnO₂} .cm ⁻²)	none	2 M NaBH ₄ in 3 M KOH stirred, 1 mL.min ⁻¹	Ambient air	25	10	20 [30]

Table 1 continued

Ref.	Anode composition	Cathode composition	Separator ^a	Anodic fuel	Cathodic fuel	T (°C)	S (cm ²)	P (mW.cm ⁻²) [j (mA.cm ⁻²)]
[74]	Au/C + Nafion [®] (2 mg _{Au} .cm ⁻²) Pd/C + Nafion [®] (2 mg _{Pd} .cm ⁻²) Pt/C + Nafion [®] (2 mg _{Pt} .cm ⁻²) Ag/C + Nafion [®] (2 mg _{Ag} .cm ⁻²) Ni/C + Nafion [®] (2 mg _{Ni} .cm ⁻²) Au/C + Nafion [®] (2 mg _{Au} .cm ⁻²)	Pt/C (2 mg _{Pt} .cm ⁻²)	N117	5 wt.% NaBH ₄ in 10 wt.% NaOH 10 mL.min ⁻¹	O ₂ 200 mL.min ⁻¹	85	4	72 [150] 90 [200] 51 [125] 44 [n.a.] 41 [75]
[120]	Au/C + Nafion [®] (2 mg _{Au} .cm ⁻²)	Pt/C (2 mg _{Pt} .cm ⁻²)	N117 CU1	1.32 M NaBH ₄ in 2.5 M NaOH 10 mL.min ⁻¹	O ₂ 200 mL.min ⁻¹	85	4	72 [150]
[113]	Pt-Ru/C + Nafion [®] on carbon paper (1 mg.cm ⁻²) ^d	Pt/C (2 mg _{Pt} .cm ⁻²) (1 mg.cm ⁻²) ^d	AEM	1 M NaBH ₄ in 1 M NaOH 2.78 mL.min ⁻¹	O ₂ 200 mL.min ⁻¹	60	4	103 [225] 150 [210]
[84]	Au/C + Nafion [®] on carbon paper (2 mg _{Au} .cm ⁻²)	FeTMPP/C (2 mg _{FeTMPP} .cm ⁻²)	N117	1.32 M NaBH ₄ in 2.5 M NaOH 10 mL.min ⁻¹	O ₂ 200 mL.min ⁻¹	85	4	56 [130]
[75]	Au/Ti mesh + Nafion [®] (2 mg _{Au} .cm ⁻²) Ag/Ti mesh + Nafion [®] (2 mg _{Ag} .cm ⁻²)	Pt/C (2 mg _{Pt} .cm ⁻²)	N117	1.32 M NaBH ₄ in 2.5 M NaOH 10 mL.min ⁻¹	O ₂ 200 mL.min ⁻¹	85	4	81 [175] 50 [125]
[126]	Electrodeposited nano Au on Ni grid (0.8 mg _{Au} .cm ⁻²)	MnO ₂ + Carbon	AEM	5 wt.% NaBH ₄ in 6 N NaOH reservoir	Ambient air	RT	13	28 [80]

^a NRE211, N112, N212, N117 and N115 are types of Nafion[®] cation-exchange membranes (DuPont). AEM stands for Anion-Exchange Membrane; 2259-60 (Pall RAI) for [12], ADP-Morgane[®] for [46, 62, 113] or supplied by the University of Cranfield for [126]. POD-DPE: an alkali-doped poly (4,4'- diphenylether-1,3,4-oxadiazole) solid electrolyte membrane. PBI: a polybenzimidazole porous membrane. CS: a chitosan-based polymer electrolyte membrane. PFM: a polymer fiber membrane. PPFM: a polypropylene fiber membrane (Scimat[®] 720/20). PD: a polyolefine diaphragm (Viledon[®] FS2227E). CU1: a radiation grafted ion-exchange membrane.

^b Ni/C was unstable upon potential cycling in alkaline sodium borohydride electrolyte [72].

^c CCH: chitosan chemical hydrogel binder.

^d It could not be categorically determined if the value of loading corresponded to the pure metal loading or the total metal/support catalyst loading.

^e The geometric surface area is not specified in [96, 97], but the corresponding author kindly answered to our inquiry and provided the appropriate value (1 cm²) [111].

^f Characterization of the DBFC was performed using voltammetry technique (scan rate of 25 mV.s⁻¹) [93] (chapter 1).

2.2 Electrocatalytic activity towards the borohydride oxidation reaction (BOR)

In order to reduce the number of experimental variables and to focus only on the anode catalyst activity towards the BOR, a three-electrode electrochemical cell is commonly used. This setup enables to isolate one material that is used as the working electrode in the electrochemical cell, and to study the behavior of this material towards the BOR with controlled (and therefore correctible) mass-transfer limitations and ohmic drop, without interference with the reaction that proceeds at the counter-electrode.

2.2.1 Rotating disk electrode (RDE) configuration

The rotating disk electrode (RDE) configuration is an interesting and reliable technique among all the experimental possibilities that offers the electrochemical cell. Indeed, the RDE configuration enables a better control of the hydrodynamics ruling the mass-transfer thanks to the revolution of the rate-adjustable RDE. Using this RDE configuration, it is possible to characterize a catalyst towards the BOR in steady-state or near-steady-state conditions, but also to expel gas bubbles that may form at the electrode surface. The use of a bulk working electrode enables to study the activity of a given material with different morphology [127] or crystallinity [128] towards the BOR. Bulk Pt electrodes (polycrystalline or single crystals) are used in the chapter 3 of this thesis to investigate the structure sensitivity of the BOR on Pt. A thin film working electrode made by the deposition of a catalyst ink (usually on a glassy carbon substrate electrode) is closer to the reality of a DBFC anode. However, the use of a thin film electrode adds experimental variables such as the type and porosity of support material, the type and content of binder in the catalyst ink, the thickness of the film [129] as well as the distribution, the size and the catalyst loading [59, 60]. Model electrodes composed of Pt nanoparticles supported on flat glassy carbon (chapter 4) and vertically-aligned carbon nanofibers (chapter 5) are used in the second part of this thesis to further understand the BOR mechanism on Pt.

Fig.2.1 presents a selected review of catalyst characterization towards the BOR in RDE configuration. The experimental conditions are given in Table 2.2. In order to build this graph, data were taken for each RDE voltammogram from a window of current density that did not exceed half the value of the mass-transfer-limited current density. By doing so, it was expected that the data would correspond to a potential range where the BOR is mainly controlled by the kinetics of the reaction and not by the mass-transfer of the reactant. For the same reason, the fastest revolution rate was considered when several voltammograms with different revolution rates were presented in a study. Note that, despite our care, the graphical review presented in Fig.2.1 cannot be considered as perfectly rigorous. Indeed, the data reported in Fig.2.1 likely do not represent conditions totally controlled by the reaction kinetics, so that differences may come from the variation in revolution rates within the different studies. The scan rate also differs from study to study (from $5 \text{ mV}\cdot\text{s}^{-1}$ to $25 \text{ mV}\cdot\text{s}^{-1}$), it is however judged to yield negligible influence in near-steady-state conditions. The concentration in NaBH_4 from the different studies was 10 mM, except for Finkelstein *et al.* [130] and Merino-Jimenez *et al.* [131] where the NaBH_4 concentrations were 5 mM and 20 mM, respectively. However, the axis of current density was not normalized by the concentration in NaBH_4 in Fig.2.1. Therefore, the value of potential at a given current density may be overestimated and underestimated for Finkelstein *et al.* [130] and Merino-Jimenez *et al.* [131], respectively, by comparison with the other studies.

Despite the small biases mentioned above, Fig.2.1 provides a good basis for the comparison of the activity of different catalyst materials towards the BOR. Platinum is the most active catalyst for the BOR, both as bulk electrodes [93, 130, 132] and carbon-supported nanoparticles [133]. Palladium displays slightly lower activity than platinum [93]; however, Pd/C exhibits the lowest open circuit potential (OCP) among the other supported catalysts [133]. Gold displays BH_4^- oxidation potentials at least 300 mV higher than platinum for the same current density (bulk [130, 131, 132] or supported materials [73, 133, 134]). Cheng *et al.* [135] characterized bulk Au in RDE configuration in order to determine kinetics parameters of the BOR on gold (the corresponding data was not reported in Fig.2.1 due to the high concentration in BH_4^- used in this work compared to the others). They also found a relatively high value of onset potential for the BOR on this surface (*ca.* 0.5 V *vs.* RHE). Simões *et al.* [136] also synthesized bimetallic $\text{Pd}_x\text{Au}_{1-x}/\text{C}$ catalysts: the behavior of these catalysts towards the BOR using the RDE setup remained similar to pure Pd/C catalyst (*i.e.* with a relatively good activity towards the BOR at low potentials) up to a Pd:Au atomic ratio of 1:1. For higher Au contents, the behavior towards the BOR of the $\text{Pd}_x\text{Au}_{1-x}/\text{C}$ bimetallic catalysts progressively got closer to the behavior of pure Au/C catalyst (*i.e.* a low activity towards the BOR at low potentials) [136]. Simões *et al.* [137] also alloyed Pd with Ni, a non-noble metal. The bimetallic catalyst $\text{Pd}_{0.5}\text{Ni}_{0.5}/\text{C}$ showed similar behavior towards the BOR in RDE setup compared to pure Pd/C catalyst [137]. Bulk silver showed even lower activity than gold [138]. Considering the low activities towards the BOR, pure gold and silver do not seem to be suitable catalyst materials for the DBFC anode. These materials are still widely employed in DBFC anodes, notably owing to their supposed faradaic efficiency; this latter property is however now questioned, at least for potentials that are relevant to the DBFC anode [130, 139, 140, 141, 142]. Bimetallic PtAu catalysts show high activity towards the BOR, close to the activity of pure Pt both in bulk [132] or supported [73] form. Yi *et al.* [134] synthesized alloyed AuFe/C catalysts which display higher activity than pure Au/C in their study; however the activity obtained is still too low to consider the use of this catalyst in the anode of a DBFC. Data were added to the Fig.2.1, coming from the mass-transfer-corrected Tafel plots for oxygen reduction on sputtered Pt in 1 M KOH at 70°C from Coudurier *et al.* [143]. Electrocatalysts that fail to promote the BOR at a reasonable current density (*ca.* 10 $\text{mA}\cdot\text{cm}^{-2}$) below *ca.* 0.3 V (leaving *ca.* less than 0.5 V of cathode - anode voltage difference) are not relevant for DBFC purposes. In these conditions, this means that pure gold (Au and Au/C) and pure silver (Ag and Ag/C) have no chance to be competitive anode materials for DBFC.

Some characterizations in RDE configuration were not placed in the graphical review of Fig.2.1, mostly because the concentration of NaBH_4 used in these studies were out of the range chosen for the figure. Among them, Geng *et al.* [72] found higher activity towards the BOR in RDE configuration for the $\text{Ni}_{41}\text{Pt}_1/\text{C}$ catalyst compared to Ni/C. Furthermore, Ni/C was not stable in these conditions, as demonstrated by the activity decay of the Ni/C RDE upon potential cycling, while the $\text{Ni}_{41}\text{Pt}_1/\text{C}$ RDE voltammograms were stable for at least 10 cycles. However, no comparison with Pt/C in similar RDE configuration was attempted in this study [72]. Wang *et al.* [144] also characterized a bimetallic NiPt/C catalyst. $\text{Ni}_3\text{Pt}_7/\text{C}$ displayed comparable or even slightly higher electrocatalytic activity than Pt/C in similar RDE configuration, while Ni/C showed almost no activity towards the BOR [144]. Sljukic *et al.* [145] also found an enhancement of the electrocatalytic activity using NiPt/C or CoPt/C bimetallic catalysts instead of pure Pt/C, $\text{Ni}_1\text{Pt}_3/\text{C}$ being slightly more active than $\text{Co}_1\text{Pt}_3/\text{C}$. Hou *et al.* [146] observed an enhancement of the electrocatalytic activity in RDE configuration using alloyed PtSn/C instead of Pt/C. All these examples demonstrate that improvement of the catalytic activity of single-constituent catalysts could still be obtained by alloying them with

(an) adequate(s) metal(s), which leaves room to breakthrough innovation in the field of DBFC electrocatalysts.

Table 2.2: Experimental conditions applied to plot BOR voltammograms on RDE voltammograms of the BOR for various catalysts. Some data of these voltammograms are reported in Fig.2.1.

Ref.	Working Electrode(s)	[NaBH ₄] (mmol.L ⁻¹)	[NaOH] (mol.L ⁻¹)	Revolution rate (rpm)	Scan rate (mV.s ⁻¹)
This work [93] (chapter 1)	Bulk Pt and Pd	10	1	1000	25
Finkelstein <i>et al.</i> [130]	Bulk Pt and Au	5	1	2000	25
Merino-Jimenez <i>et al.</i> [131]	Bulk Au	20	3	2500	10
Tegou <i>et al.</i> [132]	Bulk Pt and Au, PtAu(Ni)/GC ^a	10	1	500	5
Chatenet <i>et al.</i> [138]	Bulk Ag	10	1	1600	5
Simões <i>et al.</i> [133]	Pt/C, Pd/C and Au/C	10	1	2000	5
Yi <i>et al.</i> [134]	Au/C and AuFe/C	10	1	2000	20
Geng <i>et al.</i> [73]	Au/C and AuPt/C	10	2	800	5

^a PtAu(Ni)/GC refers to a mixed Pt/Au partial galvanic replacement of smooth nickel layers that had been electrodeposited onto glassy carbon electrode substrates. It is not strictly a bulk electrode but displays a relatively smooth and flat surface [132].

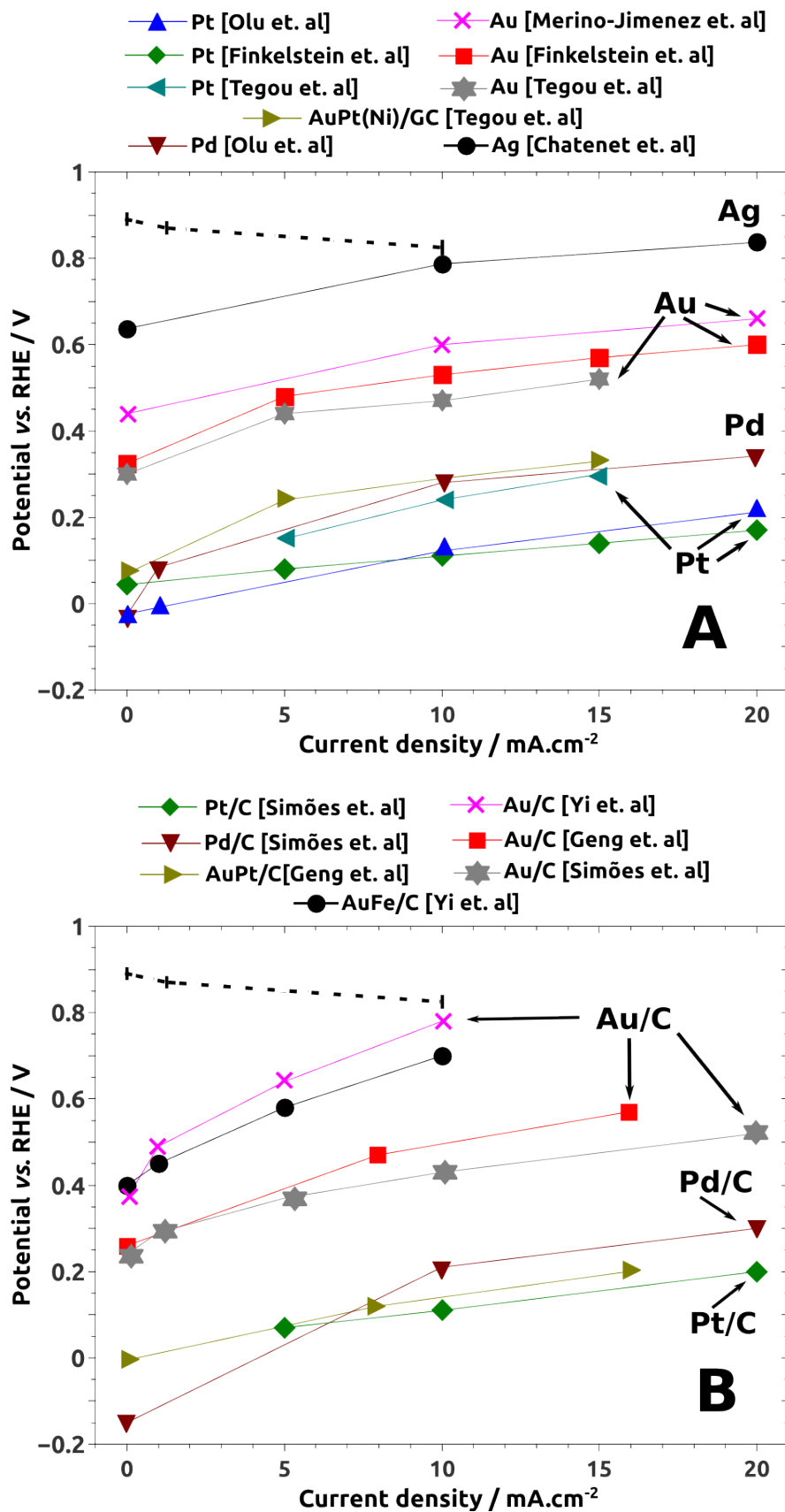


Figure 2.1: Review of RDE characterization of borohydride oxidation reaction (BOR) in alkaline media for (A): bulk electrodes and (B): carbon-supported nanoparticles. Data were taken from Olu *et al.* [93] (chapter 1), Finkelstein *et al.* [130], Merino-Jimenez *et al.* [131], Tegou *et al.* [132], Chatenet *et al.* [138], Simões *et al.* [133], Yi *et al.* [134], and Geng *et al.* [73]. Experimental conditions are specified in Table 2.2. For comparison, the dashed line was plotted from the mass-transfer-corrected Tafel plot for oxygen reduction on sputtered Pt in 1 M KOH at 70°C from Coudurier *et al.* [143].

When characterizing the activity of a novel catalyst towards the BOR, it could be useful to use the RDE configuration and to compare the result with the data presented in Fig.2.1. Note that the author has chosen to intentionally not discuss values of kinetics parameters such as kinetics constants or the number of electrons involved in the BOR. The reason is that, given the complexity of the BOR (ideally 8 electrons exchanged, unknown reaction intermediates involved, possible non-faradaic parallel reactions, etc.), a practical and common way is needed in order to be able to compare potential anode catalysts for the BOR. To that goal, it is recommended to perform the RDE characterization using the following experimental conditions:

- A NaBH_4 concentration of 10 mM in at least 1 M NaOH (10 mM in NaBH_4 is a good compromise for a stable electrolyte, without consequent hindrances from ohmic drop and hydrogen bubble generation by the hydrolysis reactions);
- A RDE revolution rate of 2000 rpm (for supported nanoparticles, the thin film may get destroyed at faster revolution rates) in order to decrease mass-transfer limitations;
- A scan rate between $5 \text{ mV}\cdot\text{s}^{-1}$ and $25 \text{ mV}\cdot\text{s}^{-1}$, a trade-off between slow and fast scan rates, in order to work in near-steady-state conditions while preventing the accumulation of the hydrogen bubbles at the electrode surface. Placing the RDE characterization of the catalyst among the review of Fig.2.1 using these conditions may give a general idea about the activity of this catalyst. For the supported catalysts, further normalization can be attempted (*e.g.* with the active surface area or the loading of the catalyst).

However, one should be aware of the limits of this method to predict the behavior of a given catalyst in practical DBFC configuration [93] (please refer to the chapter 1 of this thesis, where the predicting power of the RDE configuration for Pt and Pd is evaluated and discussed). In particular, the significant difference in BH_4^- concentration can change the behavior of a catalyst towards the BOR. Indeed, for high concentrations of BH_4^- (higher than 0.1 M), the electrocatalytic activities of Au and Ag seem to increase at low potential values [74, 135, 138, 147] (see Fig.2.2). This positive effect could make Au and Ag potential suitable anode catalysts for the DBFC when the concentration of BH_4^- in the anolyte is sufficiently high. Santos *et al.* [148] measured the OCP of several materials in contact with an electrolyte composed of 4 M NaOH and various concentrations of sodium borohydride, as shown in Fig.2.3. In this study, the OCP of Pd was measured to be slightly lower than the OCP of Pt for every borohydride concentration, which is in agreement with the observation of Simões *et al.* [133] (Fig.2.1). Santos *et al.* [148] also measured high OCP values of Au for low borohydride concentrations (between 0.1 mM and 10 mM), which is in agreement with the studies of the BOR on Au RDE (Fig.2.1). However, the OCP of Au progressively decreased for increasing borohydride concentrations, and reached values comparable to the OCP of Pt and Pd for borohydride concentrations close to 1 M [148] (see Fig.2.3). This could account for the comparable values of OCV in DBFC configuration observed using either Au, Pt or Pd as anode catalyst. Indeed, the borohydride concentration in DBFC configuration is generally close to 1 M (see Table 2.1). The understanding of the influence of the borohydride concentration on the BOR mechanism is, in the author's opinion, one of the major topics to investigate in the near future.

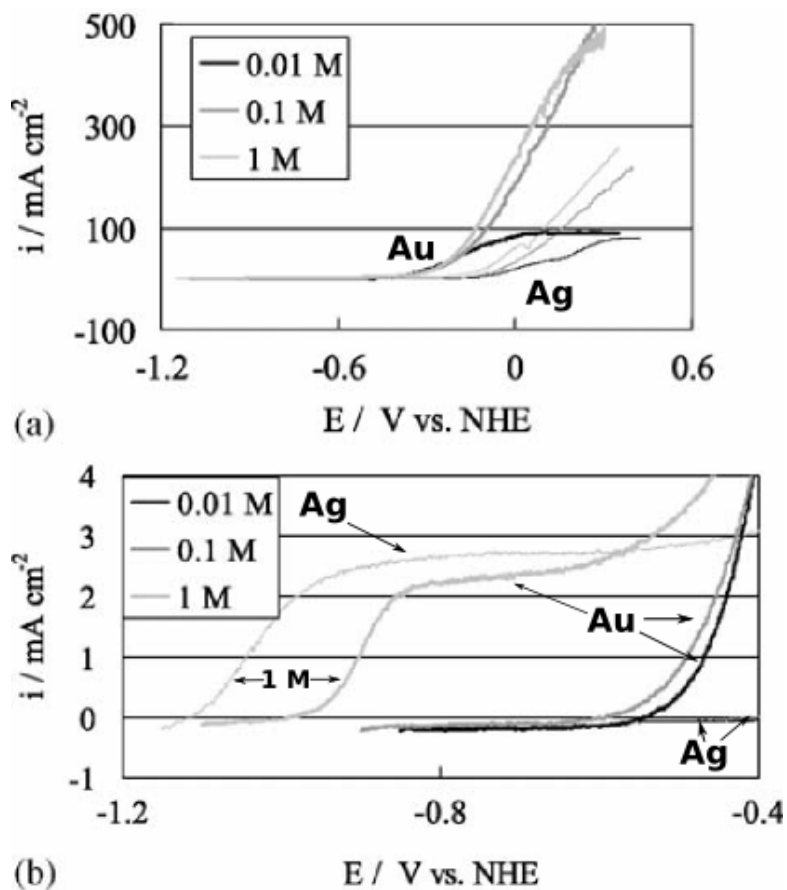


Figure 2.2: NaBH_4 oxidation RDE voltammogram plotted at $5 \text{ mV}\cdot\text{s}^{-1}$ (a) and zoom on the kinetic part (b) for bulk Au (bold) or Ag (thin) in 1 M NaOH containing various concentration of NaBH_4 , argon atmosphere; $168 \text{ rad}\cdot\text{s}^{-1}$. From Ref.[138] with permission from Elsevier.

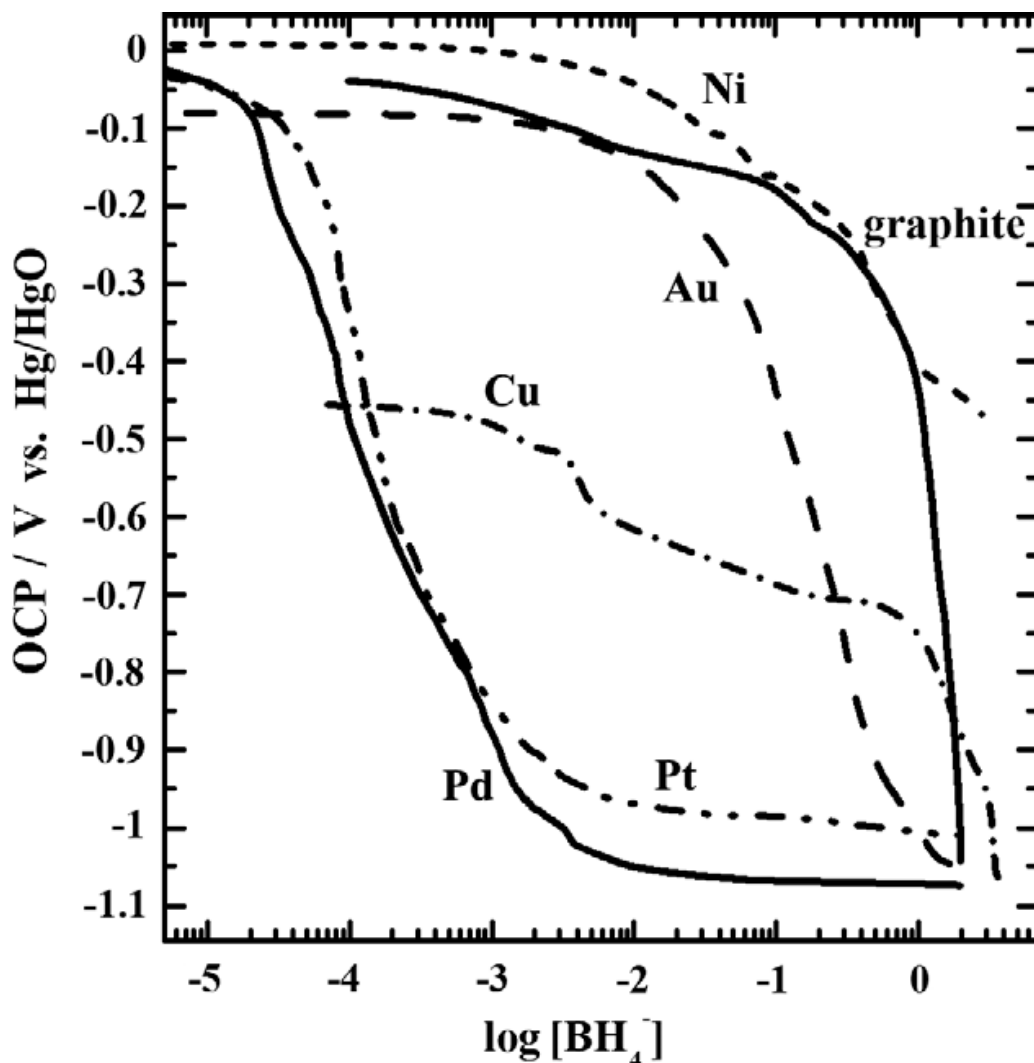


Figure 2.3: Open circuit potential (OCP) *vs.* $\log[\text{NaBH}_4]$ plots for the materials which responded to borohydride. The electrolyte was composed of 4 M NaOH and various concentrations of sodium borohydride. The reference electrode was Hg/HgO filled with 1 M NaOH. For these experimental conditions, 0.00 V *vs.* RHE = -1.00 V *vs.* Hg/HgO. Reproduced from Ref.[148] with permission from Elsevier.

The voltammogram should be selected for comparison as soon as it is stable upon potential cycling. It is worth noting that the value of the upper-potential limit may be important to get stable voltammograms. Indeed, Finkelstein *et al.* [58] showed a progressive poisoning of bulk Pt RDE surfaces during potential cycling when the upper-potential limit was too low (see Fig.2.4). A recommended practical upper-potential limit would be close to 1.5 V *vs.* RHE for noble materials like gold and platinum. However, non-noble electrodes based on hydrogen-insertion alloys, nickel or cobalt could be irreversibly destroyed at such high potential values. Besides, the time spent at OCP before performing the cyclic voltammetry on a RDE also influences the shape of the first cycles, at least for electrocatalysts that are prone to poisoning by BOR intermediates ($\text{BH}_{x,\text{ads}}$ species) and/or products (BO_x species), as it is the case for Au [149] and Pt [59, 60, 129]. This matter is further discussed in the chapter 4 of this thesis (see Fig.4.3 and Fig.4.4), where the poisoning of the Pt surface during the BOR is investigated. Masking of the electrode is even possible if H_2 bubbles form at OCP or in the course of the BOR but H_2 is not valorized, as witnessed for Au microelectrodes [150]. In clean conditions and if a high upper-potential limit is chosen, the voltammograms should be stable after *ca.* 5 cycles. If the

current continues to decay cycle after cycle, it may point towards catalyst instability in these conditions; this information may of course remain of interest for the general development of BOR catalysts.

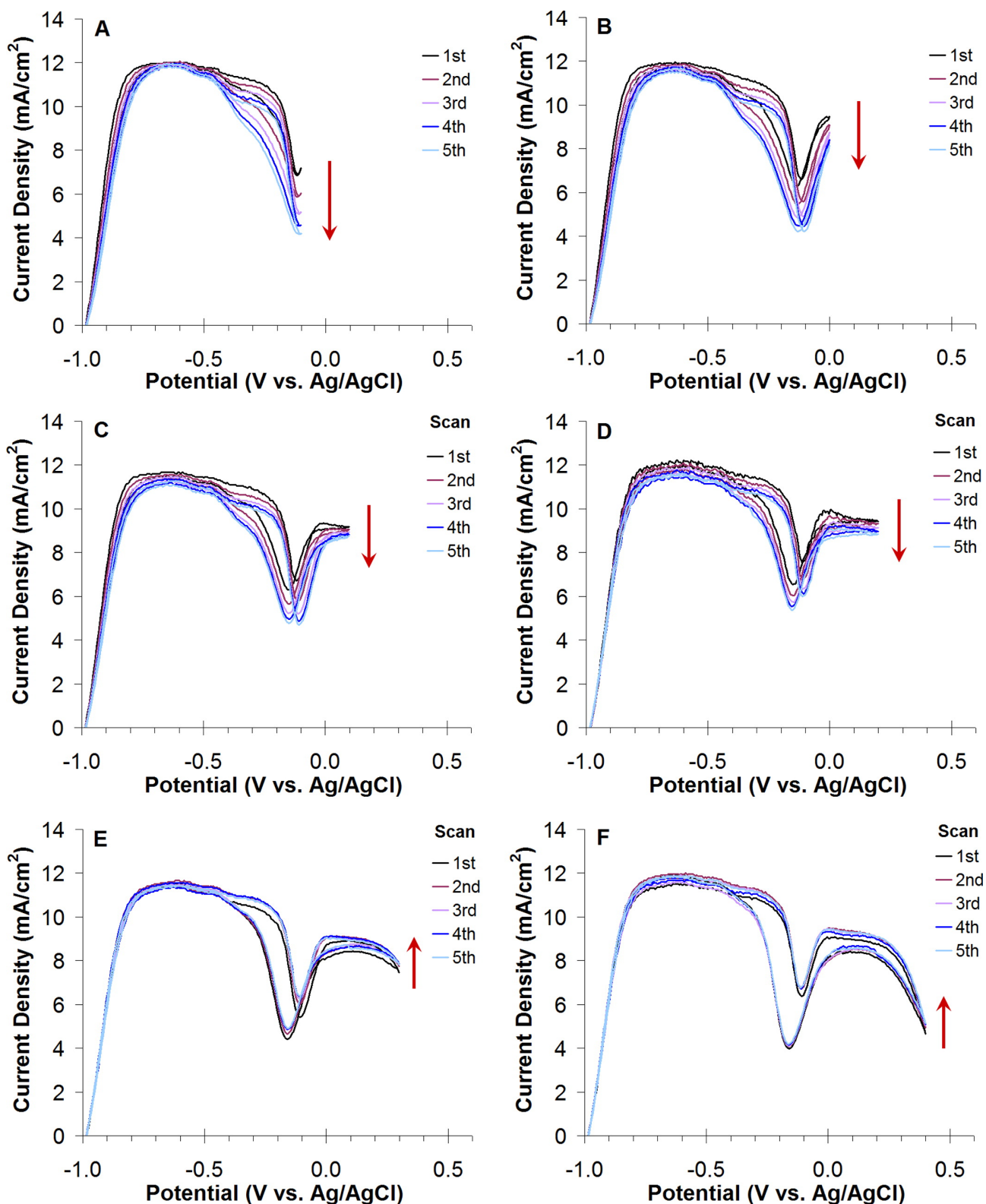


Figure 2.4: Window-opening CVs of 5 mM BH_4^- in 1 M NaOH at Pt RDE, $20 \text{ mV}\cdot\text{s}^{-1}$, 250 rpm. (a, b, c, d) Multiple CVs to +0.2 V *vs.* Ag/AgCl or less show gradual poisoning with consecutive scans. (e,f) Multiple CVs to +0.3 V *vs.* Ag/AgCl or greater show a gradual restoration of current. Reproduced from Ref. [58] with permission from the American Chemical Society.

The authors also want to point out that the practical comparison of the different results through the literature is often hindered by the representation in different scale of reference potentials (often similar to the reference used in the experiment). It is recommended to use the reversible hydrogen potential (RHE) as a common potential reference for representing voltammograms. Indeed, the RHE scale, among other advantages, accounts for differences in pH between two experiments. The difference in potential between the reference electrode used during the experiment and the RHE may be checked experimentally using a simple high-impedance multimeter, or (better) a potentiostat.

2.2.2 Chronopotentiometry (CP) and chronoamperometry (CA)

Chronopotentiometry (CP) is also a useful method to compare the electrocatalytic activity of different materials towards the BOR. Gyenge and coworkers [76, 77, 151] used similar experimental conditions in different studies to screen the activity of carbon-supported Ag [151], Au [77] and Pt [76] alloys (metal colloids prepared according to the Bönnerman method, the atomic ratio for the alloys being 1:1). By reporting the values of potential taken by the different electrodes characterized by Gyenge and coworkers 60 s after the beginning of the current step [76, 77, 151], one can range the different carbon-supported catalysts studied by this group as follows: PtIr < AgIr < AgPt < PtAu < PtNi < Pt < AuPd < AgAu < AgPd < Au, from the lowest to the highest potential (a lower potential at an identical current operation can be regarded as a better activity towards the BOR). In agreement with the CV data presented in Fig.2.1, gold displayed the lowest electrocatalytic activity (although chronoamperograms of pure Ag were not showed in [151]), but alloying gold with platinum enhanced the activity: PtAu/C even outperformed pure Pt/C in terms of activity in CP configuration. Iridium showed the best performances in CP configuration when used as a metal alloy with Pt and Ag. Every alloying composition made with Pt (PtIr, AgPt, PtAu and PtNi) enabled to enhance the performances in CP configuration compared to pure Pt/C.

Other studies used the CP method to evaluate the activity of novel catalysts. Unfortunately, it is not possible to compare these results together as they were obtained using different experimental conditions. For example, several works used the CP to demonstrate the improvement of the electrocatalytic activity towards the BOR using Au-based alloys instead of pure Au catalysts (*e.g.* AuZn/C [152], AuCo/C [153], AuCu/C [154], AuFe/C [134], Cu/Ni/AuNi [155] and Au(Co)/Ti [156]). Using CP, Yi *et al.* [154] observed the enhancement of the electrocatalytic activity of carbon-supported Pt hollow nanospheres compared to standard carbon-supported solid Pt nanoparticles. Duan *et al.* [157] synthesized core-shell Ni@Au/C and observed a significant enhancement of the performances in CP configuration compared to Au/C.

In order to evaluate the activity of a novel catalyst towards the BOR using the chronopotentiometry (CP) technique, it is recommended to follow the experimental conditions chosen by Lam *et al.* [86]. In this work, the authors observed similar activity of the Os/C catalyst compared to Pt/C or PtRu/C. They used an electrolyte made of 50 mM NaBH₄ in 2 M NaOH; this relatively high concentration in NaBH₄ enabled to avoid a control of the electrode potential by mass-transfer limitations. In addition, with a relatively high concentration in NaBH₄, it is preferred to use high NaOH concentration (at least above 2 M), so that neither the homogeneous hydrolysis of BH₄⁻ nor the (insufficient) proportion of OH⁻ anions (which is a reactant of the BOR, in amount of 8 OH⁻ per BH₄⁻) detrimentally affect the rate of the BOR. Lam *et al.* [86] performed a current step from 0 to 10 mA.cm⁻²: 10 min after the beginning of the current step, they measured electrode potential values of *ca.* 40, 30 and 20 mV *vs.* RHE for Pt/C, PtRu/C

and Os/C, respectively. The monitored potentials were stable (within a range of +/- 10 mV) over at least 3 h of constant current operation. Reproducing the experimental conditions of Lam *et al.* [86] and comparing the potential value obtained with those of this study enables a practical evaluation of the electrocatalytic activity of a novel catalyst. As for voltammetry data in RDE configuration, characterizing a catalyst using CP is likely to be influenced by (i) the 'history' of the electrode before the current step, such as the duration of the rest in OCP (especially if hydrogen bubbles are formed at OCP and stick to the electrode surface [150]) and (ii) the composition of the thin film active layer (metal loading, nanoparticle size and distribution, etc.).

Most of the studies using CP also used the chronoamperometry (CA) technique to evaluate the electrocatalyst activity of their materials: without surprise, the same trends as the CP methods were found. Among studies using only the CA method, Benhmenyar *et al.* [71] observed higher current densities using PdCu/C alloys instead of Pd/C and Li *et al.* [158, 159] also observed higher current densities using PtCo/C [158] and PtZn/C [159] alloys compared to 'pure Pt/C catalysts', for the same potential step. Santos *et al.* [160] alloyed bulk Ni electrode with Ce: this alloy led to higher current densities (for optimum Ce content) than pure Ni in similar CA configuration. However, with a few exceptions, most of the CA were performed using a potential step going to a final constant potential value of at least 0.8 V *vs.* RHE. To the author's opinion, although the studies hold a significant fundamental interest, this constant potential value is far too high to be relevant for DBFC application, as 0.8 V *vs.* RHE is not a practical value that would be taken by the DBFC anode upon operation. Indeed in this case, the cell voltage would be very close to zero, owing to the fact that alkaline oxygen reduction occurring at the cathode operate at potential close to or below 0.8 V *vs.* RHE at practical current densities (see Fig.2.1). Furthermore, at these high values of potential, the reaction is likely to be controlled by mass-transfer limitations instead of reaction kinetics. Therefore, it is recommended to perform the CA method with constant potential values of only 0.1, 0.2 and 0.3 V *vs.* RHE, and in any case not exceeding 0.3 V *vs.* RHE.

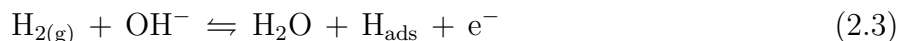
2.3 Hydrogen generation and escape during the BOR

The gaseous hydrogen generated at the anode upon the DBFC operation is one of the main issues that hinders the development of this system. Indeed, the hydrogen that escapes from the DBFC, if not valorized afterwards, reduces its anodic fuel efficiency as the ideal 8-electron BOR is not reached. Therefore, this H₂ escape hinders the competitiveness of the DBFC compared to similar systems such as the direct methanol fuel cell (DMFC) [42] or the indirect borohydride fuel cell (IBFC) [70]. The generation of gaseous hydrogen within the anode compartment also raises practical issues such as pressure instabilities, or shielding of the liquid reactants through the bipolar plate channels or inside the anode active layer [56, 106]. Therefore, research about anode catalysts for the DBFC must also consider the catalyst behavior towards hydrogen generation/oxidation during the BOR.

In the following discussion, distinction will be made between the hydrogen escape that can be monitored at the outlet of the DBFC anode, the hydrogen generated inside the DBFC anode and the hydrogen consumed inside the DBFC anode. The mass balance relation among these elements is:

$$\text{H}_2 \text{ escape} = \text{H}_2 \text{ generated} - \text{H}_2 \text{ consumed} \quad (2.1)$$

Hydrogen inside the anode can possibly be generated by: (i) the homogeneous and heterogeneous hydrolysis reactions of BH_4^- [9, 10] or of possible intermediates produced during the BOR and (ii) the recombination (Tafel step, Eq.2.2) or electro-reduction (Heyrovsky step, Eq.2.3) of adsorbed hydrogen atoms H_{ads} coming from either BH_4^- or water (Volmer step, Eq.2.4) dissociative adsorption on the catalyst surface.



Hydrogen consumption inside the anode is related to the hydrogen oxidation reaction (HOR), which can occur either by H_2 non-electrochemical (Tafel step) or electrochemical (Heyrovsky step) dissociative adsorption on the catalyst surface, followed by the electro-oxidation of H_{ads} (Volmer step). For a catalyst that is inactive towards the HOR (*e.g.* gold and silver), the H_2 escape is equal to the H_2 generation, and any hydrogen molecule generated is irreversibly lost, resulting in a faradaic efficiency lower than 100%. Another way to consume hydrogen is to use catalysts which can absorb the H_2 generated, such as Pd or other hydrogen storage materials, but this solution only exhibits a transient interest. Indeed, once all the hydrogen insertion sites are occupied, H_2 escape must proceed quantitatively.

Note that the elements introduced above may be neither distinct nor independent. For example, the heterogeneous hydrolysis is commonly seen as a purely chemical reaction and described as the reaction taking place and producing gaseous hydrogen when a catalyst is added into an electrolyte containing BH_4^- without any control of the potential. However, this production of hydrogen can also very well be described by considering the open circuit potential (OCP) of the catalyst to be a mixed potential driven by the BOR (oxidation reaction) and the hydrogen evolution reaction (HER, reduction reaction) from water. Very little is for now understood about the mechanisms of hydrogen generation inside the anode upon DBFC operation. Except for the homogeneous hydrolysis reaction, the possible steps ruling the hydrogen generation and consumption are likely sensitive to the type of catalyst. Therefore, one could possibly reduce the hydrogen escape with the development of adequate DBFC anode materials.

Fig.2.5 presents a review of studies that monitored the H_2 escape at the anode outlet in DBFC configuration. For practical comparison of the results, the so-called '2 e⁻', '4 e⁻' and '6 e⁻' reaction behavior lines were plotted in Fig.2.5A. These lines describe the deviation caused by the H_2 escape from an ideal 8-electron oxidation reaction for each BH_4^- , considering a 2-electron oxidation reaction for each escaped H_2 molecule. One should be aware that, although these reference lines are practical, the observation of zero H_2 escape would not necessarily

mean an 8-electron BOR, as other intermediates can escape during the BOR (*e.g.* BH_3OH^-). Geng *et al.* [72] observed a '4 e^- ' reaction behavior using Ni/C as anode catalyst in DBFC configuration. By addition of small amounts of Pt in the Ni nanoparticles, they achieved an increase in the performances of the DBFC without deviation from the '4 e^- ' behavior. The same team also observed a '6 e^- ' reaction behavior using Au/C catalyst [73]. The modification of the Au nanoparticles by Pt enabled to increase the performances of the DBFC and even slightly reduced the H_2 escape for higher values of power density. Jamard *et al.* [62] compared a Pt/C-based anode with a PtNi/C-based anode and observed a significant reduction of the H_2 escape from an almost '2 e^- ' behavior for Pt/C to almost no H_2 escape for PtNi/C. It is worth noting that, for a pertinent comparison of the results of the literature, the H_2 escape rate should be normalized to the geometric anode area, especially when the current and the power of the DBFC are also normalized [67, 131]. The H_2 escape rate should also be reported in standard conditions in order to account for difference in temperature and pressure.

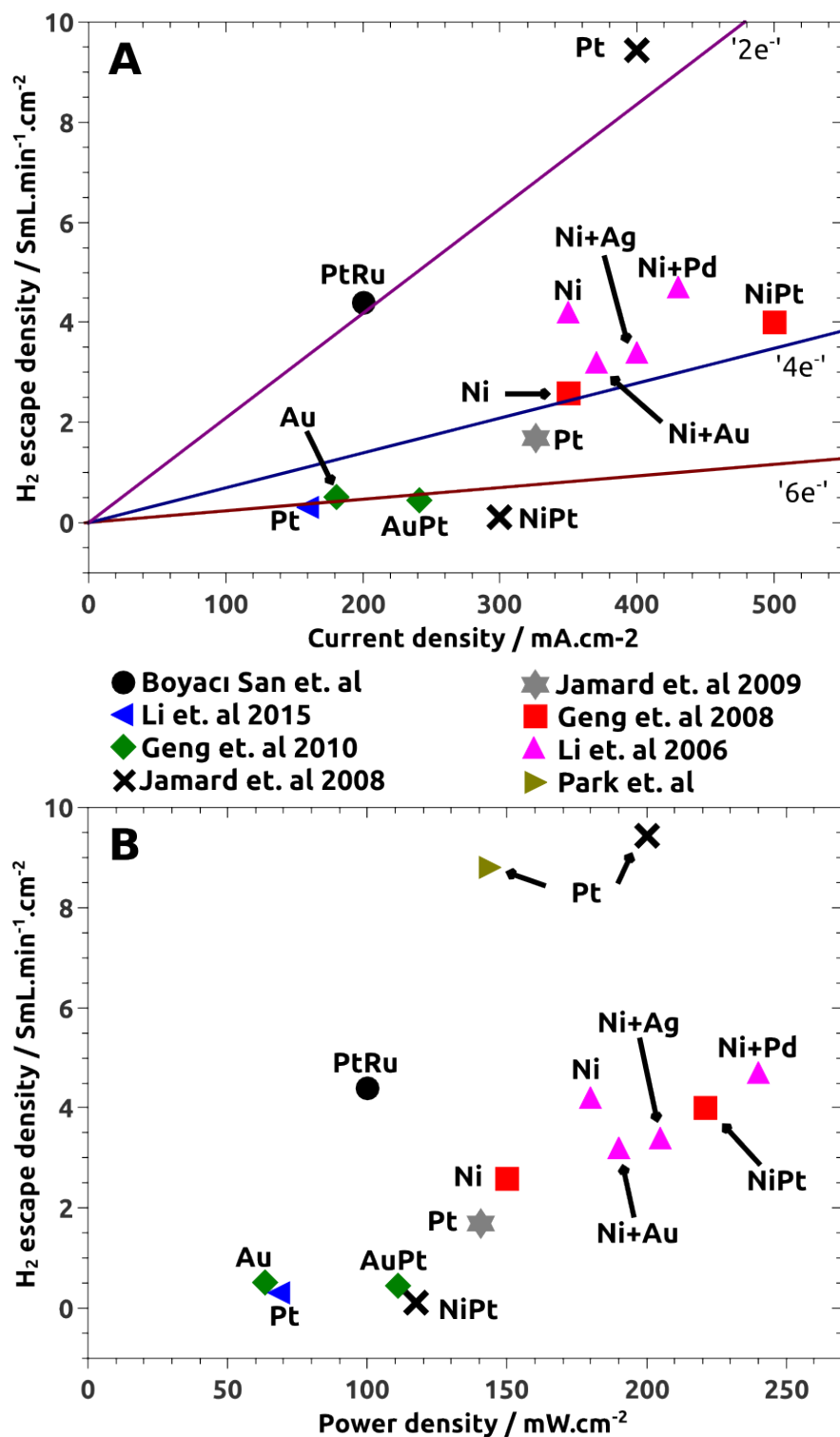


Figure 2.5: Review of hydrogen evolution upon operation in DBFC configuration against (A) the current density and (B) the power density of the DBFC. Data were taken from Boyacı San *et al.* [114], Li *et al.* 2015 [63], Geng *et al.* 2008 [72], Jamard *et al.* 2008 [62], Jamard *et al.* 2009 [46], Geng *et al.* 2010 [73], Li *et al.* 2006 [87] and Park *et al.* [55]. The experimental conditions of the different DBFC configurations can be found in Table 2.1. Please refer to the works cited above for more detailed data on hydrogen escape at other current densities values or using other experimental conditions

The H_2 escape was also monitored in several studies using half-cell configuration. For relevant values of current and BH_4^- concentrations, Liu *et al.* [161] observed the following order for

different types of electrode catalysts: Ni > Pd/C > Pt/C from the fastest to the slowest H₂ escape rate (see Fig.2.6). Using a half-cell configuration, Wang *et al.* [142] observed the following order: (i) Pt/C > Ni > LaNi_{4.7}Al_{0.3} > Au/C at low current density and (ii) Ni > Pt/C > Au/C > LaNi_{4.7}Al_{0.3} at higher current density, from the fastest to the slowest H₂ escape rate (see Fig.2.7). Copper was also investigated in the same work [142], but its electrocatalytic activity towards the BOR was too low to be further considered. The common observations between these two different studies in half-cell configuration are: (i) for high values of current, the H₂ escape for Ni follow the '4 e⁻' behavior whatever the BH₄⁻ concentration [162], whereas (ii) the H₂ escape for Pt/C depends on the BH₄⁻ concentration. Furthermore, significant discrepancies can be observed between the two studies for the H₂ escape rate using Pt/C and similar BH₄⁻ concentration (but different NaOH concentrations). Indeed, Liu *et al.* [161] observed near zero H₂ escape using Pt/C at relevant values of current and 0.52 M NaBH₄, while Wang *et al.* [142] observed a H₂ escape corresponding to a mechanism intermediate between the '4 e⁻' and '6 e⁻' reaction behaviors at 0.5 M NaBH₄. On the contrary, comparable H₂ escape rate can be observed between the two studies using Ni, whatever the BH₄⁻ concentration.

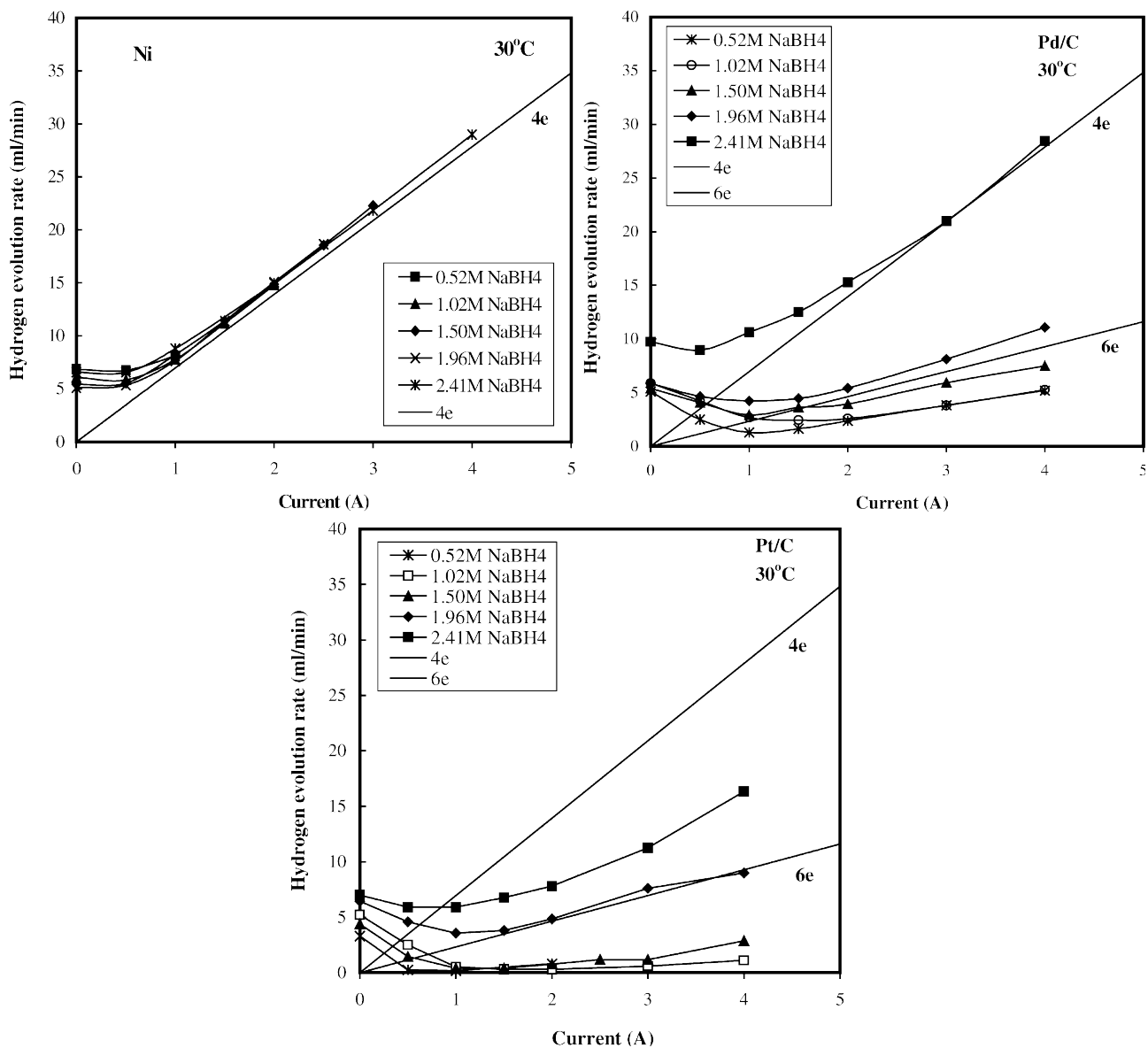


Figure 2.6: Hydrogen evolution rate in half-cell configuration. Working electrodes: Ni, Pd/C and Pt/C in 6 M NaOH with various concentrations of sodium borohydride. Electrode geometric surface area: 5 cm². Operation temperature of 30°C. Reproduced from Ref.[161] with permission from Elsevier.

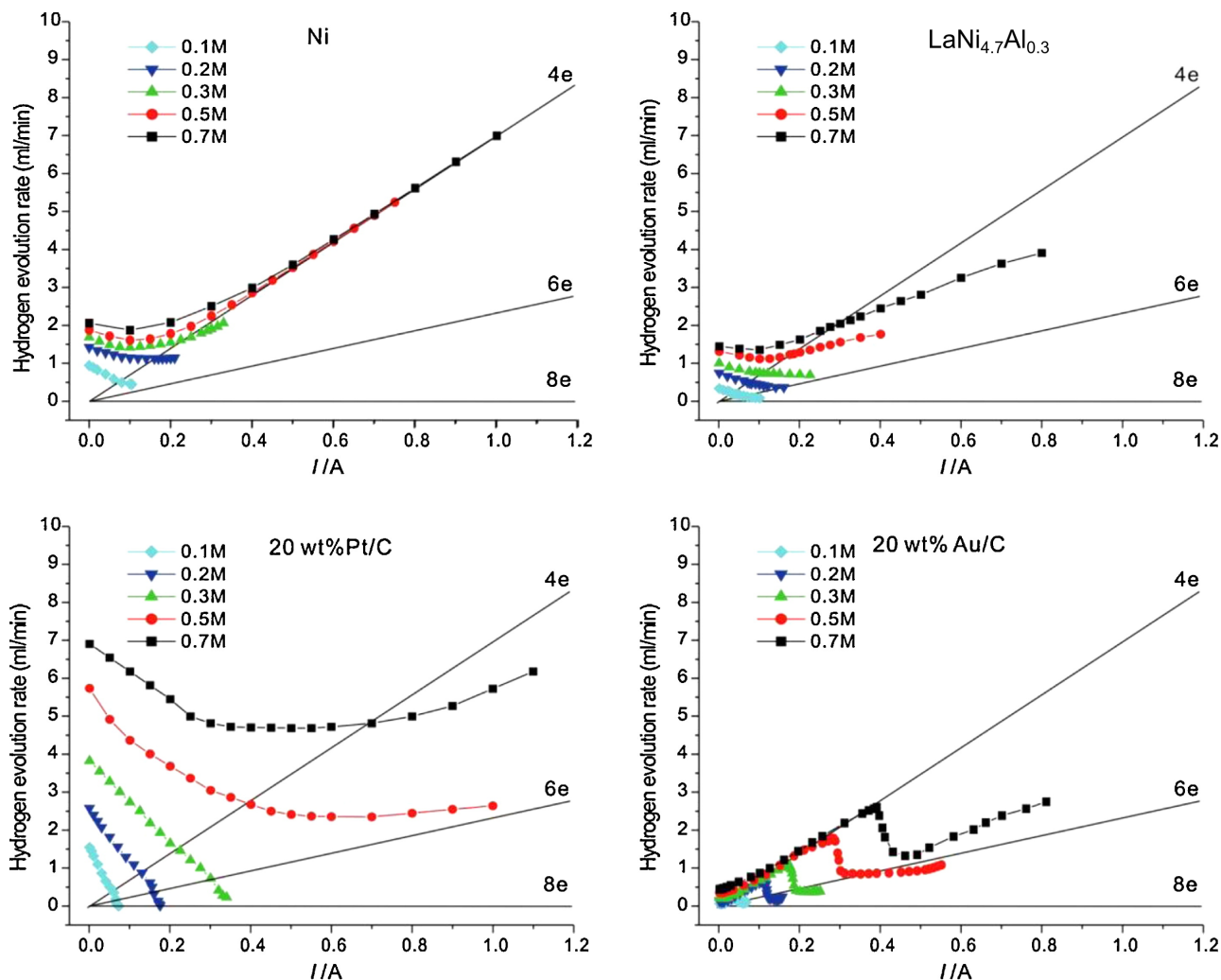


Figure 2.7: Hydrogen evolution rate in half-cell configuration. Working electrodes: Ni, LaNi_{4.7}Al_{0.3}, Pt/C and Au/C in 2 M NaOH with various concentrations of sodium borohydride. Electrode geometric surface area: 4 cm². Cells operating at room temperature. Reproduced from Ref.[142] with permission from Elsevier.

The significant discrepancy in the behavior of H₂ escape using a Pt-based anode material is also observed in DBFC configuration, ranging from a '2 e⁻' to a '6 e⁻' reaction behavior, as presented in Fig.2.5. This phenomenon can be explained by the relation presented above (Eq.2.1). Ni is almost totally inactive towards the HOR, so that the H₂ amount that escapes is equal to that generated by undesired reaction(s) occurring along with the BOR. The H₂ escape for Ni is therefore directly proportional to the current coming from the BOR, leading to a stable '4 e⁻' reaction behavior. On the contrary, Pt is highly active towards the HOR, so that the 'H₂ consumed' term of the Eq.2.1 tends to reduce the H₂ escape rate at high values of current (*i.e.* at high anodic HOR overpotentials). This reasoning can be extended to other types of catalysts. Indeed, Liu and coworkers [161, 163] observed that the H₂ escape rate depends on the BH₄⁻ concentration using Pd/C, an HOR-active catalyst, while Wang *et al.* [142] did not observe that phenomenon in the case of using Au/C, a HOR-inactive catalyst. In addition, a high BH₄⁻ concentration in the anolyte is likely to be detrimental to the H₂ consumption rate at a given current value. Indeed, a high interfacial BH₄⁻ concentration is likely to favor BH₄⁻ adsorption at the catalytic surface, to the detriment of the competitive adsorption of H₂. Gaseous hydrogen generated during side reactions of the BOR is expected to depend only on the current given by the BOR upon DBFC operation, while H₂ consumed by an HOR-active

anode catalyst is likely to be dependent on the anolyte composition and also on the design of the whole anodic compartment (including the composition of the anode). Indeed, the residence-time of generated H_2 (and thus the H_2 consumption rate) is sensitive to many variables related to the design [106, 114] and composition of the DBFC anode compartment. This may explain the discrepancies observed for the H_2 escape rate using a Pt-based anode in DBFC [46, 55, 62, 63] or half-cell [142, 161] configurations.

The residence-time of H_2 generated inside the anodic compartment can be managed through the optimization of the anode design. Lam *et al.* [110] used different supports for the HOR-active PtRu DBFC anode catalyst. They observed a faster H_2 escape rate from the PtRu black thin active layer compared to the more porous PtRu/Vulcan XC-72 active layer that could retain gaseous hydrogen. An anode made of a monolithic three-dimensional graphite felt with electrodeposited PtRu was also used and improvement of the DBFC performances was observed. This enhancement of the DBFC performances using a 3-D anode was attributed to the better management of the gaseous H_2 phase [110]. Li *et al.* [63] also used different types of carbon to support Pt nanoparticles. Increasing the pore size and volume of the anode carbon support led to a better trapping of the generated H_2 , and thus reduced the H_2 escape rate at the DBFC anode outlet. However, it is worth noting that a larger volume of trapped gaseous hydrogen can simultaneously reduce the H_2 escape rate (*i.e.* increase the fuel efficiency, a positive effect) but also increase the shielding effect of catalytic sites by the gaseous phase, leading to mass-transfer limitations and thus to lower DBFC performances [63]. An optimum configuration was found using a macroporous carbon support (MPC, see Fig.2.8) [63]. In the same way, Cheng *et al.* [75] also used a nickel mesh as a backing layer to trap and enhance the management of H_2 generated within the anode compartment. Olu *et al.* [93] compared two different morphologies of Pt/C-based anode with similar composition. In that work [93] already presented in the chapter 1 of this thesis, the active layer sprayed on the Nafion[®] membrane was relatively flat and smooth, while the active layer pasted on carbon cloth matrix was cracked (see Fig.1.6). The 'cracked' active layer displayed better DBFC performances than the 'smooth' active layer (see Fig.1.5), and this was attributed to a better management of the H_2 generated using a macroporous active layer. In the case of the 'smooth' active layer, the H_2 generated did tend to shield the Nafion[®] membrane and the active layer from the anolyte, which led to a reduction in the wetting properties of the system, thereby hindering the DBFC performances.

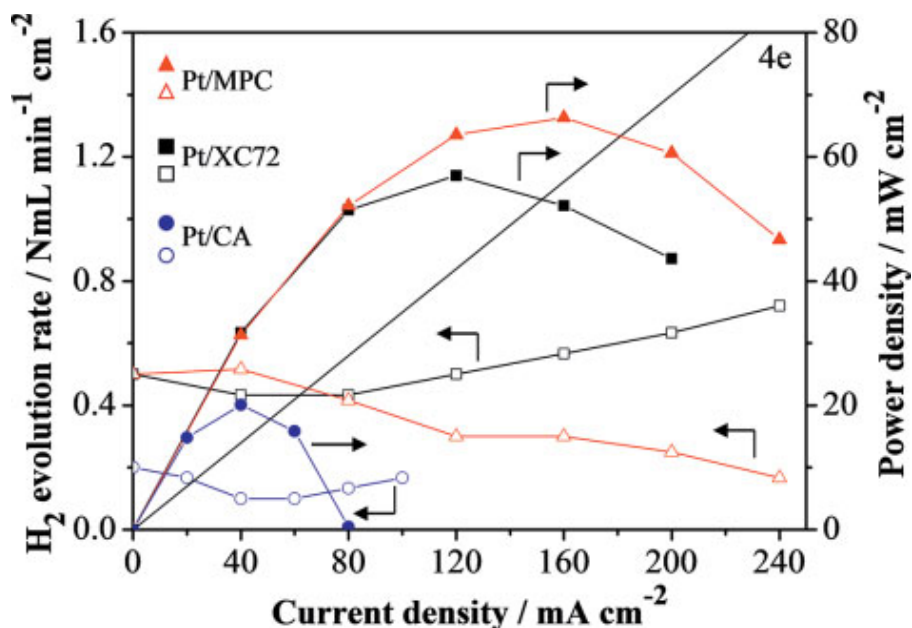


Figure 2.8: Hydrogen evolution rates and cell performances in DBFC configuration. The anode catalysts of the DBFC were composed of Pt nanoparticles supported on: carbon Vulcan (Pt/XC72), macroporous carbon (Pt/MPC) and carbon aerogel (Pt/CA). The experimental conditions are detailed in Table 2.1. Reproduced from Ref. [63] with permission from Wiley-VCH.

The type of binder material and the electrode binder loading also likely influence the residence time of the generated H₂ within the anode. Park *et al.* [55] observed a decrease in the NaBH₄ escape rate from the Pt/C-based anode with either higher contents of PTFE binder or thicker anodes; this was attributed to the increase in the H₂-retaining capacity of the electrode. Indeed, PTFE provided hydrophobic properties to the active layer, leading to a stronger binding of the gaseous hydrogen with the anode structure. On the contrary, Nafion[®] binder enhanced the wetting properties of the active layer and so the H₂ bubbles were more easily removed from the anode structure. Li *et al.* [164] observed near zero H₂ escape using PTFE binder in a composite Ni + Pd/C anode, while a '4 e⁻' reaction behavior was observed when Nafion[®] binder was used. However, in another study, the same group found lower H₂ escape using Nafion[®] binder compared to PTFE [87]. A tentative explanation regarding the observed difference can be proposed by considering the fact that a cation-exchange membrane (CEM) was used in [87] while an anion-exchange membrane (AEM) was used in [164]. As the charge carrier is mainly Na⁺ in the case of the CEM, the BOR tends to reduce the local pH of the anolyte upon DBFC operation (one BH₄⁻ can ideally react with eight OH⁻) and thus the hydrolysis can be enhanced. Besides, the Nafion[®] binder, which is made of filaments that are soluble during the ink preparation, may encapsulate the catalyst particles and reduce the interfacial BH₄⁻ concentration, lowering the hydrolysis rate [87]. This phenomenon is less likely to occur in the case of PTFE beads, which are insoluble in the ink formulation/casting process. In that frame, the use of anion-exchange membranes seems suitable to improve the issue of H₂ escape upon DBFC operation.

In order to lower the number of experimental variables, differential electrochemical mass spectrometry (DEMS) can be a useful method to investigate the H₂ escape behavior of a given catalyst. Pasqualetti *et al.* [141] monitored the on-line generation of H₂ on Au/C, Ag/C, Pt/C and Pd/C at low BH₄⁻ concentration (1 mM). For the HOR-active catalysts (Pt/C and Pd/C), gaseous H₂ was observed around OCP and at higher potential values (typically above 0.5 V *vs.*

RHE) for which the catalysts surfaces are oxidized. These oxidized surfaces are inactive towards the HOR. For the HOR-inactive catalysts (Au/C and Ag/C), gaseous H₂ was observed during the first oxidation current wave of the BOR (see Fig.2.9). In all cases, the shape of the plot of gaseous H₂ detected *vs.* the electrode potential was comparable that of BH₃OH⁻ intermediate released during the BOR detected using a Au-ring rotating disk electrodes setup. The next step for studies using the DEMS technique would be to increase the BH₄⁻ concentration in order to reach conditions comparable to the real DBFC operation. However, this raises practical issues such as the management of the ohmic drop with higher currents, or a harsh gas generation which can hinder the good functioning of the DEMS device.

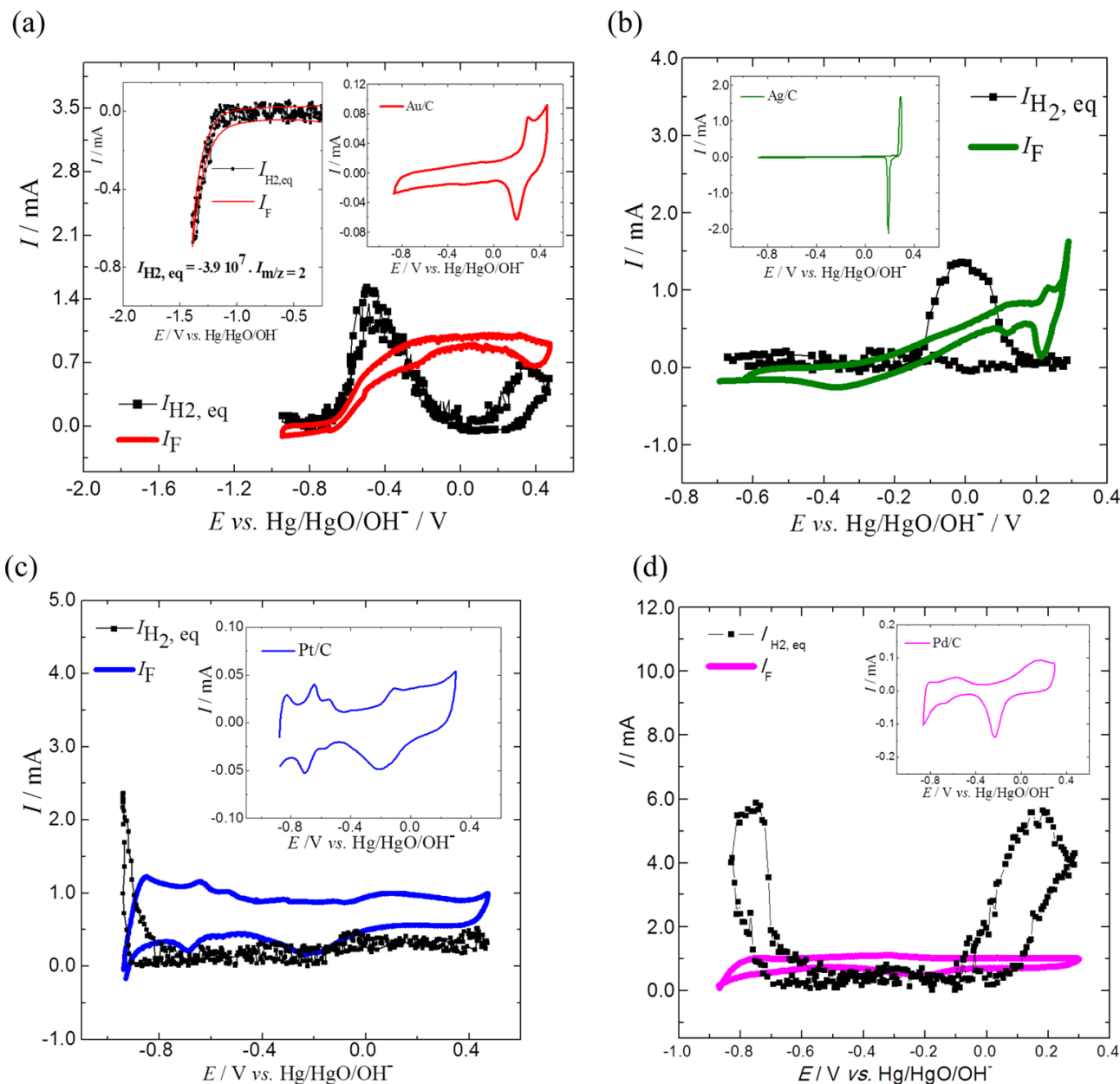


Figure 2.9: Faradaic current for the BOR and ionic current for $m/z = 2$ (H_2) detection converted into an equivalent HER current ($I_{H_2, eq}$) obtained during DEMS experiments of cyclic voltammetry for the different investigated electrocatalysts in 1.0 mM $BH_4^- + 1.0$ M NaOH electrolyte at 25°C, in Ar-saturated solution; CV was obtained at a scan rate of 5.0 mV.s⁻¹ and the electrolyte flow rate was *ca.* 15 μ L.s⁻¹. (a) Au/C (inset, left: example of the HER faradaic current and of the ionic signal for molecular hydrogen detection obtained during the calibration procedure for the Au/C electrode), (b) Ag/C, (c) Pt/C, and (d) Pd/C. The insets show the CV obtained for the investigated metal nanoparticles in Ar-saturated 1.0 M NaOH electrolyte at 5.0 mV.s⁻¹. Reproduced from Ref.[141] with permission from the American Chemical Society.

These results provide first insights into the mechanism ruling the H_2 generation during the BOR [141]. Further understanding of the mechanisms behind the BOR and the H_2 evolution in BOR conditions are needed, in parallel with practical developments of the DBFC system, in order to intelligently propose suitable anode catalysts for the DBFC. The BOR mechanism on Pt is investigated in the second part of this thesis. A tentative proposition of the mechanisms ruling the H_2 generation during the BOR on Pt is made in the chapter 6. In the author's opinion, the future

goal for the fundamental study of the BOR would be to connect the previous mechanistic findings with the experimental observations of real DBFC systems presented in this review chapter. To do so, the challenge would be to investigate the BOR mechanism with higher concentrations in sodium borohydride (a more detailed discussion about this reasoning is made in the chapter 6).

Another possibility that has been investigated for reducing the H₂ generation is the addition of thiourea (TU) in the anolyte. The hypothesis was that the TU adsorption on the catalytic surface would be site-selective, so that only the catalytic sites responsible for the hydrolysis reactions would be blocked by TU, while the catalytic sites responsible for the BOR would be left free and active. However, while the H₂ escape was indeed reduced using TU, so was the electrocatalytic activity, leading to a deterioration of the DBFC performances [62, 165, 166, 167, 168, 169]. Now, whatever this practical bias, the use of TU is still interesting from a fundamental point of view in order to further understand the mechanisms behind the H₂ escape [170]. The addition of bismuth atoms in the electrocatalyst nanoparticles could also be another way for reducing the hydrogen generation during the BOR, as the presence of bismuth is known to limit the hydrogen desorption/adsorption reactions on the catalyst surface. Simões *et al.* [171] synthesized bimetallic Pd_xBi_{1-x}/C and Pt_xBi_{1-x}/C catalysts and characterized these catalysts for the BOR using RDE setup. Although Pt_{0.9}Bi_{0.1}/C showed slightly lower activity towards the BOR compared with pure Pt/C, no gaseous hydrogen evolution was visually observed from the electrode composed of Pt_{0.9}Bi_{0.1}/C catalyst during the BOR [171]. This promising catalyst has yet to be tested upon DBFC operation conditions (especially using higher concentrations of sodium borohydride).

2.4 Stability of the anode catalyst upon DBFC operation

Among the studies in the DBFC configuration presented in section 2.1, long-term constant current operation was sometimes performed [46, 71, 74, 75, 88, 90, 94, 95, 96, 97, 98, 99, 102, 103, 104, 106, 112, 113, 119, 164]. Among others, Chen *et al.* [119] recorded a relatively stable cell potential during 350 h of constant current density operation at 200 mA.cm⁻². Duteanu *et al.* [113] recorded a stable cell potential during 360 h of constant current density operation at 100 mA.cm⁻². Jamard *et al.* [46] observed a lifespan of 475 h for a DBFC upon constant current density operation at 56 mA.cm⁻². At last, Li *et al.* [164] operated a DBFC at constant current density of 20 mA.cm⁻² for at least 1,900 h. Failure of the DBFC upon long-term operation is often attributed to the formation of solid compounds in the anode or the cathode compartment (borate-based, sodium hydroxide, sodium carbonates) [46, 75, 106], or to the stability of the membrane (especially in the case of anion-exchange membranes) [120, 164]. Few studies investigated the stability of the anode material upon DBFC operation. Li *et al.* [164] observed a degradation of the anode material when operation at higher constant current density was attempted, which was attributed to the faster H₂ generation that destroyed the integrity of the anode. Cheng *et al.* [75] pointed out that the anode catalyst dissolution and agglomeration could be part of the DBFC performance degradation. Cheng *et al.* [74] visually observed the dissolution/detachment of the Pd anode catalyst upon DBFC operation; the anode outlet tubing became black. The poor performances obtained for this DBFC configuration were partly attributed to the degradation of the anode catalyst. In the chapter 1 of this thesis, we performed TEM imaging of Pt/C and Pd/C anode catalysts prior and post DBFC and DABFC (direct ammonia borane fuel cell) operation. Even if the characterizations performed on these materials were short in duration (no long-term operation; successive voltammetry cycles instead), a fast and spectacular degradation of the carbon-supported nanoparticles was nevertheless observed (see Fig.1.7).

These results point towards a new development goal for the catalysts of the DBFC: the stability upon operation. This aspect should, in the author's opinion, be further investigated in order to enable the (short-term) commercial deployment of DBFC systems. It is worth noting that, like for the electrocatalytic activity or the H₂ escape, it is difficult to focus the study on the anode catalyst only, considering the numerous other external variables. Indeed, as already stated in chapter 1, the presence of Pt was observed within the Pd/C-based anode using X-EDS post to the DBFC operation, indicating a dissolution/redeposition of the cathode Pt at the anode [93]. There is undoubtedly some room for investigation of the degradation behavior of the anode catalyst in DBFC anolyte environment, *e.g.* using electrochemical cell or identical-location TEM techniques [64].

2.5 Summary

Various experimental variables influence the behavior of a given DBFC configuration. Because of this complexity, it is almost impossible to determine from the literature which materials are the most suitable as anode catalyst for DBFC applications. Therefore, this chapter establishes a list of recommendations for studies characterizing DBFC configurations in the aim of investigating the anode catalyst:

- Provide, with as many details as possible, the experimental conditions for the design and the characterization techniques of the DBFC.
- Reduce the influence of the cathode polarization potential on the DBFC voltage by using high cathode catalyst loadings and fast oxygen (oxidant) flow rates. In order to investigate the suitability of a given anode catalyst material for DBFC applications, comparison between potential catalysts should be performed in configurations where the anode is the main limitation of the DBFC performances. Therefore, the anode catalyst loading should also be relatively low for this kind of study.
- Perform a reference characterization of a DBFC using a Pt/C-based anode ($0.5 \text{ mg}_{\text{Pt}} \cdot \text{cm}^{-2}$) in order to compare (i) the novel anode catalyst with the active Pt noble metal in similar conditions and (ii) the influence of the whole experimental conditions with the literature for a similar anode catalyst.

These recommendations could be extended to studies investigating the cathode catalyst for the DBFC (inverting 'anode' and 'cathode' in the list above); however this is out of the scope of this thesis.

The use of the standard three-electrode electrochemical cell further enables to isolate the catalyst and to investigate its electrocatalytic activity towards the BOR at the exclusion (or correction) of other phenomena (ohmic drop, membrane resistance, fuel/oxidant cross-over, etc.). Benchmarks and propositions for common experimental procedures are presented in this chapter for the rotating disk electrode (RDE) and chronoamperometry (CP) methods. Hopefully, this would facilitate the practical evaluation of the electrocatalytic activity of a given catalyst towards the borohydride oxidation reaction (BOR). However, one should be aware that, by reducing the number of experimental variables, studies in three-electrode electrochemical cell (or any cell for 'model' experiments, *e.g.* for FTIR, DEMS, Raman, EQCM, etc.) also deviate from real DBFC operation conditions.

Finally, the hydrogen escape is a major issue for the development of the DBFC. In this chapter, distinction was made between the following terms:

- The 'hydrogen escape' that is monitored at the outlet of the DBFC anode (or of the half-cell working electrode);
- The 'hydrogen generation' that is produced within the electrode during (yet undetermined) reactions;
- The 'hydrogen consumption' of the hydrogen generated, achieved using active catalyst for the hydrogen oxidation reaction (HOR) or materials that can absorb and valorize the hydrogen generated.

Unfortunately, every catalyst that is active for the BOR also seems to generate hydrogen during the BOR. One way to achieve near zero hydrogen escape upon DBFC operation so far is to use an HOR-active catalyst (*e.g.* Pt) and to optimize the experimental conditions, such as the anolyte composition or the structure of the anode, in order to manage the residence time and the consumption rate of the hydrogen generated inside the anode. However, this strategy is likely highly sensitive to various experimental variables. The ideal solution would be to find a catalyst that is active for the BOR without any hydrogen generation. Further understanding of the BOR mechanism, especially for borohydride concentrations similar to the DBFC operation conditions, is needed in order to develop novel anode catalysts for the DBFC.

At last, in view of long-term commercial applications for the DBFC, the suitable anode catalyst should be stable upon DBFC operation conditions. This condition is often neglected but should be taken into consideration for the choice of a viable DBFC anode catalyst.

Part II

Study of the borohydride oxidation reaction (BOR) mechanism on Pt

In the first part of this thesis, the DBFC anode was investigated within the global DBFC system, in fuel cell configuration close to the 'real' operating conditions of the DBFC. However, in order to finely study the BOR mechanism on a given catalytic surface, one must reduce the number of the experimental variables and ensure a satisfactory control of these variables. Therefore, in the following second part of this thesis, the BOR mechanism is investigated using various Pt-based model working electrodes in a three-electrode cell setup.

Chapter 3

Bulk platinum

3.1 Polycrystalline Pt

A large amount of work has been done in order to resolve the mechanism of the BH_4^- oxidation reaction (BOR) on Pt in NaOH media, but no general consensus on the actual BOR mechanism has been achieved yet. The literature is for example rich in attempts to evaluate the number of electrons involved in the oxidation of BH_4^- [87, 130, 133, 161, 165, 168, 172, 173, 174, 175]; it generally varies from 2 to 8 electrons for Pt, pointing out the huge influence of the experimental conditions, such as the type of surface of the Pt-based electrode (porous volumic or flat surfaces, bulk or nanoparticles Pt, etc.) or the technique used in the study (voltammetry on static-, rotating disk-, or micro-electrodes). This great discrepancy in the determination of the BOR kinetics is not very surprising. Indeed, the BOR mechanism is complex and involves intermediate species, which can be adsorbed on the Pt surface or released from the Pt surface. Regarding the complexity of the BOR, it is clear that the oxidation mechanism is very sensitive to experimental conditions such as the purity of the reagents, NaOH and NaBH_4 concentrations, the time management of the experiment or the structure of the electrode [129, 176]. This complexity opens the way to strong effects of the Pt surface morphology, and therefore of the Pt surface preparation procedure prior BOR electrochemistry. In that frame, this section presents two different behaviors towards the BOR depending on the preparation of the polycrystalline Pt electrode.

Fig.3.1 displays a typical cyclic voltammogram of polycrystalline Pt electrode in NaOH electrolyte. Several peaks can be observed on this voltammogram. Briefly, it is commonly considered that the peaks between 0.1 V and 0.5 V *vs.* RHE ('I' on Fig.3.1) correspond to the adsorption/desorption of hydrogen atoms H_{ads} . The beginning of the gaseous hydrogen evolution/oxidation is observed below 0.1 V *vs.* RHE. The peaks between 0.5 V and 1.5 V ('II' on Fig.3.1) correspond to the formation/reduction of Pt oxides; *i.e.* the adsorption/desorption of oxygen-containing species such as OH_{ads} or O_{ads} [177].

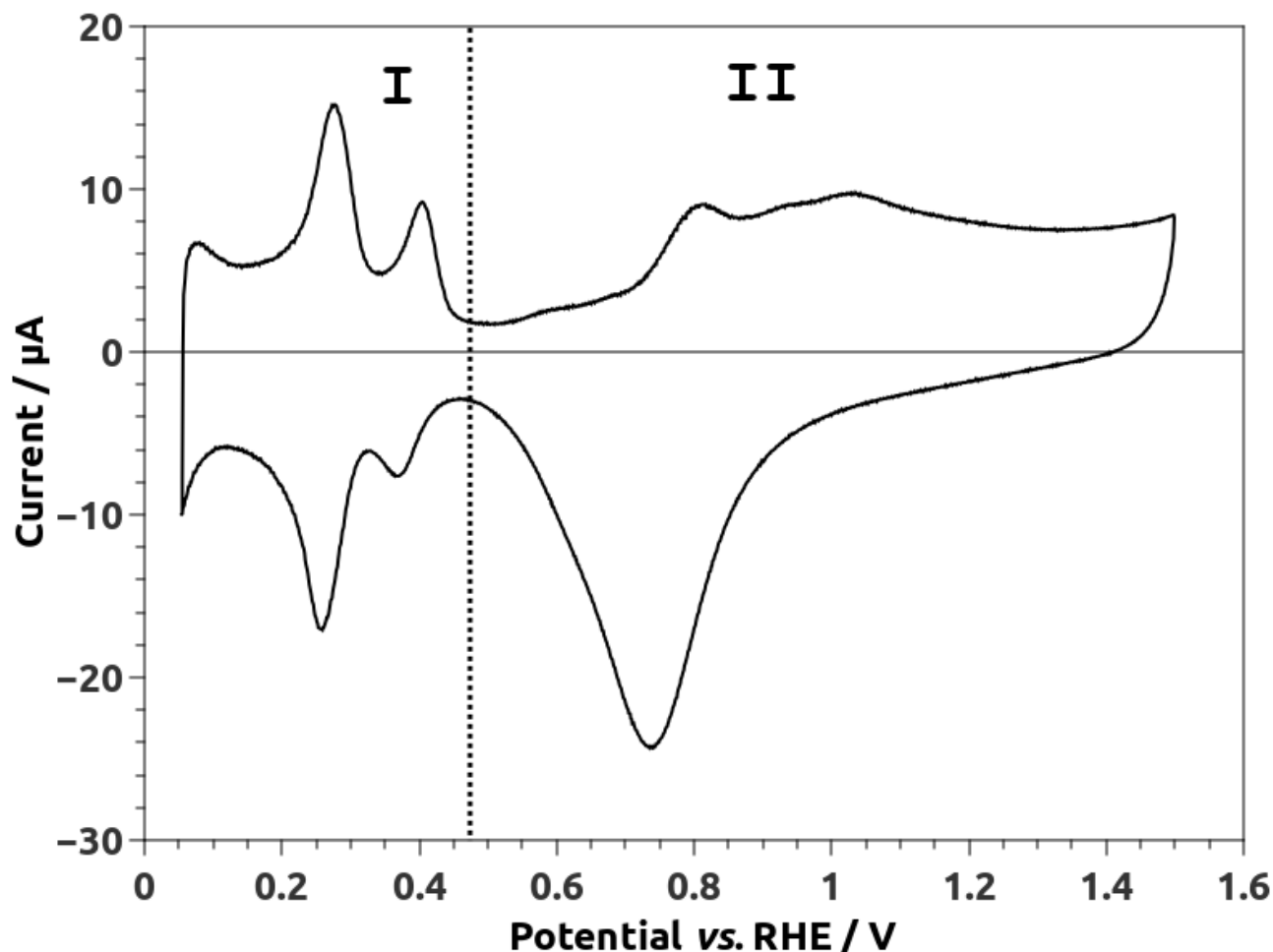


Figure 3.1: Static voltammogram recorded at $50 \text{ mV}\cdot\text{s}^{-1}$ on a polycrystalline Pt disk immersed in Ar-saturated 0.1 M NaOH at 25°C .

Fig.3.2 shows three voltammograms obtained on a polycrystalline Pt electrode in $1 \text{ M NaOH} + 10 \text{ mM NaBH}_4$ electrolyte, when different preparation procedures for the Pt electrode are employed prior the BOR characterizations (see the dedicated Appendix A.1.2 for details about polishing and ultrasonic cleaning). The Pt electrode was either (i) polished and cleaned in ultrasonic bath, or (ii) polished, cleaned in ultrasonic bath and cycled 100 times in 1 M NaOH electrolyte between -0.1 and 1.5 V vs. RHE (RDE rotated at $\Omega = 1000 \text{ rpm}$, voltammetry sweep rate $\nu = 25 \text{ mV}\cdot\text{s}^{-1}$) or (iii) polished, cleaned in ultrasonic bath, cycled 100 times in 1 M NaOH electrolyte between -0.1 and 1.5 V vs. RHE , polished and cleaned in ultrasonic bath again.

Pt electrodes prepared as described in (i) and (iii) display in Fig.3.2 a standard voltammogram shape for smooth Pt in comparable conditions [45, 129, 130]. The open circuit potential (OCP) of the Pt electrode is *ca.* -30 mV vs. RHE . Two distinguishable potential regions can be observed on these voltammograms. In the first region between the OCP and 0.9 V vs. RHE , the mass-transfer-limited oxidation current gradually decreases with the increase of the potential from 0.4 to 0.9 V vs. RHE . This decrease of the mass-transfer-limited current is attributed to the progressive adsorption of oxygen-containing species that block the Pt active surface. This hypothesis is further discussed in this second part of the thesis. The second region, between 0.9 and 1.5 V vs. RHE , is another mass-transfer-limited oxidation, where the Pt surface is progressively and ultimately blocked by oxides formation (boron oxides or/and platinum oxides) from 1.1 to 1.5 V vs. RHE . The existence of these two regions shows that Pt (low potential

region) and Pt-oxides (high potential region) surfaces both show activity towards the BOR.

A Pt electrode prepared as described in (ii) displays in Fig.3.2 a clearly different voltammogram shape compared to the cases (i) and (iii). Performing a cyclic voltammetry in 1 M NaOH + 10 mM NaBH₄ electrolyte directly after 100 cycles in 1 M NaOH electrolyte (*i.e.* without any polishing between these two procedures) yields a peculiar result. The current plateau limited by mass-transfer is well-defined in the anodic sweep between 0.5 and 0.9 V *vs.* RHE, followed by a slight decrease of the oxidation current from 0.9 to 1.2 V *vs.* RHE and a sharp decrease from 1.2 to 1.5 V *vs.* RHE. The cathodic sweep displays the same two potential regions with mass-transfer-limited oxidation, and does not exhibit the sharp hysteresis observed in cases (i) and (iii) at potential below *ca.* 1.2 V *vs.* RHE. This shows that a polycrystalline Pt electrode prepared according to the procedure (ii) does not undergo a progressive deactivation towards the BOR between 0.5 V and 0.9 V *vs.* RHE, compared to cases (i) and (iii).

From Fig.3.2, one can conclude that cycling a Pt electrode in NaOH electrolyte apparently changes the structure of the Pt surface, which then behaves differently towards the BOR compared to the polycrystalline Pt surface commonly used in most BOR studies (*i.e.* prepared without any cycling in NaOH beforehand). This particular Pt surface is nevertheless brought back to the standard one by mechanical polishing, as illustrated on Fig.3.2: the BOR voltammogram in 1 M NaOH + 10 mM NaBH₄ electrolyte of the Pt electrode prepared as described in (iii) is almost superimposed to that of the Pt electrode prepared as described in (i).

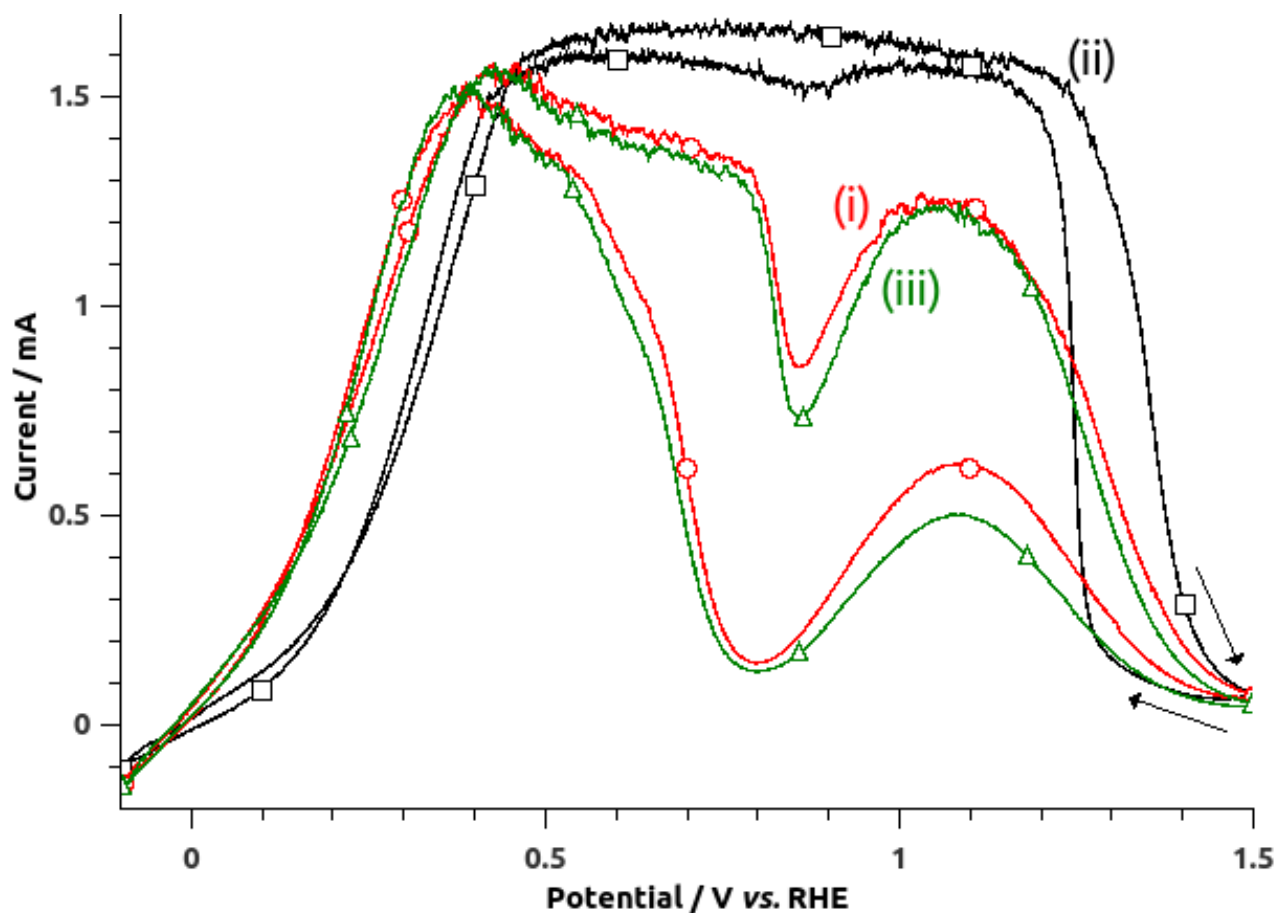


Figure 3.2: RDE voltammograms of a polycrystalline Pt disk electrode ($S_{\text{geo}} = 0.031 \text{ cm}^2$) in 10 mM $\text{NaBH}_4 + 1 \text{ M NaOH}$ electrolyte solution, $\nu = 25 \text{ mV}\cdot\text{s}^{-1}$, $\Omega = 1000 \text{ rpm}$. Influence of the electrode preparation procedure: (i) polishing and ultrasonic cleaning, (ii) polishing, ultrasonic cleaning and 100 cycles in 1 M NaOH between -0.1 and 1.5 V vs. RHE , (iii) polishing, ultrasonic cleaning, 100 cycles in 1 M NaOH between -0.1 and 1.5 V vs. RHE , polishing and ultrasonic cleaning again.

A Pt electrode was prepared following the procedure (ii) to get this particular state of surface. After plotting the voltammogram that corresponds to case (ii) on Fig.3.2, this electrode was then cycled in 1 M NaOH + 10 mM NaBH_4 electrolyte between -0.1 and 1.5 V vs. RHE . Some voltammograms of this experiment are presented in Fig.3.3. Cycling in this strongly reducing electrolyte brings back the Pt surface from the particular structure presented in case (ii) of Fig.3.2 to the standard one of cases (i) and (iii). Note that the electrolyte composition gradually changes during cycling, due to the progressive consumption of BH_4^- as a result of its irreversible electrooxidation and hydrolysis: the BH_4^- concentration is lower on the 94th cycle than on the 1st one. This accounts for the large differences in mass-transfer-limited oxidation currents monitored on Fig.3.3.

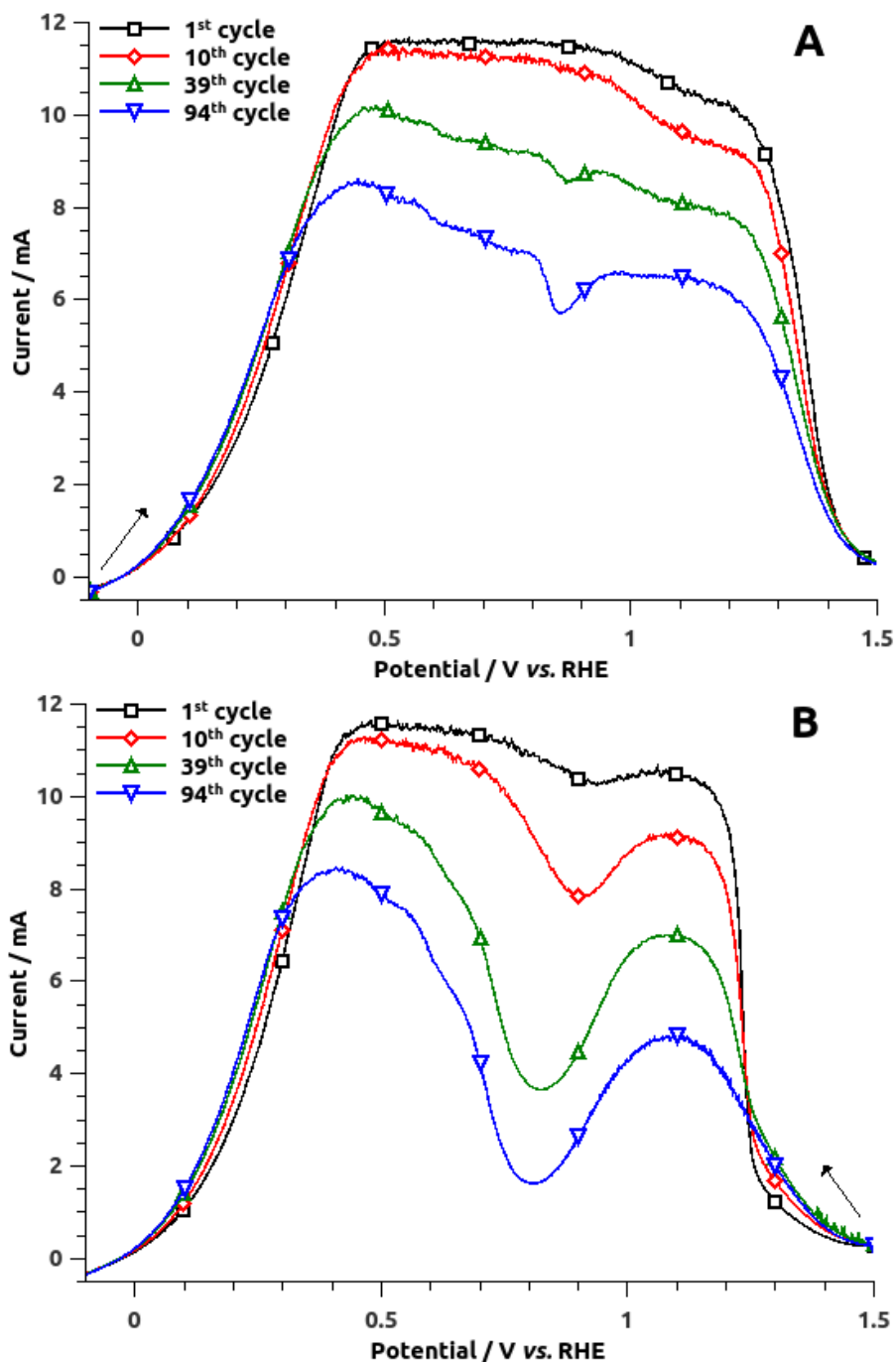


Figure 3.3: RDE (A) anodic sweep and (B) cathodic sweep of the voltammograms performed in 1 M NaOH + 10 mM NaBH₄ electrolyte solution on a polycrystalline Pt disk electrode ($S_{\text{geo}} = 0.196 \text{ cm}^2$) cycled 100 times in 1 M NaOH electrolyte beforehand between -0.1 and 1.5 V *vs.* RHE, $\nu = 25 \text{ mV}\cdot\text{s}^{-1}$, $\Omega = 1000 \text{ rpm}$.

A first attempt to physically observe a possible modification of the polycrystalline Pt surface after the voltammetric cycling in 1 M NaOH was realized. The polycrystalline Pt electrode was prepared as described before and its surface was observed using tapping mode atomic force microscopy (AFM Veeco Dimension 3100) before and after the 100 voltammetric cycles in 1 M NaOH between -0.1 and 1.5 V *vs.* RHE. From Fig.3.4, apart from the polishing scratches, no notable differences can be observed within the AFM range between the polycrystalline Pt surfaces before and after the voltammetric cycling in 1 M NaOH. Indeed, the root mean square roughness (RMS) of the surface does not change with the voltammetric cycling in 1 M NaOH

(c.a. 1.6 nm RMS in both images of Fig.3.4).

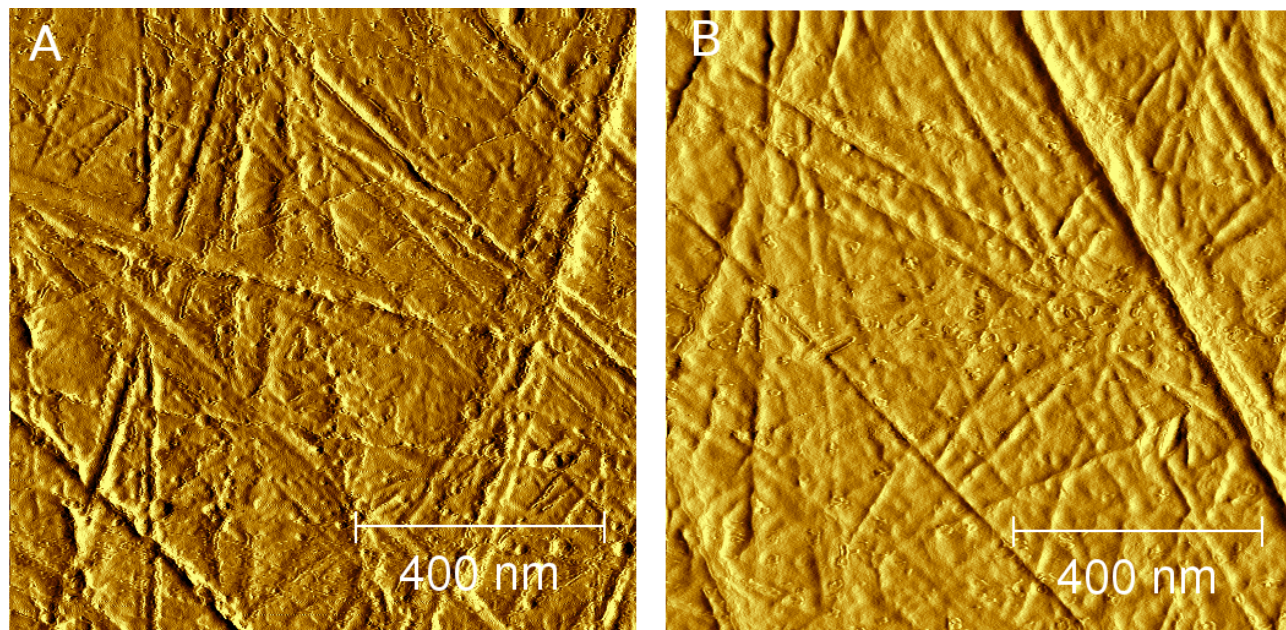


Figure 3.4: Tapping-mode AFM amplitude images of a polycrystalline Pt surface electrode (A) before and (B) after 100 voltammetric cycles in 1 M NaOH electrolyte between -0.1 and 1.5 V *vs.* RHE.

This result could suggest that our voltammetric cycling does not change considerably the surface morphology like other more brutal treatments where the growth of a relatively thick Pt oxide layer occurs [178, 179], but more likely leads to surface disorder of the polycrystalline Pt induced by oxygen place-exchange [180, 181, 182]. This disordering, not visible by AFM, could induce a difference of reactivity towards the BOR as the type of Pt sites available on the surface for the reaction is likely to change and to behave differently towards, for example, hydroxyls or BOR-intermediates adsorptions. However, at this point, this discussion is merely a hypothesis as the phenomena likely to occur are beyond the limit of the observation scale for smooth polycrystalline Pt surface. In order to get further insight on the influence of the Pt structure towards the BOR, the use of well-defined Pt single crystal electrodes is needed. The corresponding study is detailed hereafter. The author acknowledges that it would be even more convincing to perform *in situ* STM analyses at single crystal Pt surfaces to study these effects, but the trials in that direction were not successful to date.

3.2 Single crystal Pt

The structure-sensitivity of the BOR on the Pt surface is studied using the three Pt basal planes single crystal electrodes: Pt(111), Pt(110) and Pt(100). The experimental details specific to the characterizations of these well-defined surfaces are specified in the dedicated Appendix A.1.1 of this thesis.

Fig.3.5 shows the voltammograms of the three basal planes Pt working electrodes (Pt(111), Pt(110) and Pt(100)) in 0.1 M NaOH or in 0.1 M NaOH + 1 mM NaBH₄ in static hydrodynamics conditions. The voltammograms measured in NaOH supporting electrolyte (dotted line

in Fig.3.5) display the typical shapes expected for the Pt basal planes in alkaline condition, confirming that the surfaces of the Pt single crystal electrodes are indeed well-defined in our experimental conditions [183]. Typical voltammograms of the three Pt basal planes electrodes in alkaline supporting electrolyte are reproduced in Fig.3.6, where the commonly accepted attribution is indicated for the peaks of the voltammograms.

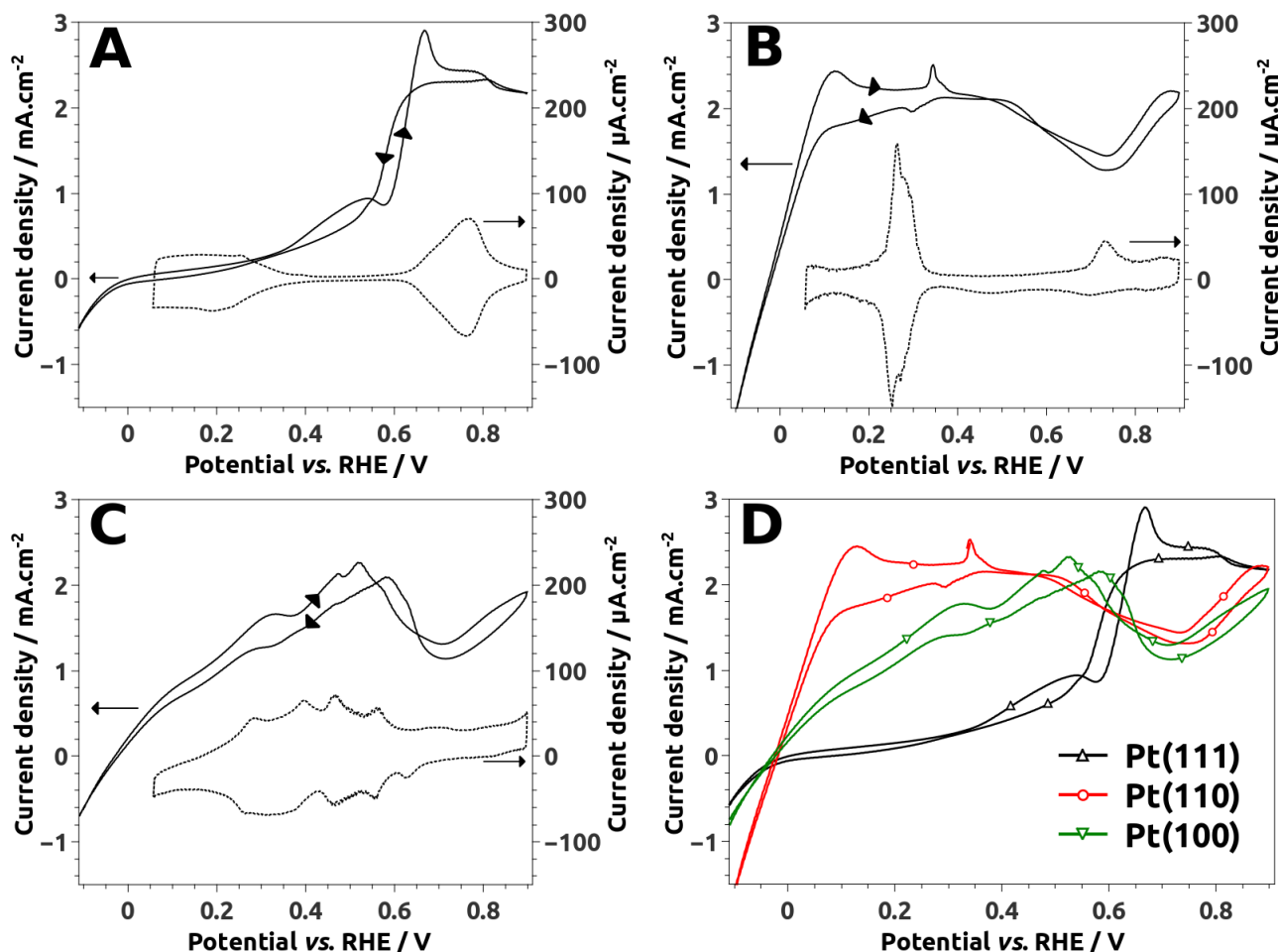


Figure 3.5: Static voltammograms of Pt basal plane single crystal electrodes in 0.1 M NaOH (dotted lines) or in 0.1 M NaOH + 1 mM NaBH₄ (plain lines) at 50 mV.s⁻¹. A: Pt(111), B: Pt(110), C: Pt(100). D: voltammograms of the three Pt basal planes electrodes (Pt(111), Pt(110) and Pt(100)) in 0.1 M NaOH + 1 mM NaBH₄ for comparison.

The voltammograms of the three Pt basal planes working electrodes in 0.1 M NaOH + 1 mM NaBH₄ (plain lines in Fig.3.5) are similar to those recently obtained by Briega-Martos *et al.* [128]. At low potential, *i.e.* at potential values for which the Pt basal planes electrodes are covered by H_{ads}, the activity order towards the BOR is Pt(110) > Pt(100) ≫ Pt(111) (Fig.3.5D). The influence of the hydroxyl adsorption on the Pt surfaces towards the BOR depends on the crystallinity of the surface. Indeed, for the surfaces which are active for the BOR at low potential (Pt(110) and Pt(100)), a first decay of the current in the BOR voltammograms is observed when the quantitative hydroxyl adsorption occurs at *ca.* 0.5 V *vs.* RHE (Fig.3.5B and Fig.3.5C). This decay in current for Pt(110) and Pt(100) is followed by a current increase at higher potential (at *ca.* 0.7 V *vs.* RHE). On the contrary, the Pt(111) surface, which is relatively inactive towards the BOR at low potential, is activated towards the BOR at *ca.* 0.6 V *vs.* RHE when the hydroxyl adsorption occurs (Fig.3.5A).

Schmidt *et al.* [184] investigated the hydrogen evolution reaction (HER) and the hydrogen oxidation reaction (HOR) on the three Pt basal planes in KOH electrolyte (Fig.3.6). A decay of the mass-transfer-limited HOR current was observed in the case of Pt(110) and Pt(100) for electrode potential values where the hydroxyl adsorption occurs on the Pt surfaces. This decay was attributed partly to OH_{ads} being a site-blocking inhibitor for the hydrogen adsorption step of the HOR [185]. Interestingly, no decay of the mass-transfer-limited HOR current was observed for Pt(111). This peculiar behavior of Pt(111) compared to Pt(110) and Pt(100) was attributed to an adsorption of the hydroxyl species on Pt(111) which would not take place on the same type of Pt site required for the hydrogen dissociative adsorption, explaining the absence of any inhibition of the HOR activity by OH_{ads} on Pt(111). The study of the HOR on the Pt basal planes in alkaline media (Fig.3.6) bears some similarities with the study of the BOR described above in this section (Fig.3.5): (i) a decay of the BOR and HOR currents related to the hydroxyl adsorption on Pt(110) and Pt(100) and (ii) a peculiar behavior of Pt(111), for which the HOR and the BOR is not inhibited by hydroxyl adsorption, but for which the surface activity is, by far, lower than in the case of the two other basal planes.

However, the BOR also behaves to some extent differently than the HOR on the three Pt basal planes. In the case of the HOR, the adsorption of hydroxyls leads to either no effect (Pt(111)) or a decrease (Pt(110) and Pt(100)) of the HOR current (Fig.3.6). In the case of the BOR, the adsorption of hydroxyls leads to either an increase (Pt(111)) or a decrease followed by an increase (Pt(110) and Pt(100)) of the BOR current (Fig.3.5). This is a first insight that OH_{ads} may have two opposite influences on the BOR. The OH_{ads} could be a site-blocking inhibitor for the adsorption of BH_4^- on the Pt surface, leading to a first decay of the BOR current for the Pt surfaces that are fully active for the BOR in hydroxyl-free form at low potentials (Pt(110) and Pt(100)). This latter influence is similar to the one observed for the HOR. However, in the case of the BOR, OH_{ads} could also be a reactant in a specific pathway of the BOR in a Langmuir-Hinshelwood-type reaction. This new BOR pathway, occurring at high potentials, leads to the activation of Pt(111), and to the re-activation of the Pt(110) and Pt(100) surfaces after the first inhibition explained above.

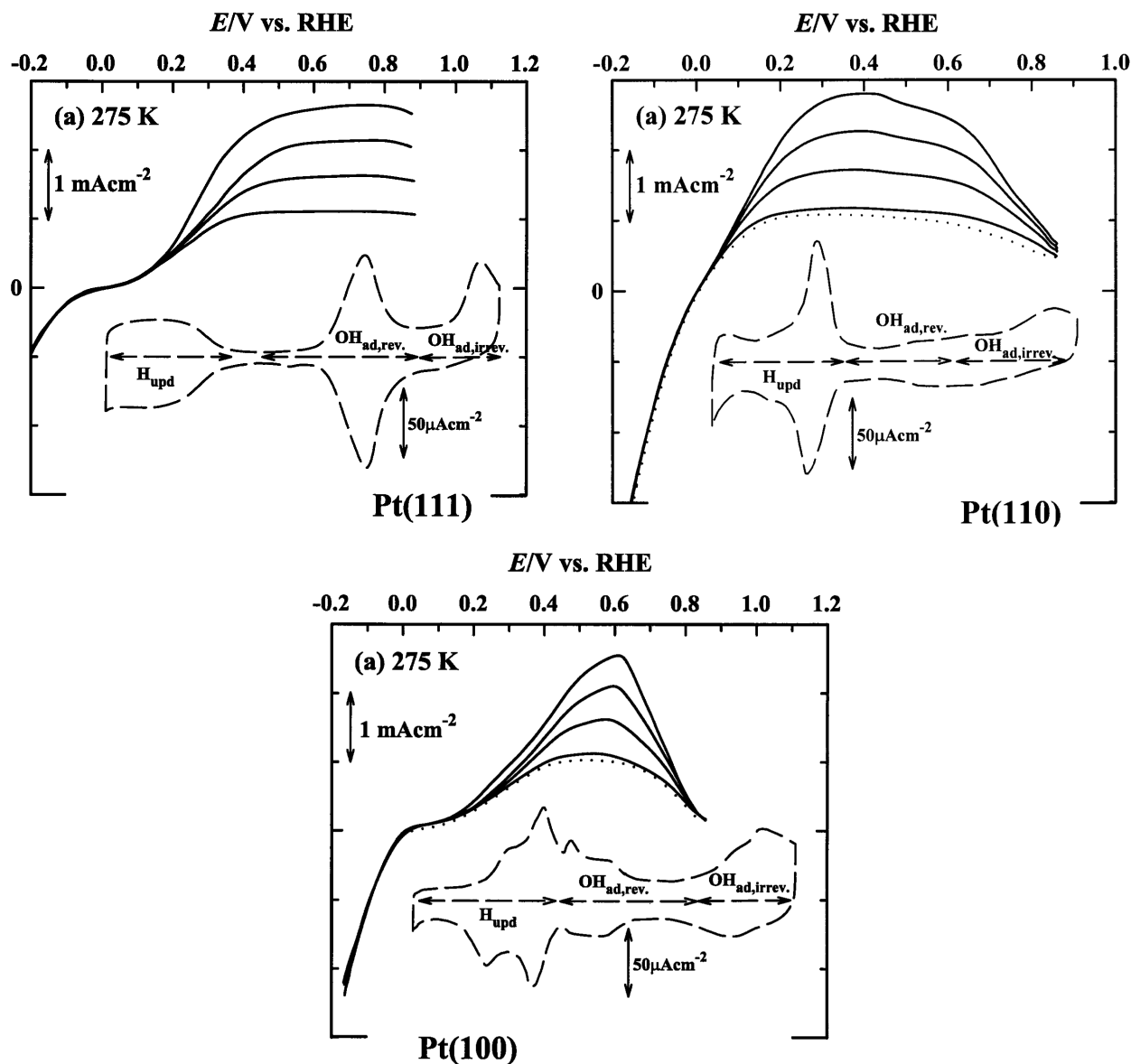


Figure 3.6: HOR/HER ($20 \text{ mV}\cdot\text{s}^{-1}$) on the three Pt basal plane electrodes in 0.1 M KOH with rotation rates of 400, 900, 1600, and 2500 rpm (plain lines) at 275 K. The dashed lines represent the base voltammograms at 275 K ($50 \text{ mV}\cdot\text{s}^{-1}$) in solution free of H_2 with approximated H_{ads} and OH_{ads} regions. Reproduced from Ref.[184] with permission from Elsevier.

The results obtained using Pt basal plane electrodes enable to reinforce the proposition concerning the behavior of polycrystalline Pt towards the BOR. Indeed, from the study of the BOR on Pt single crystal electrodes, it seems likely that the decay of the mass-transfer-limited BOR current observed for the polycrystalline Pt electrode (Fig.3 (i) and (iii), between 0.4 V and 0.9 V *vs.* RHE) is related to an inhibition of the Pt surface caused by the formation of OH_{ads} species, which blocks the Pt sites active for the adsorption of BH_4^- . Moreover, the second increase of the BOR current for the polycrystalline Pt electrode (Fig.3 (i) and (iii), above 0.9 V *vs.* RHE) is also attributed to OH_{ads} , as the presence of the hydroxyl species on the Pt surface triggers a new BOR pathway that includes a Langmuir-Hinshelwood-type reaction. Further investigation of the different BOR pathways depending on the electrode potential is attempted in the following chapters of this thesis.

Each crystal plane of the polycrystalline Pt electrode contributes to the global behavior of

this electrode towards the BOR. The study of the BOR on the three Pt basal plane electrodes shows that the Pt surface can be either (i) highly active for the BOR at low potential but inhibited at first when hydroxyl species adsorb (Pt(110) and Pt(100)) or (ii) poorly active for the BOR at low potential but activated when hydroxyl species adsorb (Pt(111)). Let us consider an electrode composed of both Pt(110) and Pt(111) planes; it is theoretically possible that this electrode is both highly active for the BOR at low potential (contribution of the Pt(110) planes) and not sensitive to the inhibition of the BOR caused by OH_{ads} , thanks to the Pt(111) planes. Indeed, during the investigation of the BOR on various types of Pt single crystal electrodes, Briega-Martos *et al.* [128] observed the lowest decay in the BOR current for the kinked Pt(331) electrode, which displays monoatomic (111) terraces and monoatomic (110) steps (or vice versa). This could be a first tentative explanation for the peculiar behavior of the polycrystalline electrode cycled in NaOH prior to BOR characterizations (Fig.3 (ii)), for which almost no decay of mass-transfer-limited BOR current was observed. However, it is still not clear what kind of structure modification happened on the polycrystalline Pt surface during the cycling in NaOH. Briega-Martos *et al.* [128] proposed that the oxygen place-exchange occurring during repetitive cycling of the polycrystalline Pt electrode in NaOH creates defects with a (110) symmetry on the Pt terraces [181], but it is still quite speculative at this point. The only global but definitive conclusion on the experiment presented in Fig.3 is that the cycling of the Pt polycrystalline electrode in NaOH, performed using our experimental conditions, changed the surface of the Pt electrode, making the BOR which proceeds on this modified surface insensitive to OH_{ads} .

3.3 Conclusions

The use of bulk Pt electrodes, either polycrystalline or single crystal, enables to get first insights into the BOR mechanism on Pt:

- The BOR is structure-sensitive. The order of BOR activity for the three Pt basal plane electrodes is $\text{Pt}(110) > \text{Pt}(100) \gg \text{Pt}(111)$ at low potential. This result suggests that at these low potentials (*i.e.* on a hydroxyl-free Pt surface), the limiting step of the BOR is related to the formation/oxidation of one or several adsorbed BOR intermediates (in other words, to the binding energy of the BOR adsorbed intermediate(s) on the Pt surface);
- The hydroxyl adsorption on the Pt surface at higher potential values has two opposite effects on the BOR activity: (i) a detrimental effect, with OH_{ads} being a Pt site-blocking inhibitor for the adsorption of BH_4^- , or (ii) a beneficial effect, with OH_{ads} being a reactant in another pathway for the BOR.

The well-defined surfaces of the single crystal electrodes are very useful in order to understand the mechanism taking place during the BOR. The voltammograms of the three Pt basal planes electrodes presented in this chapter were performed in static hydrodynamic conditions. In order to work in near steady-state conditions, one commonly uses a setup similar to the RDE used for the polycrystalline electrode in this chapter. However, one limitation of the single crystal electrode is that the well-defined surface gets destroyed at high potential values (typically above 0.9 V *vs.* RHE), where oxygen place-exchange proceeds. It was not possible to get perfectly stable near-steady state RDE voltammograms in NaOH + NaBH₄ electrolyte using the single crystal electrodes and an upper-limit vertex potential of 0.9 V *vs.* RHE. The current of the voltammograms progressively decayed upon cycling, so that no further exploitation of the experiment was attempted. This decay of the BOR activity upon cycling is attributed to the poisoning of the Pt surface during the BOR. The poisoning of the Pt surface during the BOR is

further discussed in the following chapter 4 where another type of Pt-based model electrode (Pt nanoparticles supported on flat glassy carbon) is used.

Chapter 4

Pt nanoparticles supported on flat
glassy carbon (Pt/GC)

In this chapter, a Pt/GC model electrode is used in order to study the borohydride oxidation reaction (BOR) on Pt. This model electrode is closer to the reality of the DBFC anode compared to the bulk Pt model electrodes used in the previous chapter 3. Indeed, for this Pt/GC electrode, the Pt electrocatalysts consists of Pt nanoparticles supported on a carbon substrate, similarly to the Pt/C-based anode characterized in DBFC configuration in the chapter 1 of this thesis. However, the glassy carbon (GC) substrate is flat, so that experimental variables related to a 3-D electrode active layer are not considered. The experimental details about the synthesis (A.1.2) and the characterization (CO_{ads} -stripping and TEM analysis, see A.3) of the Pt/GC electrode, as well as the electrochemical characterization of the BOR on this Pt/GC electrode (A.1.1), are specified in the dedicated Appendices of this thesis. Using this model electrode, the poisoning of the Pt active surface during the BOR is investigated, providing further insight into the BOR mechanism on Pt.

4.1 Characterization of the Pt/GC electrode

The Pt/GC electrode used in this chapter was synthesized in order to yield a Pt loading of $5 \mu\text{g}_{\text{Pt}}.\text{cm}^{-2}$ (see the dedicated Appendix A.1.2 for further details on the synthesis of this electrode). Fig.4.1A displays the CO_{ads} -stripping voltammograms measured for Pt/GC electrode before BOR electrochemistry and after BOR electrochemistry (the BOR electrochemistry consisting in the experiments presented in Fig. 4.3 and Fig. 4.4). The two sets of data feature identical characteristics: one single, well-defined CO_{ads} -stripping peak is observed; the absence of any pre-peak that would be associated to a large extent of agglomeration [186] shows that the Pt nanoparticles are mainly isolated and well-separated (distributed) onto the GC surface [187]. Moreover, as witnessed in Fig.4.1A, the difference of CO_{ads} -stripping features is minimal prior/after BOR electrochemistry, which shows that the Pt/GC nanoparticles can sustain the overall experimental treatment (CO_{ads} -stripping in acidic medium ('Pre-BOR' in Fig. 4.1), multiple BOR characterizations in strongly reducing alkaline medium (Fig. 4.3 and Fig. 4.4) and CO_{ads} -stripping in acidic medium ('Post-BOR' in Fig. 4.1)) without dramatic morphological changes. One feature, however, that can be observed in Fig.4.1A is the increase of the double-layer current (associated to the GC substrate) in the first cycle of the CO_{ads} -stripping voltammogram after BOR electrochemistry, compared to the CO_{ads} -stripping voltammogram performed prior to BOR electrochemistry. This is ascribed to the irreversible reduction of some surface-oxide groups of the GC by NaBH_4 (a strong reductant) during the BOR characterizations. Indeed, prior to the BOR electrochemistry, some surface oxide groups of the GC can be partially reduced by the CO adsorption step at low potential (0.1 V *vs.* RHE) but then may re-oxidize in the subsequent positive potential scan, which cannot occur similarly after BOR electrochemistry [188]. Whatever this small bias, it is possible to correct the CO_{ads} -stripping voltammograms from the baseline current, as shown on the example of Fig.4.1B.

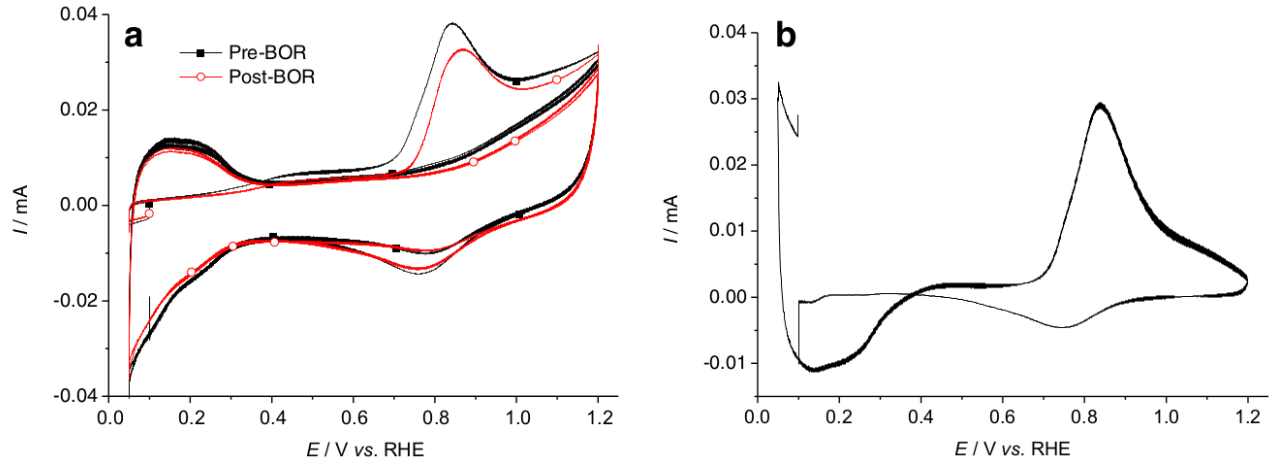


Figure 4.1: (A): CO_{ads} -stripping voltammograms measured at $20 \text{ mV}\cdot\text{s}^{-1}$ in $0.1 \text{ M H}_2\text{SO}_4$ on the Pt/GC model electrode ($5 \mu\text{g}_{\text{Pt}}\cdot\text{cm}_{\text{geometric}}^{-2}$) before and after borohydride oxidation reaction (BOR) electrochemistry and (B): corresponding subtracted (baseline-corrected) voltammogram calculated on the signal before BOR electrochemistry. The electroactive area of Pt is $0.7 \text{ cm}_{\text{Pt}}^2$, based on the coulometry of the baseline-corrected CO_{ads} -stripping peak (a similar value is calculated based on the baseline-corrected hydrogen-desorption peak, and from the mean Pt nanoparticle diameter).

From such baseline-corrected voltammogram (Fig.4.1B), one can easily extract: (i) the value of CO_{ads} -stripping peak potential indicative of the mean particle size of Pt [187] and (ii) its coulometry, yielding the electrochemical active surface area (EASA) of the Pt nanoparticles (assuming the coulometry for the desorption of one monolayer of adsorbed CO to be $422 \mu\text{C}\cdot\text{cm}_{\text{Pt}}^{-2}$). The mean Pt nanoparticle diameter derived from the CO_{ads} -stripping peak potential is *ca.* 3.6 nm and 3.9 nm before and after the BOR characterizations, respectively, according to the procedure used by Maillard *et al.* [187]. From the value of mean Pt nanoparticle diameter, the Pt surface (S_{Pt}) is calculated with Eq.4.1, assuming spherical Pt nanoparticles with identical size [189]:

$$S_{\text{Pt}} = \frac{6}{d_{\text{NP}} \rho_{\text{Pt}}} \quad (4.1)$$

Considering the mean diameter of the Pt nanoparticle d_{NP} to be $3.9 \cdot 10^{-9} \text{ m}$ (determined from the potential value of the CO_{ads} -stripping peak), and the Pt density ρ_{Pt} to be $21.4 \cdot 10^6 \text{ g}_{\text{Pt}}\cdot\text{m}_{\text{Pt}}^{-3}$, a Pt surface of $72 \text{ m}_{\text{Pt}}^2\cdot\text{g}_{\text{Pt}}^{-1}$ is calculated. Considering the target Pt loading of the Pt/GC electrode ($5 \mu\text{g}_{\text{Pt}}\cdot\text{cm}_{\text{geometric}}^{-2}$), the Pt surface per geometric surface of the GC tip is calculated to be *ca.* $3.6 \text{ cm}_{\text{Pt}}^2\cdot\text{cm}_{\text{geometric}}^{-2}$. As stated above, another way to determine the Pt surface per geometric surface of GC substrate consists in measuring the charge under the CO_{ads} -stripping peak (Fig.4.1B). Assuming that the charge for the desorption of CO_{ads} corresponds to $422 \mu\text{C}\cdot\text{cm}_{\text{Pt}}^{-2}$, the Pt surface per geometric surface of the GC tip is measured to be *ca.* $3.5 \text{ cm}_{\text{Pt}}^2\cdot\text{cm}_{\text{geometric}}^{-2}$. The calculated and measured values are in good agreement. This variable related to the electrode, defined by the Pt surface per geometric surface of the electrode, is denoted as the 'Pt roughness' of the electrode in this thesis. For comparison, the Pt roughness of a bulk polycrystalline Pt electrode was measured to be *ca.* $2.5 \text{ cm}_{\text{Pt}}^2\cdot\text{cm}_{\text{geometric}}^{-2}$ [129]. Note that the Pt roughness of the Pt-based electrode is the main variable of study in the following chapter 5.

The Pt/GC electrode was also analyzed by TEM. As the TEM analysis is destructive for the Pt/GC electrode, micrographs were taken after the BOR characterizations only, so that the

Pt/GC electrode could be subjected to nanoparticles detachment occurring during the BOR (as previously discussed in chapters 1 and 2). Fig.4.2 shows representative TEM micrographs of the Pt/GC electrode, as well as a histogram of the nanoparticle size distribution measured on the micrographs. In agreement with the CO_{ads} -stripping characterization, no extensive sign of nanoparticles agglomeration is observed, and the isolated Pt nanoparticles are well-distributed on the GC substrate. The surface-average mean diameter of the Pt nanoparticle was calculated to be 2.8 nm. This value is not similar but still comparable to the mean Pt nanoparticle diameter of 3.9 nm determined by CO_{ads} -stripping characterization. The Pt nanoparticles composing this Pt/GC model electrode are close to the Pt nanoparticles composing a typical Pt-based anode of a DBFC: isolated and well-distributed Pt nanoparticles, with a mean diameter around 3 nm.

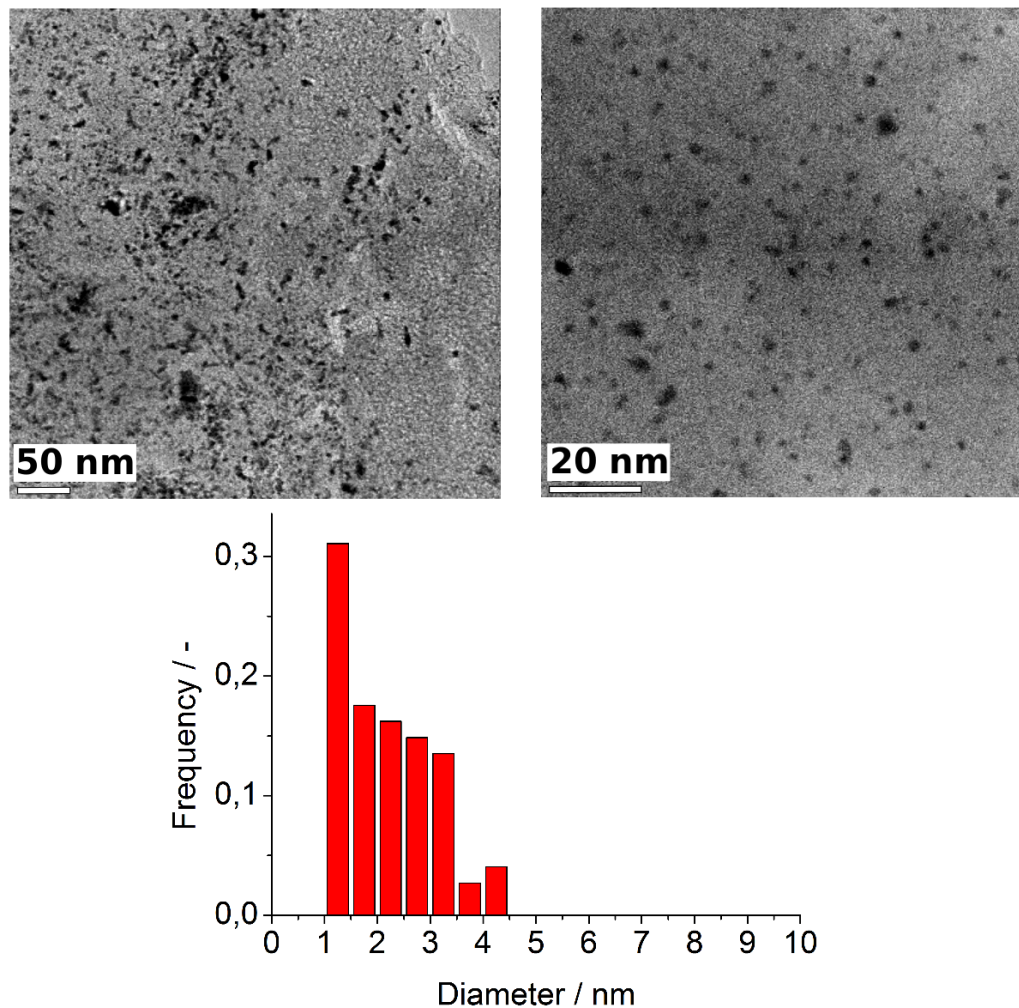


Figure 4.2: Representative TEM images of the Pt/GC nanoparticles at low (50 K, *left*) or high (200 K, *right*) magnification and corresponding nanoparticle size distribution histogram. Pt loading: $5 \mu\text{gPt} \cdot \text{cm}_{\text{geometric}}^{-2}$.

4.2 Poisoning of the Pt surface during the borohydride oxidation reaction (BOR)

Fig.4.3 presents a set of BOR RDE voltammograms measured on the Pt/GC model electrode in 1 M NaOH + 1 mM NaBH_4 with two different upper-vertex potentials: 0.8 V and 1.5 V

vs. RHE, for various revolution rates of the RDE (from 400 to 2,500 rpm, in this sequential order), which corresponds to near-steady-state conditions for this reaction [130]. It is worth mentioning here that the first BOR voltammograms at 400 rpm, plotted for the two values of upper-vertex potential, has been repeated twice and that the second one only is displayed here.

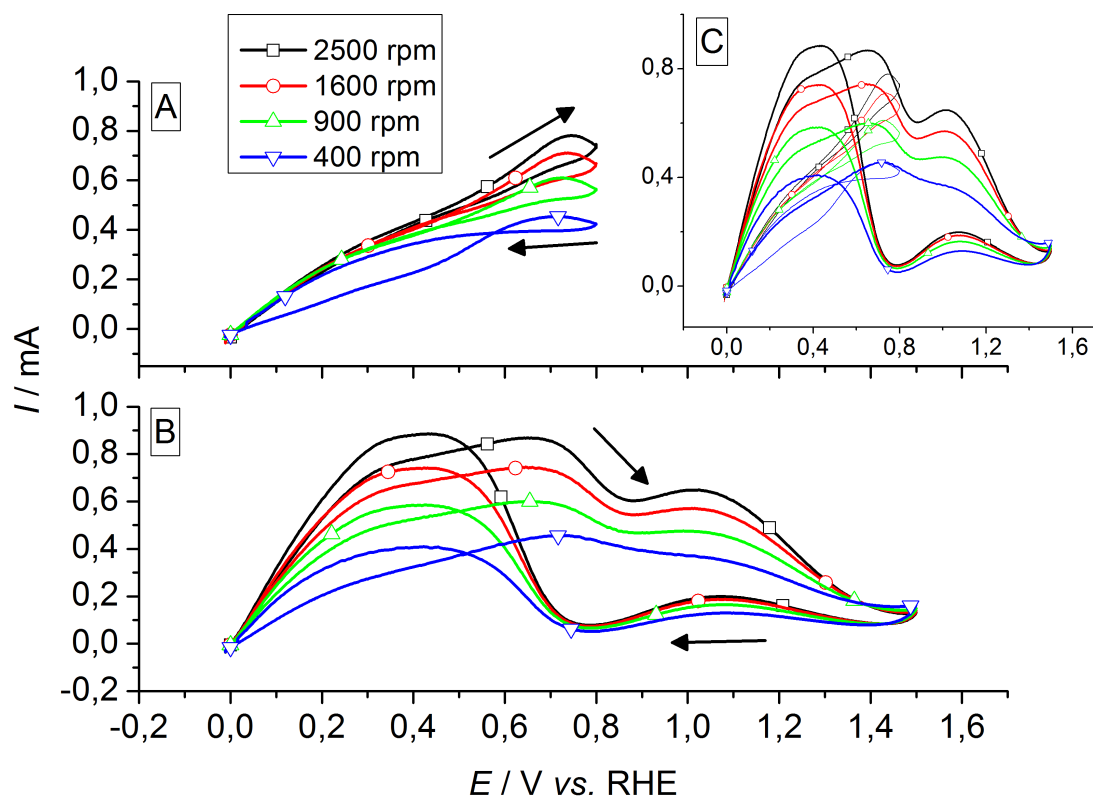


Figure 4.3: Near-steady-state NaBH_4 oxidation voltammograms measured at $20 \text{ mV}\cdot\text{s}^{-1}$ on Pt/GC model electrode ($5 \mu\text{g}_{\text{Pt}}\cdot\text{cm}^{-2}$) in $1 \text{ M NaOH} + 1 \text{ mM NaBH}_4$ with an upper-vertex potential of (A): 0.8 V vs. RHE or (B): 1.5 V vs. RHE . The inset (C) superimposes the voltammograms obtained with these two upper-vertex potentials. In any case, the voltammograms were plotted in the sequence 400, 900, 1,600, and then 2,500 rpm, first with an upper-vertex potential of 0.8 V vs. RHE , and then with an upper-vertex potential of 1.5 V vs. RHE .

Fig.4.3 shows that the Pt/GC nanoparticles cannot enable reaching a clearly-defined mass-transfer-limited plateau when the upper-vertex potential of the voltammogram is fixed at 0.8 V vs. RHE (Fig.4.3A). The current gradually levels off from the first revolution rate (400 rpm) to the last one (2,500 rpm), this effect barely being counter-balanced by the expected increase of mass-transfer rate. Additional voltammograms were plotted in similar conditions but with an upper-vertex potential of 1.5 V vs. RHE (Fig.4.3B). One must remind that the BOR voltammogram plotted in these conditions at 400 rpm was repeated twice and that the second one was displayed only. In this case, *i.e.* with upper-vertex potential of 1.5 V vs. RHE , one clearly sees that the overall shape of the voltammograms is dramatically different: well-defined kinetic, mixed, and mass transfer-limited regions are observed, as expected.

The only difference between the voltammograms of Fig.4.3A and Fig.4.3B in the potential region below 0.8 V vs. RHE is the history of the electrode. In the former case, the Pt/GC nanoparticles never experienced any incursion at high potential (above 0.8 V vs. RHE), whereas in the latter one, they were subjected to potential sweeping up to 1.5 V vs. RHE in the previous

cycle. This firstly shows that the history of the electrode has a clear influence on its ability to perform the BOR. Obviously, the incursion towards high values of potential enables to clean the Pt/GC surface and obtain much higher currents (Fig.4.3C), as recently put forth by Finkelstein *et al.* [58] (see Fig.2.4). As already stated in the chapter 2 of this thesis, this shows that the characterization of a given electrode towards the BOR should be performed with great care. Indeed, BOR kinetics calculation made using experimental conditions similar to those of Fig.4.3A will obviously lead to biased conclusions, as the surface-state of the electrode gradually changes during the experiment. Among other reasons, this issue might explain the significant discrepancies in the literature for the calculation of the number of electrons exchanged during the BOR on Pt catalytic surface.

In addition, the blocking of the Pt surface already occurs at open circuit potential (OCP). Fig.4.4 displays BOR voltammograms measured for the Pt/GC model electrode after various periods at OCP. The reference voltammogram corresponds to the second cycle of a two-cycle voltammograms procedure without any rest between the two cycles, and measured in the present operating condition. Comparing the reference voltammogram with a voltammogram performed after a given period at OCP demonstrates that the Pt/GC surface is gradually poisoned for increasing periods spent at OCP in NaBH₄-containing solutions (Fig.4.4A). Indeed, the currents monitored below 0.6 V *vs.* RHE become negligible after only 60 min at OCP in a 1 mM NaBH₄ solution. In addition, Fig.4.4A demonstrates that the Pt surface can be recovered by potential incursion beyond 0.6 V *vs.* RHE. Above this potential value, the positive scans of the 'Pt-poisoned' voltammograms exhibit larger oxidation currents than the reference voltammogram, showing that the poisoning species are electrochemically stripped from the Pt surface. After such stripping, the Pt/GC surface is completely recovered: the negative scan and subsequent cycles (the latter being not shown for clarity) of the Pt/GC electrode perfectly overlap with that of the reference voltammogram (Fig.4.4B), meaning that the electrode poisoning is reversible in this electrode potential range. This agrees with the recent findings of Finkelstein *et al.* regarding Pt and Au self-poisoning during the BOR [58].

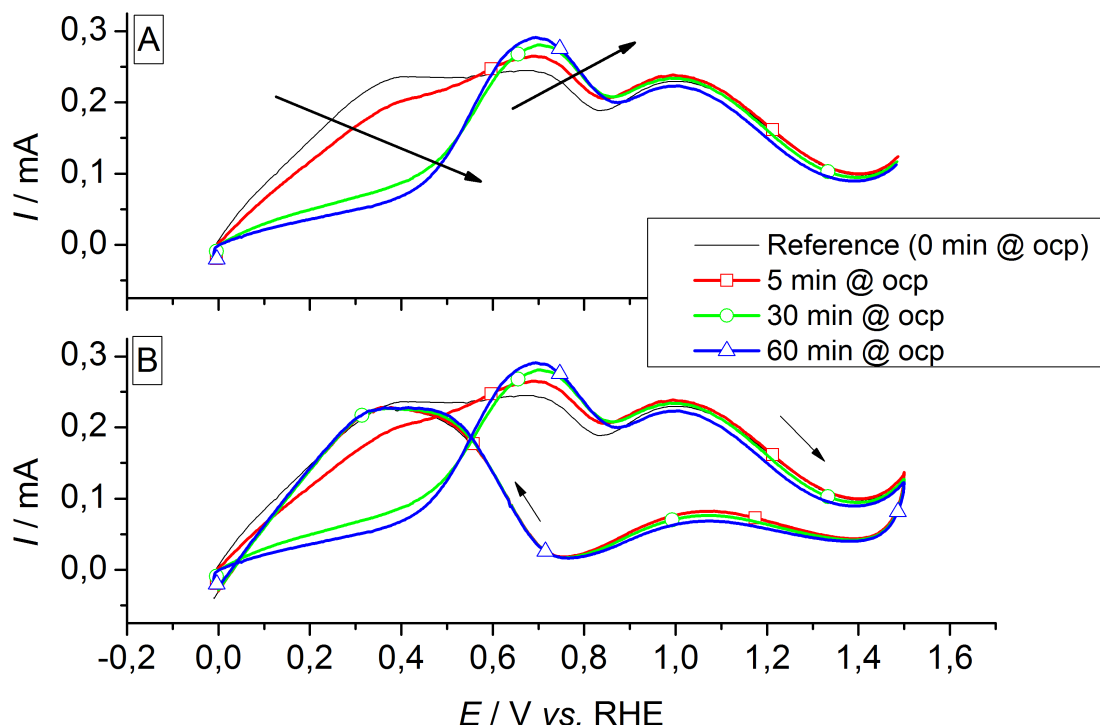


Figure 4.4: BOR voltammograms obtained at $\omega = 400$ rpm on Pt/GC model electrode ($5 \mu\text{g}_{\text{Pt}}\cdot\text{cm}^{-2}$) after various periods at open-circuit conditions (OCP). The potential sweep rate is $20 \text{ mV}\cdot\text{s}^{-1}$, and the electrolyte solution consists of $1 \text{ M NaOH} + 1 \text{ mM NaBH}_4$. (A): Positive-going scan only; (B): full cycle. Note that the voltammograms were obtained after all the electrochemical characterizations of Fig.4.3, and the remaining sodium borohydride concentration might be smaller than 1 mM NaBH_4 at that stage.

From Fig.4.3 and Fig.4.4, it is clear that, in order to get reliable BOR voltammograms in RDE near-steady-state conditions on a Pt-based electrode, it is necessary to consider the experimental history of the electrode. The recommended experimental method would be to perform several voltammetry cycles using sufficiently high upper-vertex potential. By doing so, the poisoning of the Pt surface during the BOR should not influence the results. However, this is obviously not possible for surfaces that are sensitive to higher potential values, such as Pt single crystal (see chapter 3) or non-noble alloys. When studying the latter surfaces, the gradual (and irreversible) poisoning of the working electrode might be a severe bias. Despite the experimental issue caused by poisoning as described above, this phenomenon enables to get further insight into the BOR mechanism on Pt. In the following discussion, an explanation for this poisoning is attempted.

First, one shall unveil the nature of the poison. *In situ* Fourier transform infrared spectroscopy (FTIR) of the BOR on Pt was performed by Molina Concha *et al.* [45] and pointed out to the presence of adsorbed $\text{BH}_{x,\text{ads}}$ species (x between 2 and 4) at the Pt surface during the BOR, as shown in Fig.4.5. Note that the presence of BH_{ads} was not reported in this FTIR study, probably because the infrared signature of BH_{ads} is out of the measurable range of the device for the conditions used in this work, or to the fact that the reference papers used in Ref. [45] to assign the FTIR bands were themselves incorrectly assigned (*e.g.* BH_2 assigned to BH bands). It is beyond the scope of the present thesis to try to solve this dilemma. The density

functional theory (DFT) calculations performed by Rostamikia *et al.* [190] for the BOR on Pt(111) concluded that the most favorable path for the BOR at low potential starts with the dissociative adsorption of BH_4^- to $\text{BH}_{\text{ads}} + 3\text{H}_{\text{ads}}$ onto the Pt surface, as shown in Fig.4.6. The binding energy of BH_{ads} is relatively high, and there is an energetic barrier to cross in order to further oxidize BH_{ads} into BOH_{ads} through the formation of the BHOH_{ads} intermediate, as illustrated in Fig.4.6. This suggests that BH_{ads} is a stable adsorbate on the Pt surface. From these spectroscopic [45] and theoretical [190] informations, $\text{BH}_{x,\text{ads}}$ are relevant 'poisons' of Pt at low potential, and for the sake of simplicity, BH_{ads} is proposed as the poison species in our conditions.

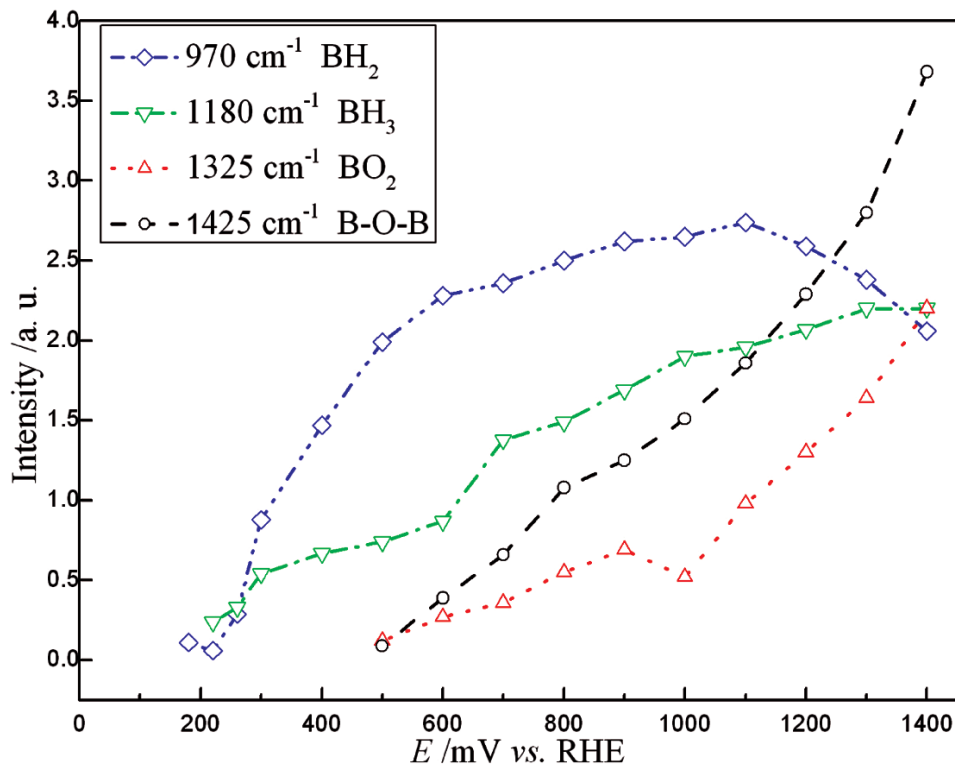


Figure 4.5: Band intensities of the p-polarized light as a function of applied potential, recorded on a platinum electrode in 1 M NaOH + 1 M NaBH₄ at room temperature. Reproduced from Ref. [45] with permission from the American Chemical Society.

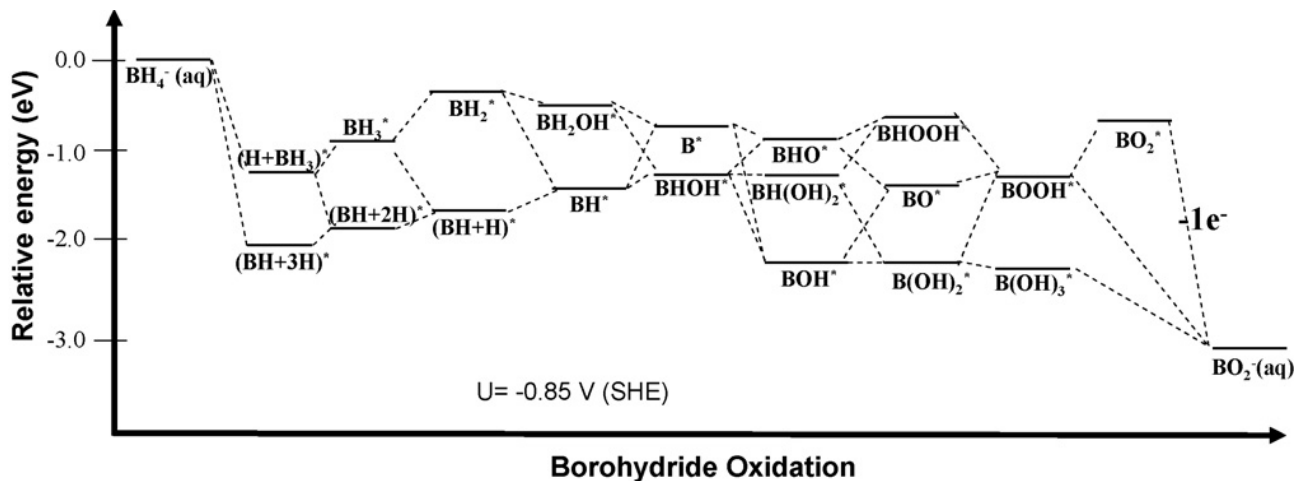


Figure 4.6: Density functional theory (DFT) calculations: borohydride oxidation reaction energy diagram over Pt(111) surface at -0.85 V *vs.* SHE. Reproduced from Ref. [190] with permission from Elsevier.

Fig.4.4 shows that BH_{ads} , supposedly blocking the Pt surface at low potential, is stripped above 0.5 V *vs.* RHE. Considering the previous chapter 3 of this thesis, where the possible beneficial role of OH_{ads} for activating the Pt surface towards the BOR was shown on bulk Pt electrode, it is likely that for this Pt/GC model electrode the removal of the BH_{ads} poisoning the active surface is triggered by the adsorption of the hydroxyls on the surface of the Pt nanoparticles. It is proposed that OH_{ads} reacts with BH_{ads} in a Langmuir-Hinshelwood-type electrooxidation, enabling the stripping of BH_{ads} from the Pt surface. This proposition concurs with the findings of Finkelstein *et al.* [58]. Indeed, they observed a fast and complete poisoning of a bulk polycrystalline RDE for electrode potential below the hydroxyl adsorption, as shown in Fig.4.7. However, at sufficiently high potential values, the consequent adsorption of hydroxyls did prevent the Pt surface to be totally poisoned by the BOR adsorbed intermediates (Fig.4.7).

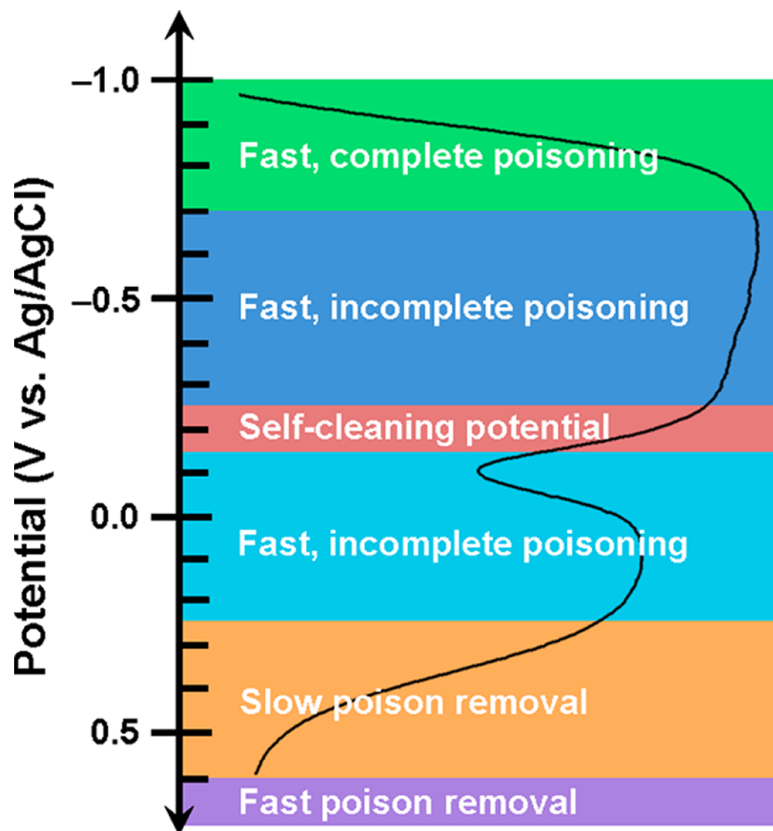


Figure 4.7: Summary of different potential-based poisoning and cleaning regimes for BH_4^- oxidation at Pt. The RDE anodic sweep for BH_4^- at Pt is superimposed for clarity (voltammogram plotted using the following experimental conditions: 5 mM BH_4^- in 1 M NaOH at Pt, 250 rpm, $20 \text{ mV}\cdot\text{s}^{-1}$). Reproduced from Ref.[58] with permission from the American Chemical Society.

The excess coulometry of the poison-stripping can be graphically determined in Fig.4.4B above 0.6 V *vs.* RHE between the plots measured after various OCP duration and the reference voltammogram plotted without any rest at OCP. The corresponding charges of 0.34, 0.59, and 0.69 mC are determined after 5, 30, and 60 min spent at OCP, respectively. The hypothesis is made that, as discussed above, BH_{ads} is the species blocking the Pt/GC active surface at low potential, until being stripped at higher potential when the hydroxyl adsorption occurs. The overall stripping reaction of BH_{ads} to BO_2^- is assumed to be a 4-electron electrooxidation reaction (the oxidation number of the boron atom is equal to -I and +III in BH_{ads} and BO_2^- , respectively). Considering the Pt surface on the Pt/GC electrode to be $0.7 \text{ cm}^2_{\text{Pt}}$ (see section 4.1 of this chapter), and knowing that the geometric surface of the Pt/GC electrode is equal to 0.196 cm^2 , these stripping charges correspond to a BH_{ads} fraction coverage on Pt of *ca.* 0.6, 1, and 1.2, after 5, 30, and 60 min spent at OCP, respectively. Of course, despite being rough and possibly overestimated by the contribution of additional faradaic currents to those of stripping, these figures show that the surface can be completely blocked by BH_{ads} species at low potential. Note that another experimental tentative for stripping this poison species is described in the dedicated Appendix B. It confirms the present trend, although the experiments may be subjected to non-negligible bias.

4.3 Conclusions

Using a Pt/GC model electrode, the poisoning of the Pt active surface during the BOR was investigated. This poisoning, that reduces the activity of the electrode, was found to occur at open circuit potential (OCP) and during the BOR at low electrode potential (below *ca.* 0.8 V *vs.* RHE). This poisoning leads to experimental issues, as the BOR voltammogram of the Pt-based electrode can possibly differ depending on the history of the electrode (duration of the rest at OCP, upper-vertex potential value of the preceding voltammogram cycles). Performing several voltammogram cycles with sufficiently high value of upper-vertex potential (around 1.5 V *vs.* RHE) is required in order to get reliable RDE voltammograms in near-steady-state conditions.

From the findings of the literature, the poisoning species was proposed to be BH_{ads} , a stable adsorbate produced by the dissociative adsorption of BH_4^- onto the Pt surface. It is shown that BH_{ads} no longer poisons the Pt surface when hydroxyls adsorb quantitatively on the surface at higher potential values (above *ca.* 0.8 V *vs.* RHE). In agreement with the findings of the previous chapter 3, the possible beneficial effect of OH_{ads} is shown. It is proposed that OH_{ads} reacts in a Langmuir-Hinshelwood-type electrooxidation with BH_{ads} . This proposition is further discussed and developed in the following chapters, where the sensitivity of the BOR towards the density of active Pt sites is investigated (chapter 5), and a mechanism for the BOR on Pt is proposed and modelled (chapter 6).

Chapter 5

Pt nanoparticles supported on
vertically-aligned carbon nanofilaments

In this chapter, the influence of the Pt site density on the borohydride oxidation reaction (BOR) is investigated. In order to do so, model electrodes consisting of Pt nanoparticles supported on vertically-aligned carbon nanofilaments (VACNF) are used. The Pt/VACNF electrodes are inserted in a gold-ring rotating ring-disk electrodes setup, which enables the detection of possible BOR intermediates released from the Pt/VACNF electrodes during the BOR. These Pt/VACNF model electrodes have previously been used for the investigation of the oxygen reduction reaction (ORR), as well as CO and hydrogen electrooxidation reactions by Savinova and coworkers [191, 192, 193, 194, 195]. The experimental details about the synthesis (A.1.2) and the characterization (CO-Stripping, SEM and TEM analysis, see A.3) of the Pt/VACNF electrodes, as well as the electrochemical characterization of the BOR on these Pt/VACNF electrodes (A.1.1), are specified in the dedicated Appendices of this thesis.

All the Pt/VACNF electrodes used in this study have identical thickness of the VACNF layer (10 μm), as well as identical initial Pt particle size (*ca.* 5 nm in diameter) and shape. The chapter 1 of this thesis has shown that such initial size and shape of the Pt nanoparticles could be altered by repetitive BOR characterizations, as will be confirmed in this present chapter. The platinum roughness (*i.e.* the ratio of the electrochemically active to the geometric surface area) is considered as the main variable distinguishing the Pt/VACNF electrodes from one another. Note that the term ‘Pt roughness’ is not strictly accurate as it does not describe a real physical roughness of the Pt/VACNF electrodes, but rather expresses the ratio of the Pt electrochemically active surface area (EASA) per geometric surface area. In that respect, the 10 μm thick VACNF layer enables to study a wide range of Pt roughness depending of the amount of Pt nanoparticles deposited at the VACNF surface. Variables such as the pore diameter, the length and the tortuosity factor of the carbon layer, or the platinum nanoparticle average size and interparticle distance are not considered. In this chapter, it is shown that the use of Pt/VACNF electrode for the borohydride oxidation allows one to shed light on the existence of two different BOR pathways, the interplay of which depends on the electrode potential.

5.1 Characterization of the Pt/VACNF electrodes

The Pt/VACNF electrodes used in this chapter were synthesized in order to yield identical thickness of the VACNF layer (10 μm), Pt particle size (*ca.* 5 nm diameter) and shape (see the dedicated Appendix A for further details on the synthesis of these electrodes). Note that it was checked that the VACNF matrix grown on the Ti rods alone (*i.e.* without the Pt nanoparticles deposited) did not show any activity towards the BOR (see Fig. C.1 in Appendix C). Fig.5.1 displays SEM photographs that were taken right after the catalytic chemical vapor deposition (CCVD) procedure and confirmed the growth of VACNF on the TiO_x rods. The average diameter of the CNF was observed to be *ca.* 50 nm.

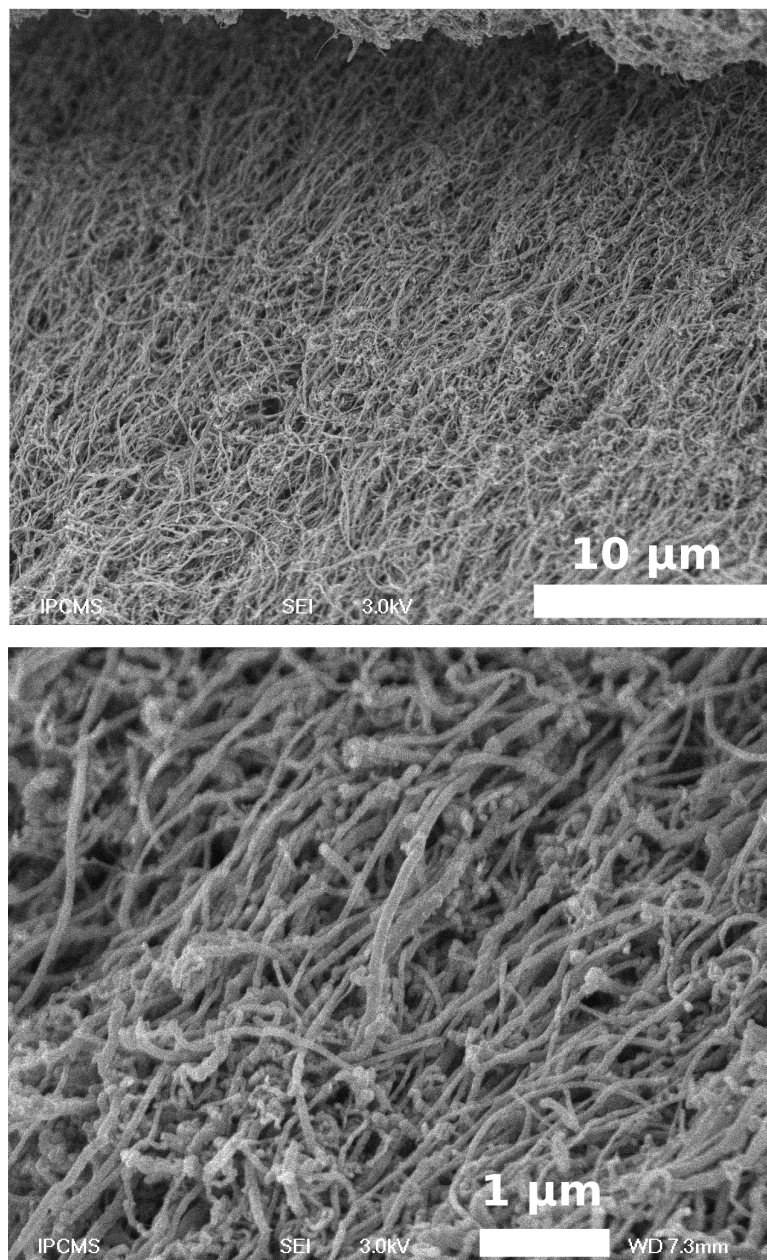


Figure 5.1: SEM images of VACNF grown by CCVD on Ti rod.

Fig.5.2 shows TEM photographs of the Pt/VACNF electrodes. As this operation destroys the integrity of the sample, the TEM images of the Pt/VACNF materials were taken after the electrochemical experiments only (*i.e.* at the 'end-of-life' of the samples). Assuming the severe modifications of the Pt/C electrocatalysts operated in DBFC (see chapter 1), this likely explains the rather large extent of agglomeration of the Pt nanoparticle observed by TEM, particularly for the highest Pt roughness sample ($15 \text{ cm}^2_{\text{Pt EASA}}/\text{cm}^2_{\text{geometric}}$). The average diameter of the isolated Pt nanoparticles (disregarding agglomerates) was observed to be *ca.* 5 nm (*i.e.* similar to the initial value), regardless of the Pt loading at the VACNF. This study does not consider the influence of the number of adjacent active Pt sites, as this variable is not limiting for *ca.* 5 nm diameter Pt nanoparticles, but rather the number of active Pt sites inside the electrode active layer. This variable is directly related to the density of Pt nanoparticles within the VACNF matrix.

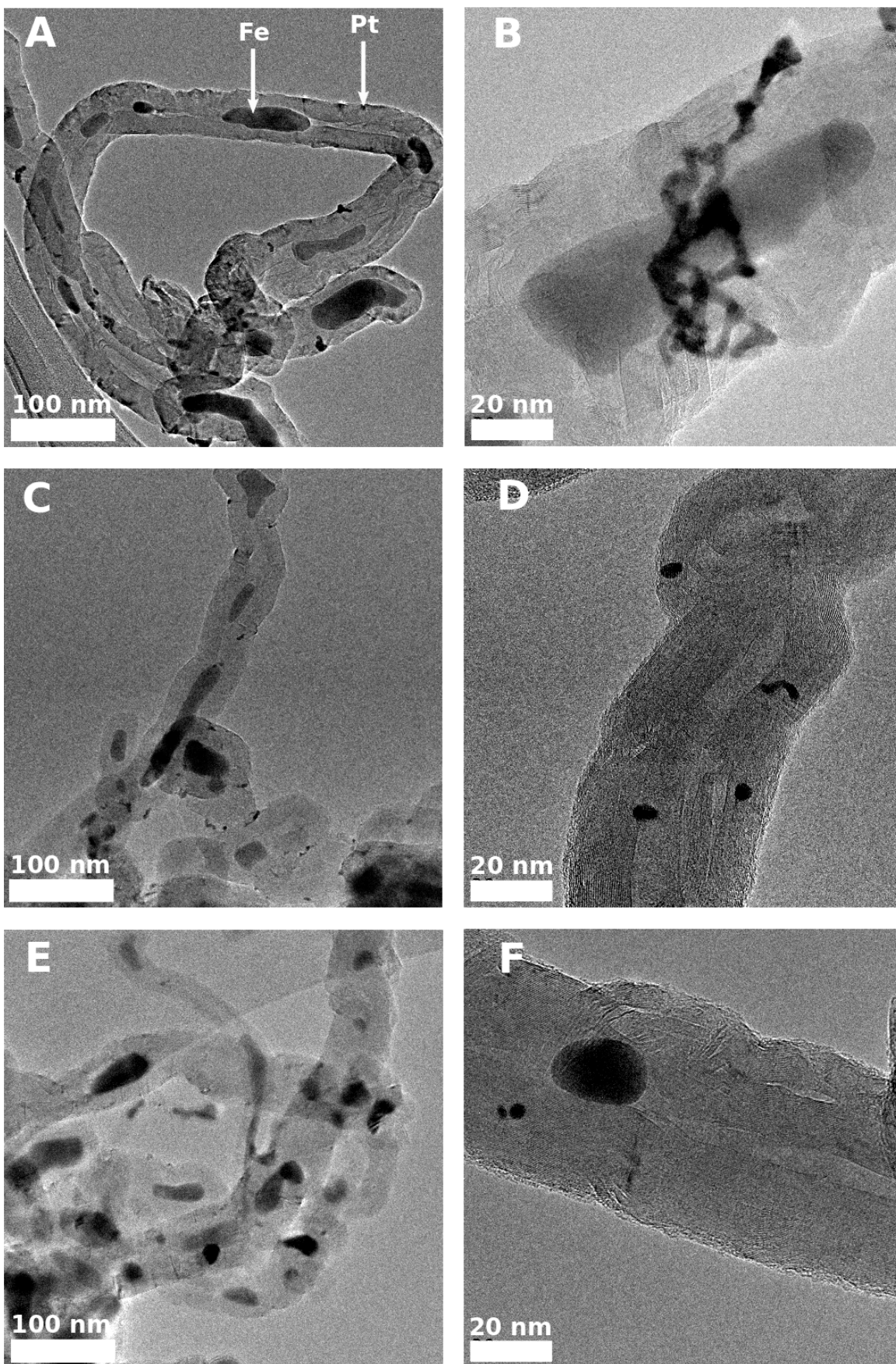


Figure 5.2: TEM image of Pt nanoparticle supported on VACNF grown on TiO_x by CCVD (one can notice Fe particles inside the channel). (A) and (B) : highest Pt roughness ($15 \text{ cm}^2_{\text{Pt EASA}}/\text{cm}^2_{\text{geometric}}$). Note the presence of agglomerated Pt nanoparticle on (B) which can be related to the BOR-induced degradation of the Pt/VACNF materials (see chapter 1). (C) and (D) : intermediate Pt roughness ($4.6 \text{ cm}^2_{\text{Pt EASA}}/\text{cm}^2_{\text{geometric}}$). (E) and (F) : lowest Pt roughness ($0.25 \text{ cm}^2_{\text{Pt EASA}}/\text{cm}^2_{\text{geometric}}$).

The electrochemically active surface area (EASA) of the Pt/VACNF electrodes was calculated by integrating the charge under the CO_{ads} oxidation peak from CO_{ads} -stripping voltammograms performed in 0.1 M sulfuric acid electrolyte. Assuming the coulometry for the desorption of one monolayer of adsorbed CO to be $422 \mu\text{C}\cdot\text{cm}_{\text{Pt}}^{-2}$, which corresponds to two electrons per Pt surface site [187, 196], the EASAs of the two Pt/VACNF electrodes with the higher Pt loadings were calculated based on the CO_{ads} -stripping experiment shown in Fig.5.3. The CO_{ads} -stripping peak for the Pt/VACNF electrode with the lowest Pt loading was not sufficiently well defined for the quantitative determination of its EASA. Thus, the EASA of this electrode was roughly estimated from the volume of Pt colloidal solution deposited on the VACNF matrix, by comparison with that of the two larger Pt loadings. This rough estimation does not affect the conclusions of this work, which are not based on a quantitative fitting of the experimental data, but rather on a qualitative analysis of the RDE voltammogram shape for the borohydride oxidation reaction (BOR) obtained at various Pt roughnesses. The measured and estimated values of Pt EASA and Pt roughness for the Pt/VACNF electrodes are summarized in Table 5.1. For comparison, the Pt roughness of a polycrystalline smooth Pt electrode was measured to be *ca.* 2.5 [129], while the Pt roughness of the Pt/GC model electrode used in chapter 4 was measured to be *ca.* 3.6.

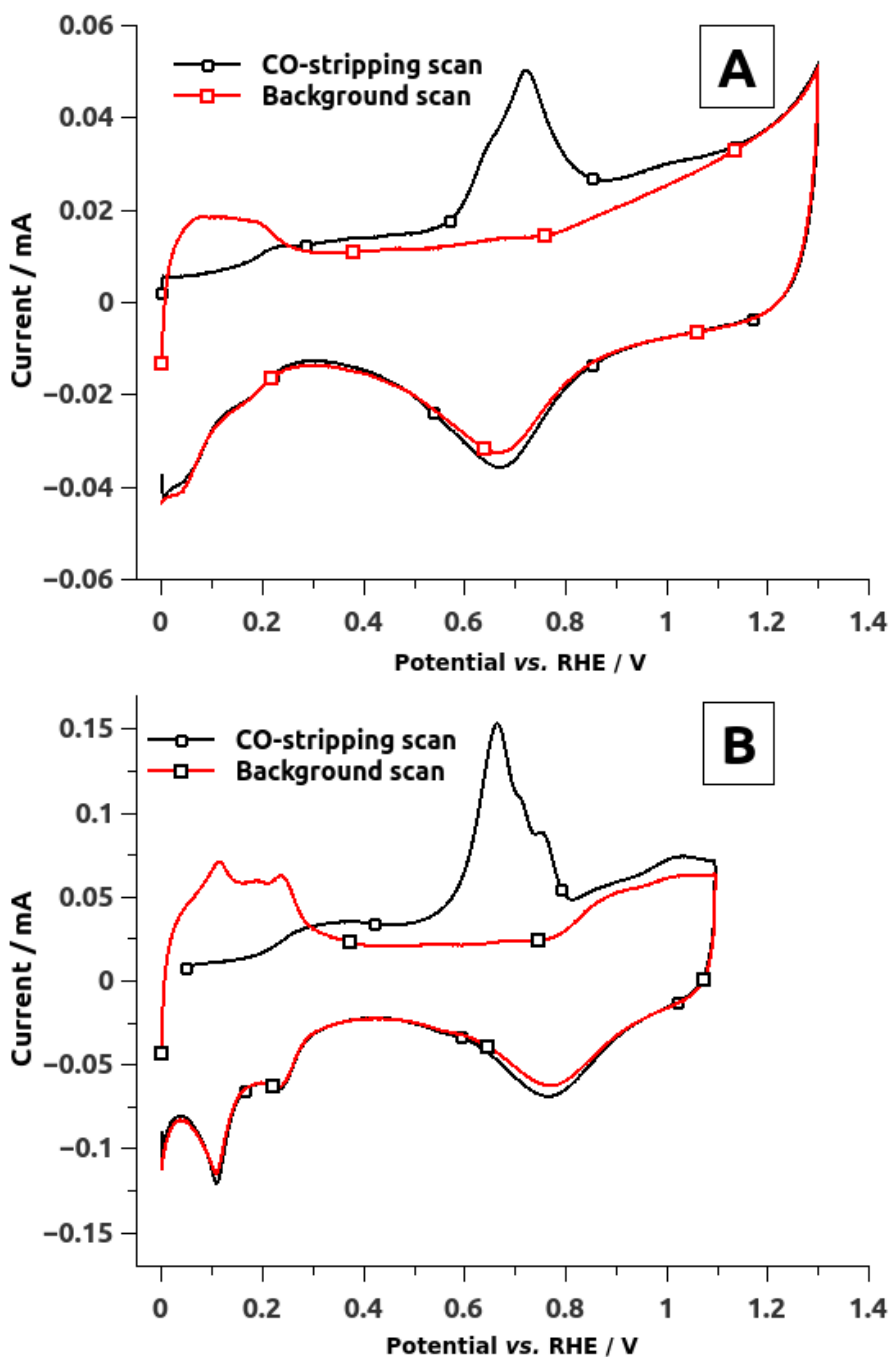


Figure 5.3: Cyclic voltammetry profile in 0.1 M H_2SO_4 and CO_{ads} -stripping voltammogram in the same electrolyte. Sweep rate: $10 \text{ mV}\cdot\text{s}^{-1}$. (A) : Pt/VACNF electrode with intermediate Pt roughness ($4.6 \text{ cm}^2_{\text{Pt EASA}}/\text{cm}^2_{\text{geometric}}$). (B) : Pt/VACNF electrode with the highest Pt roughness ($15 \text{ cm}^2_{\text{Pt EASA}}/\text{cm}^2_{\text{geometric}}$)

In this study, the electrocatalytic properties of the Pt/VACNF and smooth Pt electrodes were found to be strongly affected by their 'Pt roughness' defined as the ratio between $S_{\text{Pt EASA}}$ and $S_{\text{geometric}}$. These values are also presented in Table 5.1. Apart from the EASA determination, the CO_{ads} -stripping voltammograms of Fig.5.3 provide information on the distribution, the extent of agglomeration and the average size of the Pt nanoparticles, these values depending on the potential value(s) of the CO oxidation peak(s) [187]. In agreement with the TEM observations of Fig.5.2, the Pt/VACNF electrode with intermediate Pt roughness displays relatively well-distributed isolated Pt nanoparticles, while agglomerated Pt nanoparticles are

observed for the Pt/VACNF electrode with the highest Pt roughness (note the multiple peaks in Fig.5.3B). Note also that the iron nanoparticles inside the VACNF are not accessible and, therefore, not electrochemically active, as pointed out by the absence of any iron redox current in the voltammograms of the VACNF electrodes (see Fig.5.3).

Table 5.1: Electrochemically active surface area and Pt roughness of Pt/VACNF electrodes. Comparison with smooth Pt [129].

Electrode labeling	Volume of K_2PtCl_4 colloid deposited (μL)	Pt EASA (cm^2)	Pt roughness ($cm^2_{Pt\ EASA}/cm^2_{geometric}$)
Pt/VACNF-15	60	2.9 (measured)	15 (measured)
Pt/VACNF-4.6	20	0.91 (measured)	4.6 (measured)
Pt/VACNF-0.25	1	0.05 (estimated)	0.25 (estimated)
Pt smooth	(-)	(-)	2.5 (measured)

5.2 Electrochemistry of the borohydride oxidation reaction (BOR)

The Au-ring rotating ring-disk electrode (RRDE) setup has already been used by Krishnan *et al.* [140] for BOR studies in order to detect BH_3OH^- intermediates. However, the disk used in the study of Krishnan *et al.* [140] was a smooth Au electrode. The Au-ring enables the specific detection of BH_3OH^- in a NaOH + NaBH₄ electrolyte, as the onset potential of BH_3OH^- electrooxidation on Au is below the onset potential of BH_4^- electrooxidation on Au [52, 197, 198]. The Au-ring used in this study was polarized at +0.2 V *vs.* RHE. At this potential, Au electro-oxidizes BH_3OH^- while it is inactive towards the BH_4^- electrooxidation. To confirm this, RDE voltammograms of a smooth Au electrode in 1 M NaOH and either 10 mM ammonia borane (AB) NH_3BH_3 (assumed to be decomposed into BH_3OH^- and NH_4^+ in strong alkaline media [52]) or 10 mM NaBH₄ are compared in Fig.5.4 and validates the choice of the +0.2 V *vs.* RHE as the Au-ring potential for the specific detection of BH_3OH^- .

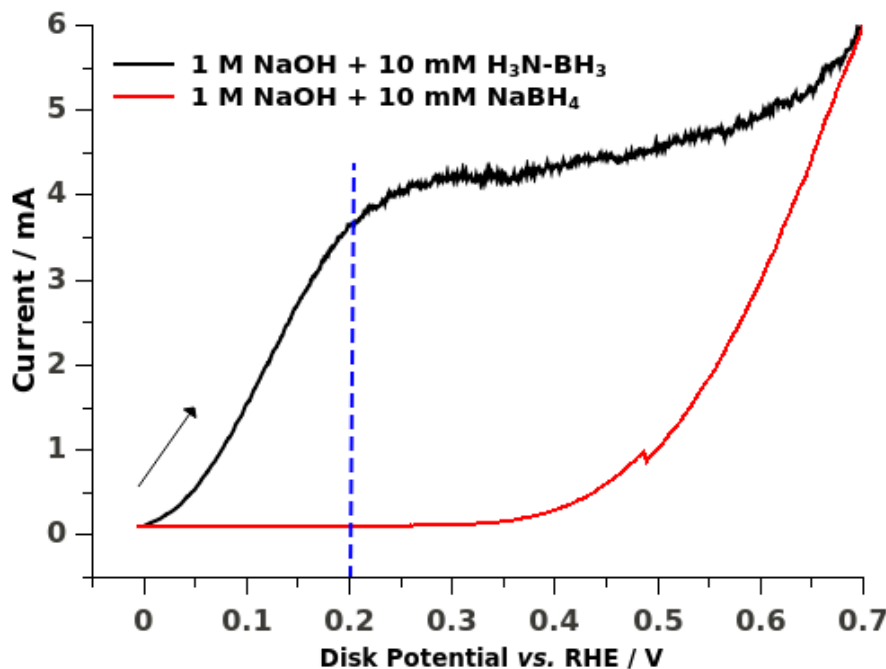


Figure 5.4: Smooth Au RDE voltammograms of 10 mM NaBH₄ or 10 mM H₃NBH₃ in 1 M NaOH at 20 mV s⁻¹ and 1000 rpm (positive-going scan). At the potential +0.2 V *vs.* RHE, only BH₃OH⁻ is electrooxidized at smooth Au.

One of the experimental difficulties encountered during the RRDE studies of the BOR is the formation of gas bubbles (H₂ in the case of the BOR on Pt or Au [141]) that can get stuck between the disk and the ring, shielding the ring signal. Photographs of such bubbles are displayed in Fig.5.5 along with the ring current detected as a function of time; they show that the ring signal is noisy due to uncontrolled ring shielding when H₂ bubbles detach from the disk and come into close proximity of the ring. Thus, the author considered difficult to attempt any quantitative calculations of the faradaic current yield from the RRDE data on this system. Note that the Au-ring current signals presented in Fig.5.6 (relative to the various Pt/VACNF disks and Au ring RRDE) have been baseline-corrected for a better comparison. The raw (non-baseline-corrected) Au-ring RRDE data can be found in the Appendix C as Fig.C.2.

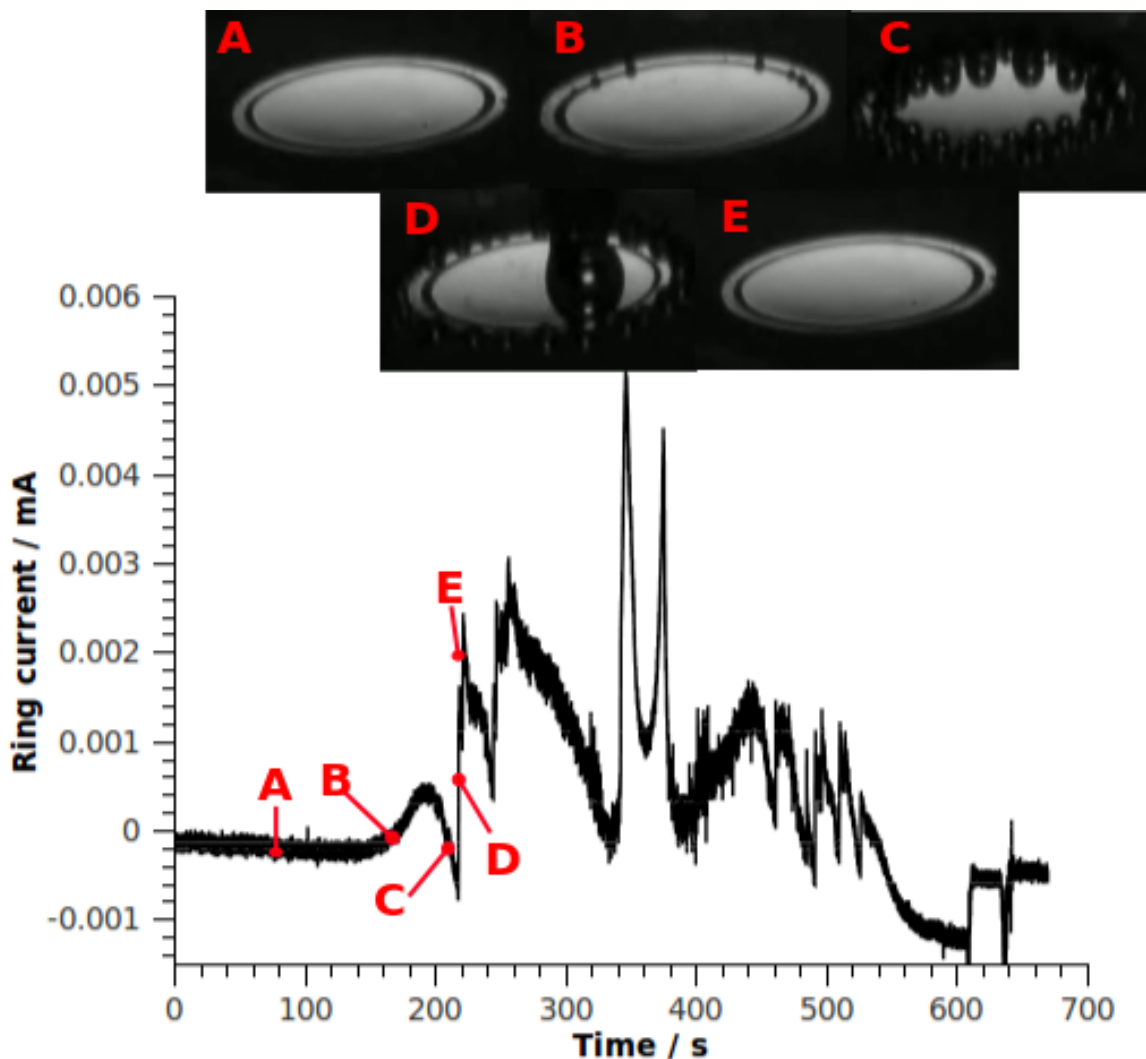


Figure 5.5: Photographs of a Au-ring Au-disk rotating ring-disk electrode (RRDE) in 10 mM NaBH_4 + 1 M NaOH at 1000 rpm. The Au disk is swept between 0 and 1.5 V *vs.* RHE (not shown in this figure) while the Au-ring is held at +0.2 V *vs.* RHE for the detection of BH_3OH^- released by the disk. These photographs show the influence of the bubble interferences on the ring signal, by shielding the electrolyte flow between the disk and the ring (B and C). This shielding transiently stops when the amount of bubble is high enough to trigger their agglomeration (D) and so, leave the RRDE surface (E).

Two distinct potential regions can be observed in the Au-RRDE voltammograms of the BOR shown in Fig.5.6. No BH_3OH^- is detected at the Au ring in the low potential region from 0 to 0.6 V *vs.* RHE, while BH_3OH^- is observed in the high potential region from 0.6 to 1.4 V *vs.* RHE. Furthermore, one may clearly see that the amount of BH_3OH^- detected at the ring increases with the decrease of Pt roughness. The disk currents are also strongly affected by the Pt roughness, and thus by the amount of available Pt surface sites. For Pt/VACNF-0.25 (with the lowest Pt roughness), the BOR current at the disk is observed in the high potential region only, *i.e.* above *ca.* 0.6 V *vs.* RHE, and reaches the mass-transfer-limited value at *ca.* 1.0 V *vs.* RHE. Increasing the Pt roughness results in (i) the emergence of non-negligible BOR currents in the low potential region (below 0.6 V *vs.* RHE), and (ii) the negative shift of the BOR onset potential. Please note that the reverse negative-going voltammetric scans are shown in the dedicated Appendix C of this thesis, as Fig.C.4.

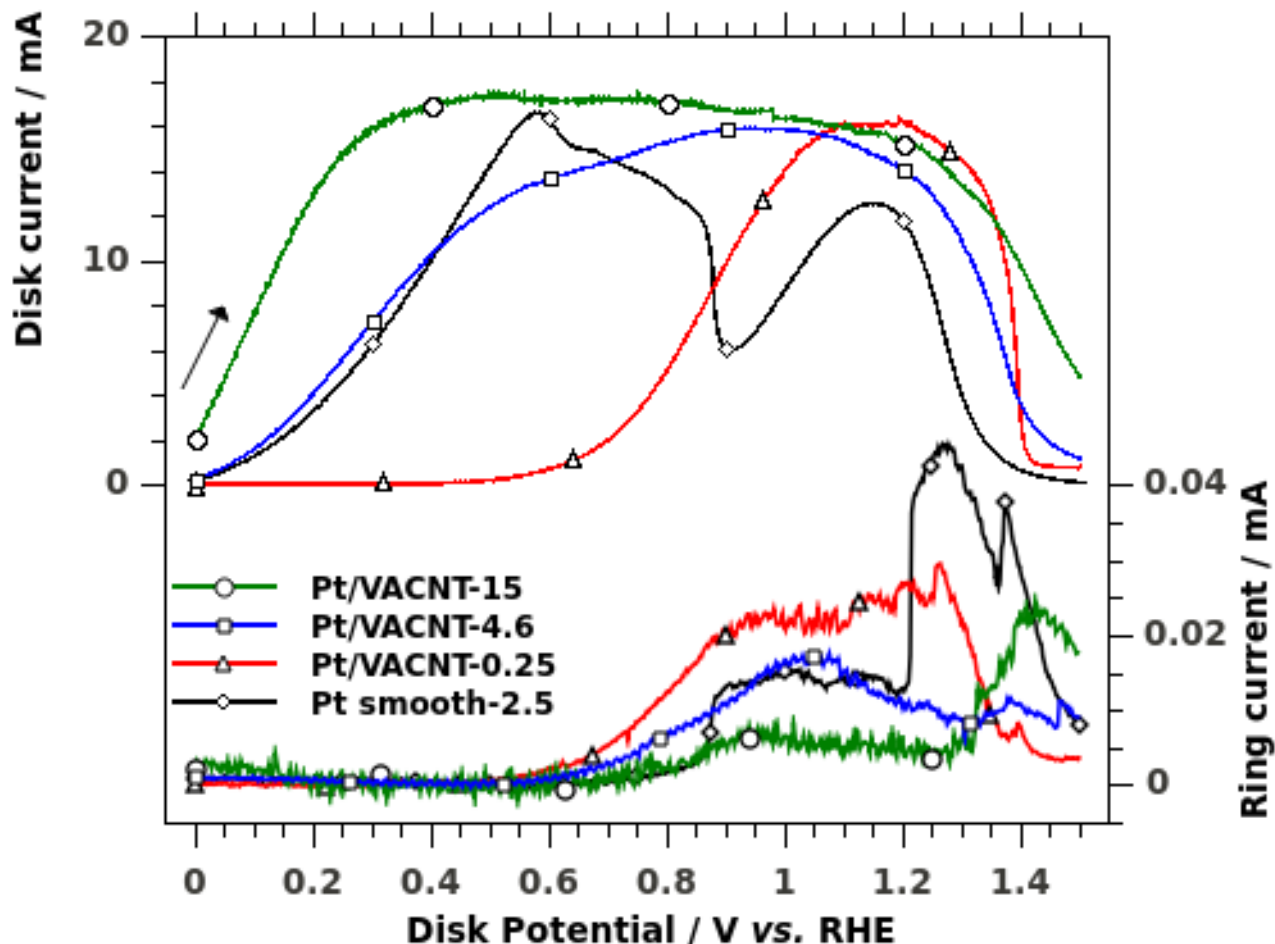
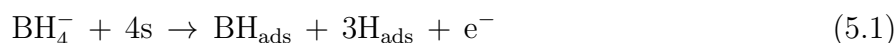


Figure 5.6: Influence of the Pt roughness on the BOR. RRDE voltammograms of 10 mM NaBH_4 in 1 M NaOH at 25 mV s^{-1} and 2500 rpm (positive-going scan). The disk was composed of the different samples described in the legend and was swept between 0 and 1.5 V *vs.* RHE, while the Au-ring was held at +0.2 V *vs.* RHE to detect BH_3OH^- intermediates. Legend: Electrode type-X, X being the Pt roughness of the electrode, in $\text{cm}^2_{\text{Pt EASA}}/\text{cm}^2_{\text{geometric}}$. Note that the Au-ring current signals were baseline-corrected to ease the comparison between the various electrodes, the raw Au-ring RRDE data can be found in the Appendix C as Fig.C.2.

The experimental observations suggest that, in agreement with the previous chapters of the second part of this thesis, the BOR follows different pathways in the 'low' and the 'high'-electrode potential regions and that these pathways require different numbers of available Pt surface sites. While the 'low-potential BOR' is highly demanding in number of free Pt sites, the 'high-potential BOR' is possible even on the electrode with a very small number of available Pt sites. Armed with these experimental observations and considering the previous chapters of this thesis, as well as the literature data, the following mechanism of the BOR on Pt was proposed.

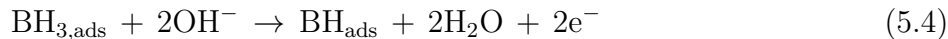
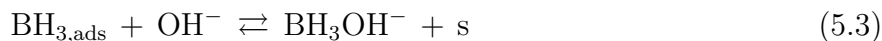
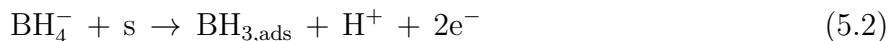
Below 0.6 V *vs.* RHE, the fully dissociative adsorption of BH_4^- is the key reaction step for the 'low-potential BOR' on Pt, as detailed in Eq.5.1 and in agreement with both DFT calculations [190] and with the discussion made in the chapter 4 of this thesis:



This fully dissociative BH_4^- adsorption reaction (Eq.5.1) is highly demanding in free Pt sites. Furthermore, the BH_{ads} species produced react slowly with OH^- species in solution (which would correspond to an Eley-Rideal-type mechanism) and tend to block the active Pt surface. In the case of the Pt/VACNF electrode with the lowest Pt roughness (Pt/VACNF-0.25), the number of active Pt sites is low, and therefore the dissociative adsorption of BH_4^- almost completely blocks the surface sites, leading to negligible BOR currents at $E < 0.6$ V *vs.* RHE under near-steady-state conditions (see Fig.5.6). On the contrary when the Pt loading is high, even if the BH_{ads} oxidation reaction is slow, a sufficient number of free Pt sites remains available for more BH_4^- to adsorb and dissociate on the Pt surface, leading to high disk currents at low potential under near-steady-state conditions (Fig.5.6). Of course, the value of Pt roughness that separates the 'blocked case' from the 'active case' described above depends on the actual concentration in sodium borohydride in solution. The present observations are therefore valid for a sodium borohydride concentration of 10 mM, but the author expects different behaviors for higher concentrations, as further discussed in the following chapter 6 of this thesis.

This is in agreement with the observations and the discussion of chapter 4, where the poisoning of the Pt surface at low potential was attributed to the site-blocking effect caused by the stable BH_{ads} (stable meaning both favorable to form and not favorable to remove). Assuming that the removal of BH_{ads} from the Pt surface by a Eley-Rideal-type reaction with OH^- is the limiting step of the BOR at low potential, it would account for the structure-sensitivity of the BOR at low potential observed among the three Pt basal planes single crystal electrodes in chapter 3. Indeed, different Pt structures lead to different values of BH_{ads} binding energies with the Pt sites. Following this reasoning, it is expected that BH_{ads} is more stable on Pt(111) than Pt(110) and Pt(100), leading to a lower BOR activity at low potential for Pt(111).

Above 0.6 V *vs.* RHE, the detection of BH_3OH^- released enables considering $\text{BH}_{3,\text{ads}}$ as one of the possible adsorbed species coming from the incomplete dissociative adsorption of BH_4^- (Eq.5.2). This incomplete dissociative adsorption of BH_4^- into $\text{BH}_{3,\text{ads}}$ is less demanding in free Pt site than the complete dissociative adsorption of BH_4^- in BH_{ads} . $\text{BH}_{3,\text{ads}}$ can either desorb as BH_3OH^- (Eq.5.3), undergo further dissociation to form $\text{BH}_{\text{ads}} + 2 \text{H}_{\text{ads}}$ if enough active Pt site are available, or react in an Eley-Rideal-type reaction with OH^- to form BH_{ads} (Eq.5.4). The 'switching' between the $\text{BH}_{3,\text{ads}}$ and BH_{ads} -mediated BOR depends on the number of available Pt sites.



The incomplete dissociative adsorption of BH_4^- into $\text{BH}_{3,\text{ads}}$ is favored when the number of free Pt sites is not sufficient to fully dissociate BH_4^- into BH_{ads} . Furthermore, there is also an increased probability for the readsorption of reaction intermediates such as BH_3OH^- or H_2 when the Pt active site density is high. Both facts explain that the amount of BH_3OH^-

detected at the Au-ring in Fig.5.6 increases with the decrease of Pt roughness. It should be mentioned that no H_2 gas release has been experimentally observed from the Pt/VACNF electrode with the lowest Pt roughness (Pt/VACNF-0.25) at low potential, while H_2 bubbling was observed at higher potentials when oxidation current was measured (bubbling accountable for the noisy Au-ring signal of Fig.5.6). Thus, the possibility of the H_2 escape or shielding explaining the absence of faradaic current for Pt/VACNF-0.25 at low potential has been ruled out.

The increase of the ring currents (and so the appearance of BH_3OH^- escape from the disk electrodes) for the Pt/VACNF and the smooth Pt electrodes at high potential can be explained by the adsorption of hydroxyl species on the Pt surface. The adsorption of OH^- on Pt occurs above *ca.* 0.65 V *vs.* RHE and accounts for the pseudo-capacitive current observed on the voltammograms of the polycrystalline Pt electrode (Fig.3.1) and Pt/VACNF-25 electrode (Fig.C.3 in Appendix C) in NaOH supporting electrolyte. As already stated in the chapters 3 and 4 of this thesis, the influence of the OH^- adsorption on the BOR may be dual. The first possible effect of OH_{ads} species is detrimental: the partial blocking the Pt active surface. This is observed by the decrease of the electrooxidation current in Fig.5.6 for the smooth Pt electrode starting from 0.6 V *vs.* RHE. This partial blocking of the Pt surface by OH_{ads} favors the BH_4^- incomplete dissociative adsorption into $\text{BH}_{3,\text{ads}}$ and the associated release of BH_3OH^- . The second possible effect of OH_{ads} is advantageous: it promotes a Langmuir-Hinshelwood-type electrooxidation reaction of BH_{ads} . In the latter case, this potential-dependent process enables the BOR to proceed, even when the number of Pt active sites is not sufficient to valorize the complete BH_4^- dissociative adsorption below 0.6 V *vs.* RHE. This behavior is observed in Fig.5.6: the electrode with the lowest Pt roughness (Pt/VACNF-0.25) yields non-negligible electrooxidation current only for $E > 0.6$ V *vs.* RHE. Such Langmuir-Hinshelwood-type electrooxidation reaction also accounts for the second oxidation wave on smooth Pt above 0.9 V *vs.* RHE, observed after a first partial blocking of the Pt surface by OH_{ads} . This step is also important since it allows consuming the OH_{ads} species that would totally block the Pt surface at high potentials. The influence of poisoning by OH_{ads} species is not observed for the electrode with the highest Pt roughness (Pt/VACNF-15), due to the large amount of available Pt site. The Pt/VACNF-4.6 electrode displays an intermediate behavior, as this electrode exhibits electrooxidation current for $E < 0.6$ V *vs.* RHE, but yields lower faradaic current values than the Pt/VACNF-15 electrode. The adsorption of OH^- induces the second oxidation wave at 0.6 V *vs.* RHE on the Pt/VACNF-4.6 BOR voltammogram in Fig.5.6. A second peak in the BH_3OH^- detection signal is observed for every electrode when the Pt surface is further blocked for $E > 1.2$ V *vs.* RHE by either Pt oxides with higher valence or boron oxides [149, 199]. This reinforces the proposition that BH_3OH^- is released from the incomplete dissociation of BH_4^- into $\text{BH}_{3,\text{ads}}$, this incomplete dissociation being favored on partially blocked Pt surfaces. Obviously, a Pt surface fully blocked does not release any BH_3OH^- , as this latter surface is not active for the BOR anymore. Indeed, neither BOR current nor BH_3OH^- release is monitored on the fully blocked Pt surfaces at 1.5 V *vs.* RHE in Fig.5.6.

The idea of a BOR mechanism depending on (i) the ability of the surface to dissociatively adsorb BH_4^- and (ii) the state of the surface (Pt surface hydride (H_{ads}) or oxides), is consistent with the studies of Gyenge *et al.* [165] as well as Dong *et al.* [168]. These studies highlighted the inhibition of the low-potential BOR pathway on Pt when thiourea (TU) is added in the electrolyte. Fig. 5.7 shows cyclic voltammograms of a Pt smooth microelectrode either in KOH + KBH_4 (Fig. 5.7A) or in KOH + KBH_4 + TU (Fig. 5.7B): the addition of TU led to the loss of BOR activity for the Pt electrode at low potential (below *ca.* 0.4 V *vs.* RHE, or *ca.* -0.6 V *vs.* HgO/Hg in the experimental conditions of Fig. 5.7). As TU is known to poison the active Pt site for the H adsorption [200], the complete dissociative adsorption of BH_4^- into BH_{ads} (Eq.5.1)

cannot proceed as this reaction needs at least 3 contiguous available Pt site for H_{ads} . The BOR behavior on a TU-poisoned Pt surface is somewhat similar to the BOR proceeding on the lowest Pt roughness Pt/VACNF electrode in this chapter (and also to the BOR proceeding on bulk polycrystalline Au surface, as seen in Fig.6.9).

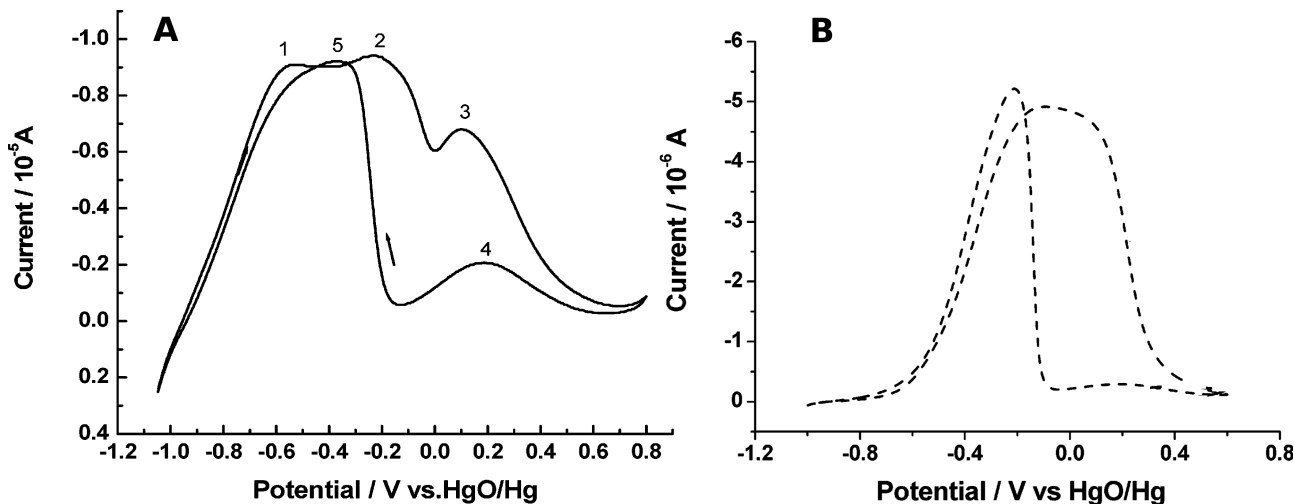


Figure 5.7: Cyclic voltammograms of a smooth Pt microelectrode in (A): 1 mol/L of KOH solution containing 0.5 g of KBH_4 at $50 \text{ mV}\cdot\text{s}^{-1}$ and in (B): 1 mol/L of KOH solution containing 0.5 g of KBH_4 and 0.01 g of TU at $10 \text{ mV}\cdot\text{s}^{-1}$ Reproduced from Ref. [168] with permission from the American Chemical Society.

The proposed BOR mechanism concurs with the first steps proposed by Lam *et al.* [170]. They used the electrochemical quartz crystal microbalance system to study the BOR on Pt and proposed that the complete dissociative adsorption of BH_4^- into $BH_{ads} + 3H_{ads}$ occurred on the Pt surface without TU. The addition of TU reduced the number of available Pt sites and thus favored the formation of $BH_{3,ads}$, less demanding in available Pt sites. In that case, non-negligible electrooxidation current were observed only when the electrode activated water (formation of OH_{ads}), *i.e.* for potential values above *ca.* 0.4 - 0.5 V *vs.* RHE.

As already stated in the previous chapter 4 of this thesis, this tentative BOR mechanism also agrees with the conclusions of Sison Escaño *et al.* [201] and Rostamikia *et al.* [190, 202, 203] relative to DFT calculations on Pt(111) surface. They concluded that when the number of adjacent available Pt sites is not limiting, the complete dissociation of BH_4^- into $BH_{ads} + 3H_{ads}$ is the main reaction on Pt at every potential of study (see Fig.4.6). Rostamikia *et al.* [190] concluded that the formation of $BH_{3,ads}$ is normally not favorable but can be considered if the number of available adjacent Pt sites becomes limiting. They calculated that $BH_{3,ads}$ is unstable, leading to either BH_3OH^- formation in solution or further dissociation.

Finkelstein *et al.* [130] performed a complete study of BH_4^- and dimethylamine borane (DMAB) oxidation reaction on bulk polycrystalline Pt and Au RDE. They reported two types of direct BH_4^- oxidation: the low-potential direct BH_4^- electrooxidation produces more electrons than the high-potential direct BH_4^- electrooxidation. This result is consistent with the BOR mechanism proposed in the present work. Indeed, as soon as the catalyst is structurally capable to fully dissociate BH_4^- and if a sufficient number of catalytic sites is available, the reaction described in Eq.5.1 proceeds. Assuming that BH_{ads} and H_{ads} are oxidized on Pt at these low potential values, the complete (on a faradaic efficiency basis) electrooxidation of

BH_4^- can be achieved. Finkelstein *et al.* [130] also assumed that the high-potential BH_4^- direct electrooxidation occurs on a Pt surface partially covered by OH_{ads} , and the overall reaction at high-potential releases BH_3OH^- and H_2 bubbles. The observation of BH_3OH^- released in solution at high potential is confirmed by the Au-ring RRDE results. H_2 bubbles were also visually observed at the surface of smooth Pt and Pt/VACNF electrodes at high potential values. The release of gaseous hydrogen was also confirmed by Lima and coworkers [139, 141] *via* differential electrochemical mass-spectrometry study of H_2 performed during the BOR voltammetry at the Pt/C electrode (see Fig.2.9). These observations are consistent with an incomplete dissociative adsorption of BH_4^- on the partially OH_{ads} -covered Pt surface at high potential. As $\text{BH}_{3,\text{ads}}$ is in equilibrium with BH_3OH^- and is not very stable on the Pt surface [190], $\text{BH}_{3,\text{ads}}$ could undergo subsequent hydrolysis upon formation, explaining the observation of H_2 bubbles. However, the H_2 formation by hydrolysis reaction during the BOR has not been considered yet in the mechanism and modelling of the reaction: it is part of further development of the model, as discussed in the chapter 6 of this thesis.

Finkelstein *et al.* [58, 130] assumed that BH_3OH^- may adsorb and poison the Pt surface during the 'low-potential BOR'. However, a platinum ring was used during their RRDE study of the BOR on Pt, so that they could not specifically detect BH_3OH^- released in solution by the smooth Pt disk depending of its potential. Actually, the results of Fig.5.6 demonstrate the absence of quantitative signal of BH_3OH^- detected at the Au-ring at low potential, regardless of the nature of the Pt-based disk employed. It seems unlikely to the author, as well as to Lam *et al.* [170], that BH_3OH^- would be formed during the 'low-potential BOR' where the complete dissociation of BH_4^- is predominant. BH_3OH^- is detected only when residence-time of $\text{BH}_{3,\text{ads}}$ on the Pt surface is significant, *i.e.* when the OH_{ads} non-negligible coverage at Pt favors the incomplete dissociative adsorption of BH_4^- into $\text{BH}_{3,\text{ads}}$. The conclusion of a poisoning by BH_3OH^- made by Finkelstein *et al.* [130] comes from their study of the DMAB oxidation on Pt. This DMAB is supposed to dissociate into BH_3OH^- in solution. However, we suspect that the absence of electrooxidation current is more likely due to the chemistry of DMAB rather than to the oxidation reaction of BH_3OH^- . It is possible that products of the dissociation of DMAB (e.g. the DMA fragment) inhibit the activity of Pt at low potential. As already stated in the chapter 4 of this thesis, we rather likely suspect BH_{ads} to be stable on the Pt surface, ultimately blocking the Pt surface until incursion at more positive potential and adsorption of OH^- that would clean the Pt surface from BH_{ads} in a Langmuir-Hinshelwood-type pathway. The poisoning of the Pt surface by impurities inherent to the use of alkaline electrolyte must also be considered although, in the present thesis, experiments were conducted with great care to limit this issue.

5.3 Conclusions

The use of Pt/VACNF model electrodes enabled to study the influence of the density of Pt sites towards the BOR. Pt/VACNF electrodes as well as a polycrystalline smooth Pt electrode were inserted in a Au-ring rotating ring-disk electrode (RRDE) setup, in order to detect the BH_3OH^- escape from the disk electrodes. The experimental observations were as follows:

- At low potential (between the onset of the BOR and *ca.* 0.65 V *vs.* RHE), no BH_3OH^- escape was detected, and the BOR is sensitive to the density of Pt sites: no quantitative BOR current was observed when the density of Pt sites was too low;
- At high potential (between 0.65 V and 1.2 V *vs.* RHE), BH_3OH^- escape was detected

and the amount of BH_3OH^- detected increased with lower density of Pt sites. The BOR was not sensitive to the density of Pt sites, as quantitative BOR current was observed whatever its value.

From these observations, gathered with the findings of the previous chapters 3 and 4 of this thesis, as well as previous findings from the literature, a tentative BOR mechanism is proposed. In this mechanism, the fully dissociative adsorption of BH_4^- into BH_{ads} is the first main step of the BOR (Eq.5.1). However, BH_{ads} is relatively stable on the Pt surface, so that its removal is the limiting reaction step of the BOR. At low potential, a sufficient density of Pt sites is needed in order to achieve quantitative BOR current. Otherwise, the whole Pt surface is blocked by BH_{ads} . When the electrode potential enables the adsorption of hydroxyl species (around 0.65 V *vs.* RHE), the removal of BH_{ads} is enhanced through a Langmuir-Hinshelwood-type electrooxidation with OH_{ads} , so that the BOR is not sensitive anymore towards the density of Pt sites at these potentials. However, OH_{ads} can possibly bear an opposite detrimental effect, as this adsorbed species is also site-blocking. The partial blocking of the Pt surface by OH_{ads} leads to an incomplete dissociative adsorption of BH_4^- into $\text{BH}_{3,\text{ads}}$ (Eq.5.2), explaining the detection of BH_3OH^- escape at these potentials (Eq.5.3). This tentative mechanism is further developed in the following chapter 6, where its numerical modelling is attempted.

Chapter 6

Modelling of the BOR on Pt

In this chapter, a tentative BOR mechanism, presented in Fig.6.1, summarizes the main ideas discussed in the previous chapters 3, 4 and 5. This mechanism is used in a mean-field microkinetics model, and the corresponding simulated curves are compared with the experimental results obtained in the chapter 5 of this thesis.

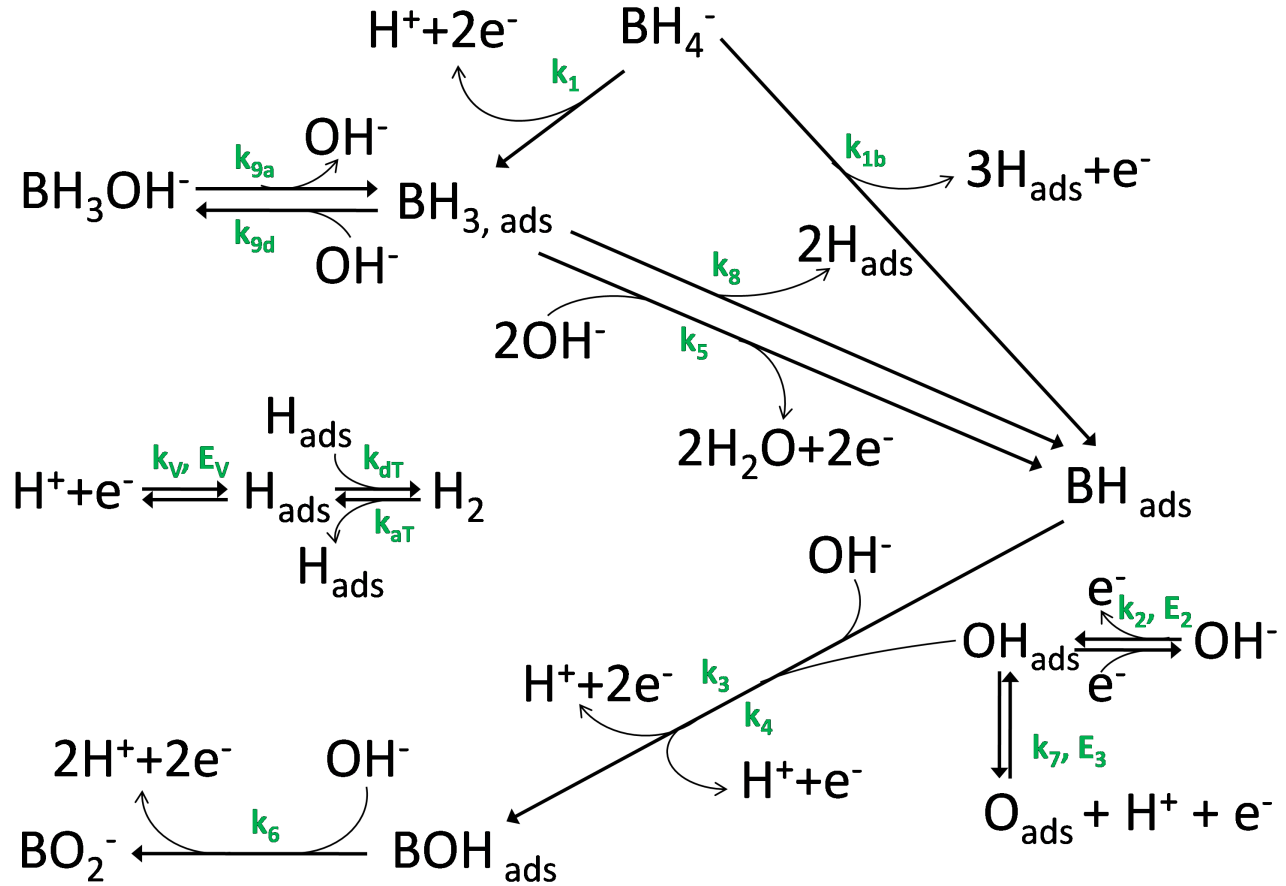


Figure 6.1: Tentative BOR mechanism: the BOR starts at low potential by the fast fully dissociative adsorption of BH_4^- into BH_{ads} (k_{1b}), but this step requires large availability of the Pt surface. Furthermore, BH_{ads} is relatively stable and possibly blocks the Pt surface: the Eley-Rideal type reaction of BH_{ads} with OH^- (k_3) is slow. At higher potential, where OH_{ads} formation on the Pt surface occurs (k_2), BH_{ads} can react with OH_{ads} in a Langmuir-Hinshelwood type reaction (k_4) overall yielding the final product of the BOR: BO_2^- (k_6). The Pt surface can be ultimately blocked by the Pt-oxide formation, modelled here by the formation of O_{ads} (k_7). Another pathway involves the partial dissociative adsorption of BH_4^- into $\text{BH}_{3,\text{ads}}$ (k_1), less favourable than the fully dissociative adsorption (k_{1b}), but less demanding in free Pt active sites. $\text{BH}_{3,\text{ads}}$ can (i) react with OH^- (k_5), (ii) further dissociate into BH_{ads} (k_8) or (iii) desorb in the form of BH_3OH^- (k_9). In addition, the Pt surface is also active for the HER/HOR, the H_{ads} species being formed either from (i) water decomposition (k_{v}), (ii) BH_4^- dissociative adsorption (k_{1b} and k_8) or (iii) H_2 dissociative adsorption (k_{aT}).

6.1 Construction and variables of the model

The equivalent cell circuit of the electrochemical cell is a double-layer capacitance, C , in parallel with the faradaic impedance Z_f , the whole in series with an external resistance, Re (see Fig. 6.2).

The absolute current going through the external resistance and measured by the potentiostat (I) is the sum of the electrical double layer current (I_{dl}) and the faradaic current (I_f), as written in Eq.6.1.

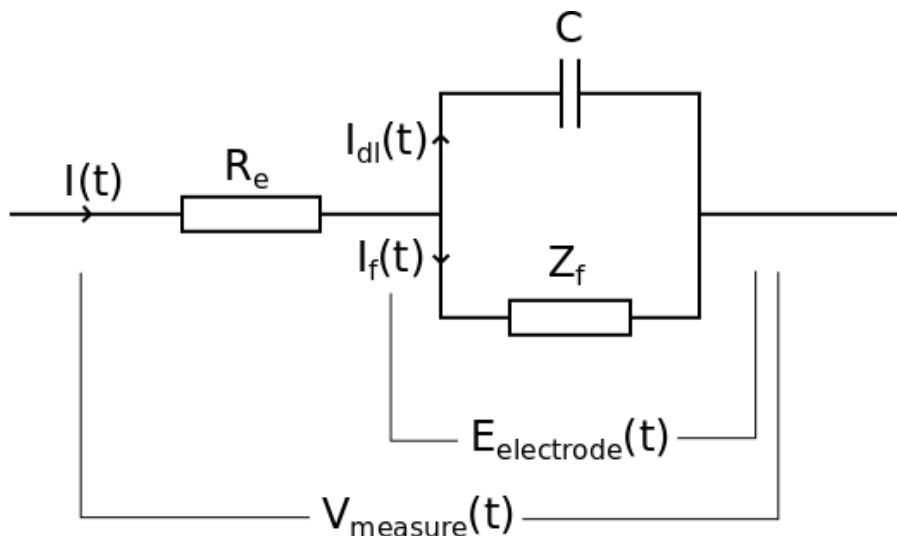


Figure 6.2: General electric equivalent cell circuit of the electrochemical cell.

$$I(t) = I_{dl}(t) + I_f(t) \quad (6.1)$$

The voltage across the whole equivalent circuit is equal to the potential measured by the potentiostat, V_{measure} (within a constant that depends on the chosen reference electrode, RHE in this study). The voltage between the double-layer capacitance and the faradaic impedance is the electrode potential ($E_{\text{electrode}}$). The derivative form of the capacitor equation gives Eq.6.2:

$$I_{dl}(t) = C \frac{dE_{\text{electrode}}(t)}{dt} \quad (6.2)$$

Using the Ohm's law, the measured current going through the external resistance is expressed as (Eq.6.3):

$$I(t) = \frac{V_{\text{measure}}(t) - E_{\text{electrode}}(t)}{R_e} \quad (6.3)$$

From Eq.6.1, Eq.6.2 and Eq.6.3 comes the differential equation on $E_{\text{electrode}}$ (Eq.6.4):

$$\frac{dE_{\text{electrode}}(t)}{dt} = \frac{V_{\text{measure}}(t) - E_{\text{electrode}}(t)}{R_e C} - \frac{I_f(t)}{C} \quad (6.4)$$

The input variable during the cyclic voltammetry is the applied (and measured) potential, V_{measure} (Eq.6.5):

$$\frac{dV_{\text{measure}}(t)}{dt} = \text{scan rate} \quad (6.5)$$

In order to express the interfacial concentrations (c_0) of the different species present in solution, it was assumed that the concentration profiles of every species in solution are linear, with a constant diffusion thickness (δ). The development of this assumption can be found elsewhere [204]. The Appendix D is dedicated to the discussion of this assumption. θ_X is the coverage fraction of the adsorbed species X on the Pt surface. α_i are the charge transfer coefficients for the electrochemical reaction steps. The other constants used in the following equations are defined in Table 6.1.

$$\frac{dc_{\text{H}_2,0}(t)}{dt} = \frac{2D_{\text{H}_2}}{\delta_{\text{H}_2}^2}(c_{\text{H}_2,\text{bulk}} - c_{\text{H}_2,0}(t)) - \frac{2}{\delta_{\text{H}_2}}c_{\text{H}_2,0}(t)\Gamma\theta_s^2(t)k_{\text{aT}} + \frac{2}{\delta_{\text{H}_2}}k_{\text{dT}}\Gamma\theta_{\text{H}}^2(t) \quad (6.6)$$

$$\begin{aligned} \frac{dc_{\text{BH}_4^-,0}(t)}{dt} = & \frac{2D_{\text{BH}_4^-}}{\delta_{\text{BH}_4^-}^2}(c_{\text{BH}_4^-,\text{bulk}} - c_{\text{BH}_4^-,0}(t)) \\ & - \frac{2}{\delta_{\text{BH}_4^-}}c_{\text{BH}_4^-,0}(t)\Gamma\theta_s^4(t)k_{1\text{b}}\exp\left(\frac{\alpha_{1\text{b}}FE_{\text{electrode}}(t)}{RT}\right) \\ & - \frac{2}{\delta_{\text{BH}_4^-}}c_{\text{BH}_4^-,0}(t)\Gamma\theta_s(t)k_1\exp\left(\frac{\alpha_1FE_{\text{electrode}}(t)}{RT}\right) \end{aligned} \quad (6.7)$$

$$\begin{aligned} \frac{dc_{\text{BH}_3\text{OH}^-,0}(t)}{dt} = & \frac{2D_{\text{BH}_3\text{OH}^-}}{\delta_{\text{BH}_3\text{OH}^-}^2}(c_{\text{BH}_3\text{OH}^-,\text{bulk}} - c_{\text{BH}_3\text{OH}^-,0}(t)) \\ & - \frac{2}{\delta_{\text{BH}_3\text{OH}^-}}c_{\text{BH}_3\text{OH}^-,0}(t)\Gamma\theta_s(t)k_{9\text{a}} \\ & + \frac{2}{\delta_{\text{BH}_3\text{OH}^-}}\Gamma\theta_{\text{BH}_3}(t)k_{9\text{d}} \end{aligned} \quad (6.8)$$

The expression of the diffusion layer thickness for the species 'x' in solution is given by the Levich equation for the RDE setup (Eq.6.9), for the expression of δ in cm:

$$\delta_x = 1.61 D_x^{\frac{1}{3}} v^{\frac{1}{6}} \left(\frac{2\pi}{60} \Omega\right)^{-\frac{1}{2}} \quad (6.9)$$

The rate equations of the reactions involved in the proposed BOR mechanism can be formulated as:

$$v_{\text{Tafel}}(t) = k_{\text{aT}}c_{\text{H}_2,0}(t)\Gamma\theta_s^2(t) - k_{\text{dT}}\Gamma\theta_{\text{H}}^2(t) \quad (6.10)$$

$$v_{\text{Volmer}}(t) = k_V \Gamma \theta_s(t) \exp\left(-\frac{\alpha_V F (E_{\text{electrode}}(t) - E_V)}{RT}\right) - k_V \Gamma \theta_H(t) \exp\left(\frac{\alpha_V F (E_{\text{electrode}}(t) - E_V)}{RT}\right) \quad (6.11)$$

$$v_1(t) = k_1 \Gamma \theta_s(t) c_{\text{BH}_4^-,0}(t) \exp\left(\frac{\alpha_1 F E_{\text{electrode}}(t)}{RT}\right) \quad (6.12)$$

$$v_{1b}(t) = k_{1b} \Gamma \theta_s(t)^4 c_{\text{BH}_4^-,0}(t) \exp\left(\frac{\alpha_{1b} F E_{\text{electrode}}(t)}{RT}\right) \quad (6.13)$$

$$v_2(t) = k_2 \Gamma \theta_s(t) \exp\left(\frac{\alpha_2 F (E_{\text{electrode}}(t) - E_2)}{RT}\right) - k_2 \Gamma \theta_{\text{OH}}(t) \exp\left(-\frac{\alpha_2 F (E_{\text{electrode}}(t) - E_2)}{RT}\right) \quad (6.14)$$

$$v_3(t) = k_3 \Gamma \theta_{\text{BH}}(t) \exp\left(\frac{\alpha_3 F E_{\text{electrode}}(t)}{RT}\right) \quad (6.15)$$

$$v_4(t) = k_4 \Gamma \theta_{\text{BH}}(t) \theta_{\text{OH}}(t) \exp\left(\frac{\alpha_4 F E_{\text{electrode}}(t)}{RT}\right) \quad (6.16)$$

$$v_5(t) = k_5 \Gamma \theta_{\text{BH}_3}(t) \exp\left(\frac{\alpha_5 F E_{\text{electrode}}(t)}{RT}\right) \quad (6.17)$$

$$v_6(t) = k_6 \Gamma \theta_{\text{BOH}}(t) \exp\left(\frac{\alpha_6 F E_{\text{electrode}}(t)}{RT}\right) \quad (6.18)$$

$$v_7(t) = k_7 \Gamma \theta_{\text{OH}}(t) \exp\left(\frac{\alpha_7 F (E_{\text{electrode}}(t) - E_3)}{RT}\right) - k_7 \Gamma \theta_{\text{O}}(t) \exp\left(-\frac{\alpha_7 F (E_{\text{electrode}}(t) - E_3)}{RT}\right) \quad (6.19)$$

$$v_8(t) = k_8 \Gamma \theta_{\text{BH}_3}(t) \theta_s(t)^2 \quad (6.20)$$

$$v_9(t) = k_{9d}\Gamma\theta_{\text{BH}_3}(t) - k_{9a}c_{\text{BH}_3\text{OH}^-,0}(t) \quad (6.21)$$

The adsorbed species coverage and the absolute faradaic current can be expressed from the reaction rates:

$$\Gamma\frac{d\theta_{\text{H}}(t)}{dt} = 2v_{\text{Tafel}}(t) + v_{\text{Volmer}}(t) + 3v_{1b}(t) + 2v_8(t) \quad (6.22)$$

$$\Gamma\frac{d\theta_{\text{BH}}(t)}{dt} = v_{1b}(t) - v_3(t) - v_4(t) + v_5(t) + v_8(t) \quad (6.23)$$

$$\Gamma\frac{d\theta_{\text{OH}}(t)}{dt} = v_2(t) - v_4(t) - v_7(t) \quad (6.24)$$

$$\Gamma\frac{d\theta_{\text{BOH}}(t)}{dt} = v_3(t) + v_4(t) - v_6(t) \quad (6.25)$$

$$\Gamma\frac{d\theta_{\text{O}}(t)}{dt} = v_7(t) \quad (6.26)$$

$$\Gamma\frac{d\theta_{\text{BH}_3}(t)}{dt} = v_1(t) - v_5(t) - v_8(t) - v_9(t) \quad (6.27)$$

$$I_f(t) = S_{\text{geo}}F(v_{1b}(t) + 2v_1(t) + v_2(t) + 2v_3(t) + v_5(t) + 2v_5(t) + 2v_6(t) + v_7(t) - v_{\text{Volmer}}(t)) \quad (6.28)$$

The Pt site being either covered by one of the adsorbed specie of the modelling (see Fig. 6.1), or free (noted 's'), the sum of the different coverage fraction is equal to the unity (Eq.6.29):

$$\theta_{\text{BH}_3}(t) + \theta_{\text{BH}}(t) + \theta_{\text{BOH}}(t) + \theta_{\text{OH}}(t) + \theta_{\text{O}}(t) + \theta_{\text{H}}(t) + \theta_s(t) = 1 \quad (6.29)$$

The BH_3OH^- escape absolute current is given by (Eq.6.30):

$$I_{\text{BH}_3\text{OH}^-}(t) = -6FS_{\text{geo}}\frac{D_{\text{BH}_3\text{OH}^-}}{\delta_{\text{BH}_3\text{OH}^-}}(c_{\text{BH}_3\text{OH}^-,\text{bulk}} - c_{\text{BH}_3\text{OH}^-,0}(t)) \quad (6.30)$$

The different constant values used in the modelling can be found in Table 6.1. A major assumption taken for this modelling concerns the mass-transfer of species in solution. The

concentration profiles of the reacting species near the electrode interface were assumed to be linear, and the diffusion thickness constant. Considering that the Pt/VACNF electrode exhibits a relatively open architecture without micropores, allowing a facile and directional mass-transfer of the reactant, products and intermediate species in the catalyst layer [191], the mass-transfer losses of the dissolved species into the 3D nanostructured VACNF matrix were not considered, even if it is known that different Pt roughnesses may induce different mass-transfer losses within the VACNF matrix. The last assumption is a significant simplification of the system, as the Pt/VACNF was in fact considered as a flat electrode with different densities of Pt sites (denoted as Γ). A more quantitative modelling would have taken into account hemispherical diffusion around each nanoparticle behaving as an independent active area in the electrode (especially for the Pt/VACNF electrode with the lowest Pt roughness: Pt/VACNF-0.25) [205]. However, the diffusion-limited currents of Pt/VACNF and flat smooth Pt electrodes reached the same value (Fig.5.6), suggesting that the diffusion layers around the Pt nanoparticles are strongly overlapping even in the case of Pt/VACNF-0.25. Therefore, radial diffusion was not considered in the model.

This modelling does not have the ambition to fit the voltammetry curves of the Pt/VACNF electrode leading to a quantitative description of the reaction kinetics, but rather to explain in a qualitative way the influence of the Pt site density on the BOR, in order to get insights into the BOR mechanism. Note that the charge transfer coefficients (noted ' α_i ') for the electrochemical reaction steps were all taken equal to 0.5, except for the Eley-Rideal electrooxidation reaction of BH_{ads} with OH^- (reaction rate v_3) where the charge transfer coefficient was taken equal to 0.2. Explanations for this choice will be given in what follows.

The relative values of the constants used for the modelling have been chosen taking into account the mechanism proposed by Rostamikia *et al.* [190] based on DFT calculations on Pt(111) surface. According to this DFT study and as already mentioned in the previous chapters 4 and 5 of this thesis, BH_4^- dissociative adsorption more likely forms BH_{ads} than $\text{BH}_{3,\text{ads}}$ at Pt surfaces. However, this complete dissociation is more demanding in free Pt sites. $\text{BH}_{3,\text{ads}}$ would preferentially undergo further dissociation into $\text{BH}_{\text{ads}} + 2\text{H}_{\text{ads}}$ when the number of free Pt sites is not limiting, rather than reacting with OH^- . BH_{ads} is a relatively stable adsorbate on the Pt surface and its oxidation reaction into BOH_{ads} , even though thermodynamically favorable, is characterized by a high activation barrier that results in slow kinetics (see Fig.4.6). Assuming a charge transfer coefficient equal to 0.2 for the Eley-Rideal electrooxidation of BH_{ads} with OH^- , as well as the low value of its charge transfer reaction constant k_3 (compared to the similar Eley-Rideal electrooxidation of BOH_{ads} with OH^- , supposedly more favorable), allows reproducing qualitatively the shape of the experimental current-potential curves. Results of the simulations using charge transfer coefficients equal to 0 and 0.5 are shown respectively in Fig.D.1 and Fig.D.2 of the dedicated Appendix D, and confirm that these values cannot reproduce the experimental observations.

The lack of data concerning the electrode surface state at the ultimate blocking for $E > 1.2$ V *vs.* RHE does not allow building a convincing model at these high potential values. In this model, O_{ads} is considered as species ultimately blocking Pt surface at high electrode potentials. However, this blocking could also come from boron oxides species ($\text{BO}_{x,\text{ads}}$) [45, 149], so that O_{ads} should merely be interpreted as the 'ultimate surface blocking adsorbates' for $E > 1.2$ V *vs.* RHE. It is unlikely that O_{ads} alone would totally block the BOR on the catalyst surface, as pointed out for example by Machado *et al.* [206], who showed that BH_4^- is still oxidized at high potential on PtO surface, thereby reducing the Pt oxides. Finally, since the surface state at these high potentials is unknown, the author did not attempt to model the experimental reverse

Table 6.1: Constants used for modelling

abbreviation	definition	units	value
Γ_{High}	Pt site density for the high Pt roughness	mol cm^{-2}	110×10^{-9}
Γ_{Medium}	Pt site density for the medium Pt roughness	mol cm^{-2}	8.8×10^{-9}
Γ_{Low}	Pt site density for the low Pt roughness	mol cm^{-2}	0.11×10^{-9}
$[\text{BH}_4^-]$	BH_4^- bulk concentration	mol cm^{-3}	10^{-5}
ν	Electrolyte kinematic viscosity	$\text{cm}^2 \text{s}^{-1}$	1×10^{-2}
$D_{\text{BH}_4^-}$	BH_4^- diffusion coefficient	$\text{cm}^2 \text{s}^{-1}$	1.6×10^{-5}
$D_{\text{BH}_3\text{OH}^-}$	BH_3OH^- diffusion coefficient	$\text{cm}^2 \text{s}^{-1}$	1.6×10^{-5}
D_{H_2}	H_2 diffusion coefficient	$\text{cm}^2 \text{s}^{-1}$	1.0×10^{-4}
k_{aT}	Tafel H_2 adsorption rate	$\text{cm}^3 \text{mol}^{-1} \text{s}^{-1}$	1.4×10^9
k_{dT}	Tafel H_2 desorption rate	s^{-1}	10^2
k_{V}	Volmer H^+ adsorption/desorption	s^{-1}	10^2
E_{V}	Volmer H^+ equilibrium potential	V	0 <i>vs.</i> RHE
k_1	BH_4^- adsorption in $\text{BH}_{3,\text{ads}}$	$\text{cm}^3 \text{mol}^{-1} \text{s}^{-1}$	10^2
$k_{1\text{b}}$	BH_4^- adsorption in BH_{ads}	$\text{cm}^3 \text{mol}^{-1} \text{s}^{-1}$	10^6
k_2	OH^- adsorption/desorption	s^{-1}	1
E_2	OH^- adsorption equilibrium potential	V	0.65 <i>vs.</i> RHE
k_3	BH_{ads} oxidation rate with OH^-	s^{-1}	2
k_4	BH_{ads} oxidation rate with OH_{ads}	s^{-1}	10^{-6}
k_5	$\text{BH}_{3,\text{ads}}$ oxidation rate with OH^-	s^{-1}	10^{-2}
k_6	BOH_{ads} oxidation rate	s^{-1}	10
k_7	O_{ads} formation rate	s^{-1}	10^{-4}
E_3	O_{ads} formation equilibrium potential	V	0.85 <i>vs.</i> RHE
k_8	$\text{BH}_{3,\text{ads}}$ dissociation rate in BH_{ads}	s^{-1}	10^6
$k_{9\text{a}}$	BH_3OH^- adsorption rate	$\text{cm}^3 \text{mol}^{-1} \text{s}^{-1}$	10^{12}
$k_{9\text{d}}$	$\text{BH}_{3,\text{ads}}$ desorption rate	s^{-1}	10^6
<i>scan rate</i>	potential sweep	mV s^{-1}	25
C	double layer capacity	F	10^{-4}
Re	ohmic drop	Ω	1
Ω	RDE rotation rate (same as exp.)	rpm	2500
S_{geo}	electrode geometric surface (same as exp.)	cm^2	0.19635

negative-going voltammetric scans shown in the dedicated Appendix C of this thesis, as Fig.C.4.

6.2 Simulation of the model

The results of the modelling presented in Fig.6.3 reproduce qualitatively the main experimental observations. One can note an absence of the disk currents for the lowest Pt roughness for $E < 0.6$ V *vs.* RHE in the simulated voltammograms. The 'High Pt roughness' and 'Medium Pt roughness' cases display oxidation current at low potentials, but the current decrease at *ca.* 0.8 V *vs.* RHE is more apparent for the 'Medium Pt roughness' than the 'High Pt roughness' case. The BH_3OH^- signal appears first for the 'Low Pt roughness' at *ca.* 0.6 V *vs.* RHE, and the amount of BH_3OH^- decreases when the Pt roughness increases. The values of simulated BH_3OH^- escape currents are comparable to the experimental ring signal (the collection efficiency of the RRDE setup accounts for the higher simulated values). The simulated open circuit potential (OCP) is a mixed potential of the BOR and the hydrogen evolution reaction (HER). Appropriate values for the HER reaction constants (Volmer and Tafel steps) result in an OCP of *ca.* -30 mV *vs.* RHE, reproducing the value of the experimental OCV. Note that this cannot be experimentally observed in the RRDE voltammograms of Fig.6.3 as intrusion in the HER potential region would form H_2 bubbles and shield the ring signal.

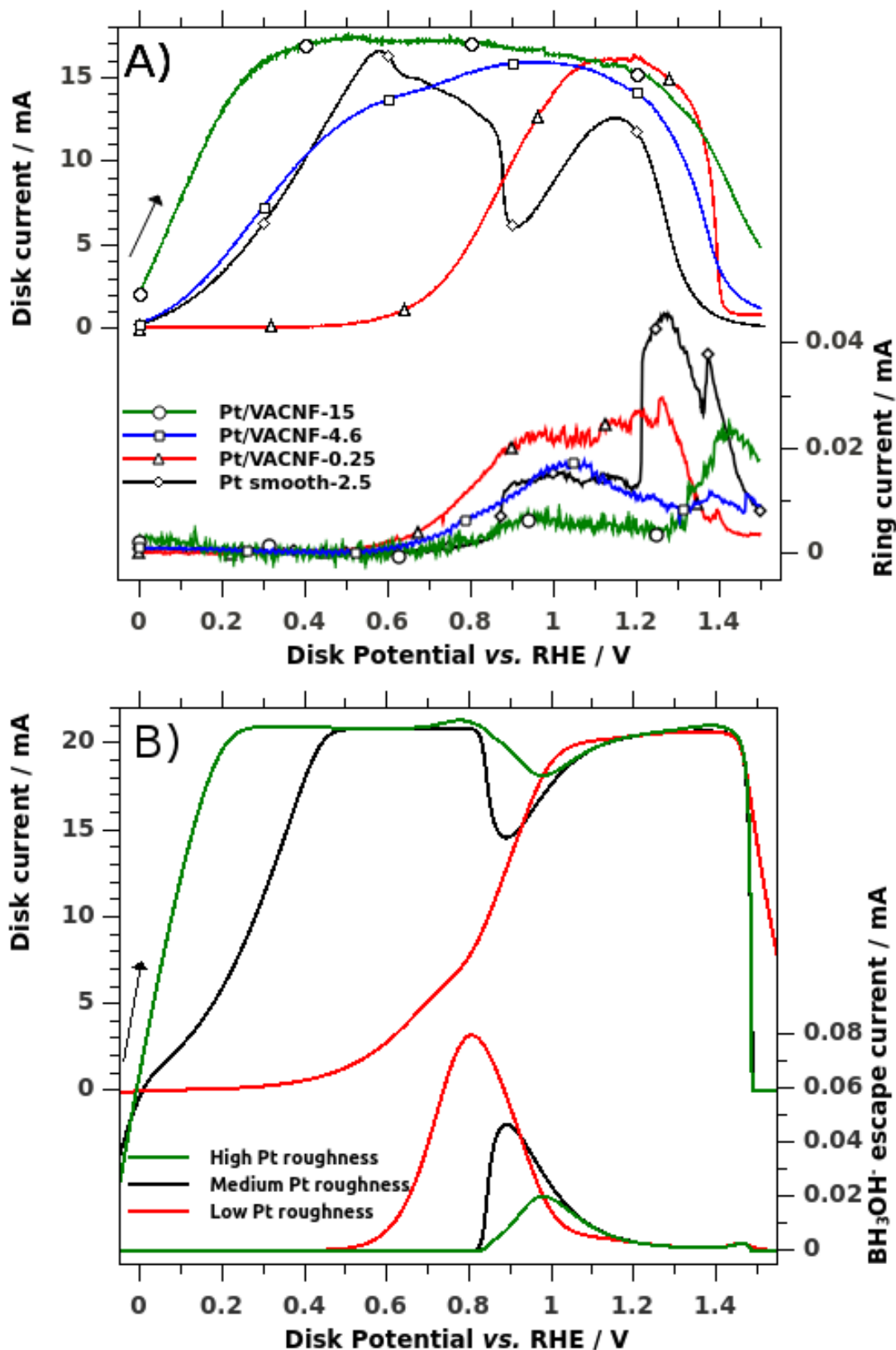


Figure 6.3: Influence of the Pt roughness on the BOR. (A) RRDE voltammograms of 10 mM NaBH_4 in 1 M NaOH at 25 mV s^{-1} and 2500 rpm (positive-going scan). The disk was composed of the different samples described in the legend and was swept between 0 and 1.5 V *vs.* RHE, while the Au-ring was held at +0.2 V *vs.* RHE to detect BH_3OH^- intermediates. Legend: Electrode type-X, X being the Pt roughness of the electrode, in $\text{cm}^2_{\text{Pt EASA}}/\text{cm}^2_{\text{geometric}}$. Note that the Au-ring current signals were baseline-corrected to ease the comparison between the various electrodes; the raw Au-ring RRDE data can be found in the Appendix C as Fig.C.2). (B) Simulated BOR RDE voltammograms and BH_3OH^- escape (values of the constants used for the modelling can be found in Table 6.1).¹³³

The kinetic modelling results support the assumptions of this study about the BOR mechanism. Indeed, for $E < 0.6$ V *vs.* RHE, the main adsorbed species on the electrode are BH_{ads} (Fig.6.4). The slow oxidation rate of this adsorbate limits the BOR depending on the Pt roughness of the electrode; Fig.6.4 shows that the BH_{ads} coverage increases with the decrease of the Pt roughness. Note that the coverage of $\text{BH}_{3,\text{ads}}$ and BOH_{ads} are not shown in Fig.6.4 as their values are too low to be observable at any potential. This apparent contradiction with the FTIR results of Molina Concha *et al.* [45] is attributed to either (i) the difference in sodium borohydride concentration (10 mM in the RRDE experiments of this thesis *vs.* 1 M in the FTIR experiments) as further discussed later in this following section of this chapter) or (ii) the fact that these species can desorb ($\text{BH}_{3,\text{ads}}$ into BH_3OH^- detected by the Au-ring of the RRDE, and BOH_{ads} into BO_x 'polymers') but still can be detected in FTIR as they are trapped in the thin film of the electrode facing the FTIR window. The coverage in free Pt sites (θ_s) can be deduced at every potential using Eq.6.29. The coverage in OH_{ads} reaches high values at 0.8 V *vs.* RHE for the 'High Pt roughness' and 'Medium Pt roughness' cases, accounting for the oxidation current decrease at 0.8 V *vs.* RHE. The oxidation current wave for $E > 0.8$ V *vs.* RHE comes from the Langmuir-Hinshelwood-type oxidation between BH_{ads} and OH_{ads} . This result strengthens the proposition of the double role of OH_{ads} : its adsorption can firstly block a catalytic surface initially active for the BOR at lower potential values if the number of total active Pt sites is not high enough (*e.g.* the smooth Pt electrode). This blocking also provokes the incomplete dissociative adsorption of BH_4^- into $\text{BH}_{3,\text{ads}}$ less demanding in free Pt sites, which explains the BH_3OH^- detection at the Au-ring. However, OH_{ads} also reacts in a Langmuir-Hinshelwood type oxidation reaction with BH_{ads} , enabling a high-potential BOR pathway that accounts for the oxidation current waves observed at $E > 0.8$ V *vs.* RHE. This tentative mechanism does not consider any H_2 formation coming from the hydrolysis reaction with a boron species. This is part of the further developments of this model, as discussed in the next section of this chapter.

Note, that in this study, the variation of the Pt nanoparticle density directly impacted the total number of active Pt sites, rather than the number of adjacent Pt sites. The latter is related to the particle size which was the same for all Pt/VACNF electrodes and equal to *ca.* 5 nm. Since the microkinetic modelling considered the Pt/VACNF electrodes as flat, and taking into account mass-transfer with linear concentration profile, low faradaic current at low potential for the Pt/VACNF with the lowest Pt roughness (Pt/VACNF-0.25) is associated to an interfacial BH_4^- concentration close to the bulk concentration. Indeed, the residence time of the stable BH_{ads} is long enough to limit the BH_4^- adsorption when the total number of active Pt sites is small, so that no measurable faradaic current is observed at low potential on Pt/VACNF-0.25. On the contrary, when the number of active Pt site increases (smooth Pt, Pt/VACNT-4.6 and Pt/VACNT-15 electrodes), enough free Pt sites (*i.e.* not occupied by BH_{ads}) are available for the BH_4^- adsorption to occur at low potential: the interfacial BH_4^- concentration is near zero and the reaction is limited by BH_4^- mass-transfer, explaining the presence of faradaic current for these electrodes at low potential. The interfacial BH_4^- concentration in the case of the Pt/VACNF-0.25 electrode starts to decrease at higher potential along with the beginning of OH^- adsorption, as the Langmuir-Hinshelwood-type oxidation between BH_{ads} and OH_{ads} reduces the residence time of BH_{ads} on the active surface.

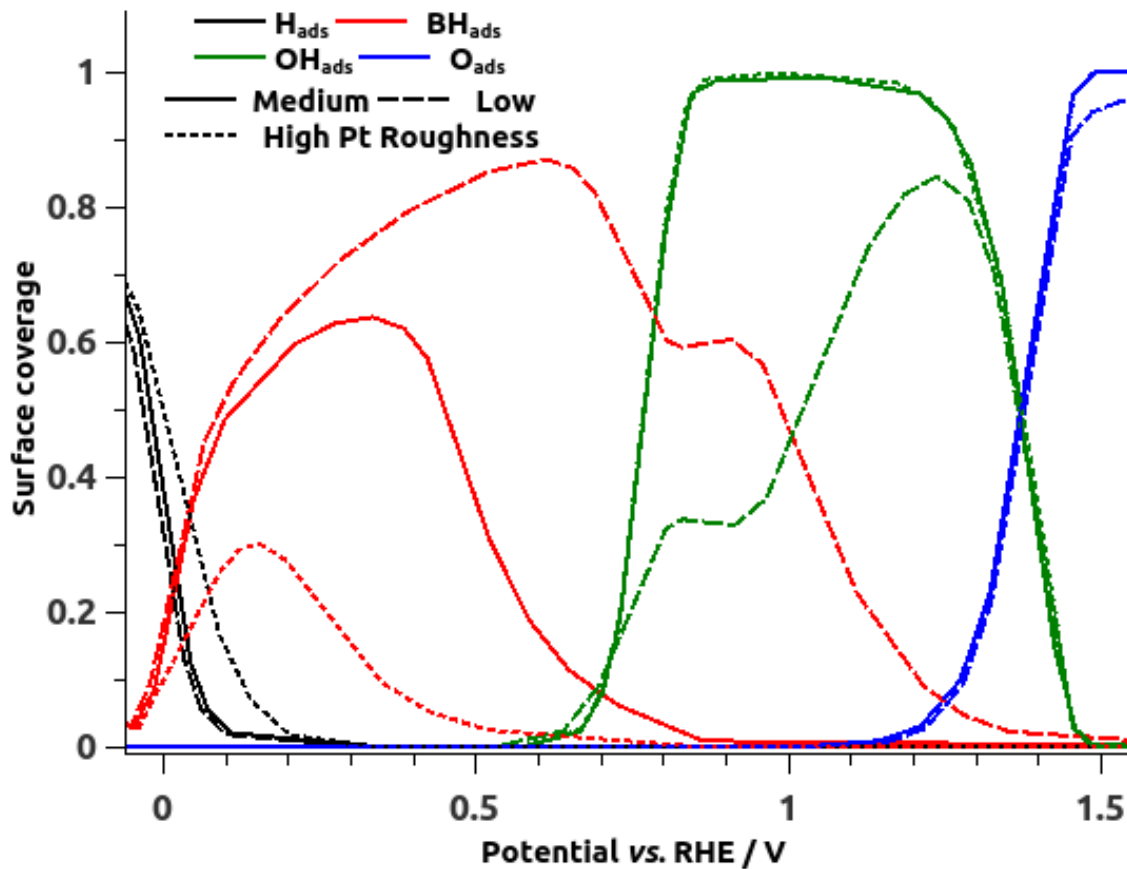


Figure 6.4: Surface adsorbate coverage for the simulated BOR RDE voltammograms (the constant values used for the modelling can be found in Table 6.1).

6.3 Model development prospects

6.3.1 Borohydride hydrolysis during the BOR

The first part of this thesis highlighted that one of the main issues of the DBFC in practical operating conditions is the gaseous hydrogen generation and escape from the DBFC anode, which lower the fuel efficiency of the DBFC and hinder the overall performances of the system. The investigation of the H_2 generation on Pt during the BOR is the next step that needs to be developed on the model presented Fig.6.1. The preliminary study of the borohydride hydrolysis during the BOR is presented in what follows.

Differential electrochemical mass-spectrometry (DEMS) is a powerful method to measure the H_2 escape from a given electrode during the BOR. Pasqualetti *et al.* [141] monitored the on-line generation of H_2 on Au/C, Ag/C, Pt/C and Pd/C at low BH_4^- concentration (1 mM), as shown in Fig.2.9. Using the same M/C electrode material, Au-ring rotating ring-disk electrode experiments were also performed [141]. Interestingly, in this study [141], the DEMS signal for the H_2 escape at high potential followed the same trend than the BH_3OH^- escape signal monitored on the Au-ring of the RRDE.

The same trend is observed in the present experiments for potential values above 0.2 V *vs.* RHE. Fig.6.5 shows the DEMS $m/z = 2$ signal (detection of gaseous H_2 escape) of a Pt electrode

sputtered on a porous PTFE membrane, and the Au-ring current (detection of BH_3OH^- escape) of a polycrystalline smooth Pt disk electrode in RRDE setup. The H_2 and BH_3OH^- escape signals follow the same trend at high potential: a first increase when Pt is quantitatively blocked by OH_{ads} around 0.9 V *vs.* RHE, and a second increase when Pt is ultimately blocked by BO_x or other oxide species around 1.2 V *vs.* RHE (for comparison, the RDE voltammogram of Pt is inserted in dotted line in Fig.6.5). As already discussed in this chapter and in the previous chapter 5, the escape of BH_3OH^- is expected to come from the formation of $\text{BH}_{3,\text{ads}}$ on the Pt surface followed by the desorption of $\text{BH}_{3,\text{ads}}$ in the form of BH_3OH^- . $\text{BH}_{3,\text{ads}}$ is less stable than BH_{ads} , but the formation of $\text{BH}_{3,\text{ads}}$ is less demanding in Pt sites, so that the appearance of $\text{BH}_{3,\text{ads}}$ becomes possible in our case when the hydroxyl species adsorb quantitatively and block the Pt surface. The fact that the DEMS H_2 escape signal follows a similar trend at high potential than the Au-ring BH_3OH^- escape current enables to consider $\text{BH}_{3,\text{ads}}$ as a source for the H_2 generation during the BOR. Please be aware that Fig.6.5 is for qualitative comparison only, as the DEMS and the RRDE experiments are quite different in their conception from one another (the two experiments notably differ in terms of electrode morphology, electrolyte hydrodynamics, etc.).

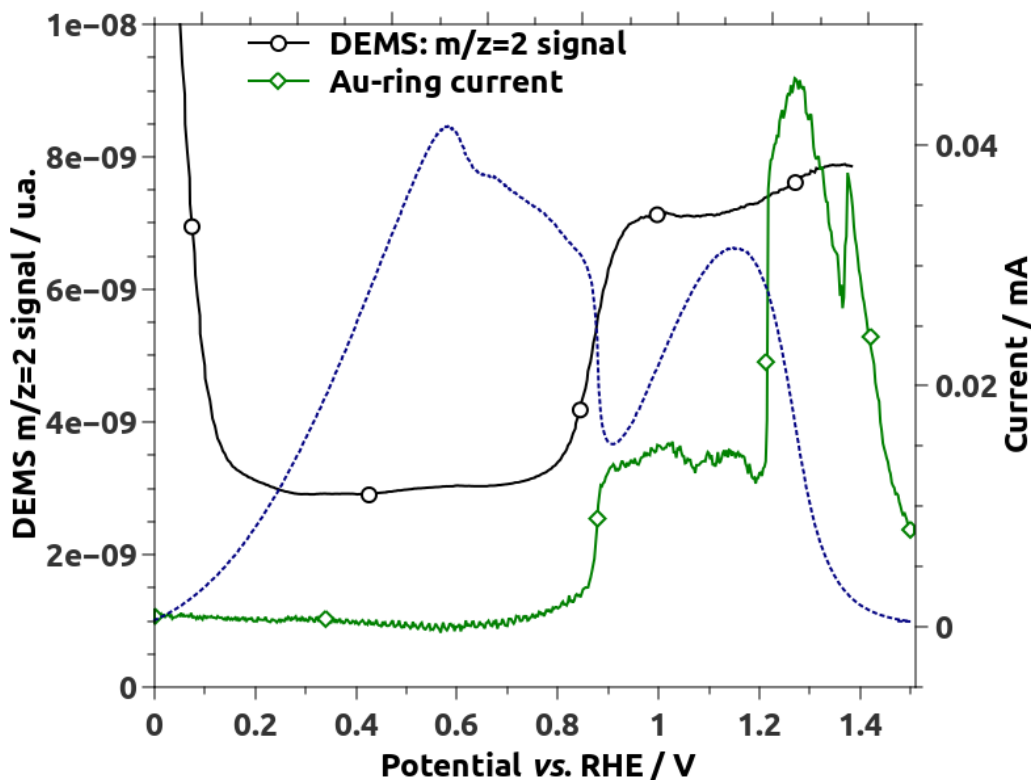


Figure 6.5: DEMS experiments for the detection of H_2 ($m/z = 2$) that is produced during the BOR for bulk Pt (sputtered) electrode, in 0.1 M NaOH and 10 mM NaBH_4 at $5 \text{ mV}\cdot\text{s}^{-1}$. Au-ring RRDE voltammogram of polycrystalline Pt electrode in 1 M NaOH and 10 mM NaBH_4 at $25 \text{ mV}\cdot\text{s}^{-1}$ and 2500 rpm (positive-going scan). The Au-ring was held at +0.2 V *vs.* RHE to detect BH_3OH^- intermediates. The RDE Pt disk voltammogram (dotted blue line) was reduced by a factor of 400 to ease the comparison.

The hydrolysis reaction of $\text{BH}_{3,\text{ads}}$ as described in Eq.6.31, was taken into account in the modelling of the BOR mechanism already developed in the beginning of this chapter. The completed mechanism is shown in Fig.6.6. The reaction constant k_{10} for this reaction (Eq.6.31) was taken equal to 10^4 s^{-1} ; the other constants used for the modelling are the same as in Table 6.1. The H_2 escape absolute current is given by Eq.6.32.



$$I_{\text{H}_2}(t) = -2F S_{\text{geo}} \frac{D_{\text{H}_2}}{\delta_{\text{H}_2}} (c_{\text{H}_2,\text{bulk}} - c_{\text{H}_2,0}(t)) \quad (6.32)$$

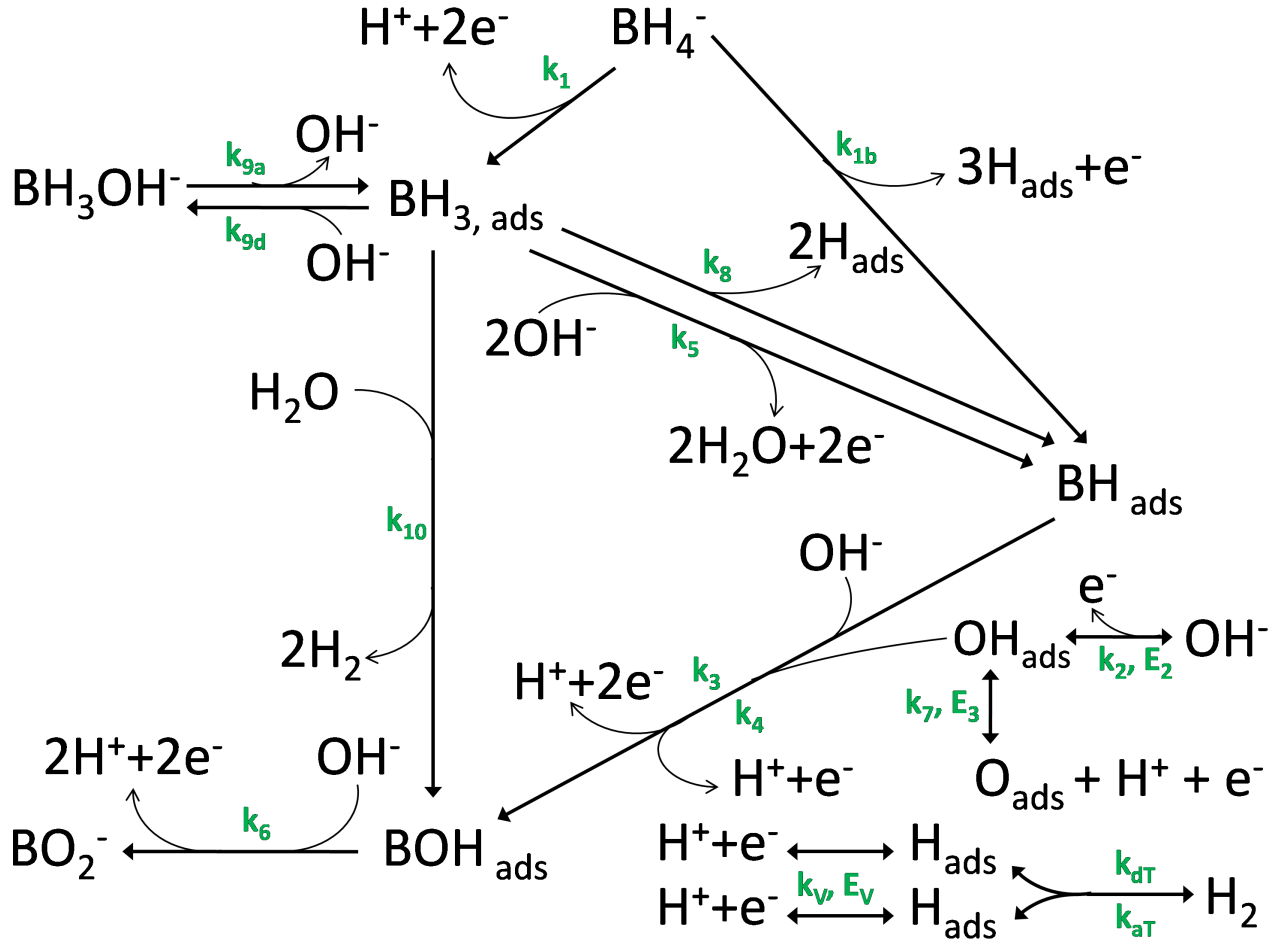


Figure 6.6: Tentative BOR mechanism, taking into account the hydrolysis of $\text{BH}_{3,\text{ads}}$ (k_{10}). See Fig. 6.1 for the description of the mechanism.

Preliminary simulated curve for the completed BOR mechanism of Fig.6.6 is shown in Fig.6.7. Similarly to what is observed in DEMS conditions, H_2 escape from Pt occurs during the BOR at: (i) potentials close to the OCP, due to the recombination of H_{ads} in a Tafel step, and (ii) around 0.8 V *vs.* RHE, when the Pt surface is quantitatively blocked by OH_{ads} , favoring the formation of $\text{BH}_{3,\text{ads}}$. However, the simulated H_2 signal does not reproduce sufficiently well the experimental DEMS signal in this preliminary result (likely because $\text{BH}_{3,\text{ads}}$ is not considered stable enough on the Pt surface in our model yet, as illustrated by the absence of any quantitative $\text{BH}_{3,\text{ads}}$ coverage in Fig.6.4). It is a first promising hypothesis which needs to be further developed.

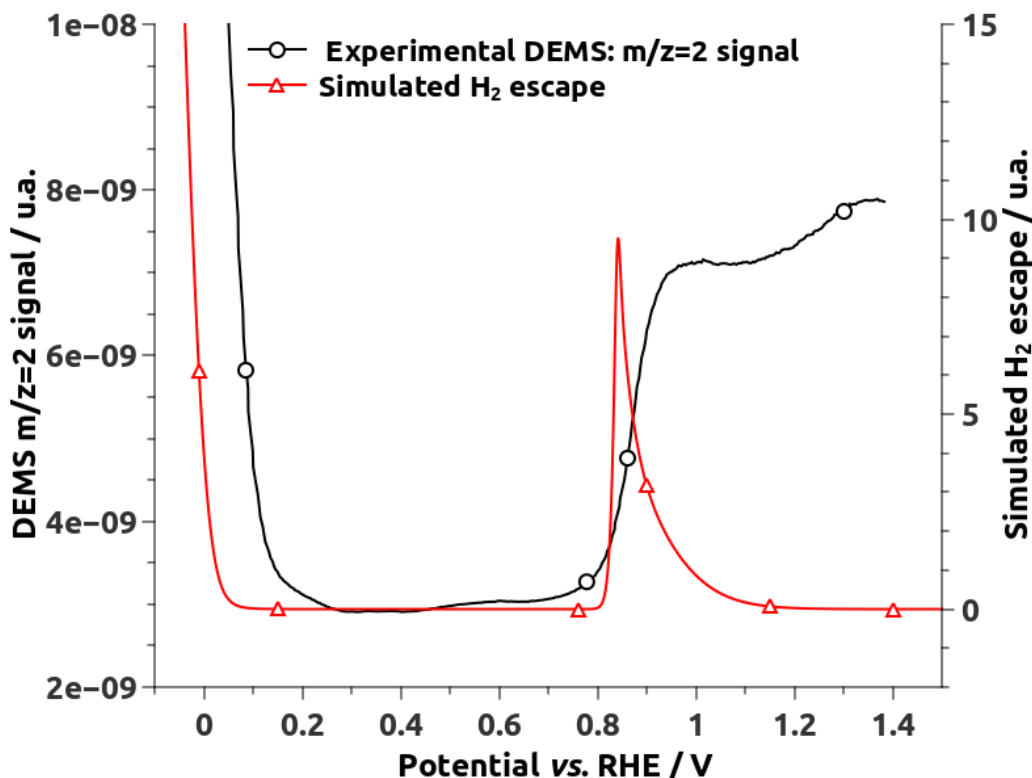


Figure 6.7: DEMS experiments for the detection of H_2 ($m/z = 2$) forming during the BOR for bulk Pt (sputtering) electrode, in 0.1 M NaOH and 10 mM $NaBH_4$ at $5 \text{ mV}\cdot\text{s}^{-1}$. Simulated H_2 escape from Pt during the BOR, from the BOR mechanism illustrated in Fig.6.6.

There is an apparent contradiction between the study of H_2 escape during the BOR on DEMS conditions and the observation of H_2 escape from the anode in DBFC operation conditions. Indeed, following the DEMS results, H_2 escape from a Pt-based DBFC anode should be quantitative around the DBFC open cell voltage (OCV) only (coming from the recombination of H_{ads} in a Tafel step), as nearly no H_2 escape from Pt is detected in DEMS conditions between *ca.* 0.1 V and 0.8 V *vs.* RHE. This means that, according to the DEMS results, the H_2 escape from the DBFC anode should be negligible at relatively high currents for the DBFC (*i.e.* when the anodic polarization overpotential is above 0.1 V, and the Volmer step oxidation of H_{ads} is quantitative), which is not the case as stated in the chapters 1 and 2 of this thesis.

In the author's opinion, this apparent contradiction could be solved considering the main variable responsible for the borohydride heterogeneous hydrolysis during the BOR, according to the mechanism developed in this thesis: the interfacial borohydride concentration ($[BH_4^-]_i$). This interfacial concentration depends at least on: the borohydride bulk concentration ($[BH_4^-]^*$), the electrode potential, the density of Pt sites and the hydrodynamics. For the DEMS and RDE methods, $[BH_4^-]_i$ is already close to zero at low potentials, as $[BH_4^-]^*$ is relatively low (typically 1 mM or 10 mM $NaBH_4$), so that the BOR is controlled by the mass-transfer of the reactants at low electrode overpotentials. As $[BH_4^-]_i$ is low, the main species covering the Pt surface at low potential in DEMS and RDE experiments is BH_{ads} , as shown in Fig.6.4. Thus, the hydrolysis reaction of $BH_{3,\text{ads}}$ (Eq.6.31) does not proceed on Pt at low potential in DEMS or RDE conditions. In DBFC operation conditions, $[BH_4^-]_i$ is relatively high, as typical values for $[BH_4^-]^*$ are around 1 M. The BOR is mainly controlled by the kinetics in DBFC conditions (obviously, one aims to reduce the anode mass-transfer overpotential). This means that BH_4^- anions are always available at the anode interface to adsorb and dissociate into BH_{ads} on free Pt

sites. However, if the electrooxidation reaction of BH_{ads} is not fast enough, the whole Pt active surface of the DBFC anode is blocked, so that the incomplete dissociative (but less demanding in Pt site) adsorption of BH_4^- in $\text{BH}_{3,\text{ads}}$ is favored. The hydrolysis reaction (Eq.6.31) of $\text{BH}_{3,\text{ads}}$ is then responsible for the H_2 generation. This tentative explanation also accounts for the results obtained using *in situ* Fourier transform infrared spectroscopy (FTIR) of the BOR on Pt performed by Molina Concha *et al.* [45], where the Pt surface was covered by $\text{BH}_{3,\text{ads}}$ and $\text{BH}_{2,\text{ads}}$ species (see Fig.4.5). In the FTIR experiment of Molina Concha *et al.* [45], the bulk borohydride concentration was equal to 1 M, *i.e.* closer to practical DBFC operation conditions. This explanation is still very speculative. In the author's opinion, the next step for the study of the BOR mechanism should be its investigation at larger borohydride concentrations, in order to bring further information for the development of the DBFC anodes in practical conditions.

6.3.2 BOR on other metal catalysts

The second part of this thesis focused only on investigating the BOR on Pt. Another prospect for the model described in this chapter would be to relate for the BOR behavior on other metal catalysts. From the DFT calculations, the major difference towards the BOR when comparing different noble metals, is the ability of the BH_4^- anions to adsorb on the catalyst surface and dissociate into BH_{ads} . As shown in Fig.6.8, DFT calculations conclude that this dissociative adsorption step is favorable on Pt, Pd and Ir surfaces, but not on Au, Ag, Os, Rh and Ru surfaces, where BH_4^- adsorbs but do not dissociate. The inability of the latter surfaces to catalyze the dissociative adsorption of BH_4^- in BH_{ads} likely accounts for the poor electrocatalytic activity of these material towards the BOR at low potentials (see chapter 2).

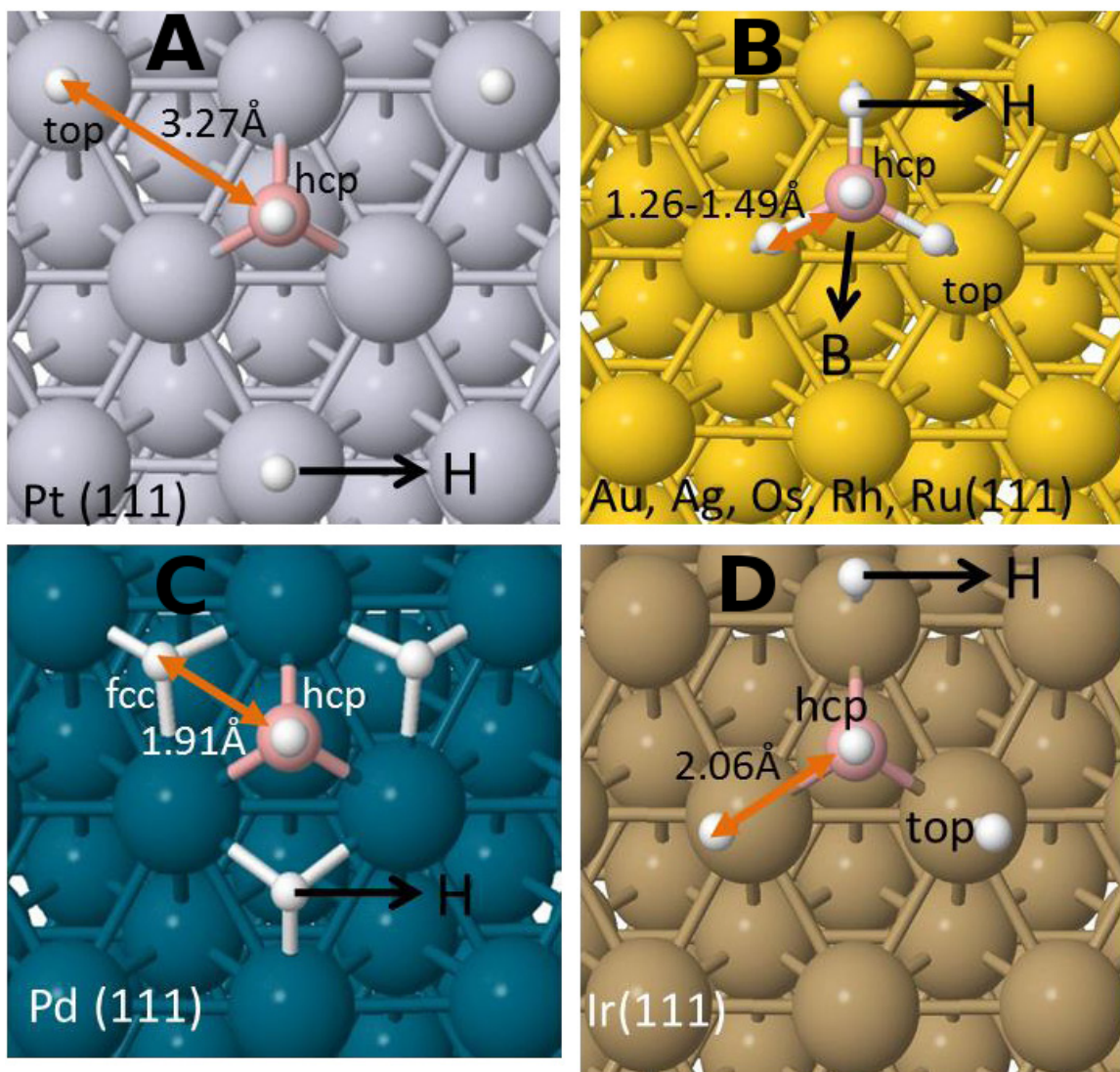


Figure 6.8: DFT calculations: $\text{BH}_{4,\text{ads}}$ most stable configuration on the metal surfaces. The metals are grouped based on adsorption structure: (A) molecular and (B, C, D) dissociated. B atoms are located at hcp-hollow sites. B-H bonds are depicted by double arrows. The H atom sites are as follows: (1) on top for molecular adsorbate (a) and for the dissociated cases (B,D) and (2) on fcc sites for dissociated case (C). 3H_{ads} on Pt diffuse toward next neighboring top sites, resulting in the largest B-H bond distance among the investigated transition metals. Reproduced from Ref.[201] with permission from the American Chemical Society.

Fig.6.9 shows RRDE voltammograms of the Pt/VACNF electrode with the lowest Pt density (Pt/VACNF-0.25) already characterized in the previous chapter 5, and a polycrystalline smooth Au electrode. The behaviors of Pt/VACNF-0.25 and smooth Au electrodes towards the BOR are interestingly similar: neither quantitative BOR current nor BH_3OH^- escape are observed until *ca.* 0.5 V *vs.* RHE. As already discussed in the chapter 5 of this thesis, the dissociative adsorption of BH_4^- into BH_{ads} likely occurs on the Pt/VACNF-0.25 active surface, but the density of Pt site is not sufficient to quantitatively valorize this stable BH_{ads} , explaining the absence of quantitative BOR current at low potential. In the case of gold, the dissociative adsorption of BH_4^- is not favorable on the Au surface, so that no quantitative BOR current is observed at low potential using the Au electrode. The simulation of BOR voltammograms for other types of catalysts is another possible development of this model which has not been attempted yet. Step by step, the development of a global BOR mechanism is reachable, to the

author's opinion.

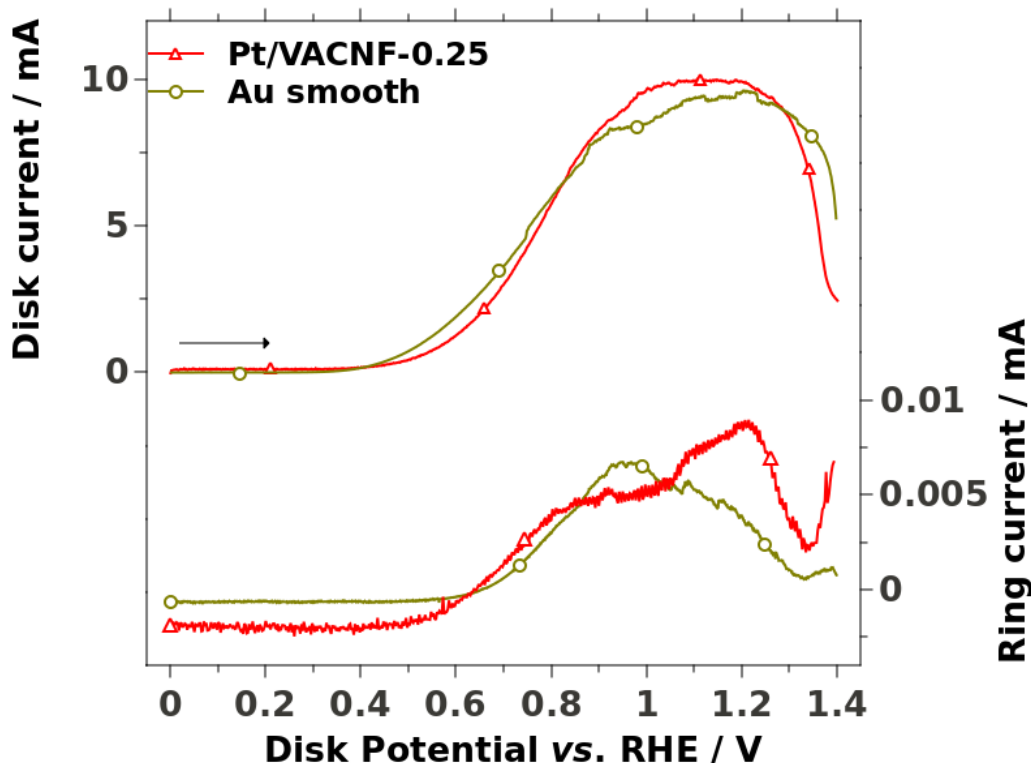


Figure 6.9: RRDE voltammogram in 1 M NaOH and 10 mM NaBH₄ at 1000 rpm of Pt/VACNF-0.25 electrode of chapter 5 (at 25 mV s⁻¹) and polycrystalline Au electrode (at 5 mV s⁻¹); positive-going scan. The Au-ring was held at +0.2 V *vs.* RHE to detect BH₃OH⁻ intermediates.

6.4 Conclusions

Synergizing the experimental and modelling results, three potential regions for the BOR on Pt can be considered :

- Below 0 V *vs.* RHE, the BOR occurs along with the fast hydrogen evolution reaction (HER). The resulting mixed open circuit potential is *ca.* -30 mV *vs.* RHE;
- Between 0 and *ca.* 0.6 V *vs.* RHE, fast dissociative adsorption of BH₄⁻ into BH_{ads} occurs. As BH_{ads} is relatively stable, its oxidation is slow and is the limiting step at these potentials;
- Above *ca.* 0.6 V *vs.* RHE, oxidation of the Pt surface occurs. The role of OH_{ads} is dual: it blocks the Pt surface and enables the BH_{ads} oxidation. The partially blocked Pt surface enables the BH_{3,ads} formation from an incomplete dissociative adsorption of BH₄⁻ (less stable reaction but also less demanding in free Pt sites). BH_{3,ads} can either desorb as BH₃OH⁻, further dissociate into BH_{ads} + 2H_{ads} or be oxidized to form BH_{ads}.

This mechanism was shown to be able to reproduce the main experimental features, such as the disappearance of the first oxidation wave for the lowest Pt loading while the second oxidation wave is observed, as well as the increase of BH₃OH⁻ escape with the decrease of the

Pt roughness. Further development of the BOR mechanism is still possible. Indeed, the BOR mechanism presented here does not account for the gaseous hydrogen generation coming from the hydrolysis of a boron-containing species. A preliminary discussion is attempted in this chapter and suggests that the source of the borohydride hydrolysis during the BOR is $\text{BH}_{3,\text{ads}}$. This latter species would quantitatively cover the Pt surface when the interfacial concentration of BH_4^- is not negligible, leading to a partial blocking of the Pt surface. This condition is met in practical DBFC operation conditions, for which the concentration of sodium borohydride in the anolyte is often much higher than in the electrolyte of the electrochemical cells. The study of the borohydride hydrolysis on Pt towards the interfacial concentration of BH_4^- should be a next development goal for this model, and would enable to get closer to the real conditions of the DBFC anode operation. Another axis of development would be to take into account other metal catalyst such as Au, the surface of which does not catalyze the complete dissociative adsorption of BH_4^- into BH_{ads} .

General conclusions

The first part of this thesis consisted in the study of the anode electrocatalyst in the direct borohydride fuel cell (DBFC). The chapter 1 of this first part characterized two different DBFC configurations using either Pt/C or Pd/C as anode catalysts. The fuel cells were also fed with another type of boron-based fuel; ammonia borane, the corresponding fuel cell being called the direct ammonia borane fuel cell (DABFC). The characterizations of the liquid fuel cells (DBFC and DABFC) were performed at various operating temperature, and the corresponding performances were compared. At room temperature, the highest values of maximum power density were obtained using Pt/C as the anode catalyst (181 and 158 $\text{mW}\cdot\text{cm}^{-2}$ for the DABFC and the DBFC, respectively), compared to Pd/C. Interestingly, the highest open-circuit cell voltage (OCV) among all the fuel cells at room temperature was obtained for the DABFC using Pd/C as the anode catalyst (1.05 V). However, Pd-based catalysts at the anode globally led to lower values of maximum power densities for the DBFC and the DABFC.

Characterizations of the fuel cells were also conducted by raising the operating temperature up to 60°C and 80°C. For these high operating temperatures, sodium borohydride was observed to be the most interesting fuel compared to ammonia borane, displaying a maximum power density value of 420 $\text{mW}\cdot\text{cm}^{-2}$ at 60°C when Pt/C was used as the anodic catalyst. Raising the operating temperature to 80°C did not lead to global improvement of the fuel cell performances: the issue of sodium borohydride and ammonia borane heterogeneous hydrolysis reactions, indirectly observed during DBFC and DABFC operation *via* the strong hydrogen gas escape, was likely at the origin of such decreased performances. In this chapter, experiments were also performed in electrochemical cell using either bulk polycrystalline Pt or Pd rotating disk electrodes (RDE) in alkaline sodium borohydride or alkaline ammonia borane electrolytes. At room temperature, the results showed that the relative electrical performances (open cell voltage and maximum power density) among the direct fuel cells could be predicted from the comparative study in electrochemical cell (*i.e.* the comparison of the open circuit potentials and electrocatalytic activities of the different bulk electrodes in the different electrolytes). For instance, the OCP of the Pd RDE in contact with ammonia borane was measured to be the lowest among all the configurations, in agreement with the highest OCV measured for the DABFC using Pd/C as the anode catalyst, compared to the other fuel cell configurations. The predicting ability of the electrochemical cell experiments was found to be however limited, due to the H_2 generation from the BH_4^- hydrolysis reactions that was not a predominant phenomenon in the experimental conditions of the electrochemical cell, on the contrary to the practical conditions used in DBFC characterizations. The major influence of the H_2 generation on the overall performances of the DBFC was shown in this chapter by changing the porosity of the DBFC anode: the decrease of the macroporosity of the DBFC anodic active layer led to a severe loss in performances, due to the detrimental shielding of the active sites by H_2 bubbles. Finally, a TEM comparison of the anode catalysts prior and post characterizations of the fuel cells raised preliminary concerns about the stability of the anode catalysts upon DBFC and/or DABFC operation: the Pt and Pd electrocatalysts were subject to severe degradation (such as the increase of particle size and extent of agglomeration, and the loss of density over the carbon substrate) upon fuel cell characterizations.

The chapter 2 of the first part presented a literature review of anode catalysts for the DBFC. Along with the experimental conditions used in the literature to characterize the DBFC and their corresponding performances, this chapter presented and discussed experimental variables external to the anode in the DBFC characterizations. It was shown that the great number of interconnected experimental variables in a practical DBFC system hinders the pertinent comparison of the different experiments through the literature. In order to overcome this issue, it is necessary to reduce and simplify the system. This chapter reviewed and discussed different methods and the corresponding results obtained in the literature to evaluate the electrocatalytic activity of several materials towards the borohydride oxidation reaction (BOR), as well as the

H₂ escape rate upon conditions close the DBFC operation. Benchmarks and recommendations were proposed in order to ensure a reliable comparison of different potential DBFC catalysts, considering these two specifications (electrocatalytic activity towards the BOR and H₂ escape rate).

The second part of this thesis investigated the BOR mechanism on platinum. In this part, the experiment were performed not in DBFC configuration as it was the case in the first part of this thesis, but in the controlled environment of the three-electrode cell setup. Different types of Pt-based model electrodes were used in order to achieve further understanding of the BOR mechanism. Each type of model electrode enabled to control a chosen variable related to the Pt electrocatalyst, and thus to focus on one particular aspect of the BOR.

In chapter 3, the use of bulk polycrystalline and single crystal Pt flat electrodes showed that the BOR is a structure-sensitive reaction. The order of BOR activity for the three Pt basal plane electrodes was found to be Pt(110) > Pt(100) ≫ Pt(111) at low potential. The hydroxyl adsorption on the Pt surface at higher potentials was observed to bear different and opposite effects on the BOR activity: (i) a detrimental effect, with OH_{ads} being a Pt site-blocking inhibitor for a Pt surface already fully active for the BOR at low potential (especially observed for the two most active Pt surfaces: Pt(110) and Pt(100)), or (ii) a beneficial effect, with OH_{ads} activating a Pt surface relatively inactive towards the BOR at low potential (especially observed for the least-active Pt surface: Pt(111)). The two opposite effects of OH_{ads} were also observed on the bulk polycrystalline Pt electrode, accounting for the 'inverted bell shape' of the BOR voltammogram of this electrode between 0.5 V and 1.0 V *vs.* RHE.

A more complex model electrode was synthesized and studied in chapter 4: Pt nanoparticles supported on flat glassy carbon (GC) substrate. The poisoning of the Pt active surface at low electrode potentials was observed. This poisoning was attributed to BH_{ads}, a stable adsorbed intermediate formed during the BOR. In agreement with the beneficial effect of OH_{ads} already observed in chapter 3, the poisoned active surface of the Pt/GC electrode was 'cleaned' at high potentials, when the quantitative adsorption of hydroxyl species occurred.

Increasing the complexity level of the model electrodes was achieved by studying Pt nanoparticles supported on vertically-aligned carbon nanofiber (VACNF) electrodes (chapter 5). The deposition of various amounts of Pt nanoparticles on the VACNF substrate enabled to study the influence of the density of Pt active sites towards the BOR. The release of BH₃OH⁻ intermediate formed during the BOR by the desorption of BH_{3,ads} was measured using a gold-ring rotating ring-disk (RRDE) electrode setup. This chapter confirmed that the BOR pathway is potential-dependent: the 'low-potential-BOR' was very sensitive to the density of active Pt sites, while the 'high-potential-BOR' was not. Indeed, neither quantitative BOR current nor BH₃OH⁻ escape was observed at low potential for the Pt/VACNF electrode with the lowest density of Pt sites. These observations reinforce the findings of the chapter 4 (using Pt/GC model electrodes): the limiting step of the low-potential BOR is the removal of the stable BH_{ads}, adsorbed on the Pt active surface during the BOR. The binding energy of BH_{ads} on Pt being likely to change depending on the crystallographic structure of the Pt surface, it would (at least partially) account for the structure sensitivity of the BOR observed on the three Pt basal plane single crystals in chapter 3. From the experimental observations of chapter 5, another pathway for the BOR was proposed to be triggered by the adsorption of hydroxyl species on the Pt surface at higher electrode potentials (higher than 0.6 V *vs.* RHE). Although OH_{ads} is site-blocking (leading to possible inhibitions of the BOR activity, as observed for the polycrystalline bulk Pt electrode and single crystals Pt(110) and Pt(100) electrodes), this latter

species can also react with BH_{ads} in a Langmuir-Hinshelwood-type electrooxidation reaction, leading to possible activation or self-cleaning of the Pt surface towards the BOR, as observed for Pt(111), Pt/VACNF with the lowest density of Pt site, or the poisoned Pt/GC electrode.

Finally, the chapter 6 gathered the findings mentioned above as well as other experimental and computational results from the literature; a tentative mechanism for the BOR on Pt was proposed. This mechanism was simulated using mean-field microkinetics modelling and the calculated curves were compared to the experimental results. The simulation of the main features observed experimentally enabled to validate the proposed mechanism.

As discussed in the chapter 6, the prospects for the work presented here would be to link the first part of this thesis (the practical characterization of DBFC in conditions close to the reality of the system) with the second part (the fundamental study of the BOR mechanism). One of the main issue of the DBFC is the H_2 generation at the anode compartment. The study of the borohydride hydrolysis during the BOR would be the next step of development for the BOR mechanism presented here. To do so, the influence of the interfacial borohydride concentration on the BOR has to be investigated. The development of a global BOR mechanism accounting for the behaviors of other metal catalysts (and not only Pt) could also be another goal to reach for this model. Synergizing practical DBFC experimentation and fundamental BOR studies, there is hope to propose a suitable anode that would enable the further development (and why not commercial deployment?) of the DBFC technology.

Appendices

Appendix A

Experimental

A.1 Characterizations in electrochemical cell

A.1.1 Electrochemical cell setup

With the exception of the characterizations of single crystal Pt electrode (see the dedicated experimental part below), the alkaline electrolytes were prepared using NaBH_4 powder (98% purity, Sigma Aldrich), NH_3BH_3 powder (97% purity, Sigma–Aldrich), monohydrated- NaOH crystals (99.99% purity, Merck Suprapur[®]) and ultra-pure water (18.2 $\text{M}\Omega\cdot\text{cm}$, < 3 ppb TOC, Millipore Elix + Gradient[®]). The acidic electrolyte solutions were prepared using H_2SO_4 96% (Merck Suprapur[®]) and ultra-pure water. All the plastic/glassware and electrochemical cell(s) that could pollute the experiment (volumetric flasks, electrochemical cell, etc.) were soaked overnight in Caro’s acid (1-1 vol.% H_2O_2 (30%)- H_2SO_4 (> 95%)) prior to each experiment and then thoroughly rinsed with ultrapure water. All experiments were performed at room temperature and pressure (*ca.* 25°C, 1 atm). For the alkaline electrolyte preparation, as recommended by Finkelstein *et al.* [130], sodium borohydride was added to the sodium hydroxide solution previously cooled down to room temperature in order to avoid any severe homogeneous hydrolysis of BH_4^- (enhanced by high temperature and low pH). However, argon purging (Air Liquide, Alphagaz 2) was used during all the electrochemical experiments, as the presence of an oxidant such as oxygen is likely to influence the results.

The characterizations in alkaline media were controlled using a VSP (Bio-Logic) potentiostat connected to a three-electrode cell bearing an internal PTFE beaker in order to avoid glass contact with the alkaline solution. A gold plate was used as counter electrode instead of platinum in order to avoid major heterogeneous hydrolysis of BH_4^- in open circuit conditions [139]. The characterizations in acidic media were controlled using an Autolab PGSTAT30 (Metrohm[®]) potentiostat connected to a three-electrode cell. A platinum plate, previously cleaned on a hydrogen-flame, was used as counter electrode. For all characterizations (except for the characterizations of the single crystal Pt electrodes) the reference electrode was a freshly prepared reversible hydrogen electrode (RHE), consisting of a platinized Pt wire in contact with a trapped hydrogen bubble (formed by electrolysis of the supporting electrolyte) and with the supporting electrolyte. The RHE was ionically connected to the electrochemical cell through a Lugin capillary filled with the supporting electrolyte. A new RHE was prepared every 2 h of experiment.

Rotating disk electrode (RDE) experiments were performed using an OrigaLys (OrigaTrod[®])

+ OrigaBox[®]) rotating disk electrode setup. The electrodes were inserted in home-made PTFE tips for the RDE experiments. Rotating ring-disk electrode (RRDE) experiments were performed using an Au-Ring RRDE 'ChangeDisk RRDE Tips AFE6R1AU' (Pine[®]) controlled with the electrode rotator 'AFMSRCE' (Pine[®]), the disk inserted being the smooth Pt, smooth Au or Pt/VACNF electrode.

In the particular case of the single crystal Pt electrodes used in chapter 3, which required a higher level of cleanness, the characterizations were performed as followed. The electrolytes were prepared using NaBH₄ powder (99.99% purity, Sigma Aldrich) and monohydrated-NaOH crystals (99.99% purity, Merck Suprapur[®]) and ultra-pure water (18.2 MΩ.cm, < 3 ppb TOC, Elga PureLab Ultra[®]). All the materials that could pollute the experiment were soaked overnight prior to each experiment in a mix of sodium permanganate and sulfuric acid in ultra-pure water, rinsed using a mix of hydrogen peroxide and sulfuric acid in ultra-pure water, boiled at least three times in ultra-pure water, and then thoroughly rinsed with ultrapure water. The characterizations were controlled using EG&G PARC 175 and eDAQ EA161 potentiostat with an eDAQ e-corder ED401 recording system. A platinum plate, previously cleaned on a butane-flame, was used as counter electrode. The reference electrode was an RHE composed of a platinized Pt wire in contact with the supporting electrolyte and a bubbling of gaseous hydrogen (Air Liquide, Alphagaz N50). The RHE was ionically connected to the electrochemical cell through a Lugin capillary filled with the supporting electrolyte. The experiments were performed at room temperature and pressure (*ca.* 25°C, 1 atm).

A.1.2 Preparation and synthesis of the model electrodes

The diameter of the different electrodes used in this thesis were: 5.0 mm for the polycrystalline Pt electrode used in chapter 1, 2.0 mm for the polycrystalline Pd electrode used in chapter 1, 2.0 mm (Fig.3.2) and 5.0 mm (Fig.3.3) for the polycrystalline Pt electrodes used in chapter 3, 5.0 mm for the Pt/GC electrode used in chapter 4, 5.0 mm for the polycrystalline Pt electrode, the polycrystalline Au electrode and the Pt/VACNF electrodes used in chapter 5. The geometric areas of the Pt single crystal electrodes used in chapter 3 were 4.80 mm², 3.88 mm² and 4.69 mm² for Pt(111), Pt(110) and Pt(100), respectively.

Bulk electrodes

The polycrystalline bulk Pt, Pd and Au electrodes were placed into a homemade PTFE holder and polished using diamond paste (Mecaprex, Presi) on polishing cloth (Presi) in the following sequence : 6, 3, 1 and 0.1 μm and then washed in an ultrasonic bath of acetone, 1-1 ultrapure water-ethanol, and ultrapure water (30 min for each bath) to remove the remaining diamond paste and any trace of impurities. For RRDE experiments, the bulk electrodes were first prepared as described above, removed from the homemade PTFE holder and inserted into the RRDE holder (a great care was taken in order to avoid the pollution of the electrode surfaces during this step of transfer).

The single crystal Pt electrodes were used as prepared by the 'Institute of Electrochemistry' laboratory of Alicante. Briefly, the electrode were prepared from small single crystal beads, *ca.* 2 mm in diameter following the method developed by Clavilier *et al.* [207]. The single crystal Pt electrodes were annealed prior to any experiment for *ca.* 30 s in a hydrogen-oxygen-flame, cooled down in a reductive atmosphere (hydrogen + argon) and quenched in ultrapure water in

equilibrium with this atmosphere [208]. The electrodes were transferred to the electrochemical cell under the protection of a droplet of deoxygenated water.

Pt/GC electrode

The deposition of the platinum nanoparticles at the glassy carbon (GC) electrode was freely adapted from the procedure of Savinova et al., detailed in [209, 210]. The GC tip was first cautiously polished using diamond paste (Mecaprex, Presi) on polishing cloth (Presi) in the following sequence : 6, 3, 1 and 0.1 μm and then washed in an ultrasonic bath of acetone, 1-1 ultrapure water-ethanol, and ultrapure water (30 min for each bath) to remove the remaining diamond paste and any trace of impurities, and then stored in water.

Prior to the Pt nanoparticle deposition, the GC tip was inserted in a homemade PTFE holder and used as working electrode in a rotating disk electrode (RDE) setup. The GC electrode was electrochemically oxidized by a 3 min potential hold at 2.23 V *vs.* RHE in a 0.1 M sulfuric acid electrolyte. Then, the GC tip was thoroughly rinsed with ultra- pure water and heated at 60°C to evaporate the water.

In order to obtain the Pt target loading of 5 $\mu\text{g}_{\text{Pt}}\cdot\text{cm}^{-2}$, the desired amount of Pt solution (composed of 6.5 mM K_2PtCl_4 in HCl medium, pH = 3, prepared using 30 % HCl, Merck Suprapur[®], 98 % $\text{K}_2\text{Pt}^{\text{II}}\text{Cl}_4$, Sigma Aldrich[®], and ultra-pure water) was pipetted onto the GC tip and heated back at 60°C for fast solvent evaporation, a prerequisite to avoid any consequent Pt nanoparticle agglomeration.

After the complete solvent evaporation, the GC tip was removed from its PTFE holder and heat-treated in reducing atmosphere, to reduce the Pt^{2+} ions into metallic platinum nanoparticles. The tubular oven (Nabertherm[®], model R50/250/12) was first outgassed by applying three successive steps of vacuum/constant argon flow (250 $\text{mL}\cdot\text{min}^{-1}$, Air Liquide[®])/vacuum, in order to eliminate traces of water/ oxygen that may interfere in the experiment. From the last vacuum step, a constant flow of hydrogen gas (50 $\text{mL}\cdot\text{min}^{-1}$, Air Liquide[®]) was set up until the internal pressure in the tube reached 370 Torr. Then, the temperature was raised to 250°C, maintained at this value for 1 h, and the oven was left to cool down overnight under a constant flow of argon (20 $\text{mL}\cdot\text{min}^{-1}$). Finally, the GC tip supporting the Pt nanoparticles was mounted back with caution on its PTFE holder and stored in dry conditions in a sealed vial prior subsequent characterization.

Pt/VACNF electrodes

The method used in this study for the preparation of Pt/VACNF electrode on Ti rod is adapted from the previous work of Ruvinskiy *et al.* [191]. Briefly, the initial electrode is a 5 mm diameter Ti rod, polished with 1, 0.3 and 0.05 μm alumina powder, cleaned in ethanol, acetone and ultra-pure water (18.2 $\text{M}\Omega\text{ cm}$, < 3 ppb Total Organic Carbon (TOC)) under ultrasonic irradiation (20 min for each solution). The Ti rod was heated at 200°C for 30 min in air to enable the growth of a native TiO_x surface.

The VACNF growth procedure on the TiO_x surface is based on a catalytic chemical vapor deposition (CCVD) procedure using a 0.3 M ferrocene solution ($\text{Fe}(\text{C}_5\text{H}_5)_2$) in toluene solvent. The CNF growth is supposed to proceed through a root growth mechanism around the Fe catalyst nanoparticles. For the CCVD, the solution of ferrocene in toluene was injected perpendicularly

to the Ti rods surface through a dry flow of argon. The CCVD did proceed inside a quartz tube reactor heated at 850°C.

Upon synthesis, the VACNF were impregnated with a cyanoacrylate resin in order to harden the VACNF matrix. The rods were then polished with 1, 0.3 and 0.05 μm alumina until the VACNF thickness reached 10 μm for every Pt/VACNF electrode considered in this study; in other words, all the Pt/VACNF samples studied herein present the same active layer thickness. The polymer resin was then removed by soaking in acetone for 12 h. The VACNF of desired thickness were subsequently cleaned and functionalized for the Pt deposition by resting at 300°C in air for 30 min followed by soaking in 0.1 M H_2SO_4 for 12 h.

The Pt deposition on the VACNF substrate was achieved using colloidal Pt nanoparticles prepared from a K_2PtCl_4 solution in ethylene glycol at pH above 12 (adjusted with addition of NaOH) exposed to microwave irradiation (600 W, 60 s). The colloid solution was deposited on the VACNF, dried at 60°C, and calcined at 250°C for 1 h in air. Finally, a thorough washing with ultra-pure water was performed in order to remove the last impurities [211]. The preparation procedure for the Pt/VACNF electrode is summarized in Fig.A.1.

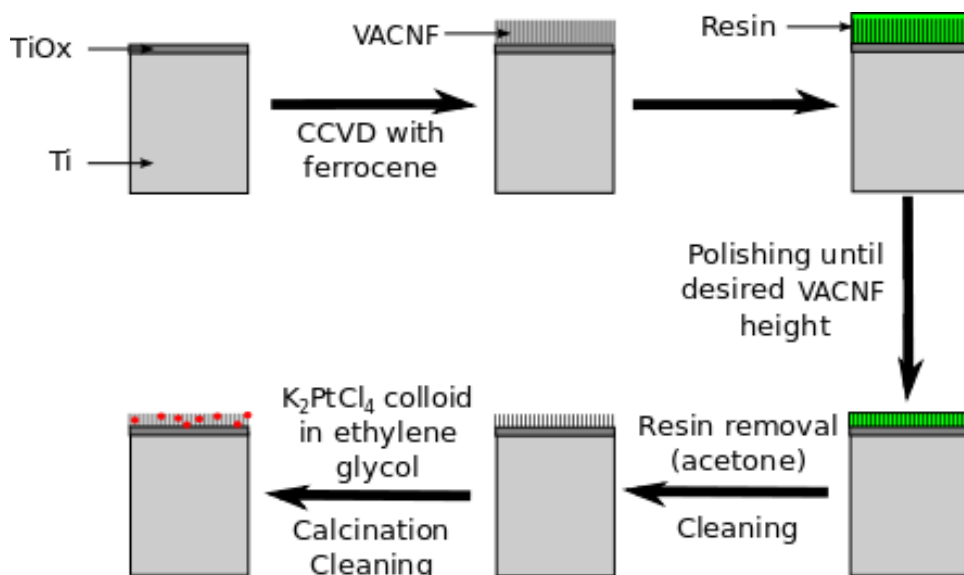


Figure A.1: Scheme of the preparation of Pt/VACNF on Ti rod electrodes.

The inactivity of the VACNF supported on Ti substrate towards the borohydride oxidation reaction (BOR) has been checked and validated. A VACNF electrode was prepared using the method mentioned before, without the Pt nanoparticle deposition step. No oxidation current was observed when performing a cycling voltammetry on this electrode in 1 M NaOH and 1 M NaOH + 10 mM NaBH_4 electrolyte. The RDE cyclic voltammograms of this electrode in 1 M NaOH + 10 mM NaBH_4 electrolytes, is compared with a smooth Pt electrode in Fig.C.1.

A.2 Characterizations in fuel cell configuration

This experimental section concerns the fuel cell configurations characterized in chapter 1.

The homemade anodic active layer for the fuel cell configuration were prepared by pasting an ink composed of 125 mg 10 wt.% Pt/C or 10 wt.% Pd/C (Premetek, carbon support: Vulcan XC-72), 2.25 g of 5 wt.% Nafion[®] in isopropanol (Ion Power, Liquion[®]-1105-1100 EW) and 3 mg of isopropanol (99.6% ACS reagent, Acros Organics) onto a 5 cm x 5 cm carbon cloth substrate (Quintech CC-060, without PTFE). The weight ratio between deposited carbon Vulcan XC-72 and the Nafion[®] binder is thus 1:1, and the target metal loading on the carbon cloth is 0.5 mg of Pt or Pd per cm² of carbon cloth. ICP-AES analyses were performed on the Pt/C and Pd/C anodic layers on carbon cloth (soaked in aqua regia for one night after the fuel cell experiments in order to dissolve the metal nanoparticles). The target metal loading of *ca.* 0.5 mg of Pt or Pd per cm² of carbon cloth was confirmed. As this operation destroys the integrity of the sample, the ICP-AES analyses were only performed after all the fuel cell experiments had been made.

The homemade fuel cell membrane electrode assembly was composed of (i) the previously described anode composed of M/C on carbon cloth (M = Pt or Pd), (ii) a 7 cm x 7 cm Nafion[®] 212 membrane (DuPont) previously cleaned by boiling in 5 wt.% H₂O₂ in ultrapure water for 1 h, boiling in ultrapure water for 2 h and exchanged for the Na⁺ Nafion[®] form by soaking in 3 M NaOH in ultrapure water for 3 h, followed by a thorough rinsing in ultrapure water, (iii) a commercial air cathode composed of Pt/C on carbon Toray paper with a loading of 2 mg_{Pt}.cm⁻² (Quintech EC-20-10-7, 20 wt.% Pt/Vulcan XC-72).

Using aluminum plate holders, the three components of the membrane-electrodes assembly were placed (without any prior compression) and compressed at a controlled pressure (using a torque-meter wrench) between two homemade graphite bipolar plates surrounded by silicon gaskets. The active area of the graphite bipolar plates was 5 cm x 5 cm. The anodic graphite bipolar plate was made of 25 serpentine flow channels (1.2 mm channel width and 0.8 mm channel depth) with a top-top flow inlet-outlet. The cathodic graphite bipolar plate was made of 20 serpentine flow channels (1.5 mm channel width and 0.9 mm channel depth) with a top-bottom flow inlet-outlet.

The anodic fuel, composed of either 1 M NaBH₄ (NaBH₄ powder, 98% purity, Sigma Aldrich) or 1 M NH₃BH₃ (NH₃BH₃ powder, 97% purity, Sigma-Aldrich) in 5 M NaOH (pellets, VWR AnalaR[®] Normapur[®]) dissolved in ultra-pure water, was fed at 7.5 mL.min⁻¹ to the anodic compartment using a tubing pump (Ismatec, ICP-N for the pump and Tygon[®] ST R-3607 for the tubes). The cathodic fuel was pure oxygen (Air Liquide, Alphagaz 1) humidified by bubbling in ultrapure water at 65°C (or 80°C for the fuel cells operating at 80°C) and feeding the cathodic compartment at 300 mL.min⁻¹, atmospheric pressure. The voltammograms in fuel cell configuration were performed using a SP-150 (Bio-Logic) potentiostat and a 80 A high current booster (Bio-Logic). The whole fuel cell system was placed into a closed oven to control the operating temperature.

Unless otherwise stated, the fuel cell voltammograms presented in this work were plotted using the same assemblies (either the 'Pt/C anodic catalyst' assembly or the 'Pd/C anodic catalyst' assembly). Before changing the anodic fuel (sodium borohydride or ammonia borane), the assemblies were cleaned by circulating ultra pure water through the anodic and cathodic compartments. The fuel cell configurations were characterized using the cyclic voltammetry technique: the fuel cells were cycled between the OCV and 0 V until a stable voltammogram was obtained. The voltammograms presented in this work are not corrected for the electrical resistance, as the influence of the latter was found to be negligible (as shown in the 'Results' section of chapter 1).

A.3 Physical characterizations

Transmission electron microscopy (TEM) was performed using a Jeol 2010 apparatus bearing a LaB₆ filament and operating at an accelerating voltage of 200 kV. The TEM grids were Lacey Formvar/Carbon 200 mesh copper grids (Ted Pella, inc.[®]).

In chapter 1 (Fig.1.7), the anodic catalysts (Pt/C or Pd/C) of the fuel cells were scratched from the carbon cloth substrate after that all experiments had been performed, using a ceramic blade and deposited with ethanol onto the TEM grid. The histograms of the used Pt or Pd nanoparticles diameter were built using the software ImageJ, counting at least 300 nanoparticles for each histogram, and compared to those of the fresh catalysts. Elemental analysis was performed under the TEM beam using an X-ray energy dispersive spectrometer (X-EDS, Oxford – INCA[®]) for the Pd/C samples in order to evaluate the possible presence of Pt which could redeposit at the anode after corrosion/dissolution at the cathode catalyst of the DBFC or DABFC.

In chapters 4 (Fig.4.2) and 5 (Fig.5.2), the electrode surface was gently scraped using a ceramic blade, to remove the top-most layers of the GC or Ti tip for the Pt/GC or Pt/VACNF electrodes, respectively. A drop of water containing the fragments of the electrode surface was transferred onto the TEM grid. As this operation destroys the integrity of the sample, the TEM images were only taken after the electrochemical experiments (*i.e.* at the 'end-of-life' of the samples).

Scanning electron microscopy (SEM) was performed using a Jeol JSM-6700F electron microscope device at an accelerating voltage 3 kV. The photographs presented on Fig.1.6 of the Pt/C anodic layers were taken after the fuel cell experiments. The photographs presented on Fig.5.1 were taken right after the CCVD procedure in order to confirm the growth of VACNF on the TiO_x rods.

Appendix B

Stripping of the BOR 'surface poisons'

In the chapter 4 of this thesis, the stripping of the 'poison species' (assumed to be BH_{ads}) accumulated at open circuit potential (OCP) on the Pt/GC electrode took place in a single electrolyte composed of sodium borohydride in sodium hydroxide (Fig.4.4). In the experiment of Fig.4.4, the stripping of the BH_{ads} , and so the cleaning of the Pt surface, took place for electrode potentials higher than *ca.* 0.6 V *vs.* RHE when the electrooxidation reaction of BH_{ads} with the hydroxyl species could occur not only in a Eley-Rideal type, but also in a Langmuir-Hinshelwood type.

Another possibility for stripping the BH_{ads} from the Pt surface would be to perform this stripping in an electrolyte composed of sodium hydroxide only, enabling to study the adsorbed poison without interferences from remaining BOR faradaic current. A tentative experiment was performed in this goal, as described in the experiment scheme of Fig.B.1. The polycrystalline bulk Pt RDE was first let to rest for a given time at OCP in a solution composed of sodium borohydride and sodium hydroxide. The RDE was then transferred for a few seconds in two successive solutions composed of sodium hydroxide only in order to remove traces of sodium borohydride from the interfacial solution. Finally, the RDE is placed into a conventional three-electrode electrochemical cell (as the working electrode) with an electrolyte composed of sodium hydroxide only, in order to perform the stripping voltammogram of any species that would have adsorbed on the Pt surface in the first step of the experiment. All cells were deaerated with argon bubbling in order to reduce the influence of the O_2 reductant. During the transfers of the Pt RDE between every cells, the Pt surface was covered with the electrolyte of the previous cell in order to avoid contact with the laboratory atmosphere.

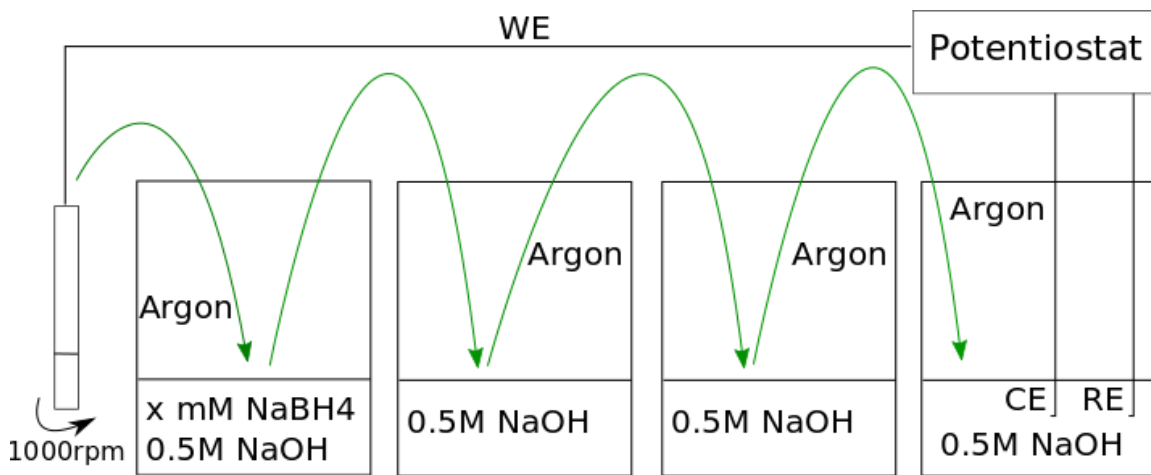
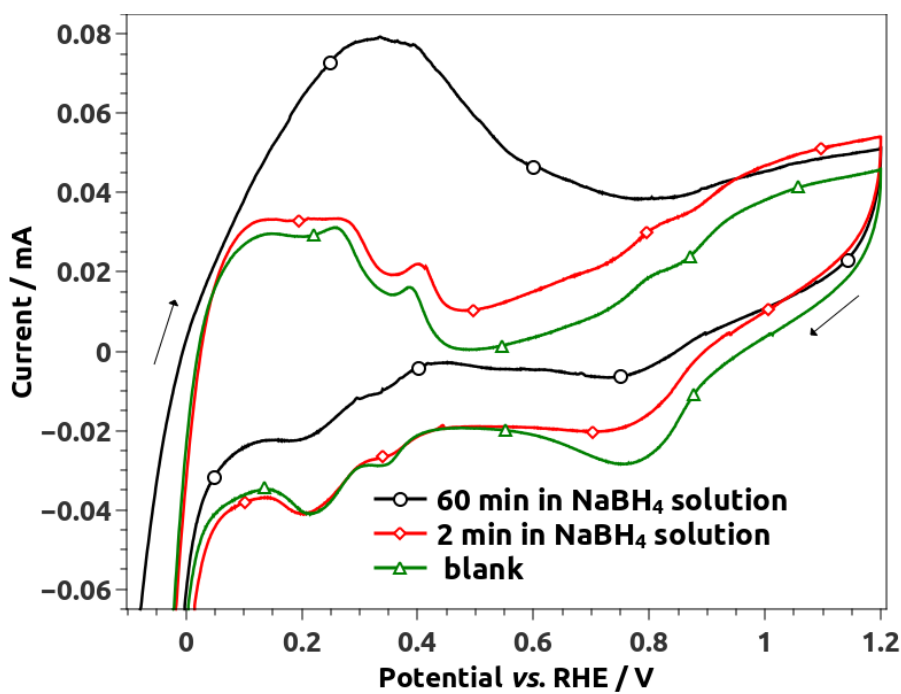


Figure B.1: Scheme of the 'BOR poison stripping' experiment.

Fig.B.2 shows the result for the experiment presented in Fig.B.1, using a concentration of sodium borohydride of 0.5 M in the first cell. The stripping voltammograms of the Pt RDE let to rest for 2 min and 60 min on the first cell (containing the sodium borohydride) are compared with the 'blank' voltammogram of a Pt RDE that went through the same procedure, except that the first cell did not contain any sodium borohydride. An oxidation stripping current is observed in Fig.B.2 when the Pt RDE was let to rest at OCP in the solution containing sodium borohydride. This stripping current is larger after the Pt RDE had been kept longer in contact with sodium borohydride, which concurs with the observation of the progressive poisoning of the Pt/GC electrode at OCP (Fig.4.4). It is in agreement with the global proposition for the BOR mechanism developed in the second part of this thesis: BH_{ads} species form on the Pt surface (even at OCP) from the dissociative adsorption of BH_4^- . The stripping of these BH_{ads} species in the last cell of this experiment leads to the oxidation current observed compared to the blank voltammogram.

Figure B.2: RDE voltammograms of a Pt RDE after various time of rest at OCP in a solution containing 0.5 M NaBH_4 and 0.5 M NaOH , at 1000 rpm and $25 \text{ mV}\cdot\text{s}^{-1}$. The blank voltammogram was performed on a Pt RDE which did not have any contact with sodium borohydride.

However, the results obtained from this experiment were not reproducible enough, so that the preliminary result presented here should be taken very carefully, and considered only as a first step for further discussion in order to achieve a more suitable experimental procedure (such as a flow-cell configuration). Indeed, the transfers of the Pt RDE from one cell to another are not very 'clean' and are likely to influence the results, especially when the voltammogram of interest is the first cycle of the linear cyclic voltammetry procedure. Also, an experimental artifact that could lead to similar results than the one presented in Fig.B.2 is the trapping of the solution containing the sodium borohydride in the electrode/electrode holder joints; the longer the Pt RDE in contact with this solution, the more solution could be trapped, leading to a higher 'stripping' oxidation current. A possible way in order to ignore this artifact would be to perform this experiment in hanging meniscus rotating disk electrode (HMRDE) configuration, *i.e.* without any holder for the Pt electrode. Even without any experimental issues, this experiment would still be tricky to interpret in the author's opinion. Indeed, according to the model presented in this thesis, BH_{ads} is not the same type of poison as CO_{ads} , which is totally electrochemically inactive on the Pt surface at low potentials, leading to a complete blocking of the Pt sites. If BH_{ads} behaved similarly to CO_{ads} , no BOR current would be observed on Pt at low potentials for any experimental conditions, which is obviously not the case. In our mechanism, BH_{ads} blocks the Pt surface because its Eley-Rideal type electrooxidation reaction with OH^- at low potential is relatively slow. However, BH_{ads} can still be oxidized on Pt at low potential, even if the rate is slow. This is likely to hinder the interpretation of any further ' BH_{ads} stripping' experiments.

Appendix C

Pt/VACNF: supplementary figures

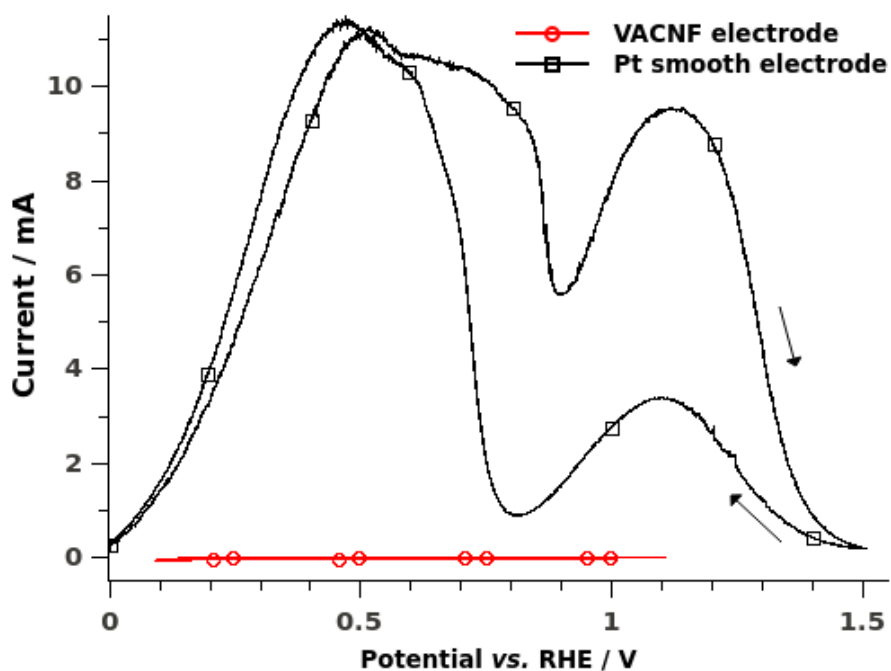


Figure C.1: Comparison of RDE BOR cyclic voltammograms of a VACNF electrode without Pt nanoparticles deposited and a smooth Pt electrode. 1000 rpm, 20 mV s^{-1} , 1 M NaOH + 10 mM NaBH_4 .

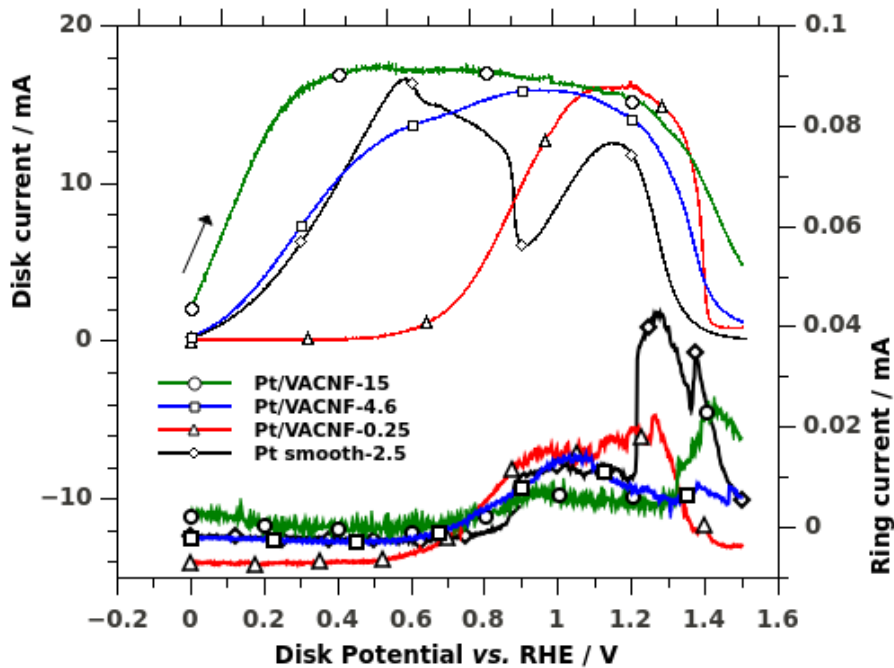


Figure C.2: RRDE voltammograms of 10 mM NaBH_4 in 1 M NaOH at 25 mV s^{-1} and 2500 rpm (positive-going scan). The disk was composed of the different samples described in the legend and was swept between 0 and 1.5 V *vs.* RHE, while the Au-ring was held at +0.2 V *vs.* RHE to detect BH_3OH^- intermediates. Legend: Electrode type-X, X being the Pt roughness of the electrode, in $\text{cm}^2_{\text{Pt EASA}}/\text{cm}^2_{\text{geometric}}$. Raw Au-ring current signals.

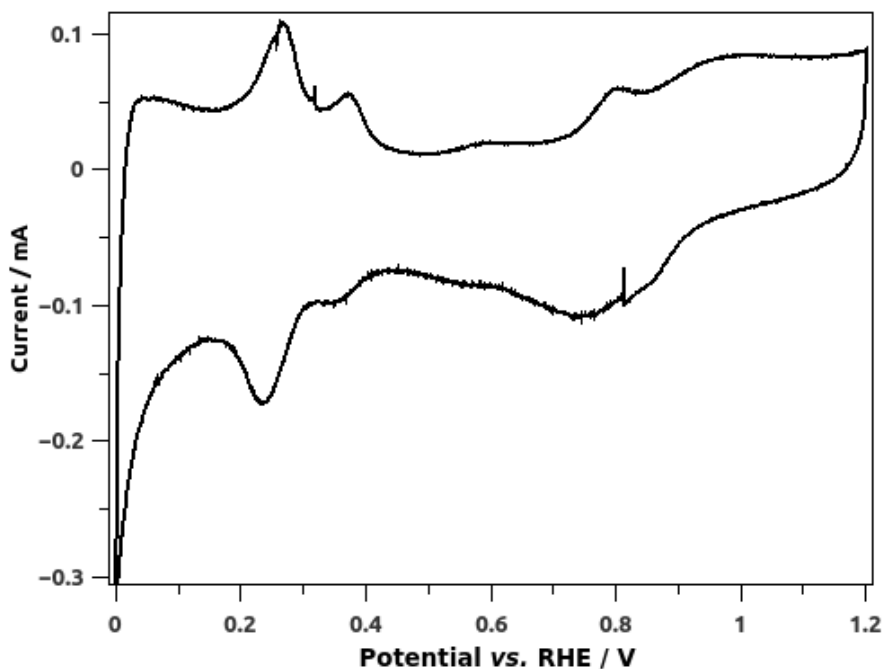


Figure C.3: Pt/VACNF-15 RDE voltammograms in 1 M NaOH at 25 mV s^{-1} and 1000 rpm (Pt/VACNF-15 is the Pt/VACNF electrode yielding the highest Pt roughness). Note the oxidative current due to OH^- adsorption above *ca.* 0.65 V *vs.* RHE.

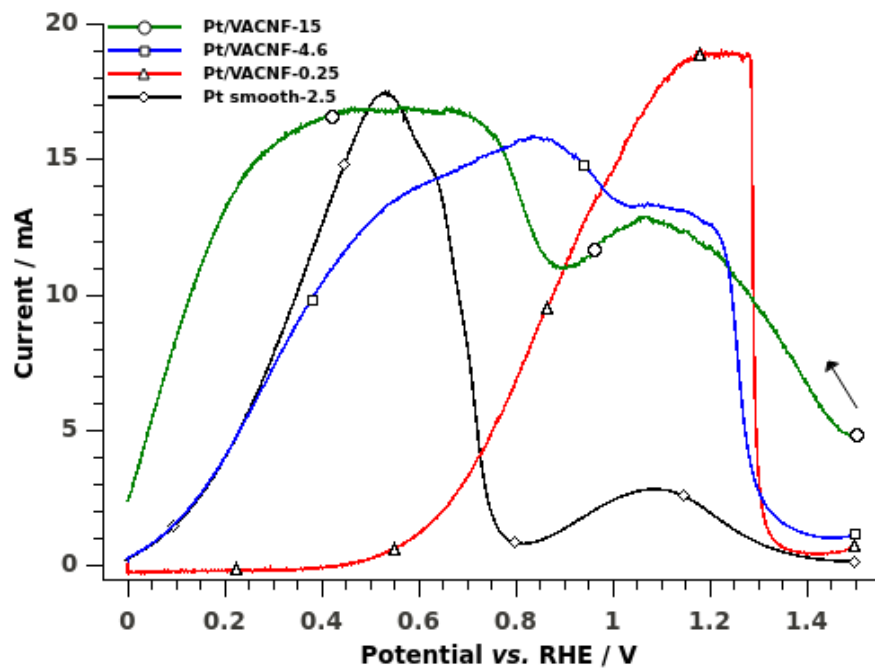


Figure C.4: RDE voltammograms of 10 mM NaBH_4 in 1 M NaOH at 25 mV s^{-1} and 2500 rpm. Negative-going scans. Legend: Electrode type-X, X being the Pt roughness of the electrode, in $\text{cm}^2_{\text{Pt EASA}}/\text{cm}^2_{\text{geometric}}$.

Appendix D

BOR Modelling

D.1 Supplementary figures

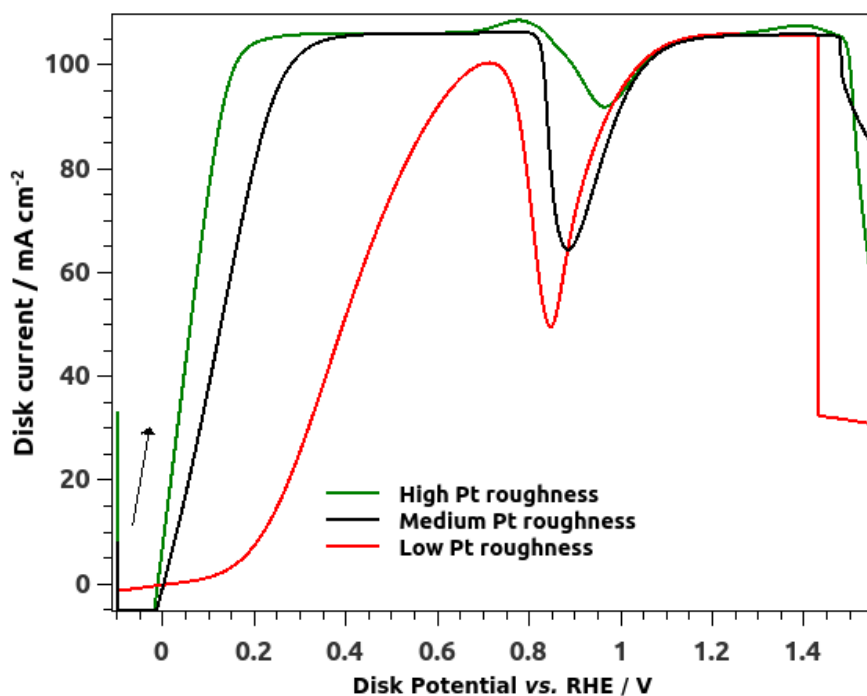


Figure D.1: Simulated RDE voltammograms of 10 mM NaBH₄ in 1 M NaOH at 25 mV s⁻¹ and 2500 rpm (positive-going scan). The constant values used for this modelling are the same as in Table 2, except for the charge transfer coefficient and the reaction constant (k_3) of the Eley-Rideal oxidation reaction of BH_{ads} equal respectively to 0 and 2000.

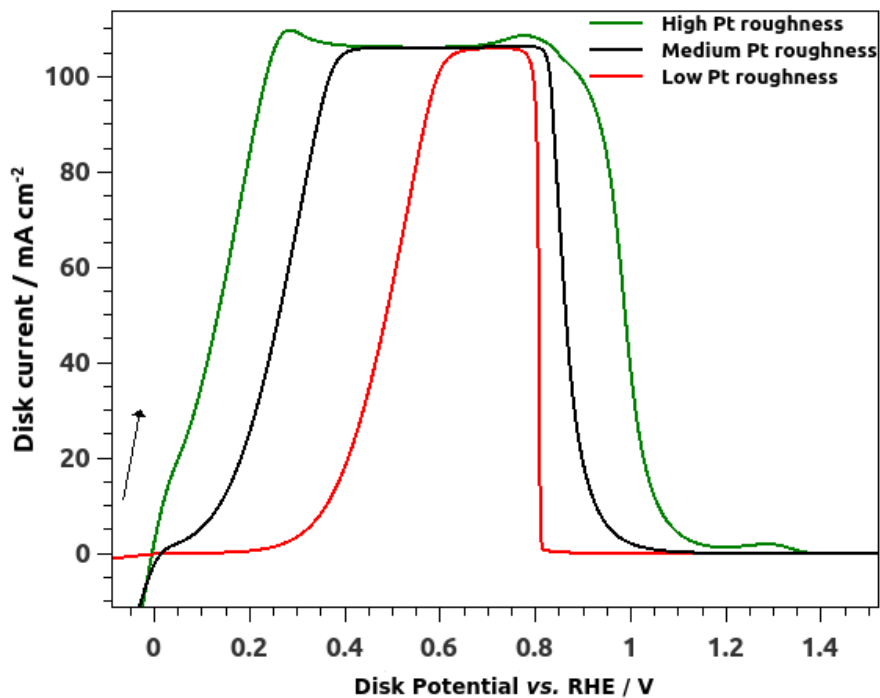


Figure D.2: Simulated RDE positive-going scan voltammograms of 10 mM NaBH₄ in 1 M NaOH at 25 mV s⁻¹ and 2500 rpm. The constant values used for this modelling are the same as in Table 2, except for the charge transfer coefficient and the reaction constant (k_3) of the Eley-Rideal oxidation reaction of BH_{ads} equal respectively to 0.5 and 0.2.

D.2 Approximation for the mass-transfer

The following Appendix comes from the fruitful discussion with Claude Montella, concerning the model presented in chapter 6. The author is grateful for the time he spent in explanation.

In the modelling presented in the chapter 6, the simplification of Koper *et al.* [204] was used. In this simplification, the concentration profile of every species in solution is assumed to be linear, with a constant diffusion thickness (δ). The principle of this simplification is shown in Fig.D.3.

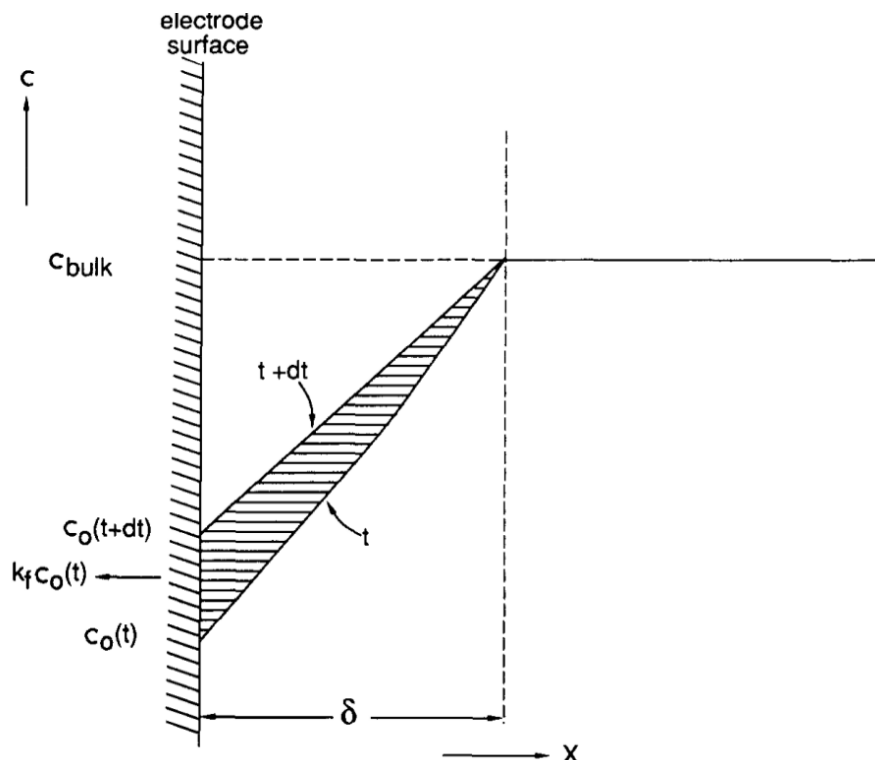


Figure D.3: The change in the concentration profile near the electrode in the time interval times a linear concentration gradient with fixed diffusion layer thickness δ . Reproduced from Ref. [204] with permission from Elsevier.

From this simplified model, the differential equation for the variation of the interfacial concentration of a given species X is as follows (Eq.D.1), considering that the species X is consumed at the electrode/electrolyte interface by electrochemical reaction(s) only (consumption rate of X being $v_X(t)$):

$$\frac{dc_X(0, t)}{dt} = 2 \left(\frac{v_X(t)}{\delta_X} + \frac{D_X}{\delta_X^2} (c_{X, \text{bulk}} - c_X(0, t)) \right) \quad (\text{D.1})$$

Where D_X is the diffusion coefficient of X and $v_X(t)$ is the consumption rate of X at the electrode surface. This Eq.D.1 was used in the chapter 6 of this thesis for the calculation of the interfacial concentrations of H_2 , BH_4^- and BH_3OH^- in Eqs. 6.6, 6.7 and 6.8, respectively.

Although simplified, a suitable model should enable the flux boundary condition (so-called continuity condition) to be satisfied at the electrode/electrolyte interface. The continuity of the

flux of X at the interface is written as:

$$J_X(0, t) = v_X(t) \quad (\text{D.2})$$

Considering the concentration profile of X in the model of Koper *et al.*, the flux of X at the electrode/electrolyte interface can also be expressed as:

$$J_X(0, t) = -\frac{D_X}{\delta_X}(c_{X,\text{bulk}} - c_X(0, t)) \quad (\text{D.3})$$

Taking Eqs.D.2 and D.3 into Eq. D.1, it gives:

$$\forall t, \frac{dc_X(0, t)}{dt} = 0 \quad (\text{D.4})$$

Eq.D.4 shows that the simplification model of Koper *et al.* does not enable the interfacial flux continuity in a dynamic state, which is not appropriate. However, considering the following decomposition of the time derivative of the interfacial concentration in X:

$$\frac{dc_X(0, t)}{dt} = \frac{dc_X(0, t)}{dE} \frac{dE(t)}{dt} \quad (\text{D.5})$$

the condition given in Eq.D.4 to fulfill the flux continuity for the Koper *et al.* simplified model is approached considering that $\frac{dE(t)}{dt}$, *i.e.* the potential sweep rate of the linear sweep voltammetry (LSV) method, tends to zero. In other words, although based on a physically incorrect simplification, the model of Koper *et al.* tends to correct results in near-steady-state conditions.

A physically-correct simplified model to approximate the mass-transfer was presented by Berthier *et al.* [212]. Briefly, the simplification was made by a first order series development of the expression of the Faradaic impedance, used together with inverse Laplace transformation of the relevant equation. This Faradaic impedance being established using the general equations of convection-diffusion in Nernst conditions (*i.e.* for the limit condition $c_X(x = \delta) = c_{X,\text{bulk}}$), for which the concentration profile of the given species is not considered linear, in opposition to the assumption of Koper *et al.* [204]. In this case, the differential equation for the variation of the interfacial concentration of a given species X is as follows (Eq.D.6):

$$\frac{dc_X(0, t)}{dt} = \frac{\pi^2}{4} \left(\frac{v_X(t)}{\delta_X} + \frac{D_X}{\delta_X^2}(c_{X,\text{bulk}} - c_X(0, t)) \right) \quad (\text{D.6})$$

One can observe that, although the reasoning behind the Koper *et al.* and the Berthier *et al.* simplified models are different, they lead to relatively close expressions (Eqs.D.1 and D.6, respectively), as $\frac{\pi^2}{4}$ is close to 2. This would explain why the simplified model of Koper *et al.* leads to relatively accurate simulated curves in dynamic conditions, although the core of this model is physically incorrect. In the particular case of the modelling presented in this thesis, the use of either the Koper *et al.* or the Berthier *et al.* simplified model (in other words, the use of either 2 or $\frac{\pi^2}{4}$, respectively, in the mass-transfer differential equations 6.6, 6.7 and 6.8) did not lead to any change in the simulated curves, as the revolution rate (2,500 rpm) and the sweep rate (25 mV.s⁻¹) were relatively fast and slow, respectively, so that our system can be considered to be in near-steady-state conditions.

Bibliography

- [1] R. L. Pecsok, *J. Am. Chem. Soc.* 75 (1953) 2862–2864. doi:[10.1021/ja01108a021](https://doi.org/10.1021/ja01108a021).
- [2] J. A. Gardiner, J. W. Collat, *Inorg. Chem.* 4 (1965) 1208–1212. doi:[10.1021/ic50030a026](https://doi.org/10.1021/ic50030a026).
- [3] W. H. Stockmayer, D. W. Rice, C. C. Stephenson, *J. Am. Chem. Soc.* 77 (1955) 1980–1983. doi:[10.1021/ja01612a082](https://doi.org/10.1021/ja01612a082).
- [4] J. H. Morris, H. J. Gysling, D. Reed, *Chem. Rev.* 85 (1985) 51–76. doi:[10.1021/cr00065a003](https://doi.org/10.1021/cr00065a003).
- [5] E. D. Marshall, R. A. Widing, U. S. A. E. Commission, U. C. Division, C. C. Carbide, C. Chemicals, Some properties of sodium borohydride solutions, U.S. Atomic Energy Commission. Technical Information Division, 1950. URL: <http://babel.hathitrust.org/cgi/pt?id=mdp.39015086572958>.
- [6] K. Mochalov, V. Khain, G. Gil'manshin, *Doklady Akademii Nauk SSSR* 162 (1965) 613–616.
- [7] S. C. Amendola, S. L. Sharp-Goldman, M. S. Janjua, M. T. Kelly, P. J. Petillo, M. Binder, *J. Power Sources* 85 (2000) 186–189. doi:[10.1016/S0378-7753\(99\)00301-8](https://doi.org/10.1016/S0378-7753(99)00301-8).
- [8] S. C. Amendola, S. L. Sharp-Goldman, M. S. Janjua, N. C. Spencer, M. T. Kelly, P. J. Petillo, M. Binder, *Int. J. Hydrogen Energy* 25 (2000) 969–975. doi:[10.1016/S0360-3199\(00\)00021-5](https://doi.org/10.1016/S0360-3199(00)00021-5).
- [9] B. Liu, Z. Li, *J. Power Sources* 187 (2009) 527–534. doi:[10.1016/j.jpowsour.2008.11.032](https://doi.org/10.1016/j.jpowsour.2008.11.032).
- [10] U. B. Demirci, *Int. J. Hydrogen Energy* 40 (2015) 2673–2691. doi:[10.1016/j.ijhydene.2014.12.067](https://doi.org/10.1016/j.ijhydene.2014.12.067).
- [11] M. E. Indig, R. N. Snyder, *Journal of The Electrochemical Society* 109 (1962) 1104–1106. doi:[10.1149/1.2425247](https://doi.org/10.1149/1.2425247).
- [12] S. C. Amendola, P. Onnerud, M. T. Kelly, P. J. Petillo, S. L. Sharp-Goldman, M. Binder, *J. Power Sources* 84 (1999) 130–133. doi:[10.1016/S0378-7753\(99\)00259-1](https://doi.org/10.1016/S0378-7753(99)00259-1).
- [13] N. Choudhury, R. Raman, S. Sampath, A. Shukla, *J. Power Sources* 143 (2005) 1–8. doi:[10.1016/j.jpowsour.2004.08.059](https://doi.org/10.1016/j.jpowsour.2004.08.059).
- [14] C. Ponce de León, F. Walsh, A. Rose, J. Lakeman, D. Browning, R. Reeve, *J. Power Sources* 164 (2007) 441–448. doi:[10.1016/j.jpowsour.2006.10.069](https://doi.org/10.1016/j.jpowsour.2006.10.069).
- [15] R. K. Raman, N. A. Choudhury, A. K. Shukla, *Electrochem. Solid State Lett.* 7 (2004) A488–A491. doi:[10.1149/1.1817855](https://doi.org/10.1149/1.1817855).

- [16] C. Ponce de Leon, F. Walsh, D. Pletcher, D. Browning, J. Lakeman, J. Power Sources 155 (2006) 172–181. doi:[10.1016/j.jpowsour.2006.01.011](https://doi.org/10.1016/j.jpowsour.2006.01.011).
- [17] H. I. Schlesinger, H. C. Brown, et al., J. Am. Chem. Soc. 75 (1953) 186–190. doi:[10.1021/ja01097a049](https://doi.org/10.1021/ja01097a049).
- [18] H. C. Brown, J. Organomet. Chem. 100 (1975) 3–15. doi:[10.1016/S0022-328X\(00\)88930-5](https://doi.org/10.1016/S0022-328X(00)88930-5).
- [19] H. I. Schlesinger, H. C. Brown, A. E. Finholt, J. Am. Chem. Soc. 75 (1953) 205–209. doi:[10.1021/ja01097a054](https://doi.org/10.1021/ja01097a054).
- [20] Y. Wu, M. T. Kelly, J. V. Ortega, Review of Chemical Processes for the Synthesis of Sodium Borohydride, DOE Cooperative Agreement DE-FC36-04GO14008, Technical Report, 2004. URL: http://www1.eere.energy.gov/hydrogenandfuelcells/pdfs/review_chemical_processes.pdf.
- [21] D. M. F. Santos, C. A. C. Sequeira, Renew. Sust. Energ. Rev. 15 (2011) 3980–4001. doi:[10.1016/j.rser.2011.07.018](https://doi.org/10.1016/j.rser.2011.07.018).
- [22] F. Schubert, K. Lang, Angew. Chemie. 72 (1960) 994–1000. doi:[10.1002/ange.19600722413](https://doi.org/10.1002/ange.19600722413).
- [23] W. Büchner, H. Niederprüm, Pure Appl. Chem. 49 (1977) 733–743. URL: <http://pubs.iupac.org/publications/pac/pdf/1977/pdf/4906x0733.pdf>.
- [24] G. Onal, F. Burat, Gospodarka Surowcami Mineralnymi 24 (2008). URL: <http://www.meeri.eu/Wydawnictwa/GSM2443/onal-burat.pdf>.
- [25] O. Yılmaz, Insight Turkey 9 (2007) 37–47. URL: http://files.setav.org/uploads/Pdf/orhan_yilmaz.pdf.
- [26] Boron, Mineral commodity summaries, Survey, U.S. Geological, 2008. URL: <http://minerals.usgs.gov/minerals/pubs/mcs/2008/mcs2008.pdf>.
- [27] J. Yamamoto, Rohm and Haas : the Sodium Borohydride Digest, Technical Report, 2003. URL: http://www.dow.com/assets/attachments/industry/pharma_medical/chemical_reagents/reducing_agents/sodium_borohydride_digest.pdf.
- [28] M. Kilpatrick, C. D. M. Jr., J. Am. Chem. Soc. 72 (1950) 5474–5476. doi:[10.1021/ja01168a027](https://doi.org/10.1021/ja01168a027).
- [29] H. I. Schlesinger, H. C. Brown, A. E. Finholt, J. R. Gilbreath, H. R. Hoekstra, E. K. Hyde, J. Am. Chem. Soc. 75 (1953) 215–219. doi:[10.1021/ja01097a057](https://doi.org/10.1021/ja01097a057).
- [30] R. E. Davis, E. Bromels, C. L. Kibby, J. Am. Chem. Soc. 84 (1962) 885–892. doi:[10.1021/ja00865a001](https://doi.org/10.1021/ja00865a001).
- [31] J. B. Brown, M. Svensson, J. Am. Chem. Soc. 79 (1957) 4241–4242. doi:[10.1021/ja01572a071](https://doi.org/10.1021/ja01572a071).
- [32] K. Mochalov, V. Khain, G. Gil'manshin, Kinetika i Kataliz 9 (1965) 541–544.
- [33] V. G. Minkina, S. I. Shabunya, V. I. Kalinin, V. V. Martynenko, Russ. J. Appl. Chem. 81 (2008) 380–385. doi:[10.1134/S1070427208030051](https://doi.org/10.1134/S1070427208030051).

- [34] Y. Kojima, T. Haga, *Int. J. Hydrogen Energy* 28 (2003) 989–993. doi:[10.1016/S0360-3199\(02\)00173-8](https://doi.org/10.1016/S0360-3199(02)00173-8).
- [35] Z. Li, B. Liu, K. Arai, N. Morigazaki, S. Suda, *J. Alloys Compd.* 356–357 (2003) 469–474. doi:[10.1016/S0925-8388\(02\)01241-0](https://doi.org/10.1016/S0925-8388(02)01241-0).
- [36] H.B.H. Cooper, *Electrocatalytic Process for the Production of Alkali Metal Borohydrides*, US Patent US3734842 A, 1973. URL: <http://www.google.com/patents/US3734842>.
- [37] E. L. Gyenge, C. W. Oloman, *J. Appl. Electrochem.* 28 (1998) 1147–1151.
- [38] D. M. F. Santos, C. A. C. Sequeira, *Int. J. Hydrogen Energy* 35 (2010) 9851–9861. doi:[10.1016/j.ijhydene.2010.01.129](https://doi.org/10.1016/j.ijhydene.2010.01.129).
- [39] U. B. Demirci, *Journal of Power Sources* 172 (2007) 676–687. doi:[10.1016/j.jpowsour.2007.05.009](https://doi.org/10.1016/j.jpowsour.2007.05.009).
- [40] Z. Li, B. Liu, K. Arai, K. Asaba, S. Suda, *J. Power Sources* 126 (2004) 28–33. doi:[10.1016/j.jpowsour.2003.08.017](https://doi.org/10.1016/j.jpowsour.2003.08.017).
- [41] Z. Li, B. Liu, K. Arai, S. Suda, *J. Alloys Compd.* 404–406 (2005) 648–652. doi:[10.1016/j.jallcom.2005.01.130](https://doi.org/10.1016/j.jallcom.2005.01.130).
- [42] J.-H. Wee, *J. Power Sources* 161 (2006) 1–10. doi:[10.1016/j.jpowsour.2006.07.032](https://doi.org/10.1016/j.jpowsour.2006.07.032).
- [43] H. Liu, C. Song, L. Zhang, J. Zhang, H. Wang, D. P. Wilkinson, *J. Power Sources* 155 (2006) 95–110. doi:[10.1016/j.jpowsour.2006.01.030](https://doi.org/10.1016/j.jpowsour.2006.01.030).
- [44] S. Mekhilef, R. Saidur, A. Safari, *Renew. Sust. Energ. Rev.* 16 (2012) 981–989. doi:[10.1016/j.rser.2011.09.020](https://doi.org/10.1016/j.rser.2011.09.020).
- [45] B. Molina Concha, M. Chatenet, E. A. Ticianelli, F. H. B. Lima, *J. Phys. Chem. C* 115 (2011) 12439–12447. doi:[10.1021/jp2002589](https://doi.org/10.1021/jp2002589).
- [46] R. Jamard, J. Salomon, A. Martinent-Beaumont, C. Coutanceau, *J. Power Sources* 193 (2009) 779–787. doi:[10.1016/j.jpowsour.2009.03.057](https://doi.org/10.1016/j.jpowsour.2009.03.057).
- [47] Website of CNET: 'Medis Power Pack: A fuel cell gadget charger', 2008, accessed: August 2015. URL: <http://www.cnet.com/news/medis-power-pack-a-fuel-cell-gadget-charger>.
- [48] Website of HAARETZ: 'Medis Tech reaches the end of its road', 2009, accessed: August 2015. URL: <http://www.haaretz.com/print-edition/business/medis-tech-reaches-the-end-of-its-road-1.3935>.
- [49] Website of MERIT Ltd., accessed: August 2015. URL: <http://www.hydrogen.co.jp/merit/R&D/DBFC/DBFC.html>.
- [50] C. Yao, H. Yang, L. Zhuang, X. Ai, Y. Cao, J. Lu, *J. Power Sources* 165 (2007) 167–171. doi:[10.1016/j.jpowsour.2006.11.050](https://doi.org/10.1016/j.jpowsour.2006.11.050).
- [51] X.-B. Zhang, S. Han, J.-M. Yan, M. Chandra, H. Shioyama, K. Yasuda, N. Kuriyama, T. Kobayashi, Q. Xu, *J. Power Sources* 168 (2007) 167–171. doi:[10.1016/j.jpowsour.2007.03.009](https://doi.org/10.1016/j.jpowsour.2007.03.009).
- [52] L. C. Nagle, J. F. Rohan, *J. Electrochem. Soc.* 153 (2006) C773–C776. doi:[10.1149/1.2344842](https://doi.org/10.1149/1.2344842).

- [53] A. de Vooy, M. Koper, R. van Santen, J. van Veen, *J. Electroanal. Chem.* 506 (2001) 127–137. doi:[10.1016/S0022-0728\(01\)00491-0](https://doi.org/10.1016/S0022-0728(01)00491-0).
- [54] V. Rosca, M. Duca, M. T. de Groot, M. T. M. Koper, *Chem. Rev.* 109 (2009) 2209–2244. doi:[10.1021/cr8003696](https://doi.org/10.1021/cr8003696).
- [55] K. T. Park, U. H. Jung, S. U. Jeong, S. H. Kim, *J. Power Sources* 162 (2006) 192–197. doi:[10.1016/j.jpowsour.2006.07.040](https://doi.org/10.1016/j.jpowsour.2006.07.040).
- [56] B. Liu, Z. Li, J. Zhu, S. Suda, *J. Power Sources* 183 (2008) 151–156. doi:[10.1016/j.jpowsour.2008.04.079](https://doi.org/10.1016/j.jpowsour.2008.04.079).
- [57] B. Liu, Z. Li, *J. Power Sources* 187 (2009) 291–297. doi:[10.1016/j.jpowsour.2008.11.017](https://doi.org/10.1016/j.jpowsour.2008.11.017).
- [58] D. A. Finkelstein, C. D. Letcher, D. J. Jones, L. M. Sandberg, D. J. Watts, H. D. Abruña, *Journal of Physical Chemistry C* 117 (2013) 1571–1581. doi:[10.1021/jp308677f](https://doi.org/10.1021/jp308677f).
- [59] P.-Y. Olu, C. R. Barros, N. Job, M. Chatenet, *Electrocatalysis* 5 (2014) 288–300. doi:[10.1007/s12678-014-0195-0](https://doi.org/10.1007/s12678-014-0195-0).
- [60] P.-Y. Olu, A. Bonnefont, M. Rouhet, S. Bozdech, N. Job, M. Chatenet, E. Savinova, *Electrochim. Acta* In Press (2015). doi:[10.1016/j.electacta.2015.02.158](https://doi.org/10.1016/j.electacta.2015.02.158).
- [61] B. H. Liu, S. Suda, *J. Power Sources* 164 (2007) 100–104. doi:[10.1016/j.jpowsour.2006.09.107](https://doi.org/10.1016/j.jpowsour.2006.09.107).
- [62] R. Jamard, A. Latour, J. Salomon, P. Capron, A. Martinent-Beaumont, *J. Power Sources* 176 (2008) 287–292. doi:[10.1016/j.jpowsour.2007.10.036](https://doi.org/10.1016/j.jpowsour.2007.10.036).
- [63] G. R. Li, Q. Q. Wang, B. H. Liu, Z. P. Li, *Fuel Cells* 15 (2015) 270–277. doi:[10.1002/fuce.201300283](https://doi.org/10.1002/fuce.201300283).
- [64] A. Zadick, L. Dubau, N. Sergent, G. Berthomé, M. Chatenet, *ACS Catal.* 5 (2015) 4819–4824. doi:[10.1021/acscatal.5b01037](https://doi.org/10.1021/acscatal.5b01037).
- [65] U. B. Demirci, P. Miele, *Energy Environ. Sci.* 2 (2009) 627–637. doi:[10.1039/b900595a](https://doi.org/10.1039/b900595a).
- [66] J. Ma, N. A. Choudhury, Y. Sahai, *Renew. Sust. Energ. Rev.* 14 (2010) 183–199. doi:[10.1016/j.rser.2009.08.002](https://doi.org/10.1016/j.rser.2009.08.002).
- [67] I. Merino-Jiménez, C. Ponce de León, A. Shah, F. Walsh, *J. Power Sources* 219 (2012) 339–357. doi:[10.1016/j.jpowsour.2012.06.091](https://doi.org/10.1016/j.jpowsour.2012.06.091).
- [68] C. P. de León, F. Walsh, *Encyclopedia of Electrochemical Power Sources* (2009) 192–205. doi:[10.1016/B978-044452745-5.00843-1](https://doi.org/10.1016/B978-044452745-5.00843-1).
- [69] C. P. de Leon, F. Walsh, *Reference Module in Chemistry, Molecular Sciences and Chemical Engineering* (2015). doi:[10.1016/B978-0-12-409547-2.11190-4](https://doi.org/10.1016/B978-0-12-409547-2.11190-4).
- [70] J.-H. Wee, *J. Power Sources* 155 (2006) 329–339. doi:[10.1016/j.jpowsour.2006.01.036](https://doi.org/10.1016/j.jpowsour.2006.01.036).
- [71] G. Behmenyar, A. N. Akin, *J. Power Sources* 249 (2014) 239–246. doi:[10.1016/j.jpowsour.2013.10.063](https://doi.org/10.1016/j.jpowsour.2013.10.063).
- [72] X. Geng, H. Zhang, W. Ye, Y. Ma, H. Zhong, *J. Power Sources* 185 (2008) 627–632. doi:[10.1016/j.jpowsour.2008.09.010](https://doi.org/10.1016/j.jpowsour.2008.09.010).

- [73] X. Geng, H. Zhang, Y. Ma, H. Zhong, *J. Power Sources* 195 (2010) 1583–1588. doi:[10.1016/j.jpowsour.2009.09.036](https://doi.org/10.1016/j.jpowsour.2009.09.036).
- [74] H. Cheng, K. Scott, K. Lovell, *Fuel Cells* 06 (2006) 367–375. doi:[10.1002/fuce.200500260](https://doi.org/10.1002/fuce.200500260).
- [75] H. Cheng, K. Scott, *J. Appl. Electrochem.* 36 (2006) 1361–1366. doi:[10.1007/s10800-006-9199-7](https://doi.org/10.1007/s10800-006-9199-7).
- [76] E. Gyenge, M. Atwan, D. Northwood, *J. Electrochem. Soc* 153 (2006) A150–A158. doi:[10.1149/1.2131831](https://doi.org/10.1149/1.2131831).
- [77] M. H. Atwan, C. L. Macdonald, D. O. Northwood, E. L. Gyenge, *J. Power Sources* 158 (2006) 36–44. doi:[10.1016/j.jpowsour.2005.09.054](https://doi.org/10.1016/j.jpowsour.2005.09.054).
- [78] A. Aziznia, C. W. Oloman, E. L. Gyenge, *J. Power Sources* 212 (2012) 154–160. doi:[10.1016/j.jpowsour.2012.03.047](https://doi.org/10.1016/j.jpowsour.2012.03.047).
- [79] A. Aziznia, C. W. Oloman, E. L. Gyenge, *ChemSusChem* 6 (2013) 847–855. doi:[10.1002/cssc.201300127](https://doi.org/10.1002/cssc.201300127).
- [80] A. Aziznia, C. W. Oloman, E. L. Gyenge, *J. Power Sources* 265 (2014) 201–213. doi:[10.1016/j.jpowsour.2014.04.037](https://doi.org/10.1016/j.jpowsour.2014.04.037).
- [81] M. Chatenet, F. Micoud, I. Roche, E. Chainet, J. Vondrak, *Electrochim. Acta.* 51 (2006) 5452–5458. doi:[10.1016/j.electacta.2006.02.014](https://doi.org/10.1016/j.electacta.2006.02.014).
- [82] A. C. Garcia, F. H. Lima, E. A. Ticianelli, M. Chatenet, *J. Power Sources* 222 (2013) 305–312. doi:[10.1016/j.jpowsour.2012.08.049](https://doi.org/10.1016/j.jpowsour.2012.08.049).
- [83] A. Verma, S. Basu, *J. Power Sources* 168 (2007) 200–210. doi:[10.1016/j.jpowsour.2007.02.069](https://doi.org/10.1016/j.jpowsour.2007.02.069).
- [84] H. Cheng, K. Scott, *J. Electroanal. Chem.* 586 (2006) 117–123. doi:[10.1016/j.jelechem.2006.07.031](https://doi.org/10.1016/j.jelechem.2006.07.031).
- [85] V. Lam, D. Kannangara, A. Alfantazi, E. Gyenge, *J. Power Sources* 212 (2012) 57–65. doi:[10.1016/j.jpowsour.2012.03.067](https://doi.org/10.1016/j.jpowsour.2012.03.067).
- [86] V. W. S. Lam, E. L. Gyenge, *J. Electrochem. Soc* 155 (2008) B1155–B1160. doi:[10.1149/1.2975191](https://doi.org/10.1149/1.2975191).
- [87] Z. Li, B. Liu, J. Zhu, S. Suda, *J. Power Sources* 163 (2006) 555–559. doi:[10.1016/j.jpowsour.2006.09.037](https://doi.org/10.1016/j.jpowsour.2006.09.037).
- [88] J. Ma, Y. Sahai, R. G. Buchheit, *J. Power Sources* 195 (2010) 4709–4713. doi:[10.1016/j.jpowsour.2010.02.034](https://doi.org/10.1016/j.jpowsour.2010.02.034).
- [89] N. A. Choudhury, J. Ma, Y. Sahai, *J. Power Sources* 210 (2012) 358–365. doi:[10.1016/j.jpowsour.2012.03.013](https://doi.org/10.1016/j.jpowsour.2012.03.013).
- [90] J. Ma, N. A. Choudhury, Y. Sahai, R. G. Buchheit, *J. Power Sources* 196 (2011) 8257–8264. doi:[10.1016/j.jpowsour.2011.06.009](https://doi.org/10.1016/j.jpowsour.2011.06.009).
- [91] J. Ma, Y. Sahai, R. G. Buchheit, *J. Power Sources* 202 (2012) 18–27. doi:[10.1016/j.jpowsour.2011.11.003](https://doi.org/10.1016/j.jpowsour.2011.11.003).

- [92] C.-C. Huang, Y.-L. Liu, W.-H. Pan, C.-M. Chang, C.-M. Shih, H.-Y. Chu, C.-H. Chien, C.-H. Juan, S. J. Lue, *J. Polym. Sci. Pol. Phys.* 51 (2013) 1779–1789. doi:[10.1002/polb.23250](https://doi.org/10.1002/polb.23250).
- [93] P.-Y. Olu, F. Deschamps, G. Caldarella, M. Chatenet, N. Job, *J. Power Sources* 297 (2015) 492–503. doi:[10.1016/j.jpowsour.2015.08.022](https://doi.org/10.1016/j.jpowsour.2015.08.022).
- [94] S. Li, Y. Liu, Y. Liu, Y. Chen, *J. Power Sources* 195 (2010) 7202–7206. doi:[10.1016/j.jpowsour.2010.05.016](https://doi.org/10.1016/j.jpowsour.2010.05.016).
- [95] S. Li, X. Yang, H. Zhu, Y. Chen, Y. Liu, *J. Power Sources* 196 (2011) 5858–5862. doi:[10.1016/j.jpowsour.2011.02.016](https://doi.org/10.1016/j.jpowsour.2011.02.016).
- [96] X. Yang, X. Wei, C. Liu, Y. Liu, *Mater. Chem. Phys.* 145 (2014) 269–273. doi:[10.1016/j.matchemphys.2014.01.044](https://doi.org/10.1016/j.matchemphys.2014.01.044).
- [97] X. Yang, Y. Liu, S. Li, X. Wei, L. Wang, Y. Chen, *Sci. Rep.* 2 (2012) 567. doi:[10.1038/srep00567](https://doi.org/10.1038/srep00567).
- [98] H. Qin, Z. Liu, W. Yin, J. Zhu, Z. Li, *J. Power Sources* 185 (2008) 909–912. doi:[10.1016/j.jpowsour.2008.08.047](https://doi.org/10.1016/j.jpowsour.2008.08.047).
- [99] H. Y. Qin, Z. X. Liu, L. Q. Ye, J. K. Zhu, Z. P. Li, *J. Power Sources* 192 (2009) 385–390. doi:[10.1016/j.jpowsour.2009.03.006](https://doi.org/10.1016/j.jpowsour.2009.03.006).
- [100] H. Qin, Z. Liu, S. Lao, J. Zhu, Z. Li, *J. Power Sources* 195 (2010) 3124–3129. doi:[10.1016/j.jpowsour.2009.12.001](https://doi.org/10.1016/j.jpowsour.2009.12.001).
- [101] H. Qin, S. Lao, Z. Liu, J. Zhu, Z. Li, *Int. J. Hydrogen Energy* 35 (2010) 1872–1878. doi:[10.1016/j.ijhydene.2010.01.014](https://doi.org/10.1016/j.ijhydene.2010.01.014).
- [102] J. Ma, J. Wang, Y. Liu, *J. Power Sources* 172 (2007) 220–224. doi:[10.1016/j.jpowsour.2007.07.031](https://doi.org/10.1016/j.jpowsour.2007.07.031).
- [103] J. Ma, Y. Liu, P. Zhang, J. Wang, *Electrochem. Commun.* 10 (2008) 100–102. doi:[10.1016/j.elecom.2007.11.006](https://doi.org/10.1016/j.elecom.2007.11.006).
- [104] J. Ma, Y. Liu, Y. Liu, Y. Yan, P. Zhang, *Fuel Cells* 8 (2008) 394–398. doi:[10.1002/fuce.200800048](https://doi.org/10.1002/fuce.200800048).
- [105] Y.-g. Wang, Y.-y. Xia, *Electrochem. Commun.* 8 (2006) 1775–1778. doi:[10.1016/j.elecom.2006.08.018](https://doi.org/10.1016/j.elecom.2006.08.018).
- [106] C. Kim, K.-J. Kim, M. Y. Ha, *J. Power Sources* 180 (2008) 154–161. doi:[10.1016/j.jpowsour.2008.01.042](https://doi.org/10.1016/j.jpowsour.2008.01.042).
- [107] Z. P. Li, B. H. Liu, K. Arai, S. Suda, *J. Electrochem. Soc.* 150 (2003) A868–A872. doi:[10.1149/1.1576767](https://doi.org/10.1149/1.1576767).
- [108] B. H. Liu, Z. P. Li, S. Suda, *J. Power Sources* 175 (2008) 226–231. doi:[10.1016/j.jpowsour.2007.09.047](https://doi.org/10.1016/j.jpowsour.2007.09.047).
- [109] J.-H. Kim, H.-S. Kim, Y.-M. Kang, M.-S. Song, S. Rajendran, S.-C. Han, D.-H. Jung, J.-Y. Lee, *J. Electrochem. Soc.* 151 (2004) A1039–A1043. doi:[10.1149/1.1756351](https://doi.org/10.1149/1.1756351).
- [110] V. W. S. Lam, A. Alfantazi, E. L. Gyenge, *J. Appl. Electrochem.* 39 (2009) 1763–1770. doi:[10.1007/s10800-009-9875-5](https://doi.org/10.1007/s10800-009-9875-5).

- [111] X. Yang, Private communication, 2015.
- [112] H. Cheng, K. Scott, J. Power Sources 160 (2006) 407–412. doi:[10.1016/j.jpowsour.2006.01.097](https://doi.org/10.1016/j.jpowsour.2006.01.097).
- [113] N. Duteanu, G. Vlachogiannopoulos, M. R. Shivhare, E. H. Yu, K. Scott, J. Appl. Electrochem. 37 (2007) 1085–1091. doi:[10.1007/s10800-007-9360-y](https://doi.org/10.1007/s10800-007-9360-y).
- [114] F. G. Boyacı San, O. Okur, C. I. Karadag, I. Isik-Gulsac, E. Okumus, Energy 71 (2014) 160–169. doi:[10.1016/j.energy.2014.04.037](https://doi.org/10.1016/j.energy.2014.04.037).
- [115] C. Celik, F. G. B. San, H. I. Sarac, J. Power Sources 185 (2008) 197–201. doi:[10.1016/j.jpowsour.2008.06.066](https://doi.org/10.1016/j.jpowsour.2008.06.066).
- [116] T. Okada, G. Xie, O. Gorseth, S. Kjelstrup, N. Nakamura, T. Arimura, Electrochim. Acta. 43 (1998) 3741–3747. doi:[10.1016/S0013-4686\(98\)00132-7](https://doi.org/10.1016/S0013-4686(98)00132-7).
- [117] B. Liu, Z. Li, K. Arai, S. Suda, Electrochim. Acta. 50 (2005) 3719–3725. doi:[10.1016/j.electacta.2005.01.018](https://doi.org/10.1016/j.electacta.2005.01.018).
- [118] Z. Mai, H. Zhang, X. Li, X. Geng, H. Zhang, Electrochem. Commun. 13 (2011) 1009–1012. doi:[10.1016/j.elecom.2011.06.029](https://doi.org/10.1016/j.elecom.2011.06.029).
- [119] D. Chen, S. Yu, X. Liu, X. Li, J. Power Sources 282 (2015) 323–327. doi:[10.1016/j.jpowsour.2015.02.082](https://doi.org/10.1016/j.jpowsour.2015.02.082).
- [120] H. Cheng, K. Scott, K. Lovell, J. Horsfall, S. Waring, J. Membr. Sci. 288 (2007) 168–174. doi:[10.1016/j.memsci.2006.11.014](https://doi.org/10.1016/j.memsci.2006.11.014).
- [121] H. A. Gasteiger, S. S. Kocha, B. Sompalli, F. T. Wagner, Appl. Catal., B. 56 (2005) 9–35. doi:[10.1016/j.apcatb.2004.06.021](https://doi.org/10.1016/j.apcatb.2004.06.021).
- [122] C. I. Karadag, G. Behmenyar, F. G. Boyacı San, T. Şener, Fuel Cells 15 (2015) 262–269. doi:[10.1002/face.201300060](https://doi.org/10.1002/face.201300060).
- [123] K. Deshmukh, K. Santhanam, J. Power Sources 159 (2006) 1084–1088. doi:[10.1016/j.jpowsour.2005.12.049](https://doi.org/10.1016/j.jpowsour.2005.12.049).
- [124] A. Verma, A. Jha, S. Basu, J. Power Sources 141 (2005) 30–34. doi:[10.1016/j.jpowsour.2004.09.005](https://doi.org/10.1016/j.jpowsour.2004.09.005).
- [125] A. Verma, S. Basu, J. Power Sources 174 (2007) 180–185. doi:[10.1016/j.jpowsour.2007.07.077](https://doi.org/10.1016/j.jpowsour.2007.07.077).
- [126] F. A. Coowar, G. Vitins, G. O. Mepsted, S. C. Waring, J. A. Horsfall, J. Power Sources 175 (2008) 317–324. doi:[10.1016/j.jpowsour.2007.09.063](https://doi.org/10.1016/j.jpowsour.2007.09.063).
- [127] P.-Y. Olu, B. Gilles, N. Job, M. Chatenet, Electrochem. Commun. 43 (2014) 47–50. doi:[10.1016/j.elecom.2014.02.018](https://doi.org/10.1016/j.elecom.2014.02.018).
- [128] V. Briega-Martos, E. Herrero, J. M. Feliu, Electrochem. Commun. 51 (2015) 144–147. doi:[10.1016/j.elecom.2014.12.024](https://doi.org/10.1016/j.elecom.2014.12.024).
- [129] K. S. Freitas, B. Molina Concha, E. A. Ticianelli, M. Chatenet, Catal. Today 170 (2011) 110–119. doi:[10.1016/j.cattod.2011.01.051](https://doi.org/10.1016/j.cattod.2011.01.051).

- [130] D. A. Finkelstein, N. D. Mota, J. L. Cohen, H. D. Abruña, *J. Phys. Chem. C* 113 (2009) 19700–19712. doi:[10.1021/jp900933c](https://doi.org/10.1021/jp900933c).
- [131] I. Merino-Jimenez, C. P. de Leon, F. Walsh, *Electrochim. Acta.* 133 (2014) 539–545. doi:[10.1016/j.electacta.2014.04.061](https://doi.org/10.1016/j.electacta.2014.04.061).
- [132] A. Tegou, S. Armyanov, E. Valova, O. Steenhaut, A. Hubin, G. Kokkinidis, S. Sotiropoulos, *J. Electroanal. Chem.* 634 (2009) 104–110. doi:[10.1016/j.jelechem.2009.07.016](https://doi.org/10.1016/j.jelechem.2009.07.016).
- [133] M. Simões, S. Baranton, C. Coutanceau, C. Lamy, J.-M. Léger, *ECS Trans.* 25 (2009) 1413–1421. doi:[10.1149/1.3210697](https://doi.org/10.1149/1.3210697).
- [134] L. Yi, W. Wei, C. Zhao, L. Tian, J. Liu, X. Wang, *J. Power Sources* 285 (2015) 325–333. doi:[10.1016/j.jpowsour.2015.03.118](https://doi.org/10.1016/j.jpowsour.2015.03.118).
- [135] H. Cheng, K. Scott, *Electrochim. Acta.* 51 (2006) 3429–3433. doi:[10.1016/j.electacta.2005.09.038](https://doi.org/10.1016/j.electacta.2005.09.038).
- [136] M. Simões, S. Baranton, C. Coutanceau, *J. Phys. Chem. C* 113 (2009) 13369–13376. doi:[10.1021/jp902741z](https://doi.org/10.1021/jp902741z).
- [137] C. Coutanceau, S. Baranton, M. Simões, in: Z.-X. Liang, T. S. Zhao (Eds.), *Catalysts for Alcohol-Fuelled Direct Oxidation Fuel Cells*, RSC Energy and Environment Series, The Royal Society of Chemistry, 2012. doi:[10.1039/9781849734783-00158](https://doi.org/10.1039/9781849734783-00158).
- [138] M. Chatenet, F. Micoud, I. Roche, E. Chainet, *Electrochim. Acta.* 51 (2006) 5459–5467. doi:[10.1016/j.electacta.2006.02.015](https://doi.org/10.1016/j.electacta.2006.02.015).
- [139] F. H. B. Lima, A. M. Pasqualetti, M. B. Molina Concha, M. Chatenet, E. A. Ticianelli, *Electrochim. Acta* 84 (2012) 202. doi:[10.1016/j.electacta.2012.05.030](https://doi.org/10.1016/j.electacta.2012.05.030).
- [140] P. Krishnan, T.-H. Yang, S. G. Advani, A. K. Prasad, *J. Power Sources* 182 (2008) 106–111. doi:[10.1016/j.jpowsour.2008.03.064](https://doi.org/10.1016/j.jpowsour.2008.03.064).
- [141] A. Pasqualetti, P.-Y. Olu, M. Chatenet, F. Lima, *ACS Catal.* 5 (2015) 2778–2787. doi:[10.1021/acscatal.5b00107](https://doi.org/10.1021/acscatal.5b00107).
- [142] K. Wang, J. Lu, L. Zhuang, *Catal. Today* 170 (2011) 99–109. doi:[10.1016/j.cattod.2010.12.023](https://doi.org/10.1016/j.cattod.2010.12.023).
- [143] G. Couturier, D. Kirk, P. Hyde, S. Srinivasan, *Electrochim. Acta.* 32 (1987) 995–1005. doi:[10.1016/0013-4686\(87\)90024-7](https://doi.org/10.1016/0013-4686(87)90024-7).
- [144] G.-j. Wang, Y.-z. Gao, Z.-b. Wang, C.-y. Du, J.-j. Wang, G.-p. Yin, *J. Power Sources* 195 (2010) 185–189. doi:[10.1016/j.jpowsour.2009.06.080](https://doi.org/10.1016/j.jpowsour.2009.06.080).
- [145] B. Sljukic, J. Milikic, D. Santos, C. Sequeira, *Electrochim. Acta.* 107 (2013) 577–583. doi:[10.1016/j.electacta.2013.06.040](https://doi.org/10.1016/j.electacta.2013.06.040).
- [146] J. Hou, M. Yang, M. W. Ellis, R. B. Moore, *J. Electrochem. Soc.* 159 (2012) F412–F418. doi:[10.1149/2.043208jes](https://doi.org/10.1149/2.043208jes).
- [147] B. H. Liu, J. Q. Yang, Z. P. Li, *Int. J. Hydrogen Energy* 34 (2009) 9436–9443. doi:[10.1016/j.ijhydene.2009.09.078](https://doi.org/10.1016/j.ijhydene.2009.09.078).
- [148] D. M. F. Santos, C. A. C. Sequeira, *J. Electroanal. Chem.* 627 (2009) 1–8. doi:[10.1016/j.jelechem.2008.12.009](https://doi.org/10.1016/j.jelechem.2008.12.009).

- [149] B. Molina Concha, M. Chatenet, F. Maillard, E. Ticianelli, F. Lima, R. de Lima, *Phys. Chem. Chem. Phys.* 12 (2010) 11507. URL: <http://pubs.rsc.org/en/content/articlelanding/2010/cp/c003652h#!divAbstract>. doi:10.1039/C003652H.
- [150] M. Chatenet, M. Molina-Concha, N. El-Kissi, G. Parrou, J.-P. Diard, *Electrochim. Acta.* 54 (2009) 4426–4435. doi:10.1016/j.electacta.2009.03.019.
- [151] M. H. Atwan, D. O. Northwood, E. L. Gyenge, *Int. J. Hydrogen Energy* 32 (2007) 3116–3125. doi:10.1016/j.ijhydene.2005.12.022.
- [152] P. He, X. Wang, Y. Liu, X. Liu, L. Yi, *Int. J. Hydrogen Energy* 37 (2012) 11984–11993. doi:10.1016/j.ijhydene.2012.05.054.
- [153] F. Pei, Y. Wang, X. Wang, P. He, Q. Chen, X. Wang, H. Wang, L. Yi, J. Guo, *Int. J. Hydrogen Energy* 35 (2010) 8136–8142. doi:10.1016/j.ijhydene.2010.01.016.
- [154] L. Yi, Y. Song, X. Liu, X. Wang, G. Zou, P. He, W. Yi, *Int. J. Hydrogen Energy* 36 (2011) 15775–15782. doi:10.1016/j.ijhydene.2011.09.019.
- [155] M. G. Hosseini, M. Abdolmaleki, F. Nasirpouri, *Electrochim. Acta.* 114 (2013) 215–222. doi:10.1016/j.electacta.2013.10.012.
- [156] L. Tamasauskaitė-Tamasiunaite, A. Jagminiene, A. Balciunaite, A. Zabielaite, A. Zieliene, L. Naruskevicius, J. Vaiciuniene, A. Selskis, R. Juskenas, E. Norkus, *Int. J. Hydrogen Energy* 38 (2013) 14232–14241. doi:10.1016/j.ijhydene.2013.08.101.
- [157] D. Duan, J. Liang, H. Liu, X. You, H. Wei, G. Wei, S. Liu, *Int. J. Hydrogen Energy* 40 (2015) 488–500. doi:10.1016/j.ijhydene.2014.10.101.
- [158] L. Yi, L. Liu, X. Liu, X. Wang, W. Yi, P. He, X. Wang, *Int. J. Hydrogen Energy* 37 (2012) 12650–12658. doi:10.1016/j.ijhydene.2012.06.065.
- [159] L. Yi, W. Wei, C. Zhao, C. Yang, L. Tian, J. Liu, X. Wang, *Electrochim. Acta.* 158 (2015) 209–218. doi:10.1016/j.electacta.2015.01.111.
- [160] D. M. F. Santos, B. Sljukic, L. Amaral, D. Maccio, A. Saccone, C. A. C. Sequeira, *J. Electrochem. Soc.* 161 (2014) F594–F599. doi:10.1149/2.023405jes.
- [161] B. H. Liu, Z. P. Li, S. Suda, *Electrochim. Acta* 49 (2004) 3097–3105. doi:10.1016/j.electacta.2004.02.023.
- [162] K. Wang, J. Lu, L. Zhuang, *J. Phys. Chem. C* 111 (2007) 7456–7462. doi:10.1021/jp0710483.
- [163] J. Q. Yang, B. H. Liu, S. Wu, *J. Power Sources* 194 (2009) 824–829. doi:10.1016/j.jpowsour.2009.06.034.
- [164] Z. Li, Z. Liu, H. Qin, K. Zhu, B. Liu, *J. Power Sources* 236 (2013) 17–24. doi:10.1016/j.jpowsour.2013.01.175.
- [165] E. Gyenge, *Electrochim. Acta* 49 (2004) 965–978. doi:10.1016/j.electacta.2003.10.008.
- [166] U. Demirci, *Electrochim. Acta* 52 (2007) 5119–5121. doi:10.1016/j.electacta.2006.12.019.

- [167] E. L. Gyenge, *Electrochim. Acta.* 52 (2007) 5122–5123. doi:[10.1016/j.electacta.2006.12.019](https://doi.org/10.1016/j.electacta.2006.12.019).
- [168] H. Dong, R. Feng, X. Ai, Y. Cao, H. Yang, C. Cha, *J. Phys. Chem. B.* 109 (2005) 10896–10901. doi:[10.1021/jp050322v](https://doi.org/10.1021/jp050322v).
- [169] J. Martins, M. Nunes, R. Koch, L. Martins, M. Bazzouai, *Electrochim. Acta.* 52 (2007) 6443–6449. doi:[10.1016/j.electacta.2007.04.066](https://doi.org/10.1016/j.electacta.2007.04.066).
- [170] V. W. S. Lam, D. C. W. Kannangara, A. Alfantazi, E. L. Gyenge, *J. Phys. Chem. C* 115 (2011) 2727–2737. doi:[10.1021/jp108771h](https://doi.org/10.1021/jp108771h).
- [171] M. Simões, S. Baranton, C. Coutanceau, *Electrochim. Acta.* 56 (2010) 580–591. doi:[10.1016/j.electacta.2010.09.006](https://doi.org/10.1016/j.electacta.2010.09.006).
- [172] J. Martins, M. Nunes, *J. Power Sources* 175 (2008) 244–249. doi:[10.1016/j.jpowsour.2007.09.028](https://doi.org/10.1016/j.jpowsour.2007.09.028).
- [173] K. Wang, K. Jiang, J. Lu, L. Zhuang, C. Cha, X. Hu, G. Z. Chen, *J. Power Sources* 185 (2008) 892–894. doi:[10.1016/j.jpowsour.2008.08.069](https://doi.org/10.1016/j.jpowsour.2008.08.069).
- [174] B. Molina Concha, M. Chatenet, *Electrochim. Acta* 54 (2009) 6119–6129. doi:[10.1016/j.electacta.2009.05.027](https://doi.org/10.1016/j.electacta.2009.05.027).
- [175] H. Celikkan, M. Sahin, M. L. Aksu, T. N. Veziroglu, *Int. J. Hydrogen Energy* 32 (2007) 588–593. doi:[10.1016/j.ijhydene.2006.06.065](https://doi.org/10.1016/j.ijhydene.2006.06.065).
- [176] G. Parrou, M. Chatenet, J.-P. Diard, *Electrochim. Acta.* 55 (2010) 9113–9124. doi:[10.1016/j.electacta.2010.07.086](https://doi.org/10.1016/j.electacta.2010.07.086).
- [177] N. M. Marković, P. N. Ross Jr., *Surf. Sci. Reports* 45 (2002) 117–229. doi:[10.1016/S0167-5729\(01\)00022-X](https://doi.org/10.1016/S0167-5729(01)00022-X).
- [178] A. Visintin, J. Canullo, W. Triaca, A. Arvia, *J. Electroanal. Chem. Interfacial. Electrochem.* 239 (1988) 67–89. doi:[10.1016/0022-0728\(88\)80270-5](https://doi.org/10.1016/0022-0728(88)80270-5).
- [179] A. Visintin, W. Triaca, A. Arvia, *J. Electroanal. Chem. Interfacial. Electrochem.* 284 (1990) 465–480. doi:[10.1016/0022-0728\(90\)85051-6](https://doi.org/10.1016/0022-0728(90)85051-6).
- [180] K. Itaya, S. Sugawara, K. Sashikata, N. Furuya, *J. Vac. Sci. Technol. A* 8 (1990) 515. URL: <http://dx.doi.org/10.1116/1.576378>.
- [181] A. Björling, E. Ahlberg, J. M. Feliu, *Electrochem. Commun.* 12 (2010) 359–361. doi:[10.1016/j.elecom.2009.12.034](https://doi.org/10.1016/j.elecom.2009.12.034).
- [182] N. Furuya, M. Shibata, *Journal of Electroanalytical Chemistry* 467 (1999) 85–91. doi:[10.1016/S0022-0728\(99\)00077-7](https://doi.org/10.1016/S0022-0728(99)00077-7).
- [183] N. Markovic, H. Gasteiger, P. Ross Jr., *Journal of Physical Chemistry* 100 (1996) 6715–6721. doi:[10.1021/jp9533382](https://doi.org/10.1021/jp9533382).
- [184] T. J. Schmidt, P. N. Ross Jr., N. M. Markovic, *J. Electroanal. Chem.* 524–525 (2002) 252–260. doi:[10.1016/S0022-0728\(02\)00683-6](https://doi.org/10.1016/S0022-0728(02)00683-6).
- [185] N. M. Markovic, S. T. Sarraf, H. A. Gasteiger, P. N. Ross Jr, *J. Chem. Soc., Faraday Trans.* 92 (1996) 3719–3725. doi:[10.1039/FT9969203719](https://doi.org/10.1039/FT9969203719).

- [186] F. Maillard, S. Schreier, M. Hanzlik, E. R. Savinova, S. Weinkauff, U. Stimming, *Phys. Chem. Chem. Phys.* 7 (2005) 385–393. doi:[10.1039/B411377B](https://doi.org/10.1039/B411377B).
- [187] F. Maillard, M. Eikerling, O. V. Cherstiouk, S. Schreier, E. Savinova, U. Stimming, *Faraday Discuss.* 125 (2004) 357–377. doi:[10.1039/B303911K](https://doi.org/10.1039/B303911K).
- [188] J. Rooke, C. d. M. Passos, M. Chatenet, R. Sescousse, T. Budtova, S. Berthon-Fabry, R. Mosdale, F. Maillard, *J. Electrochem. Soc.* 158 (2011) B779–B789. doi:[10.1149/1.3585744](https://doi.org/10.1149/1.3585744).
- [189] G. Bergeret, P. Gallezot, in: *Handbook of heterogeneous catalysis*, G. Ertl, H. Knözinger, J. Weitkamp (Eds.), Wiley, Weinheim, 1997, pp. 439–464. doi:[10.1002/9783527610044.hetcat0038](https://doi.org/10.1002/9783527610044.hetcat0038).
- [190] G. Rostamikia, M. J. Janik, *Electrochim. Acta* 55 (2010) 1175–1183. doi:[10.1016/j.electacta.2009.10.002](https://doi.org/10.1016/j.electacta.2009.10.002).
- [191] P. Ruvinskiy, A. Bonnefont, M. Houllé, C. Pham-Huu, E. Savinova, *Electrochim. Acta.* 55 (2010) 3245–3256. doi:[10.1016/j.electacta.2010.01.033](https://doi.org/10.1016/j.electacta.2010.01.033).
- [192] P. Ruvinskiy, A. Bonnefont, M. Bayati, E. Savinova, *Phys. Chem. Chem. Phys.* 12 (2010) 15207–15216. doi:[10.1039/c0cp00593b](https://doi.org/10.1039/c0cp00593b).
- [193] P. Ruvinskiy, A. Bonnefont, C. Pham-Huu, E. Savinova, *Langmuir* 27 (2011) 9018–9027. doi:[10.1021/la2006343](https://doi.org/10.1021/la2006343).
- [194] P. Ruvinskiy, A. Bonnefont, E. Savinova, *Electrochim. Acta.* 84 (2012) 174–186. doi:[10.1016/j.electacta.2012.03.134](https://doi.org/10.1016/j.electacta.2012.03.134).
- [195] M. Rouhet, S. Bozdech, A. Bonnefont, E. Savinova, *Electrochem. Commun.* 33 (2013) 111–114. doi:[10.1016/j.elecom.2013.05.003](https://doi.org/10.1016/j.elecom.2013.05.003).
- [196] Z. Jusys, R. J. Behm, *J. Phys. Chem. B.* 105 (2001) 10874–10883. doi:[10.1021/jp011510y](https://doi.org/10.1021/jp011510y).
- [197] L. C. Nagle, J. F. Rohan, *Electrochem. Solid State Lett.* 8 (2005) C77–C80. doi:[10.1149/1.1883905](https://doi.org/10.1149/1.1883905).
- [198] O. A. Sadik, H. Xu, A. Sargent, *J. Electroanal. Chem.* 583 (2005) 167–175. doi:[10.1016/j.jelechem.2005.05.013](https://doi.org/10.1016/j.jelechem.2005.05.013).
- [199] B. Molina Concha, M. Chatenet, C. Coutanceau, F. Hahn, *Electrochem. Commun.* 11 (2009) 223–226. doi:[10.1016/j.elecom.2008.11.018](https://doi.org/10.1016/j.elecom.2008.11.018).
- [200] L. Gao, B. E. Conway, *Electrochim. Acta.* 39 (1994) 1681–1693. URL: [http://dx.doi.org/10.1016/0013-4686\(94\)85154-9](http://dx.doi.org/10.1016/0013-4686(94)85154-9).
- [201] M. C. Sison Escaño, E. Gyenge, R. Lacdao Arevalo, H. Kasai, *J. Phys. Chem. C* 115 (2011) 19883–19889. doi:[10.1021/jp207768e](https://doi.org/10.1021/jp207768e).
- [202] G. Rostamikia, M. J. Janik, *Energy Environ. Sci.* 3 (2010) 1262–1274. doi:[10.1039/c0ee00115e](https://doi.org/10.1039/c0ee00115e).
- [203] G. Rostamikia, M. J. Janik, *J. Electrochem. Soc.* 156 (2009) B86–B92. doi:[10.1149/1.3010382](https://doi.org/10.1149/1.3010382).
- [204] M. Koper, J. Sluyters, *J. Electroanal. Chem.* 303 (1991) 73–94. doi:[10.1016/0022-0728\(91\)85117-8](https://doi.org/10.1016/0022-0728(91)85117-8).

- [205] S. Treimer, A. Tang, D. C. Johnson, *Electroanalysis* 14 (2002) 165–171. URL: [http://onlinelibrary.wiley.com/doi/10.1002/1521-4109\(200202\)14:3<165::AID-ELAN165>3.0.CO](http://onlinelibrary.wiley.com/doi/10.1002/1521-4109(200202)14:3<165::AID-ELAN165>3.0.CO).
- [206] E. G. Machado, E. Sitta, F. H. de Lima, J. Lee, H. Varela, *Electrochem. Commun.* 162 (2012) 107–109. doi:[10.1016/j.elecom.2011.12.011](https://doi.org/10.1016/j.elecom.2011.12.011).
- [207] J. Clavilier, D. Armand, S. G. Sun, M. Petit, *J. Electroanal. Chem. Interfacial. Electrochem.* 205 (1986) 267–277. doi:[10.1016/0022-0728\(86\)90237-8](https://doi.org/10.1016/0022-0728(86)90237-8).
- [208] J. Clavilier, K. El Actii, M. Petit, A. Rodes, M. Zamakhchari, *J. Electroanal. Chem. Interfacial. Electrochem.* 295 (1990) 333–356. doi:[10.1016/0022-0728\(90\)85026-2](https://doi.org/10.1016/0022-0728(90)85026-2).
- [209] O. Cherstiouk, P. Simonov, E. Savinova, *Electrochim. Acta.* 48 (2003) 3851–3860. doi:[10.1016/S0013-4686\(03\)00519-X](https://doi.org/10.1016/S0013-4686(03)00519-X).
- [210] O. Cherstiouk, P. Simonov, V. Zaikovskii, E. Savinova, *Electrochim. Acta.* 554–555 (2003) 241–251. doi:[10.1016/S0022-0728\(03\)00198-0](https://doi.org/10.1016/S0022-0728(03)00198-0).
- [211] W. X. Chen, J. Y. Lee, Z. Liu, *Chem. Commun.* 21 (2002) 2588 – 2589. doi:[10.1039/b208600j](https://doi.org/10.1039/b208600j).
- [212] F. Berthier, J.-P. Diard, C. Montella, *Electrochim. Acta.* 44 (1999) 2397–2404. doi:[10.1016/S0013-4686\(98\)00370-3](https://doi.org/10.1016/S0013-4686(98)00370-3).

